

# **NEW PHYSICS SEARCHES AT LONG-BASELINE EXPERIMENTS**

*By*  
**DIPYAMAN PRAMANIK**  
**PHYS08201305008**

**Harish-Chandra Research Institute, Allahabad**

*A thesis submitted to the*  
*Board of Studies in Physical Sciences*  
*In partial fulfillment of requirements*  
*for the Degree of*  
**DOCTOR OF PHILOSOPHY**  
*of*  
**HOMI BHABHA NATIONAL INSTITUTE**



**August, 2019**



# Homi Bhabha National Institute<sup>1</sup>

## Recommendations of the Viva Voce Committee

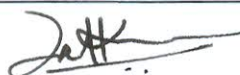
As members of the Viva Voce Committee, we certify that we have read the dissertation prepared by Dipyaman Pramanik entitled "New Physics Searches at Long-baseline experiments" and recommend that it may be accepted as fulfilling the thesis requirement for the award of Degree of Doctor of Philosophy.

Chairman – Prof. Dileep Jatkar



Date: 27/1/2020

Guide / Convener – Prof. Sandhya Choubey



Date: 27/1/2020

Examiner - Prof. S. Uma Sankar



Date:

27 Jan 2020

Member 1- Areshkrishna Datta



Date:

27/01/2020

Member 2- Santosh Kumar Rai



Date:

27/1/2020

Member 3- Tapas Kumar Das



Date:

27/1/2020

Final approval and acceptance of this thesis is contingent upon the candidate's submission of the final copies of the thesis to HBNI.

I/We hereby certify that I/we have read this thesis prepared under my/our direction and recommend that it may be accepted as fulfilling the thesis requirement.

Date: 27-01-2020

Place: Prayagraj



Prof. Sandhya Choubey

Guide

<sup>1</sup> This page is to be included only for final submission after successful completion of viva voce.





## STATEMENT BY AUTHOR

This dissertation has been submitted in partial fulfillment of requirements for an advanced degree at Homi Bhabha National Institute (HBNI) and is deposited in the Library to be made available to borrowers under rules of the HBNI.

Brief quotations from this dissertation are allowable without special permission, provided that accurate acknowledgement of source is made. Requests for permission for extended quotation from or reproduction of this manuscript in whole or in part may be granted by the Competent Authority of HBNI when in his or her judgment the proposed use of the material is in the interests of scholarship. In all other instances, however, permission must be obtained from the author.



Dipyaman Pramanik



## DECLARATION

I, hereby declare that the investigation presented in the thesis has been carried out by me. The work is original and has not been submitted earlier as a whole or in part for a degree / diploma at this or any other Institution / University.



Dipyaman Pramanik




## List of Publications arising from the thesis

### Journal

1. “A combined study of source, detector and matter non-standard neutrino interactions at DUNE”, Mattias Blennow, Sandhya Choubey, Tommy Ohlsson, Dipyaman Pramanik, Sushant K. Raut, *JHEP*, **2016**, 08, 090.
2. “Constraints on sterile neutrino oscillations using DUNE near detector”, Sandhya Choubey, Dipyaman Pramanik, *Phys. Lett.*, **2017**, B764, 135-141.
3. “Imprints of a light sterile neutrino at DUNE, T2HK and T2HKK” Sandhya Choubey, Debajyoti Dutta, Dipyaman Pramanik, *Phys. Rev.*, **2017**, D96, no.5, 056026.
4. “A study of invisible neutrino decay at DUNE and its effects on  $\theta_{23}$  measurement”, Sandhya Choubey, Srubabati Goswami, Dipyaman Pramanik, *JHEP*, **2018**, 02, 055.
5. “Measuring the sterile neutrino CP phase at DUNE and T2HK”, Sandhya Choubey, Debajyoti Dutta, Dipyaman Pramanik, *Eur. Phys. J.*, **2018**, C78, no.4, 339.
6. “Invisible neutrino decay in the light of NOvA and T2K data”, Sandhya Choubey, Debajyoti Dutta, Dipyaman Pramanik, *JHEP*, **2018**, 08, 141.
7. “Exploring fake solutions in the sterile neutrino sector at long-baseline experiments”, Sandhya Choubey, Debajyoti Dutta, Dipyaman Pramanik, *Eur. Phys. J.*, **2019**, C79, no.11, 968.

### Conferences

1. INVISIBLES16, Univ. Of Padova, Italy (Presented poster) (2016)
2. DAE-BRNS HIGH ENERGY PHYSICS SYMPOSIUM, Univ. Of Delhi, India (Presented talk) (2016)
3. WHEPP-XV, IISER Bhopal, India, (Presented talk) (2017)
4. NuHoRIzons VII, HRI, India (Presented poster) (2018)
5. INVISIBLES18, KIT, Germany (Presented talk & poster) (2018)
6. DAE-BRNS HIGH ENERGY PHYSICS SYMPOSIUM, IIT-Madras, India (Presented talk) (2018)

  
Dipyaman Pramanik



## **DEDICATIONS**

Dedicated to my grandfather





## ACKNOWLEDGEMENTS

First and foremost, I would like to express my most profound respect and sincere gratitude to my supervisor Prof. Sandhya Choubey for introducing me to the world of neutrinos and being an excellent teacher and a perfect guide. I am grateful to her for her continuous effort, unlimited patience and unremitting encouragement. I thank her for everything, from professional guidance to motivation for building confidence.

I am grateful to all my collaborators with whom I have done my research work during the journey of PhD, especially Dr Debajyoti Dutta, Dr Sushant Kr. Raut, Dr Monojit Ghosh, Prof Srubabati Goswami, Prof. Tommy Ohlsson, Prof. Mattias Blennow and Prof. Manimala Mitra. They have always enriched me with their in-depth knowledge and experience on the subject.

I would like to express my deepest gratitude to all the faculties of HRI, who taught me various topics during course work. Lectures of these faculties I made the course work an enjoyable experience. I thank Prof. Kauoro Hagiwara for a series of fascinating lectures in particle physics.

I can not but thank my friends like Chiranjib, Sreetama, Shouvik, Saubhik, Suparna, Saptarshi, Ratul, Tanaya, Ratul, Susovan, Samyadeb, Suman, Rudra, Kathakali, Ankur, Saikat, Titas, Sauri, Shiladitya, Sarif, Waleed Atri, Sankha, Stav, Nirnoy, Srijon, Chirag, Sohail, Alam, Abhass, Deepak, Samiran and Rupam. These are the people who did not let me know how six years passed at HRI.

Finally, I thank my family members, especially my parents for supporting and encouraging me from the very beginning of my life; and I must thank Sujit Debnath, the person who put the seed to love physics during my school days.



## Contents

<b>SUMMARY</b>	<b>1</b>
<b>LIST OF FIGURES</b>	<b>2</b>
<b>LIST OF TABLES</b>	<b>12</b>
<b>1 Introduction</b>	<b>15</b>
1.1 Neutrinos: nature's invisible . . . . .	15
1.2 Where do we get neutrinos? . . . . .	17
1.2.1 Natural sources . . . . .	17
1.2.2 Artificial sources . . . . .	18
1.3 Neutrino oscillation, a signature of physics beyond the standard model . .	19
1.3.1 Solar neutrino problem . . . . .	20
1.3.2 Atmospheric neutrinos . . . . .	21
1.3.3 Flavour oscillation of neutrinos . . . . .	21

1.4	Long-baseline experiments, a probe to study neutrino oscillation . . . . .	23
1.5	Possibility of new physics at long-baseline experiments . . . . .	24
1.6	Thesis overview . . . . .	25
<b>2</b>	<b>Standard Neutrino Oscillation</b>	<b>27</b>
2.1	Neutrino oscillation in vacuum . . . . .	27
2.1.1	Neutrino oscillation in vacuum: 2 generations . . . . .	28
2.1.2	Neutrino oscillation in vacuum: N generations . . . . .	32
2.2	Neutrino oscillation in matter . . . . .	35
2.2.1	Effective potential in matter . . . . .	35
2.2.2	Neutrino oscillation in matter: 2 generations . . . . .	37
2.2.3	Neutrino oscillations in matter: 3 generations . . . . .	39
2.3	Ambiguities in measuring the oscillation parameters . . . . .	42
2.3.1	The hierarchy- $\delta_{CP}$ degeneracy . . . . .	43
2.3.2	The octant & $\theta_{23} - \delta_{CP}$ degeneracy . . . . .	45
2.3.3	$\theta_{13} - \delta_{CP}$ degeneracy . . . . .	46
2.3.4	Generalized mass-hierarchy degeneracy . . . . .	47
<b>3</b>	<b>Long-Baseline Experiments</b>	<b>49</b>
3.1	Overview of accelerator based long-baseline experiments . . . . .	50
3.1.1	Physics at long-baseline experiments . . . . .	50
3.1.2	Backgrounds . . . . .	52

3.2	Presently running experiments . . . . .	53
3.2.1	NOvA . . . . .	53
3.2.2	T2K . . . . .	54
3.3	Future long-baseline experiments . . . . .	56
3.3.1	DUNE . . . . .	56
3.3.2	T2HK . . . . .	58
3.3.3	T2HKK . . . . .	60
<b>4</b>	<b>Sterile neutrino at long-baseline experiments</b>	<b>61</b>
4.1	Sterile neutrino formalism . . . . .	63
4.2	Constraining sterile neutrinos from DUNE near detector . . . . .	64
4.2.1	Probability at near detector . . . . .	65
4.2.2	Events and statistical analysis . . . . .	66
4.3	Imprints of a light sterile neutrino at DUNE and T2HK/ T2HKK . . . . .	72
4.3.1	Simulation procedure . . . . .	72
4.3.2	Numerical probabilities . . . . .	75
4.3.3	CP sensitivity . . . . .	79
4.3.4	Mass hierarchy sensitivity . . . . .	84
4.3.5	Octant discovery . . . . .	87
4.4	Measuring the sterile neutrino CP phases at DUNE and T2HK . . . . .	89
4.4.1	Sterile neutrino probability and simulation . . . . .	91

4.4.2	Measurement of the sterile phases . . . . .	95
4.4.3	Measurement of the mixing angles . . . . .	101
4.5	A new degeneracy in the sterile neutrino sector at long-baseline experiments	107
4.5.1	Fake solution in the appearance probability . . . . .	107
4.5.2	Numerical results . . . . .	111
<b>5</b>	<b>NSI at long-baseline experiments</b>	<b>117</b>
5.1	Neutrino oscillations with non-standard interactions . . . . .	118
5.2	Simulation results . . . . .	121
5.2.1	Effect on precision measurements at DUNE . . . . .	124
5.2.2	Constraining NSI parameters at DUNE . . . . .	127
5.2.3	Correlations between source/detector and matter NSIs . . . . .	128
5.2.4	Effect of statistics . . . . .	130
<b>6</b>	<b>Invisible neutrino decay at long-baseline experiments</b>	<b>135</b>
6.1	Propagation of neutrino in presence of decay . . . . .	137
6.2	Invisible neutrino decay from NOvA and T2K data . . . . .	138
6.2.1	Simulation details . . . . .	139
6.2.2	Results . . . . .	140
6.3	Invisible neutrino decay at DUNE and its effect on $\theta_{23}$ measurement . . .	147
6.3.1	Experiment and simulation details . . . . .	148
6.3.2	Numerical results . . . . .	149

<b>7</b>	<b>Conclusions and Future Prospects</b>	<b>165</b>
7.1	Conclusions . . . . .	165
7.2	Future Prospects . . . . .	173
	<b>References</b>	<b>176</b>





## SUMMARY

In this thesis, we looked at various new physics scenarios at long-baseline experiments. We studied sterile neutrino in the context of various long-baseline experiments. First, we studied the capability of DUNE near detector to probe the LSND parameter space. We simulated DUNE for 5 years in neutrino and 5 years in antineutrino mode. We varied baseline and fiducial mass of the near detector. We found that 595 m baseline gives the optimum sensitivity among three benchmark points 595 m, 1 km and 3 km, chosen by us. We also found that sensitivity increases with the fiducial mass; however, above a certain mass, the sensitivity saturates. We also studied the effect of systematic uncertainties and the effect of decay pipe length on the performance, but we did not find much effect. Next, we studied the effect of sterile neutrino on the standard measurement of T2HK/ T2HKK, DUNE and their combination. We saw that when the mass hierarchy is known, the CP-violation sensitivity, in general, reduces for all cases, especially T2HK; however, the presence of sterile state sometimes helps the sensitivity for some combination of phases. We also studied the effect of sterile neutrino on the octant and mass hierarchy at these experiments. Again we found that sometimes mass hierarchy (MH) and octant sensitivity increases and sometimes they decrease. For T2HK, the MH sensitivity is increased a lot if the sterile mixing angles are chosen to be large. After that, we investigated the expected sensitivity to the sterile phase  $\delta_{CP}$  from DUNE, T2HK and T2HKK. We found that all these experiments can measure the sterile phase pretty well, but T2HK has the best sensitivity and DUNE has worst sensitivity. For example, if  $\delta_{24} = 90^\circ$ , DUNE, T2HK and T2HKK can constrain  $\delta_{CP}$  between  $23.35^\circ \leq \delta_{24} \leq 180^\circ$ ,  $30.10^\circ \leq \delta_{24} \leq 147.9^\circ$  and  $26.27^\circ \leq \delta_{24} \leq 157.62^\circ$ , respectively at  $2\sigma$ . We also studied the effect of sterile phases on the measurement of standard CP-phase. We found that the  $\delta_{CP}$  is worsened due to the presence of sterile phase and the effect is maximum for DUNE and almost negligible for T2HK. Then, we showed the existence of a fake solution in the  $\nu_\mu \rightarrow \nu_e$  appearance probability, coming from  $\Delta m_{41}^2$ . A fake solution is obtained in  $P_{\mu e}$  at the oscillation maximum for  $\Delta m_{41}^2 = \frac{1}{2}\Delta m_{31}^2$  when the true  $\Delta m_{41}^2$  is large enough such

that the fast oscillations due to  $\Delta m_{41}^2$  get averaged out and the condition required for this is  $\delta_{13} + \delta_{24} = 0$ . We also show that this fake solution goes away if we add the  $\nu_\mu \rightarrow \nu_\mu$  disappearance channel.

We studied source, detector and matter NSI in the context of DUNE. We studied the expected sensitivity of DUNE to the NSI parameters. The bound does not improve much for source-detector NSIs, but the bound improves substantially for matter NSIs (up to a factor of about 15). We found appearances of fake solutions in the  $\theta_{23}$ - $\delta_{CP}$  plane under the assumption of both matter as well as source-detector NSIs in the data. Some correlations between source/detector and matter NSIs are observed in the analysis.

We discussed invisible neutrino decay in the context of present and future long-baseline experiments. First, we analysed the latest T2K and NOvA data to constrain the neutrino decay lifetime. We found that both the experiments prefer neutrino decay slightly over stable neutrino. The best-fit for  $\tau_3/m_3 = 5.05 \times 10^{-12}$  s/eV for the combined fit, and we found the lower bound on  $\tau_3/m_3$  as  $\tau_3/m_3 \geq 1.50 \times 10^{-12}$  s/eV at  $3\sigma$  level. We also found that if we include decay in our fit, the best-fit values for  $\sin^2 \theta_{23}$  and  $\Delta m_{32}^2$  change significantly. The best-fit  $(\sin^2 \theta_{23}, \Delta m_{32}^2)$  obtained for the standard oscillation case from analysis of NOvA, T2K and both experiments combined are  $(0.45, 2.41 \times 10^{-3} \text{ eV}^2)$ ,  $(0.52, 2.56 \times 10^{-3} \text{ eV}^2)$  and  $(0.46, 2.51 \times 10^{-3} \text{ eV}^2)$  respectively. On including decay in the fit, the corresponding best-fit points become  $(0.48, 2.39 \times 10^{-3} \text{ eV}^2)$  for NOvA,  $(0.62, 2.62 \times 10^{-3} \text{ eV}^2)$  for T2K and  $(0.48, 2.52 \times 10^{-3} \text{ eV}^2)$  for NOvA and T2K combined. Next, we studied the sensitivity of DUNE to constrain  $\tau_3$  and we obtained expected bound  $\tau_3/m_3 \geq 4.50 \times 10^{-11}$  s/eV at 90% confidence level for normal hierarchy (NH) using 5+5 years of DUNE simulation data. If we assume  $\tau_3/m_3 = 1.2 \times 10^{-11}$  s/eV in data, we found that the allowed region after 5+5 years will be  $1.71 \times 10^{-11} > \tau_3/m_3 > 9.29 \times 10^{-12}$  s/eV at  $3\sigma$ . We found an interesting correlation between the  $\theta_{23}$  and  $\tau_3/m_3$ . We found that the best-fit of  $\theta_{23}$  shifts towards a lower value in both octants and thus gives an erroneous value of  $\theta_{23}$  if decay is present but not considered in the fit.

## List of Figures

2.1	Hierarchy degeneracy for $\nu_\mu \rightarrow \nu_e$ channel at 810 km baseline. The left panel is for neutrino and the right panel is for antineutrino. . . . .	44
2.2	Hierarchy degeneracy for $\nu_\mu \rightarrow \nu_e$ channel at 1300 km baseline. The left panel is for neutrino and the right panel is for antineutrino. . . . .	45
2.3	Octant degeneracy for $\nu_\mu \rightarrow \nu_e$ channel. The left panel is for neutrino and the right panel is for antineutrino. . . . .	46
4.1	$P_{\mu e}$ probability at 595 m for different sterile neutrino oscillation parameters. . . . .	66
4.2	Left: 5 years of events at neutrino appearance channel for the case with sterile neutrino at a 5t near detector kept at a baseline of 595 m. Right: 5 years of events at neutrino appearance channel for the case with no sterile neutrino with same detector configuration. . . . .	67
4.3	Left: Exclusion contours at 3 & 4 $\sigma$ confidence levels for near detector of mass 5t with different baselines. Right: Exclusion contours at 3 & 4 $\sigma$ confidence levels for near detector at 595 m baseline with different detector mass. We consider an exposure of 5+5 for $\nu_\mu + \bar{\nu}_\mu$ . . . . .	68

4.4	Left:Exclusion contours for at 3 & 4 $\sigma$ confidence levels for different energy calibration errors for DUNE near detector at 595 m baseline with 5t mass. Right: Exclusion contours for 3 & and 4 $\sigma$ confidence levels for different signal normalisation error. We consider an exposure of 5+5 for $\nu_\mu + \bar{\nu}_\mu$ . . . . .	68
4.5	The left (right) panel shows the result for running DUNE for 5 years in the neutrino (antineutrino) mode. In both panels, the solid lines are the exclusion curves for 3 $\sigma$ C.L. and the dashed lines are the exclusion curves for 4 $\sigma$ C.L. The red lines are for 5 t detector and green lines are for 400 t detectors, while the yellow shaded region is the 90% C.L. LSND allowed region. . . . .	70
4.6	Expected sensitivity at the 3 $\sigma$ and 4 $\sigma$ C.L. for the case when there is a sterile neutrino in the data. The black star is the value for which the data is generated. The blue contour shows the 3 $\sigma$ and the green contour shows the 4 $\sigma$ C.L. . . . .	71
4.7	$P_{\mu e}$ vs $\bar{P}_{\mu e}$ bi-probability plots for JD and KD. The first row shows the plots for JD (295 km and $E = 0.5$ GeV ) and the second row shows the plots for KD (1100 km and $E = 0.66$ GeV). The left column is for lower set of sterile mixing angles and the right column is for higher set of sterile mixing angles. The shaded regions show the variation of the bi-probability when the sterile phases $\delta_{24}$ and $\delta_{34}$ are varied within $[-\pi, \pi]$ . The solid curves describe the 3+0 case. The different colours correspond to different combinations of mass hierarchy and octant of $\theta_{23}$ . . . . .	76
4.8	CP-asymmetry at JD(left) and KD(right). The bands represent the variation of $\delta_{24}$ and $\delta_{34}$ . . . . .	77

4.9	MH-asymmetry as a function of $\delta_{13}$ for JD(left) and KD(right). The bands represent the variation of $\delta_{24}$ and $\delta_{34}$ . . . . .	79
4.10	The expected CP violation sensitivity of T2HK (JD $\times$ 2), T2HKK (JD+KD) and DUNE+JD+KD under the assumption that we do not know the source of its violation. The bands correspond to variation of $\delta_{24}$ and $\delta_{34}$ in the true parameter space. The results are for true normal hierarchy. . . . .	80
4.11	The expected CP violation sensitivity of T2HK (JD $\times$ 2), T2HKK (JD+KD) and DUNE+JD+KD under the assumption that we know the source of its violation and it is due to $\delta_{13}$ . The bands correspond to variation of $\delta_{24}$ and $\delta_{34}$ in the true parameter space. The results are for true normal hierarchy. .	82
4.12	The expected CP violation sensitivity of T2HK (JD $\times$ 2), T2HKK (JD+KD) and DUNE+JD+KD under the assumption that we know the source of its violation and it is due to $\delta_{24}$ . The bands correspond to variation of $\delta_{13}$ and $\delta_{34}$ in the true parameter space. The results are for true normal hierarchy. .	82
4.13	The expected CP violation sensitivity of T2HK (JD $\times$ 2), T2HKK (JD+KD) and DUNE+JD+KD under the assumption that we do not know the source of its violation as well as the hierarchy. The bands correspond to variation of $\delta_{24}$ and $\delta_{34}$ in the true parameter space. The results are for true normal hierarchy. . . . .	83
4.14	The expected mass-hierarchy sensitivity of T2HK (JD $\times$ 2) and T2HKK (JD+KD). The upper panel is for true NH while the lower panel is for true IH. The bands correspond to the variation of the sterile phases in the true parameter space. . . . .	85

4.15	The expected octant discovery potential of T2HK (JD×2) and T2HKK (JD+KD). In the LO (HO), we consider $\theta_{23} = 40.3^\circ$ ( $49.7^\circ$ ) as the true value. The upper panel is for T2HK (JD×2) while the lower panel is for T2HKK (JD+KD). The bands correspond to the variation of the sterile phases. . . . .	87
4.16	The octant discovery potential of DUNE+T2HKK(JD+KD). . . . .	88
4.17	The $\chi^2$ vs. $\delta_{24}(\text{test})$ . The black curves are for T2HK, the red curves are for T2HKK and the blue curves are for DUNE. The top left panel is for $\delta_{24}(\text{true}) = 0^\circ$ , the top right panel is for $\delta_{24}(\text{true}) = 90^\circ$ , the bottom left panel is for $\delta_{24}(\text{true}) = -90^\circ$ and the bottom right panel is for $\delta_{24}(\text{true}) = 180^\circ$ . . . . .	94
4.18	Top panels show the appearance event spectrum for DUNE (left) and T2HK (right) for different values of $\delta_{24}$ . The green lines are for $\delta_{24} = -90^\circ$ , red lines are for $\delta_{24} = 0^\circ$ , the blue lines are for $\delta_{24} = 90^\circ$ and the dark red lines are for $\delta_{24} = 180^\circ$ . The lower panels show the appearance event rates at the oscillation maximum as a function of $\delta_{24}$ for DUNE (left) and T2HK (right). While the black curves give the expected number of events, the green and yellow bands show the $1\sigma$ and $3\sigma$ statistical uncertainties. . . . .	97
4.19	The expected 95 % C.L. contours in $\delta_{13}(\text{test})$ vs $\delta_{24}(\text{test})$ , where 95 % C.L. is defined as $\Delta\chi^2 = 5.99$ for 2 parameters. The stars show the value of $\delta_{13}(\text{true})$ and $\delta_{24}(\text{true})$ taken in the data. The top left (right) panel is for $\delta_{24} = 0^\circ$ ( $\delta_{24} = 90^\circ$ ) and the bottom left (right) panel is for $\delta_{24} = -90^\circ$ ( $\delta_{24} = 180^\circ$ ). The black dotted curve is for T2HK, the red dash-dotted curve is for T2HKK, the blue dashed curve is for DUNE, the grey solid curve is for DUNE+T2HK and the magenta solid curve is for DUNE + T2HKK. . . . .	99

- 4.20 The expected precision on  $\delta_{13}$  for the 3+0 and 3+1 scenarios. The left panel is for T2HK, the middle panel is for T2HKK and the right panel is for DUNE. The blue dash-dotted curves are for the 3+0 case and the red dashed curves are for 3+1 case in both theory and data. The curves are  $\delta_{24}(\text{true}) = -90^\circ$ . . . . . 100
- 4.21 The left panel shows the expected 95 % C.L contours in the  $\sin^2 \theta_{14}(\text{test})$ - $\Delta m_{41}^2(\text{test})$  plane, while the right panel shows the 95 % C.L. contours in the  $\sin^2 \theta_{24}(\text{test})$ - $\Delta m_{41}^2(\text{test})$  plane. The colour code is same as Fig. 4.19. . . . . 102
- 4.22 The expected 95 % C.L contours in  $\sin^2 \theta_{24}(\text{test})$ - $\sin^2 \theta_{14}(\text{test})$  plane. The colour code is same as Fig. 4.19. . . . . 103
- 4.23 The expected 95 % C.L exclusion curves in the  $\sin^2 \theta_{14}(\text{test})$ - $\Delta m_{41}^2(\text{test})$  plane shown in the left panel and in the  $\sin^2 \theta_{24}(\text{test})$ - $\Delta m_{41}^2(\text{test})$  plane shown in the right panel. The data in these plots correspond to standard three-generation oscillation scenario with no sterile mixing while the fit is done in the 3+1 framework to obtain the exclusion contours. The colour code is same as Fig. 4.19. . . . . 104
- 4.24 The expected 95 % C.L exclusion curves in the  $\sin^2 \theta_{14}(\text{test})$ - $\sin^2 \theta_{24}(\text{test})$  plane for a fixed  $\Delta m_{41}^2 = 1.0 \text{ eV}^2$ . The colour code is same as Fig. 4.19. . . . . 106
- 4.25 Appearance probability as a function of energy for T2HK (left panels) and DUNE (right panels). The solid curves are for the case  $\Delta m_{41}^2 = 1.6 \text{ eV}^2$  after averaging over the fast oscillations induced by the high mass-squared difference, while the dashed curves are for the case when  $\Delta m_{41}^2 = \frac{1}{2} \Delta m_{31}^2$ . The red solid and blue curves are for  $\Delta m_{21}^2 = 7.5 \times 10^{-3} \text{ eV}^2$  while the green and black curves are for the approximate case of  $\Delta m_{21}^2 = 0$ . The fast oscillations due  $\Delta m_{41}^2$  has been averaged out by Gaussian smearing. . . . . 110

4.26	$\chi^2$ as a function of $\Delta m_{41}^2$ for different combinations of CP-violating phases (left panels) and various values of $\Delta m_{31}^2$ (right panels). Top panels are for T2HK while bottom panels are for DUNE. . . . .	112
4.27	The figure shows the positions of the fake solutions. The red data points show the positions of the fake solutions in $\Delta m_{41}^2$ as a function of $\Delta m_{31}^2$ and the black straight line is a linear fit to red points corresponding to $\Delta m_{41}^2 = (1/2)\Delta m_{31}^2$ . . . . .	114
4.28	Impact of disappearance channel on removing the $\Delta m_{41}^2$ fake solution. The blue lines show the $\chi^2$ as a function of $\Delta m_{41}^2$ (test) for the appearance channel only for T2HK (left panel) and DUNE (right panel). The red lines show the corresponding $\chi^2$ when both disappearance and appearance data are taken together in the fit. . . . .	114
5.1	Variation in the neutrino oscillation probability $P_{\mu e}$ as a function of neutrino energy $E$ with some of the NSI parameters varied in their allowed range. The central dark curve corresponds to the case of no NSIs. The values of the standard oscillation parameters used in generating these figures are $\theta_{12} = 33.5^\circ$ , $\theta_{13} = 8.48^\circ$ , $\theta_{23} = 42^\circ$ , $\delta_{CP} = -90^\circ$ , $\Delta m_{21}^2 = 7.50 \times 10^{-5} \text{ eV}^2$ and $\Delta m_{31}^2 = 2.45 \times 10^{-3} \text{ eV}^2$ . . . . .	122
5.2	Sensitivity of DUNE in the $\theta_{23} - \delta_{CP}$ plane. The simulated true values of these parameters are $42^\circ$ and $-90^\circ$ , respectively. The contours enclose the allowed region at 90 % credible regions obtained by marginalizing over only the standard parameters, standard parameters and source/detector NSI parameters, standard parameters and matter NSI parameters, and standard parameters and all NSI parameters. In the left (right) panel, the true values of the NSI parameters are taken to be zero (non-zero). . . . .	125
5.3	Precision in the standard oscillation parameters in the presence of NSIs at DUNE. The contours shown correspond to 68 % (red), 90 % (green) and 95 % (blue) credible regions. . . . .	126



5.4	Correlations between matter NSI parameters and source/detector NSI parameters at DUNE. The 68 % (red), 90 % (green) and 95 % (blue) credible regions are shown in the $\varepsilon_{\tau e}^m - \varepsilon_{\tau e}^d$ plane in the left panel and in the $\varepsilon_{\mu e}^m - \varepsilon_{\tau e}^d$ plane in the right panel. . . . .	130
5.5	Correlations between matter NSI parameters and source NSI parameters with current bounds at DUNE. The 68 % (red), 90 % (green) and 95 % (blue) credible regions are shown. . . . .	131
5.6	Correlations between matter NSI parameters and detector NSI parameters with current bounds at DUNE. The 68 % (red), 90 % (green) and 95 % (blue) credible regions are shown. . . . .	132
5.7	Sensitivity of DUNE in the $\theta_{23} - \delta_{CP}$ plane with 3+3 years (blue, dashed contours) and 5+5 years (red, solid contours) of data. The simulated true values of these parameters are $42^\circ$ and $-90^\circ$ , respectively. The contours enclose the 90 % credible regions. . . . .	133
6.1	$\Delta\chi^2 = \chi^2 - \chi_{\min}^2$ vs $\tau_3/m_3$ obtained from the analysis of T2K data (red dashed line), NOvA data (solid green line) and T2K+NOvA data (black long dashed line). . . . .	141
6.2	Muon event spectra for NOvA and T2K. The left panel is for NOvA while the right panel is for T2K. The black dots with the error-bar are actual data points. The error bars correspond to the $1\sigma$ statistical error. . . . .	142
6.3	The 95 % C.L. allowed areas obtained in the $\sin^2 \theta_{23} - \Delta m_{32}^2$ plane, from analysis of T2K data (red lines), NOvA data (green lines) and T2K+NOvA data (black lines). The solid lines are for standard three-generation oscil- lations while the dashed lines are for oscillation with decay. . . . .	142
6.4	Muon event spectra for NOvA and T2K. The left panel is for NOvA while the right panel is for T2K. The black dots with the error-bar are actual data points. The error bars correspond to the $1\sigma$ statistical error. . . . .	143

6.5	The 95 % C.L. allowed areas obtained in the $\tau_3/m_3 - \sin^2 \theta_{23}$ plane, from analysis of T2K data (black dashed line), NOvA data (blue solid line) and T2K+NOvA data (red dashed-dotted line). . . . .	145
6.6	$\Delta\chi^2$ vs $\sin^2 \theta_{23}$ , where the $\chi^2$ is marginalised over all other parameters. . .	145
6.7	The 95 % C.L. allowed areas obtained in the $\tau_3/m_3 - \Delta m_{32}^2$ plane, from analysis of T2K data (black dashed line), NOvA data (blue solid line) and T2K+NOvA data (red dashed-dotted line). . . . .	146
6.8	$\Delta\chi^2$ vs $\Delta m_{32}^2$ , where the $\chi^2$ is marginalised over all other parameters. . . .	147
6.9	The left panel of this figure shows the expected sensitivity of DUNE to constraining the decay parameter $\tau_3/m_3$ . The right panel of this figure presents the potential of DUNE to discover a decaying $\nu_3$ . See text for details. . . . .	150
6.10	The $\chi^2$ as a function of $\tau_3/m_3(\text{test})$ , showing the precision with which $\tau_3/m_3$ could be measured at DUNE when its true value is $1.2 \times 10^{-11}$ s/eV. . . . .	151
6.11	The appearance (left panels) and disappearance (right panels) channel neutrino probabilities as a function of neutrino energy. The different lines are described in the legends and also in the text. The top panels show the effect of $\nu_3$ decay for a larger value of $\tau_3/m_3$ while the bottom panels show the effect for a smaller value of $\tau_3/m_3$ . . . . .	152
6.12	Same as in Fig. 6.11 but showing neutrino events at DUNE instead of probabilities. The left panels show the electron appearance events, while the right panels show the muon disappearance events. The top panels shows the impact of a larger $\tau_3/m_3$ , while the bottom panels are for a smaller $\tau_3/m_3$ . . . . .	153

- 6.13  $\chi^2$  as a function of  $\theta_{23}(\text{test})$ . The left, middle and right panels are for the cases when the data is generated at  $\theta_{23} = 42^\circ$ ,  $\theta_{23} = 48^\circ$  and  $\theta_{23} = 49.3^\circ$ , respectively. The dark red solid curves are for the standard case when both data and fit are done within the three-generation framework of stable neutrinos. The green dashed curves are for the case when the data is generated for unstable  $\nu_3$  with  $\tau_3/m_3 = 1.2 \times 10^{-11}$  s/eV but it is fitted assuming stable neutrinos. . . . . 156
- 6.14 The probabilities  $P_{\mu\mu}$  (blue lines) and  $P_{\mu e}$  (magenta lines), shown as a function of  $\theta_{23}$ . The plots have been drawn for the DUNE baseline and  $E = 2.5$  GeV, taking all oscillation parameters as mentioned in subsection III. The left and right panels are identical apart from the horizontal and vertical lines which show the probabilities for the cases when the data is generated at  $\theta_{23} = 42^\circ$  (left panel) and  $\theta_{23} = 49.3^\circ$  (right panel). The solid curves show the probabilities for the standard case while the dashed curves are for the case for unstable  $\nu_3$  with  $\tau_3/m_3 = 1.2 \times 10^{-11}$  s/eV. The probabilities are shown for the full three-generation framework including earth matter effect. The black dot shows the point at which data is generated for the decay case, while the green dots show the points which give the same  $P_{\mu\mu}$  as the black dot, but for the standard case. The red dots show the  $P_{\mu\mu}$  for the data generated for the standard case at  $\theta_{23} = 42^\circ$  (left panel) and  $\theta_{23} = 49.3^\circ$  (right panel) and the corresponding fake minima when fitted by the standard case. . . . . 157

- 6.15 The plots show the expected  $3\sigma$  C.L. contours in the  $\theta_{23} - \theta_{13}$  plane for the case when the data is simulated at  $\theta_{23} = 42^\circ$  (left panel),  $\theta_{23} = 48^\circ$  (middle panel), and  $\theta_{23} = 49.3^\circ$  (right panel). The value of  $\theta_{13} = 8.5^\circ$  in all panels. The black stars show the data points in the plane. The dark red solid curves show the expected  $3\sigma$  contour for the standard scenario in absence of decay in data and theory. The green dashed curves show the  $3\sigma$  contour for the case when the data corresponds to a decaying  $\nu_3$  with  $\tau_3/m_3 = 1.2 \times 10^{-11}$  s/eV, which is fitted with a theory where all neutrinos are taken as stable. . . . . 161
- 6.16 Expected octant sensitivity at DUNE. The dark red solid curve is for standard case of stable neutrinos. The green dashed curve is for the case when  $\nu_3$  is taken as unstable with  $\tau_3/m_3 = 1.2 \times 10^{-11}$  s/eV in the data, but in the fit we keep it to be stable. . . . . 162
- 6.17 Expected CP-violation sensitivity at DUNE. The dark red solid curve is for standard case of stable neutrinos. The green dashed curve is for the case when  $\nu_3$  is taken as unstable with  $\tau_3/m_3 = 1.2 \times 10^{-11}$  s/eV in the data, but in the fit we keep it to be stable. . . . . 163
- 6.18 Expected mass hierarchy sensitivity at DUNE. The dark red solid curve is for standard case of stable neutrinos. The green dashed curve is for the case when  $\nu_3$  is taken as unstable with  $\tau_3/m_3 = 1.2 \times 10^{-11}$  s/eV in the data, but in the fit we keep it to be stable. The left panel is for NH true while the right panel is for IH true. . . . . 163

## List of Tables

1.1	Current values of oscillation parameters assuming NH [24]. . . . .	22
4.1	The DUNE near detector specification used in this work. . . . .	65
4.2	The $2\sigma$ allowed ranges of $\delta_{24}(\text{test})$ for the three experiments in the 3+1 scenario. The assumed true value of $\delta_{13}$ is $-90^\circ$ . We give the allowed ranges of $\delta_{24}(\text{test})$ for $\delta_{24}^{\text{tr}} = 0^\circ, 90^\circ, -90^\circ, 180^\circ$ . Here $\delta_{24}^{\text{tr}}$ stands for $\delta_{24}(\text{true})$ . . . . .	95
4.3	The $2\sigma$ allowed $\delta_{13}(\text{test})$ ranges for the three experiments both in 3+0 and 3+1 scenario. In both the scenarios, assumed true value of $\delta_{13}$ is $-90^\circ$ while in 3+1 case, we give the allowed ranges of $\delta_{13}(\text{test})$ for $\delta_{24}^{\text{tr}} = 0^\circ, 90^\circ, -90^\circ, 180^\circ$ . Here $\delta^{\text{tr}}$ stands for $\delta(\text{true})$ . . . . .	101
5.1	Expected 90 % credible regions on NSI parameters from DUNE. . . . .	127



## 1.1 Neutrinos: nature's invisible

In 1896, Becquerel discovered radioactivity and soon it was found by Rutherford that the radiation emitted by radioactive materials are made of three beams: alpha, beta and gamma. The beta particles are basically electrons and the process in which they are emitted is called beta decay. Here a heavy nucleus emits an electron and one of the neutrons inside the nucleus becomes a proton; the nucleus gains atomic number by unity with mass number fixed. Naively it seemed like a two body decay process, however, the theory of two body decay was soon in trouble. This is because, in a two-body decay the energy of spectrum of the daughter particle is monochromatic, whereas beta decay spectrum has a broad distribution to understand the problem, let us assume that the initial nucleus has a mass of  $M_0$ . In the lab frame, its momentum is zero. Suppose the final nucleus and the electron has energies  $E_1$  and  $E_2$  and momenta  $\mathbf{p}_1$  and  $\mathbf{p}_2$  respectively. From conservation of momentum, we get,

$$\mathbf{p}_1 + \mathbf{p}_2 = 0. \quad (1.1)$$

Hence,

$$|\mathbf{p}_1| = |\mathbf{p}_2|. \quad (1.2)$$

From energy conservation we get,

$$E_1 + E_2 = M_0. \quad (1.3)$$

The energies can be expressed in terms of the momentum in the following way.

$$E_i = \sqrt{|\mathbf{p}_i|^2 + m_i^2}. \quad (1.4)$$

Where,  $m_i$  is the mass of the  $i^{th}$  particle. After solving these equations we get

$$E_1 = \frac{M_0^2 + M_1^2 - M_2^2}{2M_0}, \quad (1.5)$$

$$E_2 = \frac{M_0^2 + M_2^2 - M_1^2}{2M_0}. \quad (1.6)$$

From the above equations, it can be seen that the energies of the final particles only depend on the masses. Therefore, the final states energies are uniquely determined in a two body decay. To overcome this problem, In 1930, Pauli proposed a hypothesis which is now known as the neutrino hypothesis. He proposed existence of a new particle with zero or tiny mass which is emitted along with the electron. The new particle carries away the extra missing momentum to conserve the total linear momentum. In order to maintain the charge conservation, this new particle must be neutral. To conserve the angular momentum, the new particle has spin 1/2. Thus it is a fermion. As the neutrino is neutral, it can be either Dirac or Majorana fermion. In 1933, Fermi gave a complete theory of beta decay involving neutrino. The neutrino was finally discovered by Clyde Cowan and Fredrick Reines in 1953 when they were able to detect the particles coming out of a nuclear reactor. Now it is established that there are at least three types of neutrinos and they have tiny mass but the exact mass is yet unknown.



## 1.2 Where do we get neutrinos?

There are neutrinos everywhere. After the first observation, neutrinos have been detected from various sources. Some of them are natural sources and some are artificial.

### 1.2.1 Natural sources

One of the most common sources of neutrinos is the sun. Neutrinos are produced inside the sun as a result of the thermo-nuclear fusion processes in the core of the sun where hydrogen is converted into helium in the following process:



This process occurs through the pp chain and CNO cycle in the solar core. The energy released in this process is 26 MeV. However, most of the energy is carried away by the photons and neutrinos carry only a small fraction of it. About  $2 \times 10^{38}$  solar neutrinos are emitted per second and at the surface of the earth the flux is  $\sim 6 \times 10^{10} \text{ cm}^{-2}\text{s}^{-1}$  in the energy range  $E \geq 0.42 \text{ MeV}$  and  $\sim 5 \times 10^6 \text{ cm}^{-2}\text{s}^{-1}$  between 0.8 MeV and 15 MeV.

Another large source of neutrinos are the atmospheric neutrinos. The atmospheric neutrinos were first discovered in the Kolar Gold Field mines [1] in India and at a gold mine in South-Africa [2] in the similar time. Atmospheric neutrinos are generated from the interactions of high energy cosmic rays with atomic nuclei in the upper atmosphere. From these interactions, pions and kaons are created. These pions and kaons being unstable produce neutrinos from their decay in the following series of processes:

$$\begin{aligned} \pi^\pm(K^\pm) &\rightarrow \mu^\pm + \nu_\mu(\bar{\nu}_\mu), \\ \mu^\pm &\rightarrow e^\pm + \nu_e(\bar{\nu}_e) + \bar{\nu}_\mu(\nu_\mu). \end{aligned} \quad (1.8)$$

The above processes show that during the production of atmospheric neutrinos, the expected number of  $\nu_\mu$  is almost twice the number of  $\nu_e$ . Atmospheric neutrinos span a wide range of energy from few MeV to hundreds of GeV. The typical number of atmospheric neutrinos at the surface of the earth is  $\sim 10^{-1} \text{ cm}^{-2}\text{s}^{-1}$ .

There are other natural sources of neutrinos like the supernovae neutrinos, the ultra high energy neutrino of cosmic origin, etc. Neutrinos are emitted from supernovae explosion during the end of a star. Almost 99% of the explosion energy is carried out by the neutrinos having energies between 10-30 MeV. In 1987, 19 neutrinos were observed from supernova SN1987A [3], which exploded in the Large-Magellanic-Cloud. There are also ultra-high energy neutrinos of energies in the range of TeV to peV, which have been observed in IceCUBE [4]. There is also the cosmic neutrino background which was created after the big bang, but they are yet to be detected.

### 1.2.2 Artificial sources

Apart from the natural sources, there are also many man made sources of neutrinos.  $\bar{\nu}_e$  are emitted in nuclear reactors. These reactor antineutrinos have energies starting from 1.8 MeV to about 8 MeV. About  $7.7 \times 10^{20}$  neutrinos are generated per second in a 3 GW reactor.

Neutrinos can also be generated in high energy particle accelerators. In these experiments, a high energy proton beam is bombarded into a fixed target. Charged pions are created from the collision of the protons. Then the charged pions are decayed producing neutrinos. The decay of the pions can be either at rest, or they can decay during its flight. In the decay at rest (DAR) method, the  $\pi^-$  are absorbed and the  $\pi^+$  are brought into rest

and are allowed to decay via the following decay chain:

$$\begin{aligned}\pi^+ &\rightarrow \mu^+ + \nu_\mu \\ \mu^+ &\rightarrow e^+ + \nu_e + \bar{\nu}_\mu.\end{aligned}$$

In this type of experiment, the  $\bar{\nu}_\mu$  can have maximum energy of 52.8 MeV. The main aim of these experiments is to observe oscillation in the clean channel of  $\bar{\nu}_\mu \rightarrow \bar{\nu}_e$ . In the decay in flight experiments, the charged pions are allowed to decay in a long decay pipe. The resulting muons are absorbed before they are decayed. In this way, these experiments can achieve a  $\nu_\mu$  or  $\bar{\nu}_\mu$  beam depending on the polarity of the charged pion, which is determined by a magnet. These accelerators can give neutrinos from few 10s of MeV to few GeV neutrinos. In this thesis, we have only considered decay in flight experiments, which are also called conventional beam experiments. We will introduce long-baseline experiments later in this chapter and discuss accelerator based long-baseline in details in [chapter 3](#).

### 1.3 Neutrino oscillation, a signature of physics beyond the standard model

In the standard model of particle physics, neutrinos are massless. All standard model fermions get mass from the Higgs-Mechanism and this mass-generation requires both left and right handed fermions. In the SM, there are no right-handed neutrinos as neutrinos. Therefore, it is not possible to generate neutrino mass without extension of the standard model. However, observation of solar and atmospheric neutrinos established that neutrinos have tiny mass.

### 1.3.1 Solar neutrino problem

Solar neutrino flux was calculated in the standard solar model (SSM) [5,6]. In this model, all the neutrinos coming from the sun are  $\nu_e$ . Ray Davis and his collaborators tried to test the SSM using chlorine ( $^{37}\text{Cl}$ ) [7]. They were able to count the number of  $\nu_e$  interactions over a period of time. They observed only about one-third of the solar neutrino flux predicted by the SSM. This deficit defines "the solar neutrino problem". Many proposals were put forward, including some where it was assumed that SSM is wrong [8–10]. The idea of neutrino oscillation was also proposed to address the problem. Kamiokande [11] was a water Cherenkov detector which could observe electron-neutrino scattering in real-time. They confirmed the deficit and also confirmed that the neutrinos were coming from the sun. Then there were the Ga based experiments SAGE [12] and GALLEX [13]. These were able to detect the lower energy pp neutrinos due to their lower threshold. They also observed the discrepancy. An upgraded version of Kamiokande experiment called Super-Kamiokande [14] provided more evidence with more statistics. Both chlorine and gallium based experiments could only see the charged-current (CC) interactions while the water based experiments were able to see charged current as well as the neutral current (NC) interactions together. Finally, the heavy water based experiment SNO (Sudbury neutrino observatory) [15, 16], was able to measure the solar neutrino flux via both CC and NC interactions independently. The CC interactions gave the  $\nu_e$  flux while the NC interactions gave the total neutrino flux coming from the sun. They found the NC flux which is sum of all flavours consistent with the SSM, however, the CC events were about 1/3 of the total NC events. This showed that neutrinos indeed change their flavour while coming to the earth.

### 1.3.2 Atmospheric neutrinos

We mentioned above that during the production of atmospheric neutrinos, the expected number of  $\nu_\mu$  is almost twice the number of  $\nu_e$ . However, water Cherenkov detectors like Kamiokande [17], IMB [18, 19] and iron-calorimeter experiment like SUDAN2 [20] found this to be different. In order to reduce the flux uncertainties of the atmospheric neutrinos, they reported the following double ratio:

$$R = \frac{(N_\mu/N_e)_{obs}}{(N_\mu/N_e)_{MC}} \quad (1.9)$$

The above experiments found the value of R to be significantly less than unity. This discrepancy is called the "atmospheric neutrino anomaly". This could be explained using neutrino oscillation of type  $\nu_\mu \rightarrow \nu_e$  or  $\nu_\mu \rightarrow \nu_\tau$  or both. Finally, SK measured the zenith angle dependence of the atmospheric neutrino flux [21]. They found  $\nu_e$  flux to be consistent with the atmospheric neutrino flux prediction but, they found the upward going  $\nu_\mu$  flux to be less than the predicted flux whereas the downward going  $\nu_\mu$  flux was found to be consistent with the flux prediction. The deficit of the upward going  $\nu_\mu$  could be explained by the oscillation of neutrinos. This unambiguously showed the existence of neutrino oscillation.

### 1.3.3 Flavour oscillation of neutrinos

Neutrino oscillation is direct consequence of neutrino mass. The theory of neutrino oscillation was first given by Bruno Pontecorvo [22]. In neutrino oscillation, neutrinos are created in a certain flavour and later they can be measured in a different flavour. This is because of neutrino masses and mixing which means the mass-eigenstates and the flavour-eigenstates are not same. If mass eigenstates are given by  $\nu_i$  and  $\nu_\alpha$  represents

Parameter	bfp $\pm 1\sigma$	3 $\sigma$ range
$\theta_{12}/^\circ$	$33.82^{+0.78}_{-0.76}$	$31.61 \rightarrow 36.27$
$\theta_{13}/^\circ$	$8.60^{+0.13}_{-0.13}$	$8.22 \rightarrow 8.98$
$\theta_{23}/^\circ$	$48.6^{+1.0}_{-1.4}$	$41.1 \rightarrow 51.3$
$\delta_{CP}/^\circ$	$221^{+39}_{-28}$	$144 \rightarrow 357$
$\frac{\Delta m_{21}^2}{10^{-5} eV^2}$	$7.39^{+0.21}_{-0.20}$	$6.79 \rightarrow 8.01$
$\frac{\Delta m_{31}^2}{10^{-3} eV^2}$	$+2.528^{+0.029}_{-0.031}$	$+2.436 \rightarrow +2.618$

Table 1.1: Current values of oscillation parameters assuming NH [24].

the flavour-eigenstates, then these two bases are related by

$$|\nu_\alpha\rangle = U_{\alpha i} |\nu_i\rangle, \quad (1.10)$$

where,  $i = 1, 2, 3$ ,  $\alpha = e, \mu, \tau$  and  $U$  is a unitary matrix called Pontecorvo-Maki-Nakagawa-Sakata (PMNS) matrix [23]. The probability that a neutrino created in a state  $\nu_\alpha$  transforms to a state  $\nu_\beta$  is given by

$$P_{\alpha\beta} = |\langle \nu_\beta | \nu_\alpha(t) \rangle|^2. \quad (1.11)$$

We will derive the oscillation probability in chapter 2. We will see that the neutrino oscillation probability depends on the mass-squared differences defined by  $\Delta m_{ij}^2 \equiv m_i^2 - m_j^2$  and the mixing angles.

The standard three generation oscillation is described by three mixing angles ( $\theta_{12}, \theta_{13}, \theta_{23}$ ), two mass-squared differences ( $\Delta m_{21}^2, \Delta m_{31}^2$ ) and one CP-violating phase ( $\delta_{CP}$ ). Current values of these parameters are given in Table. 1.1. We see that  $\theta_{12}, \theta_{13}$  and  $\Delta m_{21}^2$  are known with high precision. Although the value of  $|\Delta m_{31}^2|$  is known with high precision, but we don't know its sign. If it is positive, it is called normal hierarchy, whereas, if it is negative, it is inverted hierarchy.  $\delta_{CP}$  is not known. The octant of  $\theta_{23}$  is also unknown, i.e., we don't if it is less than  $\pi/4$  or greater.

Neutrino oscillation data not only establishes neutrino mass but also say that the neutrino mixing is very different from the quark mixing. While neutrino mixing angles are

large, the quark mixing angles are very small. Moreover, the data show that the neutrino masses are unnaturally small and they are less hierarchical than quark masses. All of these hint at some non-trivial physics beyond the standard model.

## 1.4 Long-baseline experiments, a probe to study neutrino oscillation

Long-baseline experiments have baseline typically more than hundreds of kilometres. In this thesis, we will only consider accelerator based long-baseline experiments. In these experiments, a neutrino beam is produced and sent to the far site of the experiment where they are detected in a detector. There are also one or more near detectors which are put near the source to measure the flux precisely. These experiments have energies in the range of few hundred MeVs to few GeVs. The baseline is chosen such that  $L/E \sim 10^3$  km/GeV. Thus these experiments are sensitive to the oscillation driven by both  $\Delta m_{31}^2$  and  $\Delta m_{21}^2$ . As a result, the experiments become sensitive to the CP-violation phase. These experiments have matter effects due to the long baseline. Therefore these experiments can probe the sign of  $\Delta m_{31}^2$ .

Long baseline experiments like T2K [25], NOvA [26] are currently running and there are many proposed experiments planned in the near future like DUNE [27], T2HK/T2HKK [28, 29], ESSνB [30], P2O [31], etc. This work is based on the currently running experiments NOvA & T2K and future experiments DUNE & T2HK/T2HKK. We will discuss long-baseline experiments in great detail in chapter 3.

## 1.5 Possibility of new physics at long-baseline experiments

In addition to the CP-sensitivity, mass-hierarchy sensitivity and precision measurement of the oscillation parameters, long-baseline experiments can be used to search for new physics that affects the oscillation probability at the long-baseline experiments. There are some observations which hint at new physics beyond the standard oscillation framework. The solar experiments prefer the value of  $\Delta m_{21}^2$  around  $5 \times 10^{-5} \text{ eV}^2$  whereas, KamLAND reactor experiment prefers value of  $\Delta m_{21}^2$  around  $7.5 \times 10^{-5} \text{ eV}^2$ . There seems to be an inconsistency between NOvA and T2K initial result. There is also the so-called "LSND anomaly". LSND [32] at LosAlamos reported  $3.8 \sigma$  excess of positron events at short baseline experiments. These results could be best explained in terms of neutrino oscillations driven by a new mass-squared difference of  $\Delta m^2 \sim 1 \text{ eV}^2$ . While, experiments like MiniBooNE appearance experiment [33, 33, 34], reactor [35–37] and Gallium [38–41] anomaly supports the LSND result; KARMEN [42], CDHS [43], NOMAD [44], atmospheric experiments like SK IceCUBE [45] and MiniBooNE disappearance [46] disfavour the LSND claim. This is known as the LSND anomaly and it is still far from settled. LSND results could be explained by additional neutrino states. These extra states must be sterile because the number of active neutrino state has been precisely measured as 3 by LEP [47].

Presence of these anomalies motivates for new physics affecting neutrino oscillation. Sterile neutrino is one such idea. There are other ideas like invisible neutrino decay, non-standard interactions (NSI) etc. These new physics can lead to the modification of the oscillation probability at the long-baseline experiments. In this thesis, we studied these new ideas in the context of the present (NOvA, T2K) as well as future (DUNE, T2HK/T2HKK) long-baseline experiments. We performed our analysis in two ways. On the one hand, we studied the sensitivity to new physics at the experiments and on the other hand, we looked at the effect of new physics on the standard measurements at these experiments.



## 1.6 Thesis overview

The thesis is organised in the following way. In chapter 2, we discuss physics of neutrino oscillation in detail. We derive the oscillation probability in vacuum and in the presence of matter. Then we discuss various degeneracies present in the oscillation probability. Finally, we sketch the current situation of the various oscillation parameters. In chapter 3, we discuss the long-baseline experiments. We discuss a general description of the long-baseline experiments followed by an overview of the experiments on which we have worked. Chapter 4 is dedicated to the sterile neutrino searches at long-baseline experiments. First, we discuss the sensitivity to the sterile neutrino at DUNE near detector. Then, we give the results of our study, which shows the effect of sterile neutrino on the standard measurement at T2HK/T2HKK and their combination with DUNE. Next, we present the sensitivity of DUNE and T2HK to the measurement of sterile phase  $\delta_{CP}$  and the last part of chapter 4 shows the presence of a new degeneracy at sterile neutrino sector for the  $\nu_e$  appearance channel. In chapter 5, we discuss NSI at DUNE. Here we considered source, detector and matter NSI together in our analysis. Chapter 6 discusses the invisible neutrino decay at long-baseline experiments. This chapter has two parts. The first part consist of discussion of invisible neutrino decay in the context of current data from NOvA and T2K and the second part discusses the future possibility of invisible neutrino decay at DUNE. Finally, we conclude in chapter 7 with future prospects.



## Standard Neutrino Oscillation

In this chapter, we discuss various aspects of neutrino oscillation phenomena. Neutrino oscillation describes the flavour transition of neutrinos from one to another. We mentioned in the introduction that the neutrino oscillation depends on mass-squared differences of the neutrinos, the mixing angles, the ratio  $L/E$  and density of the matter it propagates through. In this chapter, we derive the expression of probabilities in various cases to understand various features of neutrino oscillations, which are relevant for long-baseline experiments. We will also show existence of degeneracies that are important for long-baseline experiments.

### 2.1 Neutrino oscillation in vacuum

In this section, we discuss neutrino oscillations in vacuum. In vacuum, neutrino oscillation probability can be exactly derived for an arbitrary number of generations. However, for matter, the exact probability can only be derived for two generations. Below, we first derive the probability expression for two generations, followed by a general derivation valid for arbitrary number of generations. The two-generation discussion will give a general idea of the neutrino oscillation phenomena and it can be used in many realistic cases as a good approximation.

### 2.1.1 Neutrino oscillation in vacuum: 2 generations

Let  $\nu_e$  and  $\nu_\mu$  be the two neutrino flavour states, and  $\nu_1$  and  $\nu_2$  be the two mass-eigenstates. In general, the bases are not the same. In that case, they are related to each other by a unitary matrix  $U$

$$|\nu_\alpha\rangle = U_{\alpha i} |\nu_i\rangle, \quad (2.1)$$

where,  $\alpha = e, \mu, i = 1, 2$  and  $U$  is a  $2 \times 2$  unitary matrix which can be parametrized by angle  $\theta$  in the following way:

$$U = \begin{pmatrix} \cos \theta & \sin \theta \\ -\sin \theta & \cos \theta \end{pmatrix}. \quad (2.2)$$

The mass-eigenstates are eigenstates of the free Hamiltonian in vacuum, therefore time evolution of flavour state  $\nu_e$  in vacuum is given by

$$|\nu_e(t)\rangle = e^{-iE_1 t} \cos \theta |\nu_1\rangle + e^{-iE_2 t} \sin \theta |\nu_2\rangle \quad (2.3)$$

and for  $\nu_\mu$ , this will be

$$|\nu_\mu(t)\rangle = -e^{-iE_1 t} \sin \theta |\nu_1\rangle + e^{-iE_2 t} \cos \theta |\nu_2\rangle. \quad (2.4)$$

Here,  $E_1$  and  $E_2$  are energies of the neutrinos in the mass eigenstates  $\nu_1$  and  $\nu_2$  with masses  $m_1$  and  $m_2$ , respectively, given by

$$E_i^2 = p^2 + m_i^2. \quad (2.5)$$

If  $m$  is very small compared to the energy, i.e., in the ultra-relativistic limit, the energy can be approximated as

$$E_i \simeq p + \frac{m_i^2}{2p} \quad (2.6)$$

Here we have assumed all massive states to have same momentum. In this approximation, we can write the probability of  $\nu_e$  to be in  $\nu_e$  as

$$\begin{aligned} P_{ee} &= |\langle \nu_e | \nu_e(t) \rangle|^2 \\ &= 1 - \sin^2 2\theta \sin^2[(E_2 - E_1)t/2]. \end{aligned} \quad (2.7)$$

In the relativistic limit,  $p \approx E$  and  $L \approx t$ . Therefore,

$$P_{ee} = 1 - \sin^2 2\theta \sin^2 \left( \frac{\Delta m_{21}^2 L}{4E} \right), \quad (2.8)$$

where,  $\Delta m_{ij}^2 = m_i^2 - m_j^2$ . We define  $\Delta_{ij} = \frac{\Delta m_{ij}^2 L}{4E}$ . If we take  $L$  in km and  $E$  in GeV,  $\Delta_{ij} = 1.27 \frac{\Delta m_{ij}^2 L}{E}$ . For two generation, the probability  $P_{e\mu}$ , .i.e. the transition from  $\nu_e$  to  $\nu_\mu$  is given by,

$$\begin{aligned} P_{e\mu} &= 1 - P_{ee} \\ &= \sin^2 2\theta \sin^2 \left( \frac{\Delta m_{21}^2 L}{4E} \right). \end{aligned} \quad (2.9)$$

From, Eq. (2.7) and Eq. (2.9), it can be seen that the oscillatory behaviour comes from the term  $\sin^2 \Delta_{ij}$ . It can be seen that if neutrino mass vanishes,  $\Delta_{ij}$  vanishes and oscillations goes away. Another thing to notice is that oscillation probabilities do not depend on the octant, .i.e.  $\theta \rightarrow \pi/2 - \theta$  leaves the probability invariant. The probability also is invariant under the transformation  $\Delta m_{21}^2 \rightarrow -\Delta m_{21}^2$ . Therefore, two generation vacuum oscillation can not distinguish if,  $m_1 < m_2$  or  $m_1 > m_2$  and octant of  $\theta$ . Neutrino oscillation also depends on  $L/E$ . If  $L/E$  is small, then the oscillatory phase  $\Delta_{21} \rightarrow 0$  and the oscillation does not occur but if  $L/E$  is large enough, there will be large number of oscillations between the source and detector and the effect of oscillation will be averaged out. Therefore,  $L/E$  plays a very important role in the oscillation experiments and the value of  $L/E$  determines the relevant  $\Delta m^2$  for an experiment. Neutrino oscillation also vanishes if the mixing angle is zero.

Next, we give a different approach of derivation of the oscillation probability in vacuum for two generations. The time dependent schrödinger equation in the mass basis is given by

$$i\frac{\partial \nu_m}{\partial t} = H\nu_m, \quad (2.10)$$

where,  $H$  is the Hamiltonian in the mass basis, and  $\nu_m$  is in neutrino mass-basis. For two generations, the Hamiltonian is given by

$$H = \begin{pmatrix} E_1 & 0 \\ 0 & E_2 \end{pmatrix}. \quad (2.11)$$

Using plane-wave and ultra-relativistic approximations, one gets

$$H = p + \frac{1}{2p} \begin{pmatrix} m_1^2 & 0 \\ 0 & m_2^2 \end{pmatrix}. \quad (2.12)$$

One can transform the Eq. (2.10) into flavour basis by using Eq. (2.1) as

$$i\frac{\partial \nu_f}{\partial t} = \tilde{H}\nu_f, \quad (2.13)$$

where,  $\tilde{H}$  is the Hamiltonian in the flavour basis given by  $\tilde{H} = UHU^\dagger$ . Now, we can subtract a constant term proportional to identity from the Hamiltonian, since this will be like a overall phase which does not affect the total probability. Thus subtracting  $\left(E + \frac{m_1^2}{2E}\right)I$  from the Hamiltonian we get,

$$i\frac{\partial}{\partial t} \begin{pmatrix} \nu_e \\ \nu_\mu \end{pmatrix} = U \begin{pmatrix} 0 & 0 \\ 0 & \frac{\Delta m_{21}^2}{2E} \end{pmatrix} U^\dagger \begin{pmatrix} \nu_e \\ \nu_\mu \end{pmatrix}. \quad (2.14)$$

Using Eq. (2.2) we can write

$$i\frac{\partial}{\partial t} \begin{pmatrix} \nu_e \\ \nu_\mu \end{pmatrix} = \begin{pmatrix} \sin^2 \theta \frac{\Delta m_{21}^2}{2E} & \sin \theta \cos \theta \frac{\Delta m_{21}^2}{2E} \\ \sin \theta \cos \theta \frac{\Delta m_{21}^2}{2E} & \cos^2 \theta \frac{\Delta m_{21}^2}{2E} \end{pmatrix} \begin{pmatrix} \nu_e \\ \nu_\mu \end{pmatrix}, \quad (2.15)$$

or,

$$i \frac{\partial}{\partial t} \begin{pmatrix} \nu_e \\ \nu_\mu \end{pmatrix} = \begin{pmatrix} \left(1 - \cos 2\theta\right) \frac{\Delta m_{21}^2}{4E} & \sin 2\theta \frac{\Delta m_{21}^2}{4E} \\ \sin 2\theta \frac{\Delta m_{21}^2}{4E} & \left(1 + \cos 2\theta\right) \frac{\Delta m_{21}^2}{4E} \end{pmatrix} \begin{pmatrix} \nu_e \\ \nu_\mu \end{pmatrix}. \quad (2.16)$$

One can again subtract a constant term  $\Delta m_{21}^2/4E$  proportional to the identity from Eq. (2.16) and get two coupled differential equations

$$i \frac{\partial \nu_e}{\partial t} = -\cos 2\theta \frac{\Delta m_{21}^2}{4E} \nu_e + \sin 2\theta \frac{\Delta m_{21}^2}{4E} \nu_\mu, \quad (2.17)$$

$$i \frac{\partial \nu_\mu}{\partial t} = \sin 2\theta \frac{\Delta m_{21}^2}{4E} \nu_e + \cos 2\theta \frac{\Delta m_{21}^2}{4E} \nu_\mu. \quad (2.18)$$

The above coupled differential equation can be exactly solved and the general solution is given by,

$$\nu_e(t) = A e^{-i\omega t} + B e^{i\omega t} \quad (2.19)$$

$$\nu_\mu(t) = C e^{-i\omega t} + D e^{i\omega t}, \quad (2.20)$$

where,  $\omega = \Delta m_{21}^2/4E$ . If the initial neutrino flavour is  $\nu_e$ , the initial conditions for the solution become,

$$\nu_e(0) = 1, \quad \nu_\mu(0) = 0. \quad (2.21)$$

And we obtain,

$$A = \sin^2 \theta, \quad B = \cos^2 \theta, \quad C = \sin \theta \cos \theta, \quad D = -\sin \theta \cos \theta. \quad (2.22)$$

Thus, the probability of oscillation between  $\nu_e \rightarrow \nu_\mu$  becomes

$$P_{e\mu} = |\nu_\mu(t)|^2 = \sin^2 2\theta \sin^2 \left( \frac{\Delta m_{21}^2 L}{4E} \right) \quad (2.23)$$

and the probability of the neutrino being in flavour state  $\nu_e$  becomes

$$P_{ee} = 1 - P_{e\mu} = 1 - \sin^2 2\theta \sin^2 \left( \frac{\Delta m_{21}^2 L}{4E} \right). \quad (2.24)$$

### 2.1.2 Neutrino oscillation in vacuum: N generations

Now we discuss the exact neutrino oscillation probability in vacuum assuming N generations of neutrino states. The time dependent Schrödinger equation in the mass basis is given by

$$i \frac{\partial \nu_m}{\partial t} = H | \nu_m \rangle. \quad (2.25)$$

In mass basis, the Hamiltonian is diagonal and has eigenvalues  $E_1$  &  $E_2$ . Therefore, the time evolution of the mass-eigenstates is given by

$$| \nu_i(t) \rangle = e^{-iE_i t} | \nu_i \rangle. \quad (2.26)$$

The mass-basis and the flavour-basis are related by the unitary matrix  $U$  as  $\nu_f = U \nu_m$ . For N generation, an  $N \times N$  unitary matrix can be parametrized by  $N^2$  number of real independent parameters. Among these,  $\frac{N(N-1)}{2}$  are mixing angles and  $\frac{N(N+1)}{2}$  are phases. If neutrinos are of Dirac type,  $(2N - 1)$  of these phases can be absorbed among the  $2N$  number of leptonic fields in the Lagrangian by global phase rotations of the fields. Therefore, there are in total  $(N - 1)(N - 2)/2$  phases. However, if the neutrinos are Majorana, the Majorana mass term is not invariant under the global U(1) transformations and there will be additional  $N - 1$  phases. But these extra phases, which are called Majorana phases, are not present in neutrino oscillation probabilities.

Time evolution of the flavour states is given by

$$| \nu_\alpha(t) \rangle = \sum_{i=1}^N U_{\alpha i} e^{-iE_i t} | \nu_i \rangle, \quad (2.27)$$



where,  $i = 1, N$  and  $\alpha$  represents  $N$  number of flavour eigenstates. Now, the oscillation probability  $\nu_\alpha \rightarrow \nu_\beta$  is given by

$$P_{\alpha\beta} = |\langle \nu_\beta | \nu_\alpha(t) \rangle|^2 \quad (2.28)$$

$$= \left| \sum_{i=1} U_{\alpha i} U_{\beta i}^* e^{-iE_i t} \right|^2 \quad (2.29)$$

$$= \sum_{i=1} \sum_{j=1} (U_{\alpha i} U_{\beta i}^* e^{-iE_i t}) (U_{\alpha j}^* U_{\beta j} e^{iE_j t}) \quad (2.30)$$

$$= \sum_{i=j} |U_{\alpha i}|^2 |U_{\beta i}|^2 + \sum_{i \neq j} U_{\alpha i} U_{\beta j} U_{\beta i}^* U_{\alpha j}^* e^{-i(E_i - E_j)t} \quad (2.31)$$

$$= \sum_{i=j} |U_{\alpha i}|^2 |U_{\beta i}|^2 + 2Re \sum_{i>j} [U_{\alpha i} U_{\beta j} U_{\beta i}^* U_{\alpha j}^* e^{-i(E_i - E_j)t}]. \quad (2.32)$$

Now,

$$\left| \sum_i U_{\alpha i} U_{\beta i}^* \right|^2 = \sum_i |U_{\alpha i}|^2 |U_{\beta i}|^2 + \sum_{i \neq j} U_{\alpha i} U_{\beta j} U_{\alpha j}^* U_{\beta i}^*. \quad (2.33)$$

Therefore, the probability becomes,

$$P_{\alpha\beta} = \left| \sum_i U_{\alpha i} U_{\beta i}^* \right|^2 - 2Re \sum_{i>j} U_{\alpha i} U_{\beta j} U_{\alpha j}^* U_{\beta i}^* \quad (2.34)$$

$$+ 2Re \sum_{i>j} U_{\alpha i} U_{\beta j} U_{\alpha j}^* U_{\beta i}^* e^{-i(E_i - E_j)t}. \quad (2.35)$$

Using the unitarity of the matrix U,

$$\sum_i U_{\alpha i} U_{\beta i}^* = \delta_{\alpha\beta}, \quad (2.36)$$

we get,

$$P_{\alpha\beta} = \delta_{\alpha\beta} - 2 \sum_{i>j} Re(U_{\alpha i} U_{\beta j} U_{\alpha j}^* U_{\beta i}^*) - 2 \sum_{i>j} Re(U_{\alpha i} U_{\beta j} U_{\alpha j}^* U_{\beta i}^*) \cos((E_i - E_j)t) \quad (2.37)$$

$$+ 2 \sum_{i>j} Im(U_{\alpha i} U_{\beta j} U_{\alpha j}^* U_{\beta i}^*) \sin((E_i - E_j)t)$$

Finally, we obtain the expression for the probability in vacuum for N generation as

$$P_{\alpha\beta} = \delta_{\alpha\beta} - 4 \sum_{i>j} \text{Re}(U_{\alpha i} U_{\beta j} U_{\alpha j}^* U_{\beta i}^*) \sin^2 \left( \frac{\Delta m_{ij}^2 L}{4E} \right) + 2 \sum_{i>j} \text{Im}(U_{\alpha i} U_{\beta j} U_{\alpha j}^* U_{\beta i}^*) \sin \left( \frac{\Delta m_{ij}^2 L}{2E} \right). \quad (2.38)$$

And the probability for antineutrinos is given by

$$P_{\alpha\beta} = \delta_{\alpha\beta} - 4 \sum_{i>j} \text{Re}(U_{\alpha i} U_{\beta j} U_{\alpha j}^* U_{\beta i}^*) \sin^2 \left( \frac{\Delta m_{ij}^2 L}{4E} \right) - 2 \sum_{i>j} \text{Im}(U_{\alpha i} U_{\beta j} U_{\alpha j}^* U_{\beta i}^*) \sin \left( \frac{\Delta m_{ij}^2 L}{2E} \right). \quad (2.39)$$

Form Eq. (2.38) and Eq. (2.39) we see that the probabilities for neutrinos and antineutrinos are not same and

$$P_{\alpha\beta}^\nu - P_{\alpha\beta}^{\bar{\nu}} = 4 \sum_{i<j} \text{Im}(U_{\alpha i} U_{\beta j} U_{\alpha j}^* U_{\beta i}^*) \sin \left( \frac{\Delta m_{ij}^2 L}{2E} \right). \quad (2.40)$$

This difference shows that neutrinos and antineutrinos oscillate differently if the imaginary term is non-zero, and it gives the measure of CP-violation in neutrino oscillation.

For three generations, the mixing matrix can be parametrized in the following way

$$U = \begin{pmatrix} c_{12}c_{13} & s_{12}c_{13} & s_{13}e^{-i\delta_{CP}} \\ -s_{12}c_{23} - c_{12}s_{23}s_{13}e^{i\delta_{CP}} & c_{12}c_{23} - s_{12}s_{23}s_{13}e^{i\delta_{CP}} & s_{23}c_{13} \\ s_{12}s_{23} - c_{12}c_{23}s_{13}e^{i\delta_{CP}} & -c_{12}s_{23} - s_{12}c_{23}s_{13}e^{i\delta_{CP}} & c_{23}c_{13} \end{pmatrix}. \quad (2.41)$$

Here,  $c_{ij} = \cos \theta_{ij}$  and  $s_{ij} = \sin \theta_{ij}$ . This is called the PMNS matrix. For the three neutrino case, the imaginary parts in Eq. (2.38) and Eq. (2.39), is given by

$$\text{Im}(U_{\alpha i} U_{\beta j} U_{\alpha j}^* U_{\beta i}^*) = s_{\alpha\beta;kj} J, \quad (2.42)$$

where, the coefficients  $s_{\alpha,\beta;k,j} = \pm 1$  are antisymmetric in  $\alpha, \beta$  and in  $k, j$ .  $J$  is a constant which is called the Jarlskog invariant and it is given by

$$J = 1/8 \sin 2\theta_{12} \sin 2\theta_{23} \cos \theta_{13} \sin 2\theta_{13} \sin \delta_{CP}. \quad (2.43)$$

From Eq. (2.43), we can see that the CP violation is directly proportional to  $\sin \delta_{CP}$ . Moreover, if any of the mixing angles is zero, CP violation can not be probed and it can be shown that in this case, by choosing appropriate permutations of the rows and column of the mixing matrix, one can make the phase disappear.

## 2.2 Neutrino oscillation in matter

Neutrino propagation inside matter is modified due to the interactions of neutrinos with the electrons and nucleons present in matter. The neutrino evolution is affected as the neutrinos encounter an effective potential in the matter created due to the coherent forward elastic charged and neutral current scatterings between the neutrinos and electrons, protons and neutrons inside the medium.

### 2.2.1 Effective potential in matter

Among the three neutrino flavours, only  $\nu_e$  interacts with the matter via charged current interactions with the electrons and these interactions in the low energy limit is given by

$$\mathcal{L}_{eff}^{CC} = \frac{G_F}{\sqrt{2}} [\bar{e} \gamma^\mu (1 - \gamma_5) \nu_e] [\bar{\nu}_e \gamma_\mu (1 - \gamma_5) e] \quad (2.44)$$

Using the Fierz transformation we get

$$\mathcal{L}_{eff}^{CC} = \frac{G_F}{\sqrt{2}} [\bar{e} \gamma^\mu (1 - \gamma_5) e] [\bar{\nu}_e \gamma_\mu (1 - \gamma_5) \nu_e] \quad (2.45)$$

The effective Hamiltonian for the charged current interactions is obtained by averaging over all electrons present in the background and it is given by

$$\bar{\mathcal{H}}_{eff}^{CC} = \frac{G_F}{\sqrt{2}} \langle \bar{e} \gamma^\mu (1 - \gamma_5) e \rangle [\bar{\nu}_e \gamma_\mu (1 - \gamma_5) \nu_e]. \quad (2.46)$$

In the non-relativistic limit, it can be shown that  $\langle \bar{e} \gamma_\mu \gamma_5 e \rangle$ ,  $\langle \bar{e} \gamma_i e \rangle$  and  $\langle \bar{e} \gamma_0 e \rangle$  give average spin, velocity and density of the electrons in the medium. Now, in a static medium, the average spin of the electrons is zero and the average velocity of the electrons vanishes. Therefore, the only term which survives is due to density and hence the effective Hamiltonian due to the charged current interaction becomes

$$\bar{\mathcal{H}}_{eff}^{CC} = \sqrt{2} G_F N_e \bar{\nu}_{eL} \gamma^0 \nu_{eL} \quad (2.47)$$

$$= V_{CC} \bar{\nu}_{eL} \gamma^0 \nu_{eL}, \quad (2.48)$$

where,  $N_e$  is the electron density and  $V_{CC}$  is the effective charged current potential. For antineutrinos,  $V_{CC}$  has opposite sign. Neutral current interactions are the same for all three flavours and it can be given by

$$\bar{\mathcal{H}}_{eff}^{NC} = V_{NC} \bar{\nu}_{\alpha L} \gamma^0 \nu_{\alpha L}. \quad (2.49)$$

Therefore, the modified Schrödinger equation in flavour basis in the presence of matter becomes

$$i \frac{\partial}{\partial t} \nu_f = (U H U^\dagger + V_{eff}) \nu_f, \quad (2.50)$$

where,  $V_{eff}$  is the effective potential and for three generations, it is given by

$$V_{eff} = \begin{pmatrix} V_{cc} + V_{NC} & 0 & 0 \\ 0 & V_{NC} & 0 \\ 0 & 0 & V_{NC} \end{pmatrix}. \quad (2.51)$$

One can see from the Eq. (2.51) that  $V_{NC}$  is a constant term proportional to the identity matrix and hence, it does not affect the neutrino oscillation probability. Thus, the effective potential for the standard three generation case becomes

$$V_{eff} = \begin{pmatrix} V_{cc} & 0 & 0 \\ 0 & 0 & 0 \\ 0 & 0 & 0 \end{pmatrix}. \quad (2.52)$$

Finally, the evolution equation of neutrinos for the standard three generation case in matter is

$$i \frac{\partial}{\partial t} \begin{pmatrix} \nu_e \\ \nu_\mu \\ \nu_\tau \end{pmatrix} = U \begin{pmatrix} 0 & 0 & 0 \\ 0 & \frac{\Delta m_{21}^2}{2E} & 0 \\ 0 & 0 & \frac{\Delta m_{31}^2}{2E} \end{pmatrix} U^\dagger \begin{pmatrix} \nu_e \\ \nu_\mu \\ \nu_\tau \end{pmatrix} + \begin{pmatrix} V_{cc} & 0 & 0 \\ 0 & 0 & 0 \\ 0 & 0 & 0 \end{pmatrix} \begin{pmatrix} \nu_e \\ \nu_\mu \\ \nu_\tau \end{pmatrix}. \quad (2.53)$$

Although this equation can be solved exactly in two generations for constant matter density but there is no useful analytical solution available for three generations. In the following, we discuss first the exactly solvable two generation case and then we give various approximate expressions that can be obtained for three generations.

### 2.2.2 Neutrino oscillation in matter: 2 generations

Here, we consider only two generations of the leptons and therefore the evolution equation in this case becomes

$$i \frac{\partial}{\partial t} \nu_f = H_{matt} \nu_f, \quad (2.54)$$

where,  $H_{matt}$  is given by

$$H_{matt} = \begin{pmatrix} \cos \theta & \sin \theta \\ -\sin \theta & \cos \theta \end{pmatrix} \begin{pmatrix} 0 & 0 \\ 0 & \frac{\Delta m^2}{2E} \end{pmatrix} \begin{pmatrix} \cos \theta & -\sin \theta \\ \sin \theta & \cos \theta \end{pmatrix} + \begin{pmatrix} V_{CC} & 0 \\ 0 & 0 \end{pmatrix} \quad (2.55)$$

$$= \frac{1}{4E} \begin{pmatrix} -\Delta m^2 \cos 2\theta + A & \Delta m^2 \sin 2\theta \\ \Delta m^2 \sin 2\theta & \Delta m^2 \cos 2\theta \end{pmatrix}, \quad (2.56)$$

where,

$$A = 2\sqrt{2}G_F N_e E. \quad (2.57)$$

We can solve the evolution by diagonalizing the Hamiltonian. The energy eigenvalues are given by

$$E_{1,2} = \frac{1}{4E} \left[ A \pm \sqrt{(\Delta m^2 \cos 2\theta - A)^2 + (\Delta m^2 \sin 2\theta)^2} \right]. \quad (2.58)$$

Now,  $2E(E_2 - E_1)$  gives the effective mass-squared difference in matter given by

$$(\Delta m^2)^M = \sqrt{(\Delta m^2 \cos 2\theta - A)^2 + (\Delta m^2 \sin 2\theta)^2}. \quad (2.59)$$

Let us define the unitary matrix  $U_M$  that diagonalizes Hamiltonian as:

$$U_M = \begin{pmatrix} \cos \theta_M & \sin \theta_M \\ -\sin \theta_M & \cos \theta_M \end{pmatrix}. \quad (2.60)$$

Now, the probability can be written similar to the case of vacuum as

$$P_{e\mu} = \sin^2 2\theta_M \sin^2 \left( \frac{(\Delta m^2)^M L}{4E} \right), \quad (2.61)$$

$$P_{ee} = 1 - \sin^2 2\theta_M \sin^2 \left( \frac{(\Delta m^2)^M L}{4E} \right), \quad (2.62)$$

where,  $\theta_M$  is obtained by setting the off-diagonal terms of  $U H_{\text{matt}} U^\dagger$  to zero and we get

$$\tan 2\theta_M = \frac{\Delta m^2 \sin 2\theta}{\Delta m^2 \cos 2\theta - A}. \quad (2.63)$$

We saw that for vacuum, the probability expressions were independent of the octant and the mass-hierarchy. However, in matter, both mixing angle and mass-squared difference are affected. In Eq. (2.63),  $A$  is positive for neutrino and negative for antineutrinos. Also, the denominator of Eq. (2.63) depends on the octant of theta and the sign of  $\Delta m^2$ . If octant of theta is known and it is in lower octant,  $\theta_M$  is increased when  $\Delta m^2$  is positive for

neutrinos and for antineutrinos, this is reversed. Thus matter effect can help in determination of mass hierarchy. There is another interesting thing to note from Eq. (2.63). If  $A = \Delta m^2 \cos 2\theta$ , the  $\theta_M$  becomes  $45^\circ$  and there is maximal mixing between two flavours and maximal flavour transition occurs. This is called the MSW (Mikheyev-Smirnov-Wolfenstein) resonance [48–51].

### 2.2.3 Neutrino oscillations in matter: 3 generations

In this subsection, we will derive an approximate expression for neutrino oscillation in constant matter for three generations. For this derivation, we will follow the analysis given in [52] using the series expansion method. Here we will do the perturbative expansions in terms of two dimensionless parameters:  $\alpha = \frac{\Delta m_{21}^2}{\Delta m_{31}^2}$  and  $\theta_{13}$ . And, we will keep terms upto the second order of the series. We start by writing the Hamiltonian in the flavour basis as

$$H_{\text{matt}} = \frac{\Delta m_{31}^2}{2E} \left[ U \text{diag}(0, \alpha, 1) U^\dagger + \text{diag}(\hat{A}, 0, 0) \right], \quad (2.64)$$

where,  $\hat{A} = A/\Delta m_{31}^2$ .  $U$  can be written as

$$U = R_{23} U_\delta R_{13} U_\delta^\dagger R_{12}, \quad (2.65)$$

where,  $R_{ij}$  are the rotation matrices in the  $i$ - $j$  plane and  $U_\delta = \text{diag}(0, 0, e^{i\delta})$ . We can rewrite the Hamiltonian as

$$H_{\text{matt}} = \frac{\Delta m_{31}^2}{2E} R_{23} U_\delta M U_\delta^\dagger R_{23}^T, \quad (2.66)$$

with  $M = R_{13} R_{12} \text{diag}(0, \alpha, 1) R_{12}^T R_{13}^T + \text{diag}(\hat{A}, 0, 0)$ . We start by diagonalizing the matrix  $M$  by  $M = X \hat{M} X^\dagger$  with  $\hat{M} = \text{diag}(\lambda_1, \lambda_2, \lambda_3)$  and  $X$  is a unitary matrix. We perform the diagonalization by using second order perturbation theory in  $\alpha$  and  $s_{13}$ . We write  $M$  as

$$M = M^{(0)} + M^{(1)} + M^{(2)}, \quad (2.67)$$

where  $M^{(0)}$ ,  $M^{(1)}$  and  $M^{(2)}$  are zeroth, first and second order terms of  $M$ . And using Eq. (2.66) we obtain

$$M^{(0)} = \text{diag}(A, 0, 1) = \text{diag}(\lambda_1^{(0)}, \lambda_2^{(0)}, \lambda_3^{(0)}), \quad (2.68)$$

$$M^{(1)} = \begin{pmatrix} \alpha s_{12}^2 & \alpha s_{12} c_{12} & s_{13} \\ \alpha s_{12} c_{12} & \alpha c_{12}^2 & 0 \\ s_{13} & 0 & 0 \end{pmatrix}, \quad (2.69)$$

$$M^{(2)} = \begin{pmatrix} s_{13}^2 & 0 & -\alpha s_{13} s_{12}^2 \\ 0 & 0 & -\alpha s_{13} s_{12} c_{12} \\ -\alpha s_{13} s_{12}^2 & -\alpha s_{13} s_{12} c_{12} & -s_{13}^2 \end{pmatrix}. \quad (2.70)$$

For eigenvalues and eigenvectors, we can similarly write perturbative expansion:

$$\lambda_i = \lambda_i^0 + \lambda_i^1 + \lambda_i^2 \quad (2.71)$$

and

$$x_i = x_i^0 + x_i^1 + x_i^2, \quad (2.72)$$

respectively. As  $M^{(0)}$  is diagonal from beginning, we have

$$x_i^0 = \hat{e}_i, \quad (2.73)$$

where  $\hat{e}_i$  are unit vectors. Now, the first and second order corrections to the eigenvalues can be written as

$$\lambda_i^{(1)} = M_{ii}^{(1)}, \quad (2.74)$$

$$\lambda_i^{(2)} = M_{ii}^{(2)} + \sum_{j \neq i} \frac{(M_{ij}^{(1)})^2}{\lambda_i^{(0)} - \lambda_j^{(0)}} \quad (2.75)$$



and the corrections to the eigenvectors are given by

$$x_i^{(1)} = \sum_{j \neq i} \frac{(M_{ii}^{(1)})^2}{\lambda_i^{(0)} - \lambda_j^{(0)}} \hat{e}_j, \quad (2.76)$$

$$x_i^{(2)} = \sum_{j \neq i} \frac{1}{\lambda_i^{(0)} - \lambda_j^{(0)}} \left[ M_{ij}^{(2)} + (M^{(1)} x_i^{(1)})_j - \lambda_i^{(1)} (x_i^{(1)})_j \right] \hat{e}_j. \quad (2.77)$$

The energy eigenvalues of the Hamiltonian are given by

$$E_i = \frac{\Delta m_{31}^2}{2E} \lambda_i. \quad (2.78)$$

Using Eq. (2.74) and Eq. (2.75), we get the expressions for energies

$$E_1 = \frac{\Delta m_{31}^2}{2E} \left( \hat{A} + \alpha s_{12}^2 + s_{13}^2 \frac{\hat{A}}{\hat{A} - 1} + \alpha^2 \frac{\sin^2 2\theta_{12}}{4\hat{A}} \right), \quad (2.79)$$

$$E_2 = \frac{\Delta m_{31}^2}{2E} \left( \alpha c_{12}^2 - \alpha^2 \frac{\sin^2 2\theta_{12}}{4\hat{A}} \right), \quad (2.80)$$

$$E_3 = \frac{\Delta m_{31}^2}{2E} \left( 1 - s_{13}^2 \frac{\hat{A}}{\hat{A} - 1} \right). \quad (2.81)$$

And using Eq. (2.76) and Eq. (2.77) the eigenvectors can be obtained as

$$x_1 = \begin{pmatrix} 1 \\ \frac{\alpha \sin 2\theta_{12}}{2\hat{A}} + \frac{\alpha^2 \sin 4\theta_{12}}{4\hat{A}^2} \\ \frac{s_{13}}{2\hat{A}} - \frac{\hat{A} \alpha s_{13} s_{12}^2}{(\hat{A}-1)^2} \end{pmatrix}, \quad (2.82)$$

$$x_2 = \begin{pmatrix} -\frac{\alpha \sin 2\theta_{12}}{2\hat{A}} - \frac{\alpha^2 \sin 4\theta_{12}}{4\hat{A}^2} \\ 1 \\ \frac{\alpha s_{13} \sin 2\theta_{12} (\hat{A}+1)}{2\hat{A}} \end{pmatrix}, \quad (2.83)$$

$$x_3 = \begin{pmatrix} \frac{-s_{13}}{\hat{A}-1} + \frac{\alpha \hat{A} s_{13} s_{12}^2}{(\hat{A}-1)^2} \\ \frac{\alpha \hat{A} s_{13} \sin 2\theta_{12}}{2(\hat{A}-1)} \\ 1 \end{pmatrix} \quad (2.84)$$

The new mixing matrix in matter is given by

$$U' = R_{23} U_\delta X. \quad (2.85)$$

Now we can derive the oscillation probabilities following similar procedure as the vacuum case but with modified mixing matrix and mass-squared differences. Therefore, using Eq. (2.38) and using the modified mixing matrix and mass-squared differences, we obtain the probabilities as

$$P_{\mu e} = 4s_{13}^2 s_{23}^2 \frac{\sin^2(\hat{A} - 1)\Delta}{(\hat{A} - 1)^2} + 2\alpha s_{13} \sin 2\theta_{12} \sin 2\theta_{23} \cos(\Delta + \delta_{CP}) \quad (2.86)$$

$$\begin{aligned} & \times \frac{\sin(\hat{A}\Delta)}{\hat{A}} \frac{\sin((\hat{A} - 1)\Delta)}{(\hat{A} - 1)} \\ & + \alpha^2 \sin^2 2\theta_{12} c_{23}^2 \frac{\sin^2(\hat{A}\Delta)}{\hat{A}^2}, \\ P_{\mu\mu} &= 1 - \sin^2 2\theta_{23} \sin^2 \Delta + \text{higher-orders}, \end{aligned} \quad (2.87)$$

where,  $\Delta = \frac{\Delta m_{31}^2}{4E}$ . For anti-neutrinos, we have to transform  $\hat{A} \rightarrow -\hat{A}$  and  $\delta_{CP} \rightarrow -\delta_{CP}$ . For inverted ordering, we have to replace  $\Delta$  by  $-\Delta$  and  $\hat{A}$  by  $-\hat{A}$ .

For long-baseline experiments, the oscillation is mainly governed by  $\Delta m_{31}^2$  and hence this approximation is valid for long-baseline experiments and we can use these expressions.

## 2.3 Ambiguities in measuring the oscillation parameters

In this section, we will discuss difficulties in measuring oscillation parameters due to the existence of degeneracies among them. Degeneracy in the context of oscillation means equal probabilities for two or more sets of parameters. Since the event rate in an oscillation experiment is directly proportional to the probability, presence of degeneracies give many solutions for oscillation parameters and it becomes very challenging to measure the

parameters.

There are three types of degeneracies widely discussed in literature: a ) the mass-hierarchy- $\delta_{CP}$  degeneracy [53]:

$$P_{\mu e}(NH, \delta_{CP}) = P_{\mu e}(IH, \delta'_{CP}), \quad (2.88)$$

b) the  $\theta_{23}$  octant degeneracy [54]:

$$P_{\mu\mu}(\theta_{23}) = P_{\mu\mu}(\pi/2 - \theta_{23}) \quad (2.89)$$

and c) the intrinsic  $\theta_{13} - \delta_{CP}$  degeneracy [55]:

$$P_{\mu e}(\theta_{13}, \delta_{CP}) = P_{\mu e}(\theta'_{13}, \delta'_{CP}). \quad (2.90)$$

Together these three degeneracies form an eight-fold degeneracy [56]. There are also other degeneracies like  $\theta_{23} - \delta_{CP}$  degeneracy and the generalized mass hierarchy degeneracy. In the following, we will briefly discuss each of the three degeneracies:

### 2.3.1 The hierarchy- $\delta_{CP}$ degeneracy

The hierarchy degeneracy as defined by Eq. (2.88) means that probability that is obtained for normal hierarchy and certain  $\delta_{CP}$  can also be obtained for some other values of  $\delta_{CP}$  with inverted hierarchy. We illustrate this degeneracy in Fig. 2.1. Here, the left panel gives the  $\nu_\mu \rightarrow \nu_e$  probability for neutrinos and the right panel gives the  $\bar{\nu}_\mu \rightarrow \bar{\nu}_e$  probability for antineutrino. The bands are for the variation of  $\delta_{CP}$  in its full range. The cyan horizontal-crossed bands are for normal hierarchy and the green diagonally crossed bands are for inverted hierarchy. The overlapping regions in both panels show the existence of degeneracy for those values of  $\delta_{CP}$ .

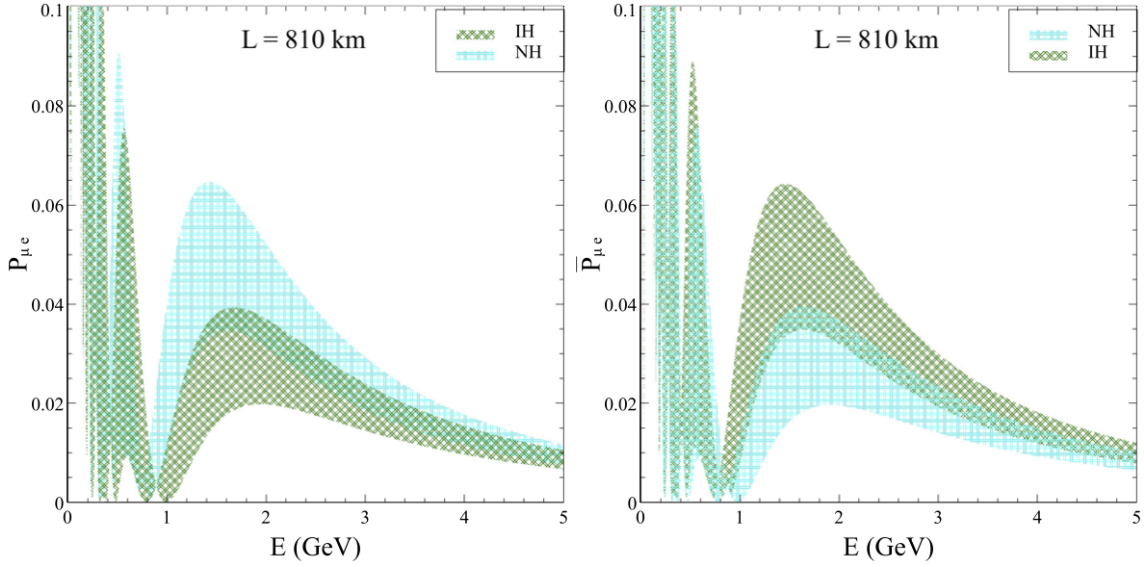


Figure 2.1: Hierarchy degeneracy for  $\nu_\mu \rightarrow \nu_e$  channel at 810 km baseline. The left panel is for neutrino and the right panel is for antineutrino.

We see from this figure that for neutrinos NH probability band is higher than the IH probability band and this is opposite for the antineutrinos. For neutrinos,  $\delta_{CP} = -90^\circ$  are the highest points and  $\delta_{CP} = 90^\circ$  are the lowest points in the bands (both for NH and IH), whereas, for the antineutrinos, this is also reversed. We can divide the entire range of  $\delta_{CP}$  in two halves: the lower half plane (LHP) is for  $-180^\circ \leq \delta_{CP} \leq 0^\circ$  and the upper half plane is for  $0^\circ \leq \delta_{CP} \leq 180^\circ$ . For both panels, we see that the NH-LHP and IH-UHP are at far away from the overlapping regions. Therefore, if NH is true in nature, LHP has less degeneracy and if IH is true in nature, UHP has less degeneracy. On the other hand degeneracies are more for NH-UHP and IH-LHP cases. Hence, for NH, hierarchy sensitivity will be more for  $\delta_{CP} < 0^\circ$  and less for  $\delta_{CP} > 0$  and opposite behaviour will be expected for true IH.

One way to resolve the hierarchy- $\delta_{CP}$  degeneracy is to go for a longer baseline as longer baseline will require larger energy to maintain the same  $L/E$  ratio and hence increasing the matter effect thereby. As the matter effect is increased for longer baseline, the two bands will be more separated and there will be less overlapping regions. Therefore the degeneracy will also get reduced. This is shown in Fig. 2.2, where we give the similar

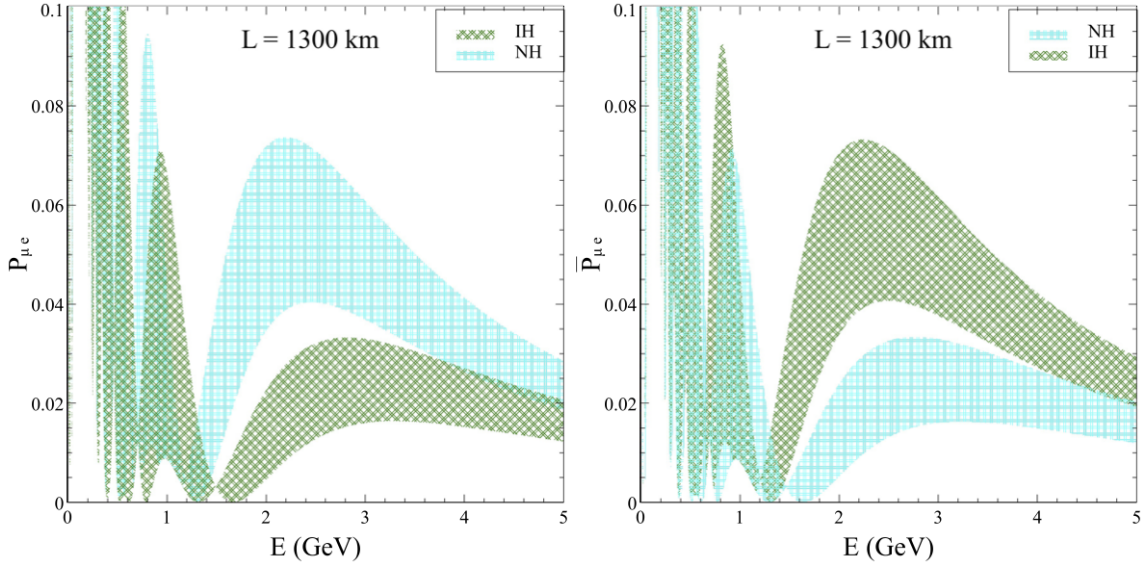


Figure 2.2: Hierarchy degeneracy for  $\nu_\mu \rightarrow \nu_e$  channel at 1300 km baseline. The left panel is for neutrino and the right panel is for antineutrino.

figure like Fig. 2.1, but with a longer baseline of 1300 km. In this figure, we see that the overlapping region is less compared to the smaller one and thus this baseline will have less hierarchy- $\delta_{CP}$  degeneracy.

### 2.3.2 The octant & $\theta_{23} - \delta_{CP}$ degeneracy

As the Eq. (2.89) suggests, there is an intrinsic degeneracy between  $\theta_{23}$  and  $\pi/2 - \theta_{23}$  for the  $\nu_\mu \rightarrow \nu_\mu$  channel as the expression for  $P_{\mu\mu}$  does not contain any term proportional to  $\sin^2 \theta_{23}$  at leading order. Therefore this channel can not differentiate between the two octants of  $\theta_{23}$ . However,  $P_{\mu e}$  has  $\sin^2 \theta_{23}$  dependence and therefore, in principle  $\nu_\mu \rightarrow \nu_e$  can distinguish the octants. But with unknown  $\delta_{CP}$ , some value of  $P_{\mu e}$  for  $\theta_{23}$  and certain  $\delta_{CP}$  can also be obtained for another value of  $\delta_{CP}$  but with  $\theta_{23}$  in the other octant [57]. This is illustrated in the Fig. 2.3. This figure shows the octant- $\delta_{CP}$  degeneracy for neutrino and antineutrinos in left and right panels at 810 km baseline. The bands, like the hierarchy figure, are for variation of  $\delta_{CP}$  in its entire range. Here, the cyan horizontally crossed bands are generated assuming lower octant of  $\theta_{23}$  ( $\theta_{23} = 42^\circ$ ) and the green diagonally crossed bands are generated assuming higher octant of  $\theta_{23}$  ( $\theta_{23} = 48^\circ$ ). In both panels, normal

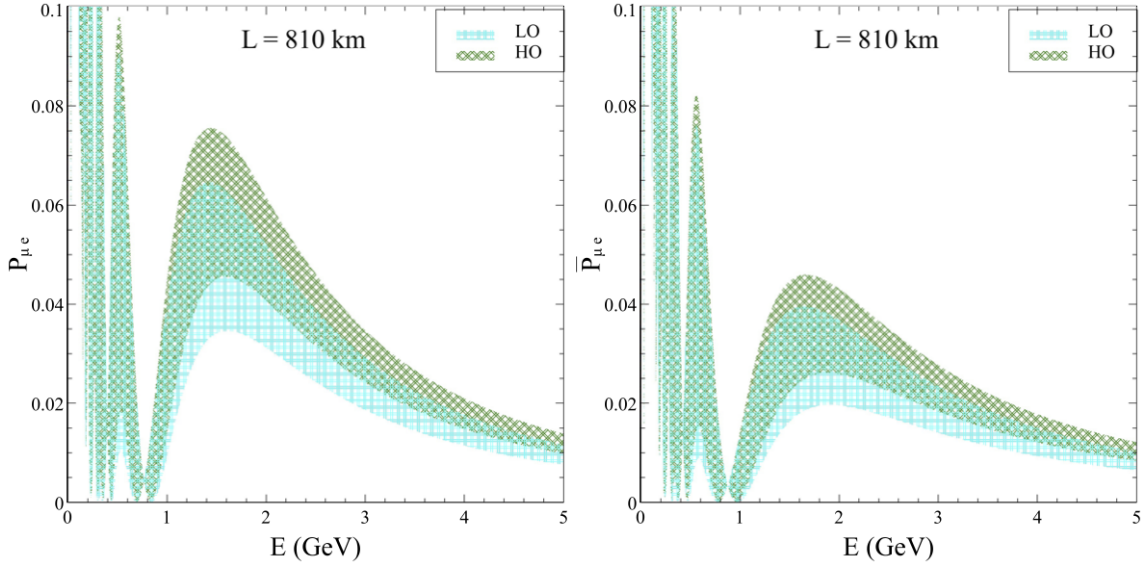


Figure 2.3: Octant degeneracy for  $\nu_\mu \rightarrow \nu_e$  channel. The left panel is for neutrino and the right panel is for antineutrino.

hierarchy is assumed to be true. Like Fig. 2.1, here also the overlapping regions show the effect of degeneracy. Now, the leading order terms of the  $\nu_\mu \rightarrow \nu_e$  appearance probability depends on  $\sin^2 \theta_{23}$  for both neutrinos and antineutrinos, therefore, the probability is higher for higher values of  $\theta_{23}$  for a given  $\delta_{CP}$  and thus the higher octant (HO) bands are always higher than the lower octant (LO) bands in both panels. Again, like Fig. 2.1, the lowest (highest) points in the bands correspond to  $\delta_{CP} = 90^\circ (-90^\circ)$  for neutrinos and opposite for antineutrinos. Therefore, for neutrinos, HO-LHP and LO-UHP are further away but for antineutrinos, LO-UHP and HO-LHP are far away. So, here unlike hierarchy, octant sensitivity is low for LO if  $\delta_{CP}$  is in LHP for neutrinos, whereas for antineutrinos this is reversed and octant sensitivity is high for LO if  $\delta_{CP}$  is in LHP. Therefore, unlike hierarchy sensitivity, neutrino-antineutrino runtime ratio plays a very important role for the resolution of octant.

### 2.3.3 $\theta_{13} - \delta_{CP}$ degeneracy

The  $\theta_{13} - \delta_{CP}$  degeneracy defined in Eq. (2.90) means that there are two sets of  $(\theta_{13}, \delta_{CP})$  at a given energy and baseline giving same  $\nu_\mu \rightarrow \nu_e$  probability. This can be understood

form Eq. (3.1) in the following way. We start by writing Eq. (3.1) in a simpler form:

$$P_{\mu e} = A_{\pm} \theta_{13}^2 + B_{\pm} \theta_{13} \cos(\Delta \pm \delta_{CP}) + P_{sol}. \quad (2.91)$$

For, antineutrinos the  $\delta_{CP} \rightarrow -\delta_{CP}$ ,  $A_+ \rightarrow A_-$  and  $B_+ \rightarrow B_-$ . We can solve the above equation to get  $\theta_{13}$  as a function of  $\delta_{CP}$ :

$$\theta_{13} = -\frac{B_+}{2A_+} \cos(\Delta - \delta_{CP}) \pm \left[ \left( \frac{B_+}{2A_+} \cos(\Delta - \delta_{CP}) \right)^2 + \frac{1}{A_+} (P_{\mu e}(\hat{\theta}_{13}, \hat{\delta}_{CP}) - P_{sol}) \right]. \quad (2.92)$$

Here,  $\hat{\theta}_{13}$  and  $\hat{\delta}_{CP}$  are the values of these parameters, chosen by nature. From the above equation it can be seen that for each values of  $\delta_{CP}$ , we get different values of  $\theta_{13}$  for a particular probability  $P_{\mu e}(\hat{\theta}_{13}, \hat{\delta}_{CP})$ . Similar exercise can also be done for antineutrino. After the precise measurement of  $\theta_{13}$ , now the degeneracy associated with the  $\theta_{13}$  is resolved.

### 2.3.4 Generalized mass-hierarchy degeneracy

Apart from the eight-fold degeneracy discussed above, there is also another important degeneracy in neutrino oscillation [58]. Neutrino oscillation is invariant under the transformation of vacuum Hamiltonian as  $H^v \rightarrow -(H^v)^*$ . This is a direct consequence of CPT symmetry. The above transformation translates into

$$\Delta m_{31}^2 \rightarrow -\Delta m_{31}^2 + \Delta m_{21}^2, \quad (2.93)$$

$$\sin \theta_{12} \rightarrow \cos \theta_{12},$$

$$\delta_{CP} \rightarrow \pi - \delta_{CP}.$$

This degeneracy is always present in vacuum. However, if NSI <sup>1</sup> (non-standard interactions) are present, the situation becomes worse. If the NSI parameters transform along

---

<sup>1</sup>We will discuss NSI in detail in chapter 5

with the above transformations as

$$\begin{aligned}
(\epsilon_{ee} - \epsilon_{\mu\mu}) &\rightarrow -(\epsilon_{ee} - \epsilon_{\mu\mu}) - 2, \\
(\epsilon_{\tau\tau} - \epsilon_{\mu\mu}) &\rightarrow -(\epsilon_{\tau\tau} - \epsilon_{\mu\mu}), \\
\epsilon_{\alpha\beta} &\rightarrow -\epsilon_{\alpha\beta}^* \quad (\alpha \neq \beta),
\end{aligned} \tag{2.94}$$

neutrino oscillation remains invariant even in the presence of matter and this can not be resolved using oscillation experiments only.

From the above discussion, it is clear that the existence of these degeneracies makes it very difficult to measure the oscillation parameters. Particularly  $\delta_{CP}$  makes all the degeneracies complicated. Hierarchy and octant degeneracy together make a four-fold degeneracy. As the two degeneracies are intertwined, measurement of one of the observables depends on knowledge about the others. The hierarchy and octant sensitivity of the long-baseline experiments suffer due to these degeneracies as  $\delta_{CP}$  is unknown now. Hence these degeneracies become very important for the discussion of the long-baseline experiments. In the next chapter, we will discuss long-baseline experiments in detail.



## Long-Baseline Experiments

In this chapter, we will discuss long-baseline experiments in detail. First, we will give a brief general idea about long-baseline followed by descriptions of some of the present and future long-baseline experiments for which we have done our analysis. Long-baseline experiments, as the name suggests, refer to earth-based neutrino oscillation experiments with long baseline. i.e. long distance between the source and the detector of the neutrinos typically distances being more than kilometres. These experiments can be of two types: the reactor based experiments and accelerator based experiments. The reactor based experiments have baselines of the order of few kilometres. As the energies of the reactor neutrinos lie around few MeV, these reactor based experiments can probe the  $\Delta m^2 \sim 10^{-3} \text{ eV}^2$ . Examples of this types of experiments include CHOOZ [59], Palo-Verde [60], Double-CHOOZ [61], RENO [62], DayaBAY [63], etc. On the other hand accelerator based long-baseline experiments typically have baselines in the range of hundreds to thousands of kilometres. The accelerator based experiments can generates neutrinos with energies around hundreds of MeV to GeV range. Therefore, these can explore  $\Delta m^2 \sim 10^{-3} \text{ eV}^2$ . In this thesis, we will only discuss these type of experiments.

## 3.1 Overview of accelerator based long-baseline experiments

In a typical accelerator based long-baseline experiment, a high energy proton beam is first created using an accelerator and the proton beam is bombarded on a fixed target. From the collision of the protons with the nucleons in the target, lots of pions and kaons are created. The charged pions of a pre-decided polarity are then directed to a long decay pipe using a horn magnet. Finally, the charged pions are allowed to decay, producing neutrinos inside the decay pipe during their flight. If the charged pions are  $\pi^-$ , the created neutrinos are mostly  $\nu_\mu$  and if the charged pions are  $\pi^+$ , the created neutrinos are mostly  $\bar{\nu}_\mu$ . The decay of the charged pions mostly gives muon-type neutrinos because of the helicity suppression. There is also  $\sim 1\%$   $\nu_e$  contamination, which results from the decays of  $K^0$  and  $\mu^+$ . The polarity of the charged pions can be controlled by the polarity of the horn magnet. The neutrino beam is sent through the earth to a detector located at a long distance from the accelerator complex. A near detector is also placed near the decay pipe to measure the flux with high precision. The beam at the far detector can be either narrow or wide depending on the off-axis or on-axis location of the detector with respect to the beam-line.

### 3.1.1 Physics at long-baseline experiments

Long-baseline experiments have  $L$  and  $E$  such that they see oscillations both due to  $\Delta m_{31}^2$  and  $\Delta m_{21}^2$ . For example, if  $L$  is 1300 km, the first oscillation maximum for  $\Delta m_{31}^2$  occurs around 2.6 GeV. For DUNE, the flux is peaked around 2.6 GeV. Therefore, the baseline is chosen as 1300 km so that the first oscillation maximum occurs at the peak of the flux. Also at 2.6 GeV the oscillation due to  $\Delta m_{21}^2$  is not very small as  $\sin(1.27\Delta m_{21}^2 L/E) \sim 0.04$ . Therefore, with this choice of  $L$  and  $E$ , the experiments can see both  $\Delta m_{31}^2$  and  $\Delta m_{21}^2$  oscillations. So, this can probe CP violating phase  $\delta_{CP}$ .

The  $\nu_\mu \rightarrow \nu_e$  probability at long-baseline experiments is given by

$$P_{\mu e} \simeq 4s_{13}^2 s_{23}^2 \frac{\sin^2(\hat{A} - 1)\Delta}{(\hat{A} - 1)^2} + 2\alpha s_{13} \sin 2\theta_{12} \sin 2\theta_{23} \cos(\Delta + \delta_{CP}) \\ \times \frac{\sin(\hat{A}\Delta)}{\hat{A}} \frac{\sin((\hat{A} - 1)\Delta)}{(\hat{A} - 1)} + \alpha^2 \sin^2 2\theta_{12} c_{23}^2 \frac{\sin^2(\hat{A}\Delta)}{\hat{A}^2}. \quad (3.1)$$

From this equation, we can see that the  $\nu_\mu \rightarrow \nu_e$  oscillation probability indeed depends on the CP-violating phase.

In the above equation,  $\Delta = \Delta m_{31}^2 L/4E$  and  $\hat{A} = A/\Delta m_{31}^2$ , where,  $A$  is the matter term. Under the change of hierarchy, both  $\Delta$  and  $\hat{A}$  flip signs. So, from Eq. (3.1), we see that the first two terms are not invariant under hierarchy flip. And it is increased as the matter effect is increased. Hence, long-baseline can investigate mass-hierarchy.

Also from Eq. (3.1), we see that there are terms which depend on  $\sin^2 \theta_{23}$  or  $\cos^2 \theta_{23}$ . Therefore,  $\nu_e$  appearance channel can also differentiate between the octant of  $\theta_{23}$ .

Long-baseline detectors can be either on-axis or off-axis. For on-axis experiments the detectors are set at such locations which coincide with the beam axis, whereas, for the off-axis case, they are slightly away from the beam axis.

The off-axis location gives a narrow and sharply peaked neutrino beam. In the meson rest frame, pions and kaons decay mono-energetically and isotropically. However, when they are boosted, the energy spectrum in the lab frame has a broad distribution. The flux falls off with the angle between the boost direction and neutrino production angle. If there is a detector of area,  $A$  located at a distance of,  $z$  from the target, the flux and energy distribution of the neutrinos can be written as

$$\Phi = \left( \frac{2\gamma}{1 + \gamma^2 \theta^2} \right)^2 \frac{A}{4\pi z^2}, \quad (3.2)$$

$$E = \frac{x E_{mes}}{1 + \gamma^2 \theta^2}, \quad (3.3)$$

where,  $\Phi$  is the flux,  $E$  is the neutrino energy,  $\gamma$  is the boost factor given by  $\gamma = E_{mes}/m_{mes}$ , with  $E_{mes}$  and  $m_{mes}$  being parent meson energy and mass respectively,  $\theta$  is the angle between the boost direction and neutrino production direction and  $x$  is a numerical factor which is 0.43 for pions and 0.96 for kaons. Therefore, kaons have more energetic and wider energy distribution for a given meson energy compared to the pions. The main advantage is that the off-axis location makes the beam narrower compared to the on-axis beams.

Another important advantage of the off-axis beam is the increased background rejection. Although pions decay into  $\nu_\mu$  via two body process, the kaons decay into  $\nu_e$  through three body decay. So, there are always some  $\nu_e$  present in the neutrino beam and these  $\nu_e$  make intrinsic background for the  $\nu_e$  appearance channel. As these neutrinos come from three body decays, they have much wider energy distribution compared to the  $\nu_\mu$  which are produced in two body processes. Therefore, this intrinsic  $\nu_e$  background is always reduced in off-axis setup.

Earlier, before the measurement of  $\theta_{13}$ , the long-baseline experiments were designed with the aim of precise measurement of  $\theta_{13}$ . This required high signal to background ratio for the experiments. Therefore, off-axis position was preferred for experiments like NOvA and T2K.

### 3.1.2 Backgrounds

Before going to describe individual experiments, we present here the general backgrounds of a long-baseline experiment. For appearance channel, there are intrinsic background, neutral current background, tau background and the mis-id background. The intrinsic background comes from the contamination of  $\nu_e$  in the beam. Event topology of neutral current events and tau events are similar to the  $\nu_e$  signal events. Therefore, NC and tau also form important backgrounds. Sometimes  $\nu_\mu$  CC events can be mis-interpreted as  $\nu_e$  signal

events and this makes the mis-id background. Usually, disappearance channel has large statistics and therefore backgrounds for the disappearance channel are less important.

## 3.2 Presently running experiments

In this section, we briefly overview the currently running long-baseline experiments. NOvA [26] and T2K [25] fall into this category. Both the experiments are running now and results have been published from both the experiments, although final results of these experiments are yet to come. We will give brief description of each of these experiments in the following.

### 3.2.1 NOvA

NOvA [26] or NuMI Off-axis  $\nu_e$  Appearance experiment is the presently running experiment at Fermilab, USA. NOvA consists of the upgraded NuMI beam at Fermilab accelerator complex which can produce beam power of 700 KW. This creates a proton beam of 120 GeV energy. This high energy beam is bombarded into a 1.2 m graphite target creating pions and kaons from the collision. Then the pions and kaons are focused in a 675 m long decay pipe by horn magnet. Finally, the mesons are allowed to decay during the flight in the decay to create the neutrino beam. The accelerator facility can deliver  $6 \times 10^{20}$  protons per year and hence it will give  $36 \times 10^{20}$  protons on target during its total runtime of 6 years.

NOvA has two detectors, located at 1 km and 810 km away from the beam target. Both detectors are situated at an off-axis angle of 14.7 mrad with respect to the beam axis. But the near detector is much smaller compared to the far detector. The detectors are totally active scintillator detectors. Each detector is made of scintillator cells containing mineral oil and 5 % pseudo-cumene as the scintillator material. The near detector (ND)

has a total mass of about 290 tons and the far detector has a total mass of 14 kton.

The physics goals of NOvA are the following:

- It was set up to observe the  $\nu_\mu \rightarrow \nu_e$  appearance at a  $L/E$  in the range of  $10^2$  to  $10^3$  km/GeV. This gives NOvA sensitive to  $\sin^2 2\theta_{13}$ .
- With 810 km baseline, NOvA has matter effect which enables it to determine mass-hierarchy with some significance.
- $\nu_\mu \rightarrow \nu_e$  channel also has sensitivity to the CP-violation phase.
- NOvA can also determine how close  $\theta_{23}$  is to maximal mixing by precise measurement of  $\nu_\mu \rightarrow \nu_\mu$  disappearance.

### 3.2.2 T2K

T2K (Tokai to Kamiokande) [25] is another current experiment in Japan. T2K neutrino beam is created by the J-PARC (Japan Proton Accelerator Research Complex) accelerator facility situated in Tokai. J-PARC can generate a proton beam of 30 GeV corresponding to a beam power of 240 KW. The beam is then bombarded into the graphite target which gives the mesons after collisions. These charged pions and kaons are then focused in a decay pipe using three horn magnets. The decay pipe has length 96 m where the pions and kaons decay to create the neutrino beam. After the decay pipe, there is a beam dump and a muon counter. Then there is the near detector complex at about 280 m away from the target. There are two near detectors for T2K: the INGRID detector which is a on-axis detector and ND280, the off-axis detector which is at  $2.5^\circ$  off-axis from the beam-line. The far detector is the Super-Kamiokande (SK) detector, which is situated at 295 km away from the target. This is also located at  $2.5^\circ$  off-axis from the beam axis.

The on-axis INGRID near detector is made of  $7 \times 7$  identical modules arranged in a cross-configuration and two diagonal modules. The INGRID detector has a total mass of

about 160 tons. It can detect more than  $10^5$  neutrino events/day. This detector measures the beam direction and profile everyday. This helps in reducing the systematic from the uncertainty of the off-axis angle.

ND280 is the main near detector of the T2K experiment placed 100 m deep underground. It is made of three time projection chambers (TPC) and two Fine Grain Trackers (FGT). Each FGT has a mass of about 1.1 tons.

The far detector of T2K experiment is the SK water Cherenkov detector situated in the Kamioka village. In a charged current interactions, neutrinos produce their corresponding charged leptons. These charged leptons produce Cherenkov light inside the water if they have energy more than a certain threshold (0.76 MeV for electrons and 158.7 MeV for muons). The Cherenkov light propagates in the water as a cone. When these Cherenkov photons reach the inner PMTs, they create ring like pattern. Then the algorithm can extract information like vertex and momenta of the daughter particles. The strategy of SK detector is to find the flavour composition of the T2K beam by counting the charged-current-quasi-elastic(CCQE) interactions for  $\nu_\mu$  and  $\nu_e$ s. Electrons, as they are light, continuously scatter as they travel through the water. The electron scattering emits Bremsstrahlung photons which can further create  $e^-e^+$  pairs which again produce Cherenkov radiation or may scatter like before creating an electromagnetic shower. The overlapping Cherenkov cones produce a diffuse ring in the detector. Muons, on the other hand, being heavy, do not deflect much and thus create sharp rings in the detector.

The physics potential of T2K is given below:

- The main purpose of the experiment is to precisely measure  $\Delta m_{32}^2$  and  $\sin^2 2\theta_{23}$  by  $\nu_\mu$  disappearance channel ( $\delta(\Delta m_{32}^2) \sim 10^{-4} \text{ eV}^2$  and  $\delta(\sin^2 2\theta_{23}) \sim 0.01$ ).
- When this was first proposed,  $\theta_{13}$  was not known and it has sensitivity to  $\theta_{13}$  of about 20 times more than the then best limit obtained from CHOOZ [64]. T2K was the first experiment that reported a nonzero  $\theta_{13}$ . Later reactor experiments confirmed

this.

- T2K also has good sensitivity to  $\delta_{CP}$  at 90 % C.L. or more for over a significant range. Latest data from T2K rules out CP conserving values at more than  $2\sigma$  [65].
- Apart from the oscillation studies T2K has also potential in measuring neutrino cross-section in the resonance production and deep inelastic scattering regions.

### 3.3 Future long-baseline experiments

In this section, we will talk about the next generation of long-baseline experiments that are going to be built in the near future. There are many experiments that are planned all over the world. DUNE [27], T2HK/T2HKK [28,29], ESS [30], P2O [31] are some of the future long-baseline experiments. However, in this thesis, we have done phenomenology for only DUNE and T2HK/T2HKK and therefore, we will limit our discussions only to DUNE and T2HK/T2HKK.

#### 3.3.1 DUNE

DUNE (Deep Underground Neutrino Experiment) is the next-generation international neutrino experiment which will be built in USA. It will generate its high intensity (1.2 MW to 2.4 MW) neutrino beam at the Long Baseline Neutrino Facility (LBNF) at Fermilab. The target will be graphite target based on the NuMI target design. The secondary particles produced from the collision of the protons will be then focused to the 195 m long decay pipe using two magnetic horns, which will use pulsed toroidal magnetic field for focusing. There will be two detectors for the DUNE experiment. One will be a near detector which will be placed about 575 m from the target and there will be a far detector about 1300 km away at Sanford Underground Research Facility (SURF) in South Dakota.

DUNE near detector is not yet finalized. It will be placed at a distance of about 575 m



in the underground near detector hall from the target. Currently, the plan is to make a near detector consisting of a Fine Grain Tracker (FGT) and an electromagnetic calorimeter (ECal) inside a 0.4 T magnetic dipole. This design is expected to have 8 tonne mass. Its primary purpose is to precisely measure of neutrino fluxes, cross-sections, signal and background rates. However, the design is not yet not final.

The far detector of DUNE will be built in an underground cavern 1475 meters deep in Sanford Underground Research Facility (SURF) in Lead, South Dakota and this far detector will be on-axis. Therefore, DUNE will have wide band beam. There will be four detector modules which will be placed in two long caverns. These modules will be four liquid argon time projection chambers (LArTPC). In liquid argon, neutrino interactions with argon produce charged particles which ionize the liquid as well as produce scintillation. In a time projection chamber, a uniform electric field is applied so that the electrons produced by the ionization drift towards the wall where they are picked up by the wires that are kept on the wall perpendicular to the electric field. Readings from the wires give information about the amount of charge and the position inside the liquid, from where the charges drifted. There will also be PMTs put behind the walls to pick the scintillation signal created during the interaction and this will help in determining the initial time of the interaction.  $\nu_\mu$  produces muon in a charged-current interaction. As muons are heavy, they produce long tracks in the TPC readout.  $\nu_e$  on the hand produces electrons during charged-current interactions and these electrons produce shower in the TPC. Liquid argon TPCs have very good energy resolution. DUNE is expected to have  $20\%/\sqrt{E}$  and  $15\%/\sqrt{E}$  energy resolutions for muons and electrons, respectively. The total fiducial mass of the detectors will be around 34 kton. There are two proposed designs for the detector modules: the single phase time projection chambers and the dual phase time projection chambers. In single phase TPCs, charge generation, drift and collection all happen inside the liquid argon whereas in the dual phase detector, the ionization electrons are first extracted into gaseous phase and then amplified before collection by the wires.

DUNE has very rich physics program planned for the coming years.

- Its main goal is to find the CP-violation phase in the leptonic sector and to determine mass hierarchy. DUNE can discover CP-violation for 75% of the  $\delta_{CP}$  values at more than  $5\sigma$  level in 9 years.
- It can determine the mass hierarchy for all values of  $\delta_{CP}$  in 6 years of running at more than  $5\sigma$  significance and at more than  $3\sigma$  significance in less than 3 years.
- DUNE has also potential in measuring other oscillation parameters with high-precision.
- Apart from standard neutrino oscillation physics, DUNE can also probe subdominant new physics effects that affect the oscillation probability. [66–78] show some of such possibilities.
- Apart from oscillation, DUNE near detector can also serve as a probe to explore physics beyond standard model like dark matter searches [79, 80].

### 3.3.2 T2HK

T2HK [28, 29] (Tokai to Hyper-Kamiokande) is an upgradation program of the currently running T2K experiment. It plans to use an upgraded version of the J-PARC beam for neutrino generation. Currently, the horn magnet is operated by a pulsed current of 250 kA, by the time of operation of T2HK, the current is expected to be 320 kA. Currently, the J-PARC beam power is around 470 KW but it is planned to be increased beyond 1.3 MW by 2025, which will be before T2HK becomes operational.

For the near detector of T2HK, upgradation of the current near detector ND280 is under consideration. There is also plan to build a water Cherenkov detector as a near detector. As there are many uncertainties in modelling neutrino interactions with the nuclear targets due to complicated nuclear effects, it will be best to use identical types of detectors at both near and far sites. However, a water Cherenkov near detector should be

large enough to contain the muons up to the energy of interest relevant at the far detector and it should be at enough distance from the neutrino production region to have minimal pile up. These conditions imply a kiloton size detector about 1-2 km away from the target. Water Cherenkov detectors also have good particle identification capability. The water Cherenkov detector will also be complimented by the magnetized ND280 detector which can operate below the Cherenkov light threshold in water and can separate neutrino and antineutrino beam components by measuring lepton charge.

As the far detector, T2HK is going to use the Hyper-Kamiokande (HK) which will be upgradation of the currently running SK detector. The HK detector is going to be built at Tochibora at 295 km away from the source and, near to Mozumi, the site for super-K. Location of HK will also be at  $2.5^\circ$  off-axis from the beam-line. The HK detector will consist of two identical cylindrical tanks placed upright. Each tank will be filled with pure water which will give a total fiducial mass of about 187 ktons and 374 ktons for two tanks. The detector will use recently developed high efficiency and high resolution (timing) PMTs which will be able to detect more photons compared to the SK PMTs and will enhance sensitivity to low energy events like neutron capture and nuclear de-excitations. This will, in turn, increase the sensitivity to the proton decay search and detection of supernova antineutrinos. Physics programs of T2HK are the following:

- Main goal of T2HK is to probe CP-violation in the leptonic sector. With 1.3 MW beam power, T2HK can discover CP-violation at more than  $5\sigma$  significance for 55 % of the  $\delta_{CP}$  values within 10 years of operation if mass-hierarchy is known beforehand.
- Another goal of T2HK is to measure  $\theta_{23}$  and  $\Delta m_{31}^2$  precisely.
- Apart from these, it is also possible to search for various new physics using T2HK.

### 3.3.3 T2HKK

Although T2HK has great sensitivity to the CP-violation for known mass-hierarchy, it has very low mass-hierarchy sensitivity, therefore if mass-hierarchy is unknown, hierarchy-CP degeneracy discussed in subsection. 2.3.1 will come into play and the CP-violation sensitivity will drop significantly. In order to overcome this difficulty, there is a proposal to shift one of the tanks of HK to Korea. This proposal is known as T2HKK (the second K is for Korea). The advantage of shifting the detector is that it will have longer baseline and therefore will have more matter effect due to the larger densities of earth matter. Thus the mass hierarchy sensitivity will be increased significantly and hence the CP-violation sensitivity will also increase. However, in this case the second detector at Korea will be at a distance such that beam energy peak will be at second oscillation maximum instead of the first.

The location of the Korean detector is not yet final. There are many possible sites mentioned in the letter of intent [29]. And, these sites are in the southern part of the Korean peninsula which is at about 1100 km away from the Tokai source and are exposed to the JPARC beam at 1-3 ° range of off-axis angle. There are many off-axis angles considered in the letter of intent from 1.5°-2.5° but we have taken the 2.5° off-axis beam at 1100 km baseline for our analysis.

In this chapter, we described various long-baseline experiments for which we have done our analysis. We have used GLoBES (Global Long Baseline Experiment Simulator) [81,82] along with additional codes [83–85] for all our analysis. In the next three chapters, we will discuss the phenomenology of new physics like sterile neutrino, non-standard interactions and neutrino decay at these experiments.

## Sterile neutrino at long-baseline experiments

Data from some oscillation experiments suggest oscillation of high frequency corresponding to a mass-squared difference of  $\Delta m^2 \sim 1 \text{ eV}^2$ . LSND [32] experiment at Los-Alamos, USA was the first experiment which presented result suggesting this new oscillation frequency. LSND used a  $\bar{\nu}_\mu$  beam. The beam was sent to a detector at a short distance of 30 m. However, the collaboration reported  $3.8\sigma$  excess of positron events which can be explained by  $\bar{\nu}_\mu \rightarrow \bar{\nu}_e$  oscillation corresponding to a mass-squared difference of  $\Delta m^2 \sim 1 \text{ eV}^2$ . Since this oscillation requires mass-squared difference completely different from the solar and atmospheric mass-squared differences, we need another neutrino state in order to explain everything. Together, however, LEP [47] data showed that the number of active neutrinos is strictly 3. Therefore, the new state must be a singlet of the standard model gauge group and hence it is called a sterile neutrino. And this scenario is called the 3+1 scenario [86], if masses of the three active states are consistent with the solar and atmospheric observations. KARMEN [42] and MiniBooNE [33, 34] tested the LSND claim. KARMEN did not find any oscillation in  $\bar{\nu}_\mu \rightarrow \bar{\nu}_e$ . However, it could not entirely rule out the LSND allowed region of the parameter space. MiniBooNE also did not see any excess in its neutrino mode but it indeed reported some excess in its antineutrino mode consistent with the LSND parameter space. It also reported some excess events in the low energy bins of both electron and positron channels but this could not be explained by any oscillation physics. Main challenges came to the 3+1 scenario from

the short-baseline  $\nu_\mu$  disappearance experiments like CDHS [43] and NOMAD [44], atmospheric experiments like super-Kamiokande [87] and MiniBooNE disappearance [46] channel. Neither of these experiments saw any deficit of  $\nu_\mu(\bar{\nu}_\mu)$ . Therefore, there is a strong tension between these results. 3+1 scenario was proposed to explain the so-called reactor [35–37] and Gallium anomalies [38–41]. These reactor experiments explored  $\bar{\nu}_e \rightarrow \bar{\nu}_e$ , therefore, the parameter space probed by these set of experiments were different from the LSND parameter space. Recently data from reactor experiments NEOS [88] and DANSS [89] also disfavours this parameter space as they did not observe any deficit of positrons that can be explained by neutrino oscillation. Long-baseline experiments like MINOS/MINOS+ [90, 91], NOvA [92] and T2K [93] also prefer 3+0 case over the 3+1 case. And atmospheric experiment IceCUBE put strong constraints on the sterile neutrino hypothesis by ruling out most of the LSND parameter space [45]. But, recently MiniBooNE again published their new result [94] which not only saw excess consistent with their old data but combining the LSND result they reported an excess of  $6.0\sigma$ . Combining all the available data together in global fits show strong tension between various data and the topic is highly debatable.

Another challenge to the sterile neutrino hypothesis comes from cosmology. The existence of a light sterile neutrino in the eV mass range affects various cosmological observations like big bang nucleosynthesis, CMB anisotropy and large scale structure formations and it is very difficult to accommodate a sterile neutrino consistent with all the cosmological observations. Therefore, to address the problem of light sterile neutrino we have to wait for the future. Many experiments are planned in the future to test the sterile neutrino hypothesis, some of them are Short Base- line Neutrino Program (SBN) [95], stopped pion beam experiments (OscSNS [96], LSND reloaded [97]), kaon decay at rest beams [98], decay in flight neutrino beams (BooNE, LArTPC detectors at CERN [99], MicroBooNE [100], Very Low Energy Neutrino Factory [101, 102]) and reactor experiments like STEREO [103], PROSPECT [104], SOLID [105] etc. Although these are dedicated experiments designed for testing the 3+1 scenario, it has been shown in liter-

ature that sterile neutrino can also be probed in long-baseline experiments and existence of a sterile neutrino affects the performance of long-baseline experiments. In this work, sterile neutrino at long-baseline experiments like DUNE, T2HK/T2HKK is discussed.

## 4.1 Sterile neutrino formalism

We assume there is one sterile state with  $\Delta m^2 \sim \text{eV}^2$ . This is the 3+1 case. For the 3+1 case, the full neutrino mixing matrix will have six mixing angles, three phases and three mass-squared differences. This mixing matrix can be parametrized in the following way:

$$U_{\text{PMNS}}^{3+1} = O(\theta_{34}, \delta_{34})O(\theta_{24}, \delta_{24})R(\theta_{14})R(\theta_{23})O(\theta_{13}, \delta_{13})R(\theta_{12}) \quad (4.1)$$

Here,  $O(\theta_{ij}, \delta_{ij})$  are  $4 \times 4$  unitary matrices with associated phase  $\delta_{ij}$  in the  $ij$  sector.  $O$  matrices are defined as

$$O(\theta_{13}, \delta_{13}) = \begin{pmatrix} \cos \theta_{13} & 0 & \sin \theta_{13} e^{-i\delta_{13}} & 0 \\ 0 & 1 & 0 & 0 \\ -\sin \theta_{13} e^{i\delta_{13}} & 0 & \cos \theta_{13} & 0 \\ 0 & 0 & 0 & 1 \end{pmatrix}, \quad (4.2)$$

$$O(\theta_{24}, \delta_{24}) = \begin{pmatrix} 1 & 0 & 0 & 0 \\ 0 & \cos \theta_{24} & 0 & \sin \theta_{24} e^{-i\delta_{24}} \\ 0 & 0 & 1 & 0 \\ 0 & -\sin \theta_{24} e^{i\delta_{24}} & 0 & \cos \theta_{24} \end{pmatrix}, \quad (4.3)$$

$$O(\theta_{34}, \delta_{34}) = \begin{pmatrix} 1 & 0 & 0 & 0 \\ 0 & 1 & 0 & 0 \\ 0 & 0 & \cos \theta_{34} & \sin \theta_{34} e^{-i\delta_{34}} \\ 0 & 0 & -\sin \theta_{34} e^{i\delta_{34}} & \cos \theta_{34} \end{pmatrix}. \quad (4.4)$$

$R(\theta_{ij})$  are the rotation matrices in the  $ij$  sector. For example, Since  $\Delta m_{41}^2 \sim 1 \text{ eV}^2$ , the oscillations driven by this mass parameter would be averaged out at the far detectors of T2HK, T2HKK as well as DUNE.

## 4.2 Constraining sterile neutrinos from DUNE near detector

In this section, we explore the capability of DUNE to probe the sterile neutrino hypothesis using its near detector [106]. We check the impact of the baseline, detector fiducial mass and systematic uncertainties on the sensitivity of the DUNE near detector to sterile neutrino oscillations.

The benchmark near detector configuration in our analysis is summarised in the Table 4.1. The energy resolution, detector mass and baseline are taken from the near detector specifications given in the DUNE near detector document [107]. In addition to the benchmark choices for these parameters given in [107], we use two other choices of baseline and detector mass to show the impact of these on the sensitivity of the experiment. For detector mass, we also show results for 400 t and 1 kt. The mass of 400 t is motivated by the ProtoDUNE proposal, which is expected to have 400 t of LArTPC [108] and could at some point be placed along the LBNF beam-line. The 1 kt mass is just an ad-hoc choice of a very large fiducial mass to show that the experiment reaches its statistical saturation already at 400 t and the LSND sensitivity becomes insensitive to any further increase in statistics. For baselines, we also show results for 1 km and 3 km. For the systematic uncertainties, since the possible near detector systematics are not yet clear, we assume the same as that given for the DUNE far detector [109]. We vary this benchmark systematic uncertainties to showcase their impact of the mass and mixing sensitivity.

We use the DUNE flux provided by [110] for this work. A beam power of 1.2 MW



Baseline	595 m /1km /3km
Fiducial mass	5t /400t /1kt
Detector type	HiResMnu
Energy Resolution $e$	$6\% / \sqrt{E}$
Energy Resolution $\mu$	3.7%
Signal Normalization Error	1%
Background Normalization Error	5%
Energy Calibration Error	2%
Energy Range	0-8 GeV
Bin Width	0.25 GeV
Backgrounds	0.1% $\nu_\mu$ CC mis-identification , 0.1% NC background

Table 4.1: The DUNE near detector specification used in this work.

and an exposure of 5 years in  $\nu_\mu$  and 5 years in  $\bar{\nu}_\mu$  mode is used in our analysis. We use the GLoBES package [81, 82] for simulating the DUNE experiment. The neutrino oscillation probabilities in the presence of sterile neutrino are calculated using snu, which is a neutrino oscillation code for calculating oscillation probabilities for GLoBES in the presence of sterile neutrino [83, 84].

### 4.2.1 Probability at near detector

As at short baselines, the oscillations due to  $\Delta m_{31}^2$  and  $\Delta m_{21}^2$  do not develop, at such distance we can approximate the oscillation probability by an effective two-generation framework, which can be written as

$$P(\nu_\mu \rightarrow \nu_e) \simeq \sin^2 2\theta_{\mu e} \sin^2 \left( \frac{\Delta m^2 L}{4E} \right), \quad (4.5)$$

where,  $\theta_{\mu e}$  is the effective mixing angle and  $\Delta m^2$  is the new mass squared difference. Throughout this article, we work in this approximation and study everything in terms of electron appearance data only.

The Fig. 4.25 shows the probability of  $\nu_\mu$  going to  $\nu_e$  as a function of energy at the 595 m baseline, in the presence of one extra sterile neutrino. The red solid curve depicts prob-

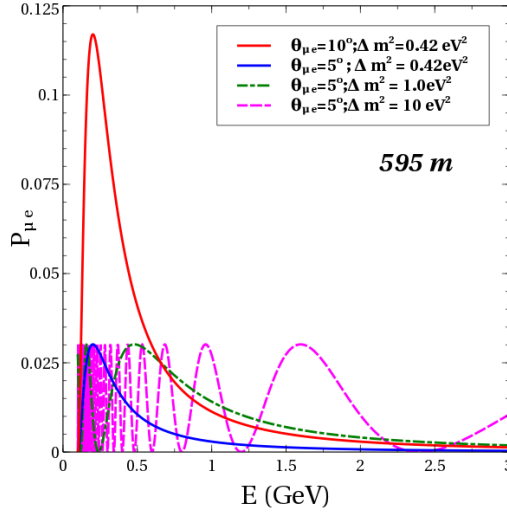


Figure 4.1:  $P_{\mu e}$  probability at 595 m for different sterile neutrino oscillation parameters.

ability for  $\theta_{\mu e} = 10^\circ$  and  $\Delta m^2 = 0.42 \text{ eV}^2$ . The blue solid, green dot-dashed and magenta dashed curves are for  $\theta_{\mu e} = 5^\circ$  and  $\Delta m^2 = 0.42 \text{ eV}^2$ ,  $1.0 \text{ eV}^2$  and  $10.0 \text{ eV}^2$ , respectively. We see that for higher mixing angles, the amplitude of the oscillation increases, and for higher mass-squared differences, the oscillations become faster. In all of the cases depicted in Fig. 4.25, we can see substantial oscillations between  $\nu_\mu$  and  $\nu_e$  in the presence of sterile neutrino. The DUNE beam has huge flux in this energy window. Therefore, DUNE near detector should be highly sensitive in this region of the parameter space.

#### 4.2.2 Events and statistical analysis

Fig. 4.2 shows the event rates for 5 years exposure from a 1.2 MW beam at the near detector for  $\theta_{\mu e} = 5^\circ$  and  $\Delta m^2 = 0.42 \text{ eV}^2$  for the appearance channel. The left panel shows the event rate when there is a sterile neutrino, whereas the right panel shows the event rate when there is no sterile neutrino. We can see that oscillations due to the sterile neutrino state changes the number of events significantly for the appearance channel. Note that the high flux at the near detector magnifies the effects of any oscillation at this small baseline.

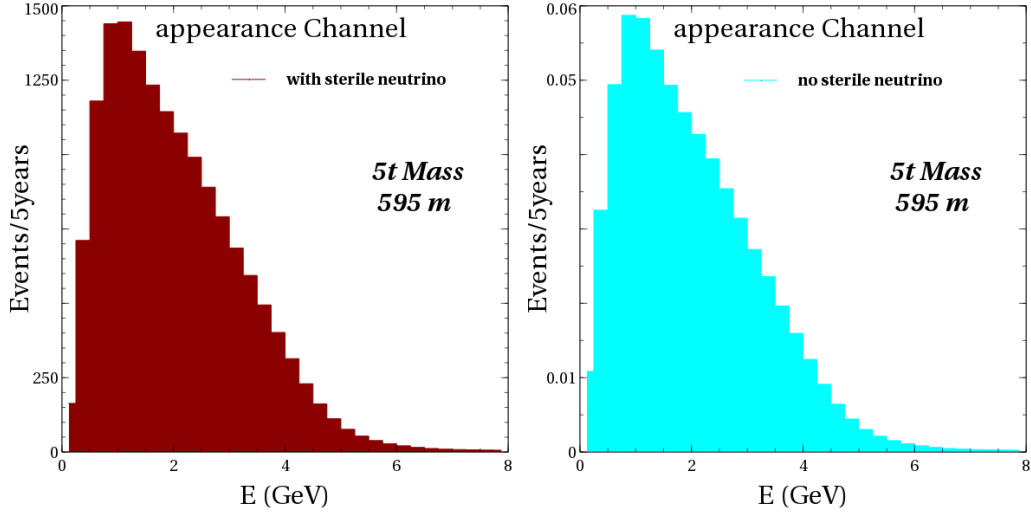


Figure 4.2: Left: 5 years of events at neutrino appearance channel for the case with sterile neutrino at a 5t near detector kept at a baseline of 595 m. Right: 5 years of events at neutrino appearance channel for the case with no sterile neutrino with same detector configuration.

We next define a  $\chi^2$  as

$$\chi^2(\mathbf{n}^{true}, \mathbf{n}^{test}, f) = 2 \sum_i^{N_{reco}} \left( n_i^{true} \ln \frac{n_i^{true}}{n_i^{test}(f)} + n_i^{test}(f) - n_i^{true} \right) + f^2, \quad (4.6)$$

where,  $n_i$  is the number of events,  $i$  is the bin index,  $f$  represents the nuisance parameters, and 'true' and 'test' represent data and fit respectively. The systematic uncertainties and backgrounds assumed in the simulations are given in Table 4.1. Using Eq. (4.6) we present exclusion plots in the  $\Delta m^2 - \sin^2 2\theta_{\mu e}$  plane. In order to do that we take no sterile neutrino in data and scan the  $\Delta m^2 - \sin^2 2\theta_{\mu e}$  parameter space in the fit. The following plots depict how much region of the LSND parameter space can be excluded by the DUNE near detector. In our fit, we consider only the appearance data.

The plots in Fig. 4.3 are exclusion curves for different near detector configurations. The simulation is done for 5+5 years of  $\nu_\mu, \bar{\nu}_\mu$  beam at 1.2 MW. The solid and dashed lines give the  $3\sigma$  and  $4\sigma$  exclusion limits, respectively. The yellow shaded area shows the 90% C.L. allowed region from LSND [32]. The left panel shows how exclusion limit changes as we go to higher baselines, for a fixed detector mass of 5 t. We have

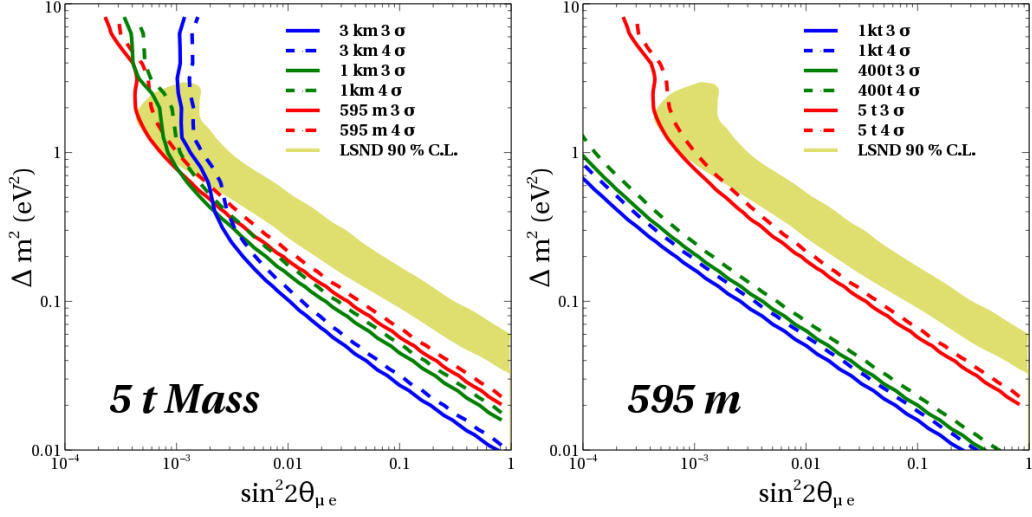


Figure 4.3: Left: Exclusion contours at 3 & 4  $\sigma$  confidence levels for near detector of mass 5t with different baselines. Right: Exclusion contours at 3 & 4  $\sigma$  confidence levels for near detector at 595 m baseline with different detector mass. We consider an exposure of 5+5 for  $\nu_\mu + \bar{\nu}_\mu$ .

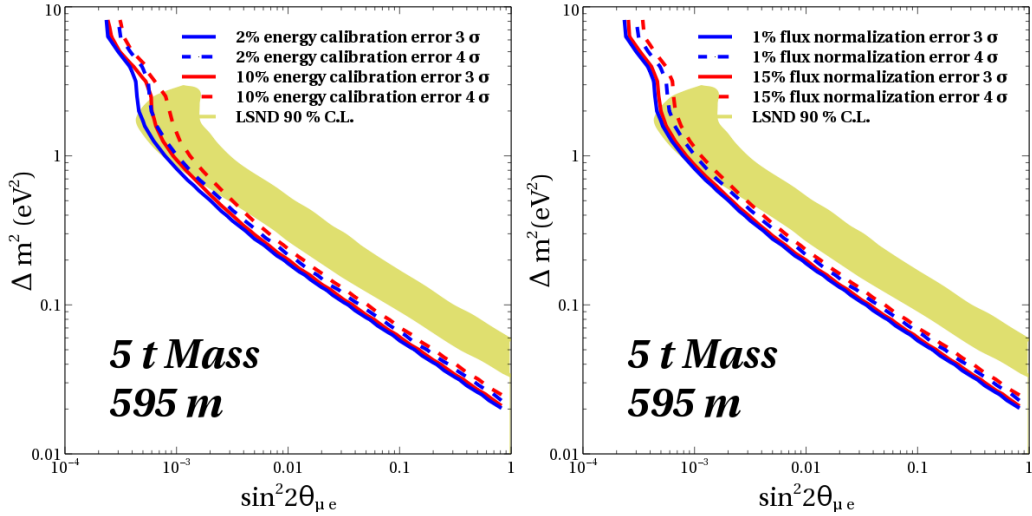


Figure 4.4: Left: Exclusion contours for at 3 & 4  $\sigma$  confidence levels for different energy calibration errors for DUNE near detector at 595 m baseline with 5t mass. Right: Exclusion contours for 3 & 4  $\sigma$  confidence levels for different signal normalisation error. We consider an exposure of 5+5 for  $\nu_\mu + \bar{\nu}_\mu$ .

kept the other detector parameters same as described in Table 4.1. We can see that the DUNE near detector is able to almost rule out the LSND results [32] for all the baseline options. However, we notice that the curve showing exclusion limit changes shape as we change the baseline. We see that as we move to longer baselines, the sensitivity to lower mixing angle is reduced while sensitivity to mass-squared difference at higher mixing angle is increased. The main reason is that the statistics at the higher baselines are  $1/L^2$  suppressed, leading to loss of sensitivity for lower mixing angles for which the oscillation probability is proportionally suppressed. However, longer baselines allow for oscillations of lower  $\Delta m^2$  better, leading for better sensitivity for these parameter regions. The shorter baseline, on the other hand, has higher statistics due to lower  $L$ , allowing it to measure lower mixing angles better. However, the oscillations for lower  $\Delta m^2$  do not develop and the corresponding sensitivity drops.<sup>1</sup>

The right panel of Fig. 4.3 gives the variation of the exclusion limits as we vary the fiducial mass. We have kept the baseline fixed at 595 m for all cases in this panel. Results for the three benchmark masses of 5 t, 400 t and 1 kt are shown. The 5 t is chosen for it is given in the DUNE near detector proposal [107], 400 t is chosen because it is going to be the mass of the ProtoDUNE detector [108] and 1 kt is just another benchmark point. We can see that the 400 t configuration can comfortably rule out the LSND result. The 5 t detector can also almost rule out the LSND allowed region with about  $3\sigma$  C.L.. The figure also shows that fiducial mass has reached its plateau at 400 t, such that any further increase in detector mass and/or exposure does not change the sensitivity by any significant amount. So 400 t LArTPC ProtoDUNE placed at a baseline of about 595 m can be a good choice for the near detector for testing LSND. We have checked that the detector energy resolution does not bring any significant change to our final results.

In Fig. 4.4 we have shown the effect of systematic uncertainties on the sensitivity of

---

<sup>1</sup>The decay pipe of the DUNE beam has a length of about 210 m. This could bring uncertainty in the distance of flight of the neutrinos which might have a bearing on the oscillation signal at the near detector. We have explicitly checked that the impact of this uncertainty is not very significant. We stress that the sensitivity plots shown in this paper are for illustration only.

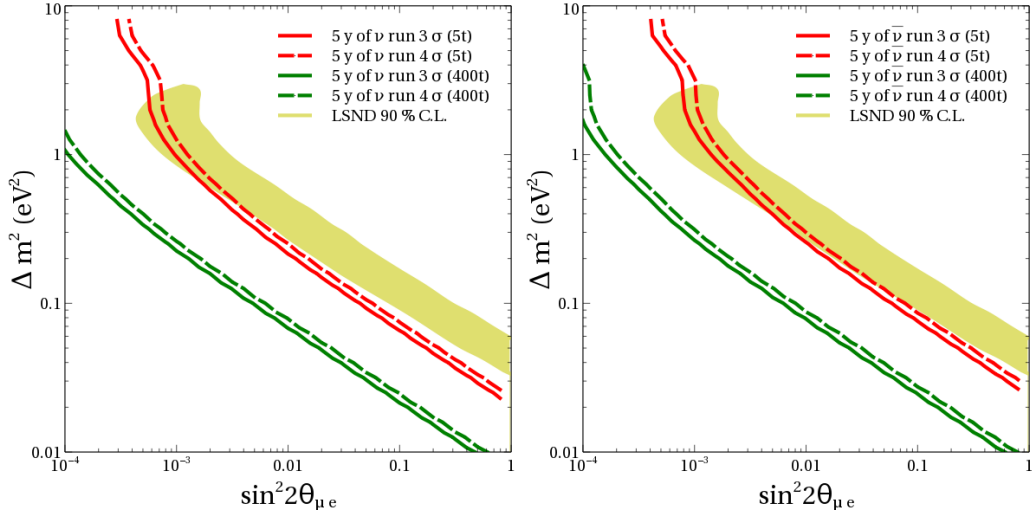


Figure 4.5: The left (right) panel shows the result for running DUNE for 5 years in the neutrino (antineutrino) mode. In both panels, the solid lines are the exclusion curves for  $3\sigma$  C.L. and the dashed lines are the exclusion curves for  $4\sigma$  C.L. The red lines are for 5 t detector and green lines are for 400 t detectors, while the yellow shaded region is the 90% C.L. LSND allowed region.

the near detector to the LSND region. We have considered one optimal (2%) and one conservative (10%) energy calibration error as systematic error in the left panel. In the right panel, we have considered 1% and 15% flux normalisation error of signal. We can see from this figure that the systematic uncertainties have a very small effect on the sensitivity.

In Fig. 4.5 we study the sensitivity of DUNE near detectors separately in the neutrino and the antineutrino modes. Both LSND [32] and MiniBooNE [33, 34, 111] have reported electron excess compatible with oscillations only in the antineutrino channel. Since DUNE will be running for 5 years in the neutrino and 5 years in the antineutrino mode, we can probe sterile neutrino oscillations separately in the two data sets. The results of our study has been shown in Fig. 4.5. The left (right) panel shows the result for running DUNE for 5 years in the neutrino (antineutrino) mode. In both cases we show the sensitivity curves for the 5 t and 400 t detector mass cases. One can see that the neutrino mode can better exclude the parameter space for both 5 t as well as 400 t options, but the antineutrino mode also performs well and can test the LSND region.

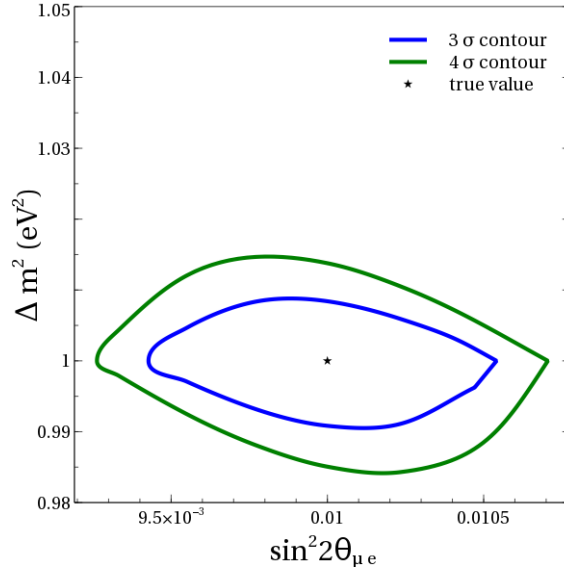


Figure 4.6: Expected sensitivity at the  $3\sigma$  and  $4\sigma$  C.L. for the case when there is a sterile neutrino in the data. The black star is the value for which the data is generated. The blue contour shows the  $3\sigma$  and the green contour shows the  $4\sigma$  C.L.

There are quite a few experimental proposals that plan to test the LSND signal before DUNE near detector becomes operational. If any of these experiments manage to see a signal compatible with sterile neutrino oscillations, then it is pertinent to ask how well the DUNE near detector could measure the  $\Delta m^2$  and  $\sin^2 2\theta_{\mu e}$ . To that end, we perform a study of the projected reach of the DUNE near detector by generating the data at one benchmark point in the  $\Delta m^2 - \sin^2 2\theta_{\mu e}$  plane. This data is then fitted and the results shown in Fig. 4.6. The black star shows the benchmark point chosen. The blue contour shows the bound at  $3\sigma$  C.L. and the green contour shows the  $4\sigma$  C.L. We see that the sensitivity is very good at the  $3\sigma$  and  $4\sigma$  confidence levels and DUNE near detector can tightly constrain the parameter space.

## 4.3 Imprints of a light sterile neutrino at DUNE and T2HK/T2HKK

This section is based on the paper [69]. In this work, we focus on two main purposes. Firstly, we consider the impact of sterile neutrino mixing in the 3+1 scenario on the physics reach of the T2HK and T2HKK set-ups. We calculate the expected sensitivity to neutrino mass hierarchy, CP violation and octant of  $\theta_{23}$  both in the absence (referred to as the 3+0 case) as well as presence (referred to as the 3+1 case) of a sterile neutrino. Secondly, we present a combined analysis of the T2HKK set-up with DUNE to check for possible synergies between the two experiments. We present the expected sensitivity of the T2HK and T2HKK set-ups to the oscillation parameters in both 3+0 and 3+1 scenarios.

### 4.3.1 Simulation procedure

In our analysis, we have used GLOBES (Global Long Baseline Experiment Simulator) [81, 82] to perform all our computations, along with additional sterile neutrino codes [83, 84]. In all the results presented in this paper, we do a full four-generation analysis in the 3+1 framework and calculate the oscillation probabilities in matter using exact numerical codes. Throughout this analysis, we choose the true values of the standard neutrino oscillation parameters as follows [112]:

$$\theta_{12} = 33.5^\circ, \theta_{13} = 8.5^\circ, \Delta m_{21}^2 = 7.5 \times 10^{-5} \text{ eV}^2, \Delta m_{31}^2 = 2.52 \times 10^{-3} \text{ eV}^2 \quad (4.7)$$

We choose true value of  $\theta_{23} = 45.0^\circ$  for CPV and mass hierarchy studies, whereas for the octant sensitivity studies we generate data at  $\theta_{23} = 40.3^\circ$  (we call this case Lower Octant (LO)) and  $49.7^\circ$  (we call this case Higher Octant (HO)). The true mass hierarchy is always taken as normal hierarchy. The true  $\delta_{13}$  is varied in its full range  $[-\pi, \pi]$ . Since



there are twelve parameters in the 3+1 scenario, it is impossible to marginalise overall parameters. Therefore, we check the impact of the relevant parameters on each sensitivity study performed in this work and marginalise the resultant  $\chi^2$  only over the ones that bring any significant change. We will state clearly our marginalisation procedure for every result shown in this paper. Wherever relevant, the marginalisation is performed for  $\theta_{13}$ ,  $\theta_{23}$  and  $\Delta m_{31}^2$  in the ranges are  $[7.99^0, 8.91^0]$ ,  $[38.4^0, 53.0^0]$  and  $[2.40, 2.64] \times 10^{-3} \text{ eV}^2$  for NH &  $[-2.64, -2.40] \times 10^{-3} \text{ eV}^2$  for IH, respectively.

The issue regarding sterile neutrino mass squared difference and mixing angles is far from settled. While LSND [32, 113], MiniBooNE [33, 34, 111], gallium [38–41, 114] and reactor anomaly [35–37] require sterile neutrinos mixed with the active ones, the Bugey-3 [115], Daya Bay [116, 117], NEOS [88], IceCube [45], MINOS [118] and NOvA [92] experiments are consistent with no active-sterile oscillations and put severe upper limits on the mixing angles  $\theta_{14}$  [115–117, 119],  $\theta_{24}$  [45] and  $\theta_{34}$  [118] (see also [92]). The phases are completely unconstrained at the moment. Since there is a certain degree of uncertainty regarding the active-sterile mixing angles, we perform our analysis for two sets of benchmark true values:

$$(\theta_{14}, \theta_{24}, \theta_{34}) = (6.5^\circ, 3.5^\circ, 12.5^\circ), \quad (4.8)$$

$$(\theta_{14}, \theta_{24}, \theta_{34}) = (12^\circ, 7^\circ, 25^\circ), \quad (4.9)$$

where, the former is the set of smaller values of the mixing angles, while the latter are at the higher values. The marginalisation over these mixing angles are done in the range  $\theta_{14} \leq 13^\circ$  [116],  $\theta_{24} \leq 7^\circ$  [45] and  $\theta_{34} \leq 26^\circ$  [118]. The phases are taken over their full range  $[-\pi, \pi]$ . The mass squared difference was taken fixed at  $\Delta m_{41}^2 = 1 \text{ eV}^2$ . The true value of  $\Delta m_{41}^2$  (as well marginalisation over it) has absolutely no impact on our results since the oscillations driven by  $\Delta m_{41}^2$  get effectively averaged as long as they are significantly higher than  $10^{-3} \text{ eV}^2$ . For the numerical simulation we have used the following

specifications for the experiments: <sup>2</sup>

#### 4.3.1.1 DUNE

In this work, we have considered a Liquid Argon detector of fiducial mass 34 kt at a baseline of 1300 km. The neutrino flux is given by the 120 GeV, 1.2 MW proton beam. Here we have considered 5 years of neutrino and 5 years of antineutrino. Appearance and disappearance channels are combined for the analysis. The energy resolutions for the  $\mu$  and  $e$  are taken to be  $20\%/\sqrt{E}$  and  $15\%/\sqrt{E}$ , respectively. The signal efficiency is taken to be 85%. The backgrounds are taken from [27]. In the neutrino (antineutrino) mode, the signal normalization error is 2% (5%), the background normalization error is 10% (10%) and the energy calibration error is 5% (5%). This choice of systematics is conservative compared to the projected systematics in [27]. <sup>3</sup>

#### 4.3.1.2 T2HK

For our analysis, we take a beam power of 1.3 MW and the  $2.5^\circ$  off-axis flux. We consider a baseline of 295 km and the total fiducial mass of 374 kt (two tank each of which is 187 kt). We consider 2.5 years of neutrino and 7.5 years of antineutrino runs in both appearance and disappearance channels. The energy resolution is taken to be  $15\%/\sqrt{E}$ . The number of events are matched with the TABLE II and TABLE III of [29]. The signal normalization error in  $\nu_e(\bar{\nu}_e)$  appearance and  $\nu_\mu(\bar{\nu}_\mu)$  disappearance channel are 3.2% (3.6%) and 3.9% (3.6%), respectively. The background and energy calibration errors in all channels are 10% and 5%, respectively.

---

<sup>2</sup>Recently, in [120], the authors have put strong constraints on the sterile mixing angles from global analysis. The upper limit, used in this work for  $\theta_{34}$  is far outside the range specified in [120]. But we have explicitly checked our results with the new constrain on  $\theta_{34}$  and found that the results reported in this work will not change by 5%.

<sup>3</sup>The experimental specifications for DUNE has been updated in [121]. However, we have explicitly checked that the physics results do not differ much for the two specifications. The older version was for 5+5 years of run while the newer one is for 3.5+3.5 years of run and yet inspite of lower statistics the newer version is able to achieve similar physics goal because of the optimised fluxes, detector response and systematics.

#### 4.3.1.3 T2HKK

In our analysis, we have considered signal normalization error of 3.2% (3.6%) in  $\nu_e$  ( $\bar{\nu}_e$ ) appearance channel and 3.9% (3.6%) in  $\nu_\mu$  ( $\bar{\nu}_\mu$ ) disappearance channel, respectively. The background and energy calibration errors are 10% and 5% in all the channels, respectively.

#### 4.3.2 Numerical probabilities

In this section, we present some of our results at the probability level in order to understand the physics potential of these experiments. The Fig. 4.7 gives the bi-probability plots for JD (the Japan detector at 295 km) at its first oscillation maximum at 0.5 GeV and KD (the Korean detector at 1100 km) at its second oscillation maximum at 0.66 GeV. For each case we have considered all the four combinations of octant (Higher Octant (HO) or Lower Octant (LO)) and mass hierarchy (Normal Hierarchy (NH) or Inverted Hierarchy (IH)) *i.e.*, NH-LO (red), IH-LO (blue), NH-HO (green) and IH-HO (black). As stated before, for LO we have chosen  $\theta_{23} = 40.3^\circ$  as the benchmark value and for HO we take  $\theta_{23} = 49.7^\circ$ . For NH we have chosen  $|\Delta m_{31}^2| = 2.457 \times 10^{-3} \text{eV}^2$  and for IH we have chosen  $|\Delta m_{31}^2| = 2.449 \times 10^{-3} \text{eV}^2$ . The effect of the variation in the bi-probability plots due to the sterile sector phases  $\delta_{24}$  and  $\delta_{34}$  varying in their  $[-\pi, \pi]$  range is shown by the shaded regions. For comparison, we also show the bi-probability ellipse for the standard 3+0 case by the solid curves of the same colour.

The top-left panel shows that for JD there is a strong overlap for NH and IH bi-probability curves even for the 3+0 case and for both LO and HO. This reflects the fact that JD has a smaller baseline and energy and hence, small matter effects. As a result, the sensitivity of JD to CP violation is expected to suffer from mass hierarchy degeneracy. As we switch on the sterile neutrino mixing, the sharp bi-probability lines start to spread and there is a whole band of bi-probabilities coming from the fact that now in addition to  $\delta_{13}$  there are 2 additional phases  $\delta_{24}$  and  $\delta_{34}$ . The bi-probability bands for the different

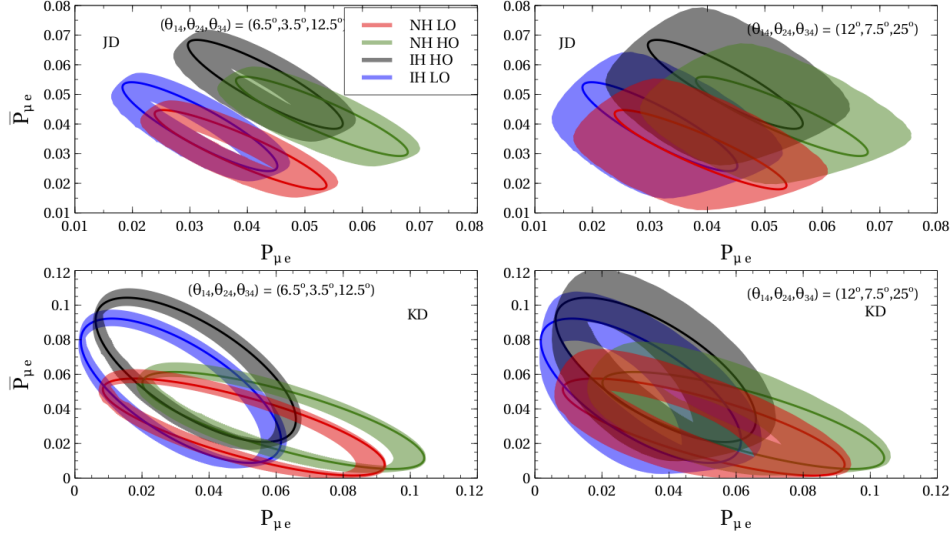


Figure 4.7:  $P_{\mu e}$  vs  $\bar{P}_{\mu e}$  bi-probability plots for JD and KD. The first row shows the plots for JD (295 km and  $E = 0.5$  GeV) and the second row shows the plots for KD (1100 km and  $E = 0.66$  GeV). The left column is for lower set of sterile mixing angles and the right column is for higher set of sterile mixing angles. The shaded regions show the variation of the bi-probability when the sterile phases  $\delta_{24}$  and  $\delta_{34}$  are varied within  $[-\pi, \pi]$ . The solid curves describe the 3+0 case. The different colours correspond to different combinations of mass hierarchy and octant of  $\theta_{23}$ .

colours representing different cases start to overlap more with each other. The overlap increases significantly as we increase the sterile mixing angles, shown in the top-right panel, owing to the fact that the effect of the phases  $\delta_{24}$  and  $\delta_{34}$  increase. The corresponding bi-probability results for the KD baseline and peak energy of 0.66 GeV is shown in the lower panels. As for JD, the bi-probability curves for 3+0 overlap between the different hierarchies even for KD, but the overlap is less. As we switch on the sterile mixing angle (bottom-left panel) the bi-probability lines blur into a band, though the spread in the case of KD appears to be slightly less. As the sterile mixing angles increase (bottom-right panel) the blurring increases showing the increased effect of the phases associated with the sterile mixing angles. We have checked that the main contribution to the blurring of the bi-probability plot comes from the phase  $\delta_{24}$ . The effect of  $\delta_{34}$  is subdominant, although non-zero.

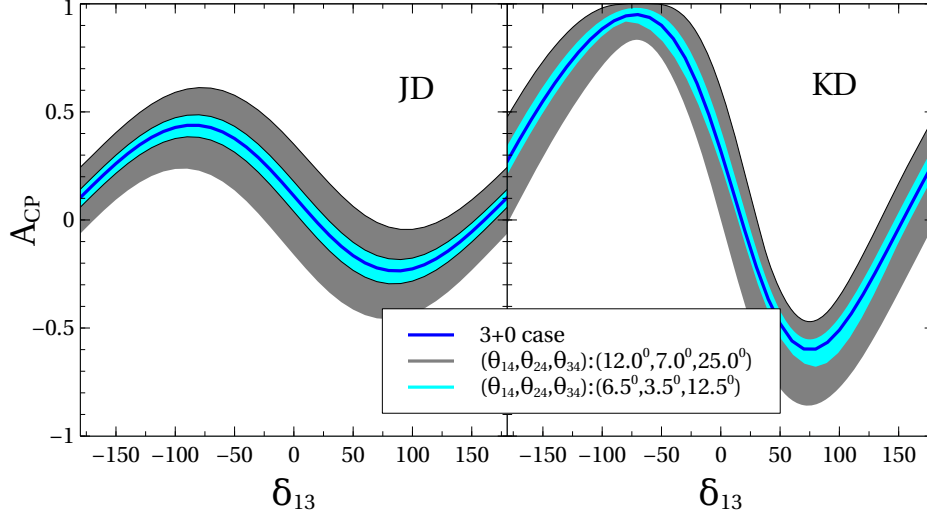


Figure 4.8: CP-asymmetry at JD(left) and KD(right). The bands represent the variation of  $\delta_{24}$  and  $\delta_{34}$ .

Here in Fig. 4.8, we show the CP violation in terms of an asymmetry defined at the probability level to provide some additional insight. We define the CP asymmetry as

$$A_{CP} = \frac{P_{\mu e} - \bar{P}_{\mu e}}{P_{\mu e} + \bar{P}_{\mu e}}. \quad (4.10)$$

The left panel of Fig. 4.8 shows the CP-asymmetry as a function of  $\delta_{CP}$  for the JD baseline of 295 km and at a fixed energy 0.5 GeV, which corresponds to the first oscillation maximum at this baseline. The right panel shows the CP-asymmetry for the KD baseline of 1100 km and at a fixed energy of 0.66 GeV, which corresponds to the second oscillation maximum for this baseline. The solid blue curves depict the  $A_{CP}$  for the 3+0  $\nu$  case in both panels. The bands represent the effect of the sterile phases. For each  $\delta_{13}$ , the bands show the range of  $A_{CP}$  for the full range of values of  $\delta_{24}$  and  $\delta_{34}$  between  $[-\pi, \pi]$ . The cyan bands show the effect of the sterile phases for the lower set of sterile mixing angles and the grey bands show the same for the higher set of mixing angles. We see that the presence of the sterile neutrino mixing spreads the  $A_{CP}$  in both sides of the standard 3+0 case. This implies that for a given true value of  $\delta_{13}$ , the CP asymmetry in the presence of sterile neutrinos could either increase or decrease for both JD and KD baselines and

energies, depending on the true values of  $\delta_{24}$  and  $\delta_{34}$ . Looking from another angle, this also implies that the presence of sterile neutrino mixing brings in an uncertainty in the expected CP asymmetry at long-baseline experiments. Observation of a certain CP asymmetry signal in the data could come from degenerate solutions involving mixing angles and phases in the 3+0 sector and the sterile sector. We can also see from the plots that with higher mixing, widths of the bands increase and hence the uncertainties in the CP-sector introduced by the sterile phases increases. We also note that the CP-asymmetry is significantly higher for KD than for JD. The reason is that, the shape and magnitude of the curves largely depend on the baseline and energy value chosen, or more precisely on the  $L/E$  factor.

The Fig. 4.9 shows the MH-asymmetry for JD(left) and KD(right) baselines at a fixed energies of 0.5 GeV and 0.66 GeV, respectively. The MH-asymmetry is defined as:

$$A_{MH} = \frac{P_{\mu e}^{NH} - P_{\mu e}^{IH}}{P_{\mu e}^{NH} + P_{\mu e}^{IH}} \quad (4.11)$$

In NH we have taken  $\Delta m_{31}^2 = 2.45 \times 10^{-3} \text{ eV}^2$  while in IH we have taken  $\Delta m_{31}^2 = -\Delta m_{31}^2 + \Delta m_{21}^2$ . Just as in the previous figure, the blue solid curves show the MH-asymmetry for the standard (3+0) case. As before the bands are obtained when the sterile mixing angles  $\delta_{24}$  and  $\delta_{34}$  are varied in their full range  $[-\pi, \pi]$ . The cyan bands are for the lower set of sterile mixing angles and the grey bands are for a higher set of sterile mixing angles. From the Fig. 4.9, we can see the effect of the new physics at the probability level. We can see naively that at the probability level it appears that for the 3+1 scenario, the mass hierarchy asymmetry has a chance of either increasing or decreasing compared to its 3+0 expected reach, depending on the true values of  $\delta_{24}$  and  $\delta_{34}$ . We can see that with the increase of the sterile mixing angles the effect increases. As in Fig. 4.8, we find that the MH-asymmetry expected in KD is more than in JD and the reason for this is its higher chosen energy value and earth matter effects.

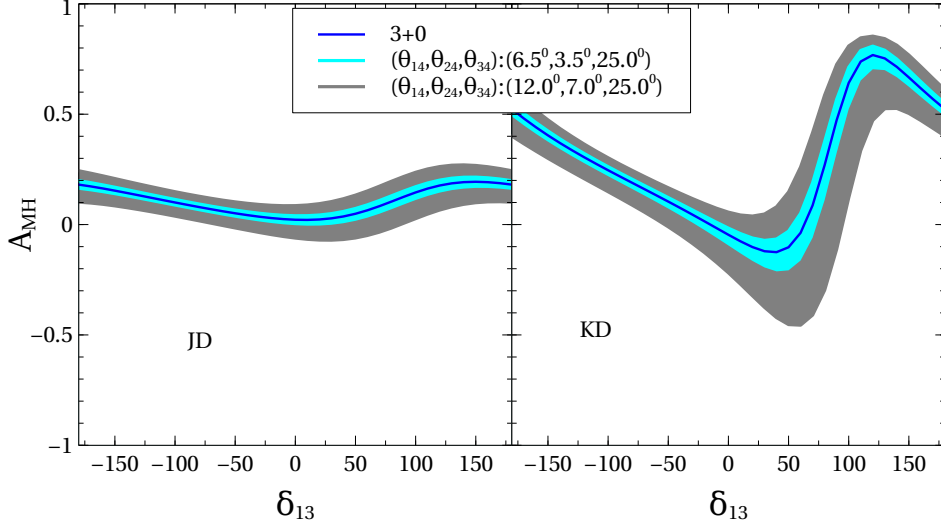


Figure 4.9: MH-asymmetry as a function of  $\delta_{13}$  for JD(left) and KD(right). The bands represent the variation of  $\delta_{24}$  and  $\delta_{34}$ .

### 4.3.3 CP sensitivity

In this section, we present our CP violation sensitivity results in the presence of a light sterile neutrino. That is, we are addressing the following question: If CP is violated in Nature, then at what C.L., T2HK(JD $\times$ 2) and T2HKK(JD+KD) can exclude the CP conserving scenarios in the presence of a sterile neutrino? In the 3+1 scenario, we have two more phases  $\theta_{24}$  and  $\theta_{34}$  in addition to the standard CP phase  $\delta_{13}$ . So while studying CP violation sensitivity of these experiments in the presence of sterile neutrinos, we consider the following two situations:

1. CP is violated and we do not know the source of its violation. That is, it can be due to any of the three phases.
2. CP is violated and we know the source of its violation. For instance, say we assume that it is due to the standard Dirac CP phase  $\delta_{13}$ .

As explained above, we have presented our results for two sets of sterile mixing angles and for each set we fix the standard oscillation parameters to their best fit values in ‘data’ and vary all the three true phases in their full range  $[-\pi, \pi]$ . While answering the question

of CP violation in the first scenario, we generate the data at a given true value of  $\delta_{13}$ ,  $\delta_{24}$  and  $\delta_{34}$  and calculate the  $\Delta\chi^2_{\min}$  by considering all the eight possible CP conserving scenarios in the ‘fit’. We marginalise over a fine grid of  $\theta_{14}$ ,  $\theta_{24}$ ,  $\theta_{34}$  in their allowed range in the ‘fit’. In addition, we have marginalised over the test  $\theta_{13}$  in its  $3\sigma$  allowed range.

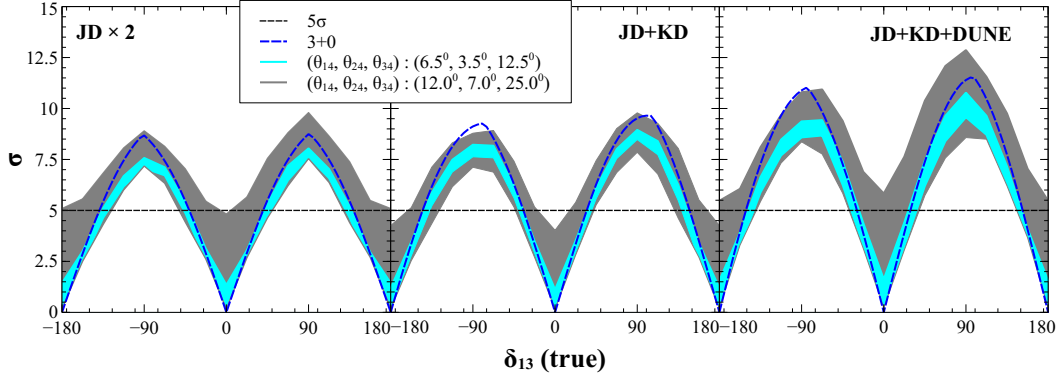


Figure 4.10: The expected CP violation sensitivity of T2HK (JD $\times$ 2), T2HKK (JD+KD) and DUNE+JD+KD under the assumption that we do not know the source of its violation. The bands correspond to variation of  $\delta_{24}$  and  $\delta_{34}$  in the true parameter space. The results are for true normal hierarchy.

The results of CP violation sensitivity in the first scenario are presented in Fig. 4.10. The mass hierarchy is kept fixed as NH in both the ‘data’ as well as the ‘fit’ for this figure and in the next two figures in this subsection. The blue dashed line corresponds to the standard CP sensitivity in the 3+0 case as a function of  $\delta_{13}(\text{true})$ . The bands correspond to the 3+1 case with all possible choices for the other two phases  $\delta_{24}(\text{true})$  and  $\delta_{34}(\text{true})$ . The thinner cyan band gives this band for  $\delta_{24}(\text{true})$  and  $\delta_{34}(\text{true})$  when the sterile mixing angles are taken to be at their smaller benchmark value while the grey band is obtained for the corresponding case when the sterile mixing angles are kept at their limiting benchmark value. In both cases, these are the value of the sterile mixing angles in the ‘data’, kept fixed in the entire band, while in the ‘fit’ they are marginalised as discussed above. We observe that for all  $\delta_{13}(\text{true})$  which give more than  $5\sigma$  CP sensitivity, the cyan band almost lies below the blue line. So for relatively small 3+1 mixing angles, sensitivity to CP violation in the 3+1 case decreases compared to the standard 3+0 case. But as the mixing angles increases, the 3+1 grey band spans both sides of the 3+0 plot. In the 3+1 case,



as discussed in [67], there are two effects that come into play. Firstly, the number of parameters to be marginalised in the ‘fit’ is higher than the 3+0 case and marginalising over a large number of parameters brings the  $\chi^2_{min}$  down. Secondly, the effect of the variation of the true phases changes with the variation of the true values of the mixing angles. When mixing angles are small, the effect of the true phases are also small and hence the first effect dominates the second one. As a result, the  $\chi^2_{min}$  decreases compared to the 3+0 case. But as the true mixing angles increase, the effect of the variation of the true phases increases simultaneously and as a result, the width of the grey band increases. So for higher values of the mixing angles, the second effect tends to increase the  $\chi^2_{min}$  and as a result, overall sensitivity increases and the grey band spreads on both side of the 3+0 plot.

As seen from Fig. 4.10, T2HKK (JD+KD) has slightly better sensitivity to CP violation in the 3+0 case than T2HK(JD $\times$ 2). But in the 3+1 case, we observe that T2HK and T2HKK have almost equal sensitivity to CP violation at  $\delta_{13} = \pm\pi/2$  when mixing angle are large. But for smaller mixing angles, T2HKK gives slightly better sensitivity than T2HK (JD $\times$ 2). Also note that in the 3+1 case, we have non zero CP violation sensitivity even at the CP conserving values of  $\delta_{13}(\text{true})$ . For the higher mixing angle case and for  $\delta_{13}(\text{true}) = 0$  or  $\pm\pi$ , we have more than  $3\sigma$  CP violation sensitivity for  $\delta_{24}(\text{true})$  in the range  $[45^\circ, 135^\circ]$  and  $[-135^\circ, -45^\circ]$ . The effect of  $\delta_{34}(\text{true})$  is less important. Combining JD and KD with DUNE enhances the CP violation sensitivity and we observe that even when  $\delta_{13}(\text{true}) = 0$  or  $\pm\pi$ , it is possible to achieve more than  $5\sigma$  CP violation sensitivity in the higher mixing angle case for  $\delta_{24}(\text{true})$  in the range  $[90^\circ, 112^\circ]$  and  $[-112^\circ, 90^\circ]$ . Again the impact of  $\delta_{34}$  is not important.

To address the second scenario, we consider the CP conserving cases for  $\delta_{13}$  alone in the ‘fit’ while we have marginalised over the two new phases,  $\delta_{24}$  and  $\delta_{34}$  in the allowed  $3\sigma$  range. All other 3+1 mixing angles and  $\theta_{13}$  are marginalised, as explained above. The results are shown in Fig. 4.11, where we observe that the CP violation sensitivity in the

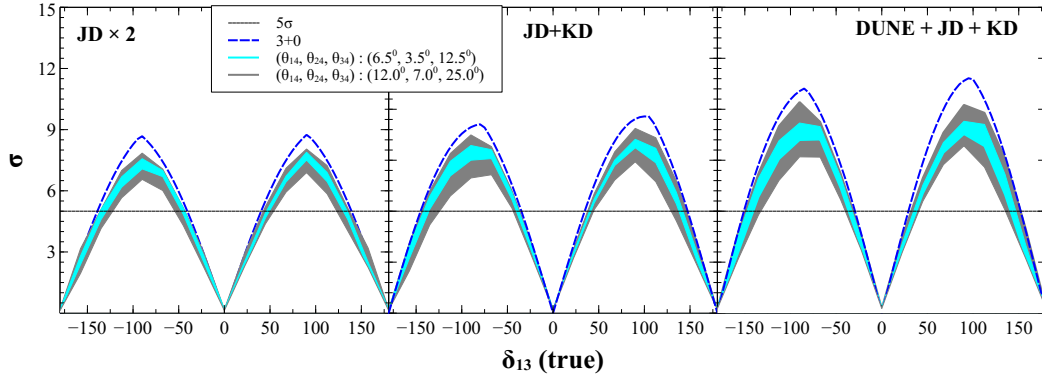


Figure 4.11: The expected CP violation sensitivity of T2HK ( $\text{JD} \times 2$ ), T2HKK ( $\text{JD} + \text{KD}$ ) and DUNE+JD+KD under the assumption that we know the source of its violation and it is due to  $\delta_{13}$ . The bands correspond to variation of  $\delta_{24}$  and  $\delta_{34}$  in the true parameter space. The results are for true normal hierarchy.

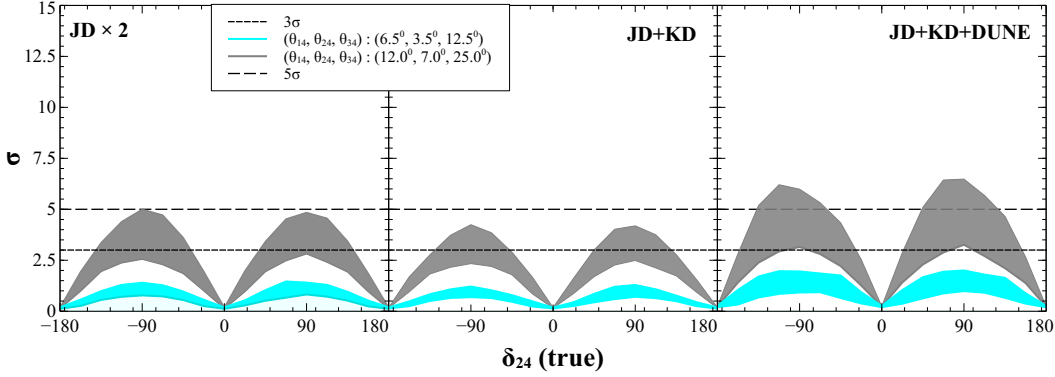


Figure 4.12: The expected CP violation sensitivity of T2HK ( $\text{JD} \times 2$ ), T2HKK ( $\text{JD} + \text{KD}$ ) and DUNE+JD+KD under the assumption that we know the source of its violation and it is due to  $\delta_{24}$ . The bands correspond to variation of  $\delta_{13}$  and  $\delta_{34}$  in the true parameter space. The results are for true normal hierarchy.

3+1 case decreases compared to the standard 3+0 sensitivity in all the three experimental set-ups. Both the cyan and grey bands lie below the 3+0 sensitivity plot for all true  $\delta_{13}$ . We also observe that the minima of the grey band are nearly at the same level in T2HKK and DUNE+T2HKK while it is slightly lower in the case of T2HK. From Fig. 4.11 (Fig. 4.12), we observe that restricting the source of CP violation to only  $\delta_{13}$  ( $\delta_{24}$ ) in the ‘fit’ brings down the sensitivity. In the previous case (Fig. 4.10), we have considered only eight combinations of the phases in the ‘fit’ while in this case, we have marginalised over two phases in their full allowed range. Marginalising over a large number of parameters lead to decrease in sensitivity.

In Fig. 4.12, we have shown the results for CP violation due to  $\delta_{24}$  and here the widths of the bands are due to the variation of  $\delta_{13}(\text{true})$  and  $\delta_{34}(\text{true})$  in their full allowed range. Also in the ‘fit’ we have marginalised over these two phases in their full range and choose CP conserving values for  $\delta_{24}$ . CP violation sensitivity, in this case, is much lower than the previous two cases and the two bands are well separated from each other. So if there is a sterile neutrino and CP violation is considered to be solely due to  $\delta_{24}$ , then T2HK and T2HKK can measure it at  $3\sigma$  C.L. only for some fraction of true  $\delta_{24}$  and as seen from Fig. 4.12, T2HK is better than T2HKK. Even after combining with DUNE, we can achieve  $5\sigma$  CP violation sensitivity for some fraction of true  $\delta_{24}$  only around the peak when the mixing angles are large.

#### 4.3.3.1 CP Violation sensitivity if hierarchy is unknown

The results presented in the previous section is under the assumption that the mass hierarchy will be known by the time of operation of these experiments. We have also checked the CP violation sensitivity for the true inverted hierarchy and the behaviours of the results are consistent.

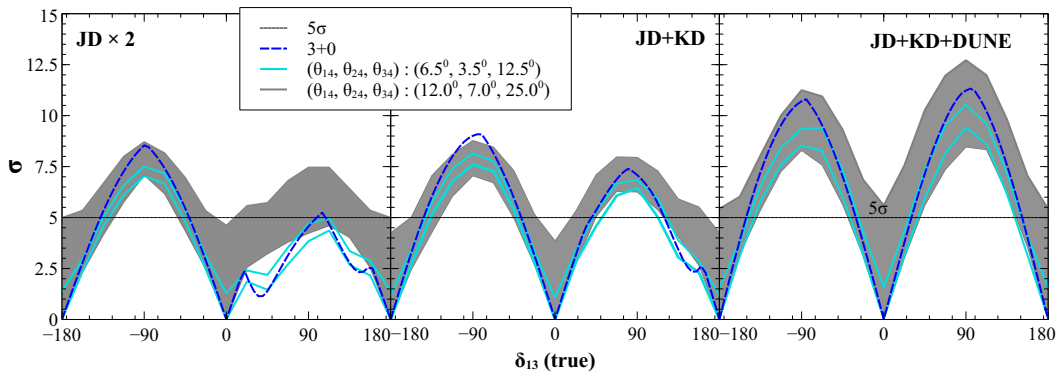


Figure 4.13: The expected CP violation sensitivity of T2HK ( $\text{JD} \times 2$ ), T2HKK ( $\text{JD} + \text{KD}$ ) and DUNE+ $\text{JD} + \text{KD}$  under the assumption that we do not know the source of its violation as well as the hierarchy. The bands correspond to variation of  $\delta_{24}$  and  $\delta_{34}$  in the true parameter space. The results are for true normal hierarchy.

In this section, we show the CP violation sensitivity in the 3+1 case without fixing the mass hierarchy to its true case in the ‘fit’. In Fig. 4.13, we show the results for

expected CP violation sensitivity for the first scenario where we rule out CP conserving values of all the three phases and with marginalisation over MH in the ‘fit’. We have assumed the NH to be true in this figure. That is, for each ‘simulated data’ case, we find the  $\chi^2$  for eight combinations of CP conserving phases for each hierarchy in the ‘fit’ and hence sixteen combinations in total. The minimum  $\Delta\chi^2_{\min}$  amongst these sixteen combinations are plotted in Fig. 4.13 as a function of  $\delta_{13}(\text{true})$  where the full range of  $\delta_{24}(\text{true})$  and  $\delta_{34}(\text{true})$  are represented in the bands. Marginalisation over other parameters are the same as explained in the previous subsection. The regions between the two cyan lines represent the CP violation sensitivity for the small mixing angles benchmark point, while the grey band depicts the sensitivity for the higher mixing angles benchmark case. The blue dashed lines show the 3+0 sensitivity for each of the three experimental set-ups. We observe that in the 3+0 scenario, CP violation sensitivity decreases significantly for T2HK, specially in the upper half-plane (UHP) ( $\delta_{13}(\text{true}) > 0$ ) if the MH is taken to be unknown. For T2HKK although there is a drop in the sensitivity in the UHP for the 3+0 case compared to its counterpart in Fig. 4.10, the effect of marginalising over hierarchy is less here than for T2HK. This happens because KD can resolve the mass hierarchy degeneracy to a large extent in the T2HKK set-up. Once we combine DUNE with T2HKK, the effect of the unknown hierarchy almost vanishes. On the other hand, in the presence of a sterile neutrino, the CP violation sensitivity decreases if the new mixing angles are small. But for the larger mixing angles case, the sensitivity increases in the UHP and for some combinations of  $\delta_{24}(\text{true})$  and  $\delta_{34}(\text{true})$ , we can have more than  $5\sigma$  sensitivity at  $\delta_{13} = +\pi/2$  for T2HK. Adding DUNE not only enhances the sensitivity but also nullifies the effect of unknown MH even in the presence of a sterile neutrino.

#### 4.3.4 Mass hierarchy sensitivity

In this section, we discuss the expected sensitivity to neutrino mass hierarchy of T2HK and T2HKK in the 3+1 scenario. For that, we generate the data at a given true MH and

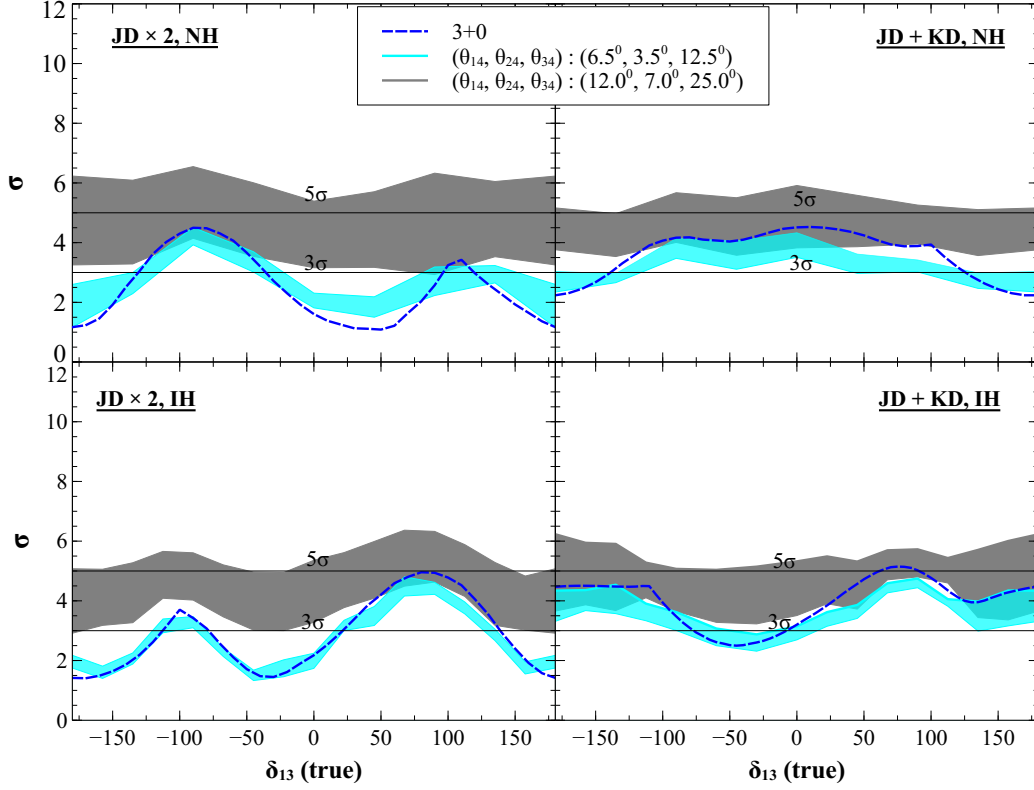


Figure 4.14: The expected mass-hierarchy sensitivity of T2HK (JD×2) and T2HKK (JD+KD). The upper panel is for true NH while the lower panel is for true IH. The bands correspond to the variation of the sterile phases in the true parameter space.

‘fit’ it with the wrong hierarchy. We marginalise over all the three phases in the ‘fit’ and all the sterile mixing angles and also  $|\Delta m_{31}^2|$  and  $\sin^2 \theta_{23}$ . Here we have not marginalised over  $\theta_{13}$  due to computational challenges. We have seen in Fig. 4.9 that the MH-asymmetry can change due to the presence of sterile neutrino mixing. However, there we have done everything only at the probability level and for fixed values of oscillation parameters as well as for a fixed energy. We will now show how the expected sensitivity to MH changes due to sterile neutrinos from a full analysis of expected data when one takes all relevant marginalisation into account.

The results for T2HK and T2HKK for both NH (upper panel) and IH (lower panel) as true are shown in Fig. 4.14. The presentation and description of the bands are the same as that in the previous subsection. We observe that the sensitivity to mass hierarchy in

the presence of a sterile neutrino changes significantly in both the experiments. We have explicitly checked the effect of marginalisation on mass hierarchy sensitivity. Here also, we notice the two features discussed in section V B. We observe that,

1. For the higher sterile mixing angles, the impact of the variation of the true phases increases and it tends to increase the  $\chi^2_{min}$ .
2. Effect of marginalisation over test  $|\Delta m^2_{31}|$  in the wrong hierarchy is very important for the MH sensitivity study. Its effect is seen to be most for the 3+0 case and keeps decreasing with the strength of the true sterile mixing. As a result, the  $\chi^2_{min}$  goes up for the higher set of sterile mixing angles.

For smaller sterile mixing angles, we observe that the width of the cyan band is small in both the hierarchies and the sensitivity for the 3+1 scenario, in this case, is nearly same as 3+0. In case of T2HK, the cyan band swings around the 3+0 plot but in T2HKK, it lies below the 3+0 line for most of the  $\delta_{13}(\text{true})$  values, in both the hierarchies. However, the mass hierarchy sensitivity seems to increase for the larger mixing angle case. This apparently appears counter-intuitive to what we have observed in Fig. 4.7 where the overlap between the bi-probability plots was seen to increase when we increased the sterile mixing angles, making it appear as though the sensitivity to mass hierarchy would decrease as the sterile mixing angle was increased. We can also note that in Fig. 4.14 the grey band does not span equally on both sides of the cyan band. Instead, the two bands get separated for most values of  $\delta_{13}(\text{true})$ . This again appears to be in contrast to Fig. 4.9 where the cyan band was embedded nearly symmetrically inside the grey band. The reason for both these apparent conflicts can be traced back to the impact of marginalisation of the mass hierarchy  $\chi^2$  over  $|\Delta m^2_{31}|$ . We have checked that the marginalisation over  $|\Delta m^2_{31}|$  alone reduces the mass hierarchy  $\chi^2$  by nearly an order of magnitude for the 3+0 scenario. For the smaller sterile mixing angle case, the effect of sterile neutrino parameters is less and the final marginalised  $\chi^2$  is close what we have for the 3+0 case. However, as the sterile

mixing angle is increased the effect of marginalisation over  $|\Delta m_{31}^2|$  is able to reduce the  $\chi^2$  relatively less and as the result the final mass hierarchy sensitivity appears to rise. For the same reason, the cyan band becomes asymmetric with respect to the grey band. For the largest sterile mixing angle case, we have more than  $5\sigma$  sensitivity for mass hierarchy for any  $\delta_{13}(\text{true})$ .

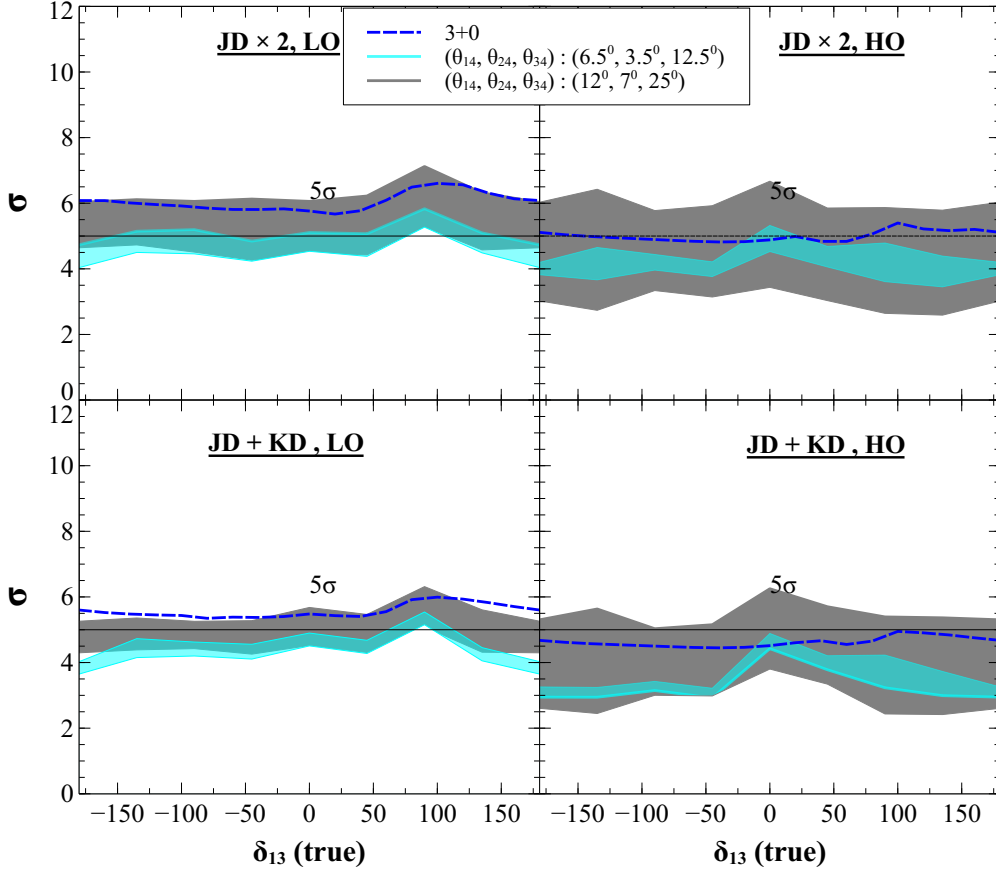


Figure 4.15: The expected octant discovery potential of T2HK (JD $\times$ 2) and T2HKK (JD+KD). In the LO (HO), we consider  $\theta_{23} = 40.3^\circ$  ( $49.7^\circ$ ) as the true value. The upper panel is for T2HK (JD $\times$ 2) while the lower panel is for T2HKK (JD+KD). The bands correspond to the variation of the sterile phases.

### 4.3.5 Octant discovery

In this section, we study the octant discovery potential of T2HK and T2HKK in the 3+1 scenario. We also present a combined analysis of T2HKK with DUNE. We consider the same benchmark value of true  $\theta_{23}$  for which we have shown the bi-probability plots in Fig. 4.7. We then show the potential of these experiments to exclude the wrong octant for

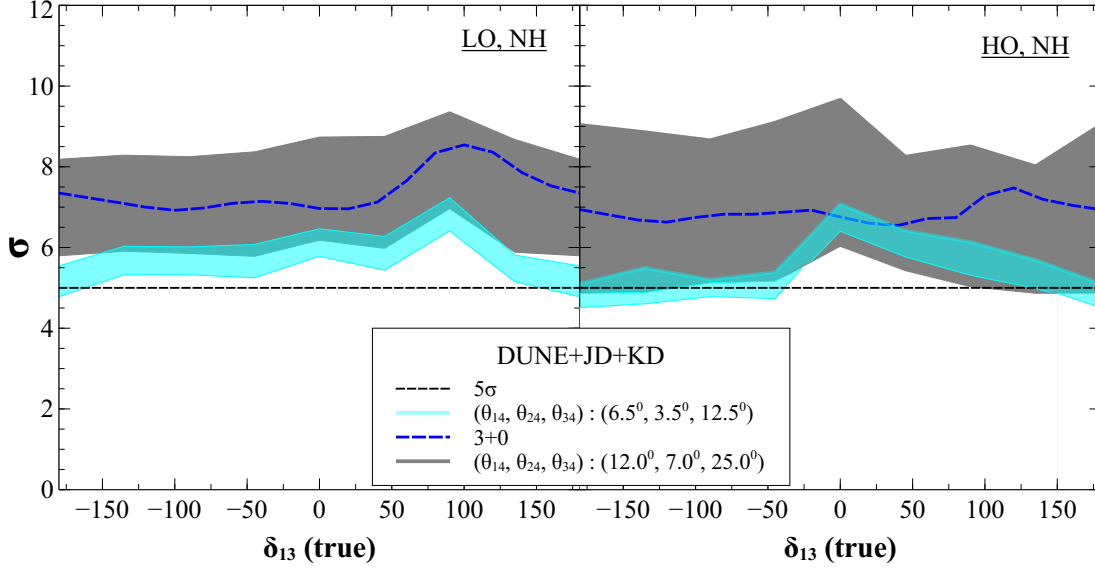


Figure 4.16: The octant discovery potential of DUNE+T2HKK(JD+KD).

the two sets of sterile mixing angles. In data, we vary all the three phases, as discussed above, we show the band of  $\Delta\chi^2_{\min}$  as a function of the  $\delta_{13}(\text{true})$ . The band corresponds to the full range of  $\delta_{24}(\text{true})$  and  $\delta_{34}(\text{true})$ . In the ‘fit’, we marginalise over the sterile mixing angles and the phases in their allowed ranges. In addition, we marginalise over  $\theta_{13}$  and for a true LO (HO),  $\theta_{23}$  is marginalised in the HO (LO). We consider the full  $3\sigma$  allowed range for both  $\theta_{13}$  and  $\theta_{23}$ . We show the results only for the assumed true normal mass hierarchy.

From Fig. 6.4, we observe that the potential of T2HK to exclude the wrong octant is slightly higher than for T2HKK. If LO is the true octant in the standard  $3\nu$  scenario, then both T2HK and T2HKK can exclude the wrong HO at  $5\sigma$  for all  $\delta_{13}(\text{true})$ . However, for true HO, excluding the LO is not possible at  $5\sigma$  for all  $\delta_{13}(\text{true})$ , though the expected sensitivity reach is seen to remain high. In the presence of a sterile neutrino, the expected sensitivity gets modified and we observe that for small sterile mixing, the potential to exclude the wrong HO is significantly less than the standard 3+0 case. For large mixing angles, the width of the band increases and for some combinations of  $\delta_{24}(\text{true})$  and  $\delta_{34}(\text{true})$ , the grey band slightly crosses the 3+0 plot for some fraction of  $\delta_{13}(\text{true})$ . On the other hand for true HO, the standard 3+0 plot lies within the grey band while the cyan



band lies below it except for some small fraction of  $\delta_{13}(\text{true})$  around zero. Also, one can note that for large sterile mixing angles, some combinations of the new phases give more than  $5\sigma$  HO discovery potential for both the setup.

If we add DUNE with T2HKK (Fig. 4.16), the octant discovery potential changes significantly. For large (small) sterile mixing angles, if LO is the true octant, then it is possible to exclude the HO at  $5\sigma$  for all  $\delta_{13}(\text{true})$  (all  $\delta_{13}(\text{true})$  except some fraction around  $\delta_{13}(\text{true}) = \pm\pi$ ), irrespective of the true values of the other two phases. Even in the case of true HO, we can rule out the LO at  $5\sigma$  C.L. except for some fraction of  $\delta_{13}(\text{true})$ .

## 4.4 Measuring the sterile neutrino CP phases at DUNE and T2HK

In this section, we discuss the capability of DUNE and T2HK for measuring sterile phases [76]. At short-baseline experiments, the oscillation probabilities  $P_{ee}$ ,  $P_{\mu\mu}$  and  $P_{\mu e}$  in the 3+1 scenario can be written in an effective two-generation framework which depends only on  $\Delta m_{41}^2$  and an effective mixing term given as a combination of the sterile mixing angles  $\theta_{14}$ ,  $\theta_{24}$  and  $\theta_{34}$ . As a result, the short-baseline experiments are completely insensitive to the sterile CP phases  $\delta_{24}$  and  $\delta_{34}$ . On the other hand, it is now well known that even though the  $\Delta m_{41}^2$ -driven oscillations get averaged out, these phases show up in the oscillation probabilities at the long-baseline experiments. A lot of effort in the last couple of years has gone into estimating the impact of the sterile neutrino mixing angles and phases on the measurement of standard oscillation parameters at long-baseline experiments [66–69, 71–74, 122, 123].<sup>4</sup> These papers showed that in the presence of sterile neutrino mixing the sensitivity to the measurement of CP violation, mass hierarchy, as well as octant of  $\theta_{23}$  becomes a band, where the width of the band comes from the uncertainty on both the

---

<sup>4</sup>Some recent studies on other new physics scenarios in the context of DUNE and T2HK can be found here [124–145].

values of the sterile mixing angles as well as the sterile phases. While the sterile neutrino mixing angles are constrained by the global short-baseline data, there are no constraints on the sterile phases. In the future, bounds on the sterile neutrino mixing angles are expected to improve by the data from forthcoming short-baseline experiments [95, 99, 100]. Studies have shown that the long-baseline experiments could also give constraints on the sterile neutrino mixing at their near [106] and far [74, 75] detectors. The sterile phases, on the other hand, can be constrained *only* in the long-baseline experiments. A short discussion on the study of sterile phases were done at T2K+reactor [123] and T2K+NOvA [72] and the sensitivity was shown to be poor. In this paper, we study how well the next-generation experiments DUNE and T2HK will be able to measure the sterile phases. We give the expected sensitivity of DUNE and T2HK alone as well as by combining data from the two experiments. To the best of our knowledge, this is the first time such a complete study is being performed. While the authors in [68] did attempt to present the expected precision on the sterile phase (which in their parametrisation was  $\delta_{14}$ ) in the DUNE experiment, the analysis they performed has several short-comings. In their analysis, the authors of [68] keep the sterile mixing angles  $\theta_{14}$ ,  $\theta_{24}$  and  $\theta_{34}$  fixed in the fit at their assumed true values. We allow these angles to vary freely in the fit we perform in this paper. This allows the uncertainty due to both the mixing angles as well as the phases to impact our final results. We also keep our sterile neutrino mixing angles within the currently allowed limits, which have been updated following the results from the NEOS, MINOS and MINOS+ experiments [120]. Expected precision on the sterile phase from T2HK has never been studied before and we present them for the first time. We will also show the combined expected sensitivity of DUNE and T2HK to constrain the sterile mixing angles  $\theta_{24}$  and  $\theta_{14}$ , both when the 3+1 scenario is true as well as when there is no positive evidence for sterile neutrino oscillations.

#### 4.4.1 Sterile neutrino probability and simulation

In long-baseline experiments such as T2HK and DUNE, the oscillations driven by  $\Delta m_{31}^2$  dominate while those driven by  $\Delta m_{21}^2$  are sub-dominant, while the very fast oscillations driven by  $\Delta m_{41}^2 \sim O(1\text{eV}^2)$  get averaged out. The transition probability  $P_{\mu e}$  in the limit  $\sin^2(\Delta m_{41}^2 L/4E) \sim 1/2$  and neglecting earth matter effect is [66]:

$$P_{\mu e}^{4\nu} = P_1 + P_2(\delta_{13}) + P_3(\delta_{24}) + P_4(\delta_{13} + \delta_{24}). \quad (4.12)$$

Here  $P_1$  is the term independent of any phase,  $P_2(\delta_{13})$  depends only on  $\delta_{13}$ ,  $P_3(\delta_{24})$  depends only on  $\delta_{24}$  and  $P_4(\delta_{13} + \delta_{24})$  depends on the combination  $(\delta_{13} + \delta_{24})$ . The full expression of the different terms in Eq. (4.25) are as follows:

$$\begin{aligned} P_1 = & \frac{1}{2} \sin^2 2\theta_{\mu e}^{4\nu} \\ & + (X^2 \sin^2 2\theta_{\mu e}^{3\nu} - \frac{1}{4} \sin^2 2\theta_{13} \sin^2 2\theta_{\mu e}^{4\nu})(\cos^2 \theta_{12} \sin^2 \Delta_{31} + \sin^2 \theta_{12} \sin^2 \Delta_{32}) \\ & + (X^2 Y^2 - \frac{1}{4} X^2 \sin^2 2\theta_{12} \sin^2 2\theta_{\mu e}^{3\nu} - \frac{1}{4} \cos^4 \theta_{13} \sin^2 2\theta_{12} \sin^2 2\theta_{\mu e}^{4\nu}) \sin^2 \Delta_{41} \end{aligned} \quad (4.13)$$

$$\begin{aligned} P_2(\delta_{13}) = & Y X^2 \sin 2\theta_{\mu e}^{3\nu} [\cos(\delta_{13})(\cos 2\theta_{12} \sin^2 \Delta_{21} + \sin^2 \Delta_{31} - \sin^2 \Delta_{32}) \\ & - \frac{1}{2} \sin(\delta_{13})(\sin 2\Delta_{21} - \sin 2\Delta_{31} + \sin 2\Delta_{32})], \end{aligned} \quad (4.14)$$

$$\begin{aligned} P_3(\delta_{24}) = & X Y \sin 2\theta_{\mu e}^{4\nu} [\cos(\delta_{24})(\cos 2\theta_{12} \cos^2 \theta_{13} \sin^2 \Delta_{21} - \sin^2 \theta_{13}(\sin^2 \Delta_{31} - \sin^2 \Delta_{32})) \\ & + \frac{1}{2} \sin(\delta_{24})(\cos^2 \theta_{13} \sin 2\Delta_{21} + \sin^2 \theta_{13}(\sin 2\Delta_{31} - \sin 2\Delta_{32}))], \end{aligned} \quad (4.15)$$

$$\begin{aligned} P_4(\delta_{13} + \delta_{24}) = & X \sin 2\theta_{\mu e}^{3\nu} \sin 2\theta_{\mu e}^{4\nu} [\cos(\delta_{13} + \delta_{24})(-\frac{1}{2} \sin^2 2\theta_{12} \cos^2 \theta_{13} \sin^2 \Delta_{21} \\ & + \cos 2\theta_{13}(\cos^2 \theta_{12} \sin^2 \Delta_{31} + \sin^2 \theta_{12} \sin^2 \Delta_{32})) \\ & + \frac{1}{2} \sin(\delta_{13} + \delta_{24})(\cos^2 \theta_{12} \sin 2\Delta_{31} + \sin^2 \theta_{12} \sin 2\Delta_{32})], \end{aligned} \quad (4.16)$$

where,

$$\sin 2\theta_{\mu e}^{3\nu} = \sin 2\theta_{13} \sin \theta_{23} \quad (4.17)$$

$$\sin 2\theta_{\mu e}^{4\nu} = \sin 2\theta_{14} \sin \theta_{24} \quad (4.18)$$

$$X = \cos \theta_{14} \cos \theta_{24} \quad (4.19)$$

$$Y = \cos \theta_{13} \cos \theta_{23} \sin 2\theta_{12}, \quad (4.20)$$

and,

$$\Delta_{ij} = \frac{\Delta m_{ij}^2 L}{4E} \quad (4.21)$$

We can see from Eq. (4.25) that even though the  $\Delta m_{41}^2$ -driven oscillations are averaged out, the CP phases associated with the sterile sector still appear in the neutrino oscillation probability  $P_{\mu e}$ . This dependence comes in term  $P_3(\delta_{24})$  that depend only on the sterile phase  $\delta_{24}$  as well as in term  $P_4(\delta_{13} + \delta_{24})$  which depends on combination of  $\delta_{13}$  and  $\delta_{24}$ . Hence, we can expect the next-generation long-baseline experiments to be sensitive to the sterile phases. We will see the anti-correlation between  $\delta_{13}$  and  $\delta_{24}$  manifest in our results on the measurement of these phases in the long-baseline experiments. In fact, as has been pointed above, the sterile CP phases cannot be measured in the short-baseline experiments which are dedicated to measuring the sterile neutrino mixing. Hence, experiments like DUNE and T2HK are the only place where  $\delta_{24}$  can be measured in the 3+1 scenario. Note that in Eq. (4.25) the probability  $P_{\mu e}$  does not depend on the mixing angle  $\theta_{34}$ ; hence, the corresponding phase associated with this angle  $\delta_{34}$  also does not appear. Once earth matter effects are taken into account, the probability  $P_{\mu e}$  picks up a  $\theta_{34}$  dependence and hence depends on  $\delta_{34}$  as well. However, for DUNE and T2HK experiments, earth matter effects are rather weak and hence their corresponding sensitivity to  $\delta_{34}$  cannot be expected to be strong. Therefore, as we will see in the Results section, these experiments are mainly able to put constraints on  $\delta_{24}$ .

Prior to proceeding, we briefly discuss our simulation procedure as well as the present status of the neutrino oscillation parameters. For our analysis, we have used GLOBES (Global Long Baseline Experiment Simulator) [81, 82] along with the additional codes [83, 84] for calculating probabilities in the 3+1 scenario. We have used constant matter density for all the cases. Throughout the analysis we choose the true values<sup>5</sup> of the standard oscillation parameters as:  $\theta_{12} = 33.56^\circ$ ,  $\theta_{13} = 8.46^\circ$ ,  $\theta_{23} = 45^\circ$ ,  $\Delta m_{21}^2 = 7.5 \times 10^{-5} \text{ eV}^2$ ,  $\Delta m_{31}^2 = 2.5 \times 10^{-5} \text{ eV}^2$  and  $\delta_{13} = -90^\circ$  unless specified otherwise. This choice of parameters is consistent with the current limits [112]. Although one should marginalize over all the free parameters whenever one introduces some new physics, but new physics scenarios often give large number of parameters. Marginalisation over these large number of parameters is computationally challenging, so one has to do some approximation. For our analysis, we have checked that the effect of marginalisation over the standard three neutrino parameters other than  $\delta_{13}$  have no significant effect. So to save computational time we did not marginalise over these not so relevant set of parameters.

For the sterile neutrino mixing, we have considered two scenarios. We first start by assuming that active-sterile neutrino oscillations indeed exist and find the expected constraints on the sterile neutrino mixing angles and phase  $\delta_{24}$  assuming non-zero sterile neutrino mixing angles in the “data”. For this case, we generate the “data” at true values  $\Delta m_{41}^2 \approx 1.7 \text{ eV}^2$ ,  $\theta_{14} \approx 8.13^\circ$ ,  $\theta_{24} \approx 7.14^\circ$ ,  $\theta_{34} = 0^\circ$ , which are the current best-fit values taken from [120]. The true values of the sterile phases will be specified. We marginalise our  $\chi^2$  overall sterile mixing parameters except  $\Delta m_{41}^2$  in the fit. The  $\chi^2$  is marginalised by varying  $\theta_{14}$ ,  $\theta_{24}$  and  $\theta_{34}$  in the range  $[5^\circ, 10.5^\circ]$ ,  $[4^\circ, 9.5^\circ]$ , and  $[0^\circ, 12^\circ]$ , respectively [120] without any Gaussian prior, while the phases  $\delta_{24}$  and  $\delta_{34}$  are varied in their full range  $\in [-180^\circ, 180^\circ]$ .

We next assume a scenario where the sterile neutrino mixing does not exist in nature and we show how well would then the long-baseline experiments DUNE and T2HK con-

---

<sup>5</sup>Throughout this paper we refer to the oscillation parameter values at which the “data” is generated as the “true value” and values in the fit as “test values”.

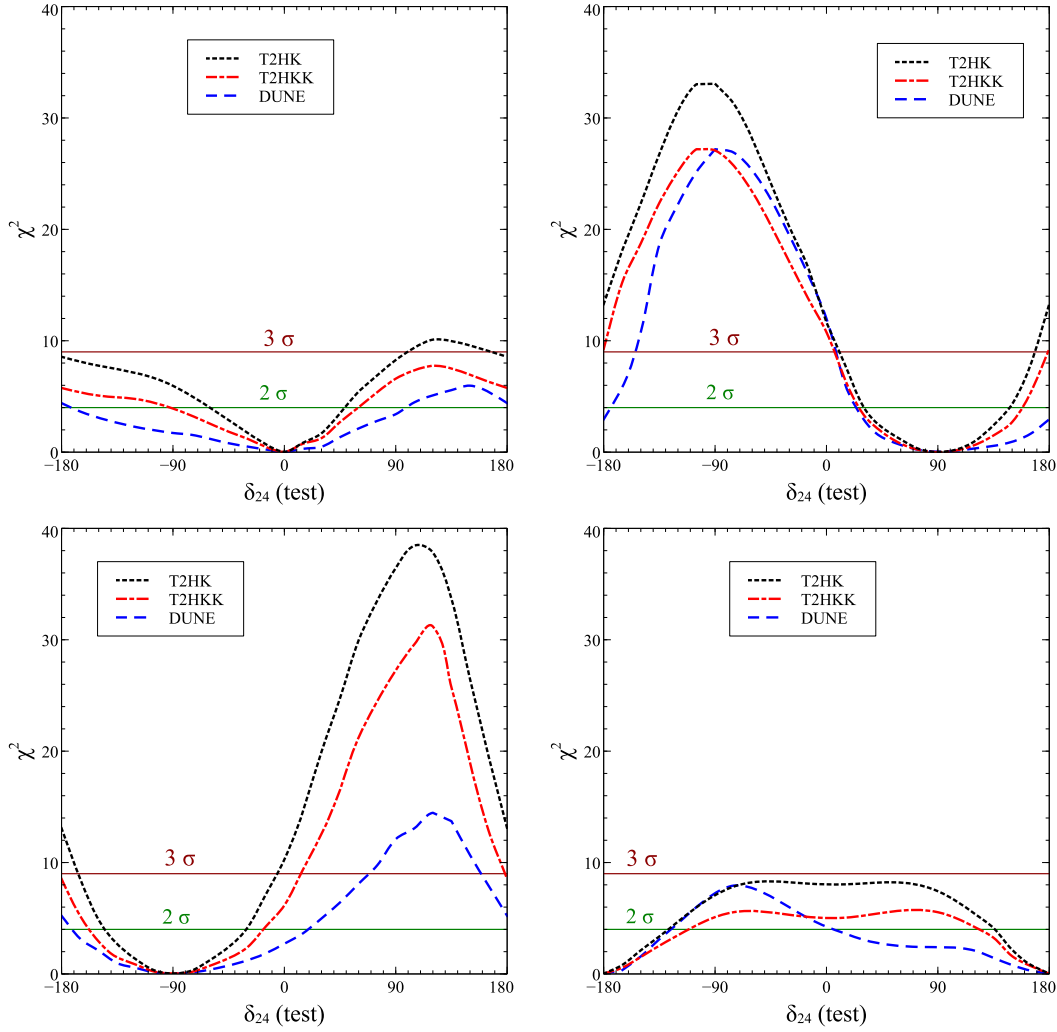


Figure 4.17: The  $\chi^2$  vs.  $\delta_{24}(\text{test})$ . The black curves are for T2HK, the red curves are for T2HKK and the blue curves are for DUNE. The top left panel is for  $\delta_{24}(\text{true}) = 0^\circ$ , the top right panel is for  $\delta_{24}(\text{true}) = 90^\circ$ , the bottom left panel is for  $\delta_{24}(\text{true}) = -90^\circ$  and the bottom right panel is for  $\delta_{24}(\text{true}) = 180^\circ$ .

strain the sterile neutrino mixing angles. For this case, the data of course corresponds to true sterile mixing angles zero. The marginalisation of the  $\chi^2$  is done over all the three sterile mixing angles and the three phases. Mixing angles  $\theta_{14}$ ,  $\theta_{24}$  and  $\theta_{34}$  are marginalised in the range  $[0^\circ, 10^\circ]$ ,  $[0^\circ, 10^\circ]$ , and  $[0^\circ, 12^\circ]$ , respectively, while the phases are allowed to vary in their full range  $\in [-180^\circ, 180^\circ]$ .

### 4.4.2 Measurement of the sterile phases

In this subsection, we discuss the ability of the long-baseline experiments to constrain the sterile phases. The “data” is generated for the 3+1 scenario for the values of mixing parameters discussed in subsection 4.4.1. In particular, for the sterile neutrino parameters we take the following values:  $\Delta m_{41}^2(\text{true}) = 1.7 \text{ eV}^2$ ,  $\theta_{14}(\text{true}) = 8.13^\circ$ ,  $\theta_{24}(\text{true}) = 7.14^\circ$ ,  $\theta_{34}(\text{true}) = 0^\circ$ . The true values of the phases  $\delta_{24}$  will be taken at some benchmark values and will be mentioned whenever needed. The true values of standard oscillation parameters are taken at their current best-fit values, mentioned in subsection 4.4.1. The  $\chi^2$  is marginalised over the relevant oscillation parameters in the 3+1 scenario, as discussed in subsection 4.4.1, where the parameters are allowed to vary within their current  $3\sigma$  ranges. Although there are three phases in the 3+1 scenario, the role of the phase  $\delta_{34}$  is weak. As was discussed in the previous subsection, the mixing angle  $\theta_{34}$  affects the oscillation probability  $P_{\mu e}$  only when matter effects become important. For DUNE and T2HKK, earth matter effects are not very strong, while for T2HK the effect of earth matter is even weaker. Since the impact of the phase  $\delta_{34}$  on  $P_{\mu e}$  is proportional to the mixing angle  $\theta_{34}$ , the phase  $\delta_{34}$  is also less important for  $P_{\mu e}$  for the same reason. Moreover, the current global best-fit for the angle  $\theta_{34}$  turns out to be zero [120]. Therefore, in this work, we set  $\theta_{34}(\text{true}) = 0^\circ$  in the data. As a result, the phase  $\delta_{34}$  is not expected to be very crucial in our analysis and hence we take  $\delta_{34}(\text{true}) = 0^\circ$  in the data and show our results only in the  $\delta_{13}$  -  $\delta_{24}$  plane. We reiterate that the  $\chi^2$  is marginalised over the mixing angle  $\theta_{34}$  and phase  $\delta_{34}$  in the fit, where the mixing angle is allowed to vary between  $[0^\circ, 12^\circ]$  [120].

Exps	$(\delta_{24}^{\text{tr}} = 0^\circ)$ $\delta_{24}(\text{test})$	$(\delta_{24}^{\text{tr}} = 90^\circ)$ $\delta_{24}(\text{test})$	$(\delta_{24}^{\text{tr}} = -90^\circ)$ $\delta_{24}(\text{test})$	$(\delta_{24}^{\text{tr}} = 180^\circ)$ $\delta_{24}(\text{test})$
<b>DUNE</b>	$[-175.1^\circ, 98.8^\circ]$	$[23.35^\circ, 180^\circ]$ $\delta_{24} \lesssim -175.1^\circ$	$[-172.21^\circ, 18.49^\circ]$	$\delta_{24} \lesssim -126.4^\circ, \delta_{24} \gtrsim 6.9^\circ$
<b>T2HK</b>	$[-63.0^\circ, 47.9^\circ]$	$[30.10^\circ, 147.9^\circ]$	$[-145.8^\circ, -31.60^\circ]$	$\delta_{24} \lesssim -128.4^\circ, \delta_{24} \gtrsim 136.2^\circ$
<b>T2HKK</b>	$[-94.0^\circ, 60.0^\circ]$	$[26.27^\circ, 157.62^\circ]$	$[-158.59^\circ, -17.51^\circ]$	$\delta_{24} \lesssim -111.8^\circ, \delta_{24} \gtrsim 124.3^\circ$

Table 4.2: The  $2\sigma$  allowed ranges of  $\delta_{24}(\text{test})$  for the three experiments in the 3+1 scenario. The assumed true value of  $\delta_{13}$  is  $-90^\circ$ . We give the allowed ranges of  $\delta_{24}(\text{test})$  for  $\delta_{24}^{\text{tr}} = 0^\circ, 90^\circ, -90^\circ, 180^\circ$ . Here  $\delta_{24}^{\text{tr}}$  stands for  $\delta_{24}(\text{true})$ .

The Fig. 4.17 shows the capability of DUNE, T2HK and T2HKK to measure the phase  $\delta_{24}$ . We show the plots of  $\chi^2$  as a function of  $\delta_{24}(\text{test})$  for T2HK (dotted black lines), T2HKK (dash-dotted red lines) and DUNE (dashed blue lines) for  $\delta_{24}(\text{true})$  of  $0^\circ$  (top-left panel),  $90^\circ$  (top-right panel),  $-90^\circ$  (bottom-left panel) and  $180^\circ$  (bottom-right panel). The true values of all other parameters are taken as detailed in subsection 4.4.1 and the previous paragraph. The  $\chi^2$  plot has been marginalised over all relevant parameters as discussed before. The green solid horizontal lines show the  $\Delta\chi^2$  corresponding to  $2\sigma$  C.L. Table 4.2 shows that T2HK can better constrain the phase  $\delta_{24}$  as compared to DUNE, while T2HKK is expected to perform better than DUNE but worse than T2HK. Note that the sensitivity of DUNE and T2HKK is marginally better for  $\delta_{24}(\text{true}) = 90^\circ$  than for  $\delta_{24}(\text{true}) = -90^\circ$  while the reverse is true in case of T2HK (see Table 4.2).

In order to understand why the measurement of  $\delta_{24}$  is expected to be better at T2HK than DUNE, we show in Fig. 4.18 the expected electron events at DUNE (top left panel) and T2HK (top right panel). The four lines in each panel show the expected events for four values of  $\delta_{24} = 0^\circ$  (solid red lines),  $90^\circ$  (dashed blue lines),  $-90^\circ$  (dotted green lines) and  $180^\circ$  (dash-dotted dark red lines). The upper panels of the figure reveal that the two experiments behave in almost the same way as far as the dependence of the probability  $P_{\mu e}$  to  $\delta_{24}$  is concerned. However, there is a clear difference between the two when it comes to the overall statistics. T2HK expects to see nearly 14 times more events than DUNE due to its bigger detector size. Hence the corresponding  $\chi^2$  for T2HK is also expected to be higher. Of course, the systematic uncertainty for DUNE is considerably less than for T2HK and that compensates the effect of the lower statistics, however, the effect of statistics shows up in a non-trivial way for  $\delta_{24}$  measurement at the long baseline experiments and T2HK with its bigger detector emerges as a better option in this regard.

The lower panels of Fig. 4.18 show the event rate at the oscillation maximum for DUNE (lower left panel) and T2HK (lower right panel) as a function of  $\delta_{24}$ . The black solid curves show the expected number of events, whereas the green and yellow bands



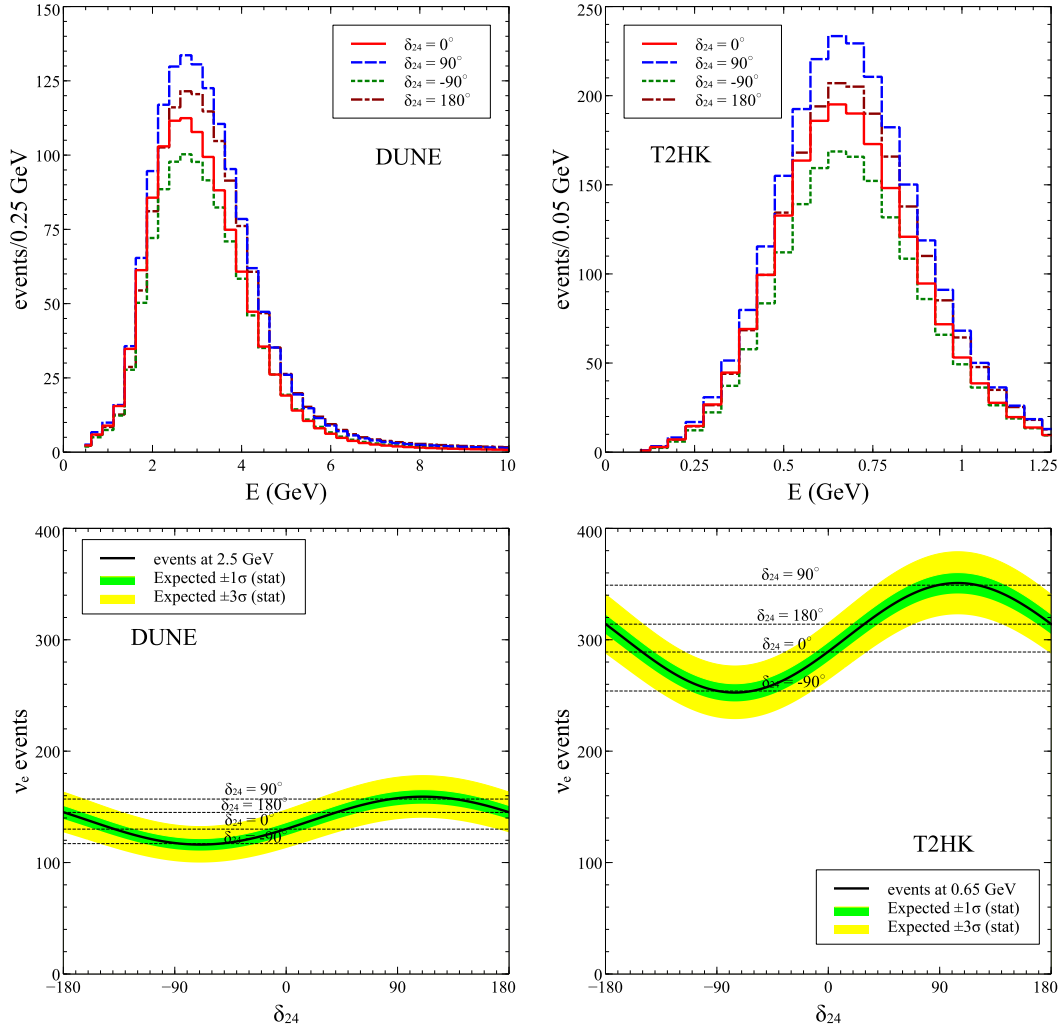


Figure 4.18: Top panels show the appearance event spectrum for DUNE (left) and T2HK (right) for different values of  $\delta_{24}$ . The green lines are for  $\delta_{24} = -90^\circ$ , red lines are for  $\delta_{24} = 0^\circ$ , the blue lines are for  $\delta_{24} = 90^\circ$  and the dark red lines are for  $\delta_{24} = 180^\circ$ . The lower panels show the appearance event rates at the oscillation maximum as a function of  $\delta_{24}$  for DUNE (left) and T2HK (right). While the black curves give the expected number of events, the green and yellow bands show the  $1\sigma$  and  $3\sigma$  statistical uncertainties.

show the  $1\sigma$  and  $3\sigma$  statistical deviation. The black short-dashed straight lines show the event rate at oscillation maxima for the four benchmark values of  $\delta_{24} = 0^\circ$ ,  $180^\circ$ ,  $90^\circ$  and  $-90^\circ$ . The Fig. 4.17 had revealed that the  $\chi^2$  corresponding to  $\delta_{24}(\text{true}) = 0^\circ$  and  $\delta_{24}(\text{true}) = 180^\circ$  are much lower compared to that for  $\delta_{24}(\text{true}) = \pm 90^\circ$ . This can be understood from the lower panels of Fig. 4.18 as follows. Fig. 4.18 shows that the predicted number of events at oscillation maximum for  $\delta_{24}(\text{true}) = 0^\circ$  and  $180^\circ$  lie between the predicted events for  $\delta_{24}(\text{true}) = \pm 90^\circ$ . Therefore, for the cases where data is generated for  $\delta_{24}(\text{true}) = 0^\circ$  and

180°, it is easier for other  $\delta_{24}$  values to fit the data and give a smaller  $\chi^2$ . However, data corresponding to  $\delta_{24}(\text{true}) = \pm 90^\circ$  takes a more extreme value and the difference between the data and fit for other values of  $\delta_{24}$  for these cases becomes larger, giving larger  $\chi^2$ .

Another interesting feature, visible in the event plots in Fig. 4.18 is that the maxima and minima of the events are not at  $\delta_{24} = 90^\circ$  or  $-90^\circ$ . Rather they are slightly shifted towards the right. For the same reason, the  $\chi^2$  plots in Fig. 4.17 are also asymmetric about the true value of  $\delta_{24}$ . One can explain this using Eq. (4.25). By inspecting the probability, one can see that the correlation between  $\Delta m_{21}^2$  and  $\delta_{24}$  is negligible. Also, we have taken  $\delta_{13} = -90^\circ$  everywhere. Hence, for  $\Delta m_{21}^2 = 0$  and  $\delta_{13} = -90^\circ$ , the Eq. (4.25) can be rearranged as

$$P_{\mu e} = A + B \cos 2\theta_{13} \sin \delta_{24} - \frac{1}{2} B \cos \delta_{24}, \quad (4.22)$$

where, A and B are independent of  $\delta_{24}$ . In the absence of the last term, the probability would be a sine function shifted by the constant A. However, the presence of the cosine term shifts the curve and the shift is towards right because of the minus sign in front of the cosine term. In particular, the extrema of the probability in Eq. (4.22) is given by the condition,

$$\cos \delta_{24} = -\frac{1}{2} \sin \delta_{24}, \quad (4.23)$$

which corresponds to minimum at  $\delta_{24} = -63.4^\circ$  and maximum at  $\delta_{24} = 116.6^\circ$ . This agrees very well with the event plots in the lower panels of Fig. 4.18, which is obtained using the exact numerical probability.

We next show in Fig. 4.19 the expected 95 % C.L. allowed areas in the  $\delta_{13}(\text{test})$ – $\delta_{24}(\text{test})$  plane, expected to be measured by the next generation long-baseline experiments T2HK (or T2HKK) and DUNE, and by combining them. The four panels of Fig. 4.19 have been generated for four different choices of  $\delta_{24}(\text{true})$ . The value of  $\delta_{13}(\text{true}) = -90^\circ$  in all the panels. In each panel, the benchmark point where the data is generated is shown by the black star. The four panels correspond to  $\delta_{24}(\text{true}) = 0^\circ$  (top left),  $90^\circ$  (top right),

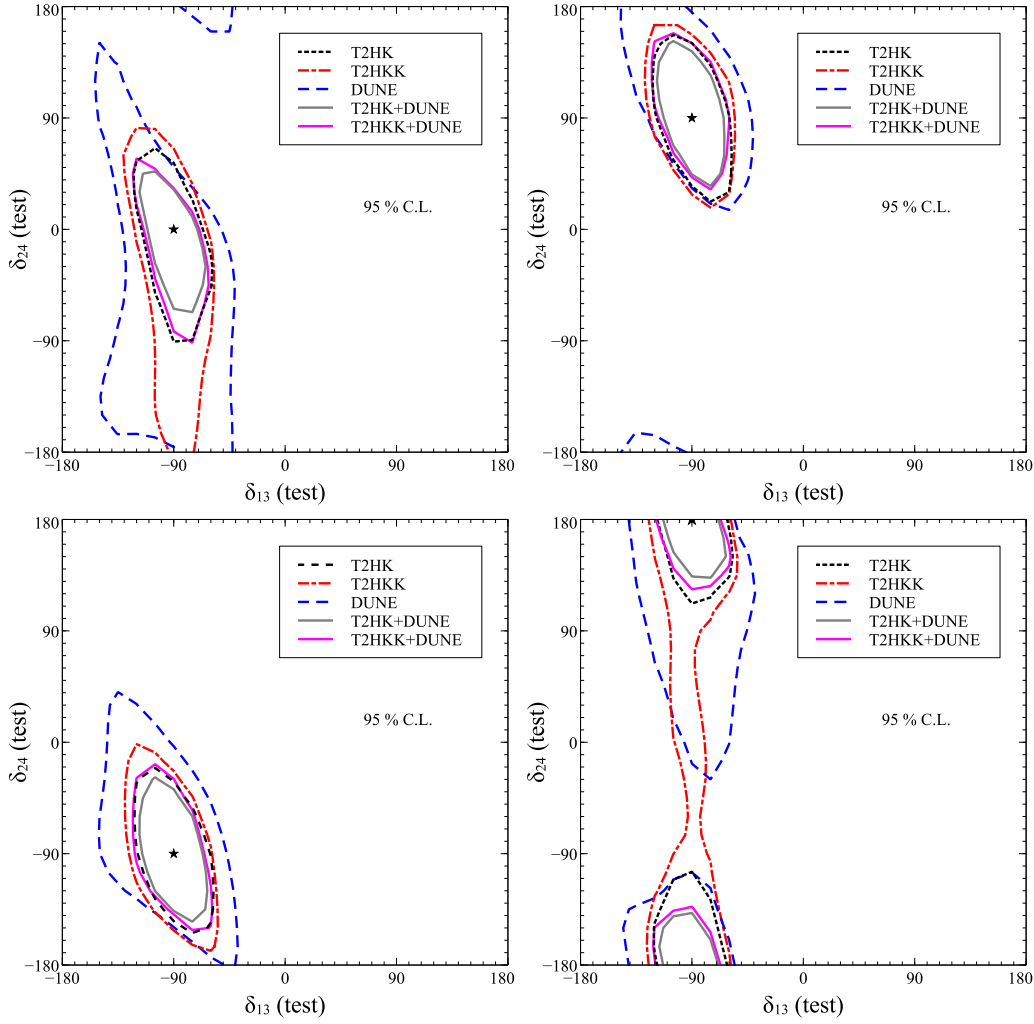


Figure 4.19: The expected 95 % C.L. contours in  $\delta_{13}(\text{test})$  vs  $\delta_{24}(\text{test})$ , where 95 % C.L. is defined as  $\Delta\chi^2 = 5.99$  for 2 parameters. The stars show the value of  $\delta_{13}(\text{true})$  and  $\delta_{24}(\text{true})$  taken in the data. The top left (right) panel is for  $\delta_{24} = 0^\circ$  ( $\delta_{24} = 90^\circ$ ) and the bottom left (right) panel is for  $\delta_{24} = -90^\circ$  ( $\delta_{24} = 180^\circ$ ). The black dotted curve is for T2HK, the red dash-dotted curve is for T2HKK, the blue dashed curve is for DUNE, the grey solid curve is for DUNE+T2HK and the magenta solid curve is for DUNE + T2HKK.

$-90^\circ$  (bottom left) and  $180^\circ$  (bottom right). In all the four cases we have considered 3+1 scenario both in the ‘data’ and in the ‘fit’ or ‘theory’. The  $\chi^2$  thus generated is then marginalised over the sterile mixing angles  $\theta_{14}$ ,  $\theta_{24}$ ,  $\theta_{34}$  and  $\delta_{34}$ , as discussed before. The black dotted, red dash-dotted and blue dashed contours are for T2HK, T2HKK and DUNE, respectively, while the grey and magenta solid contours are for DUNE+T2HK and DUNE+T2HKK. As in Fig. 4.17 we note that T2HK can constrain the phase  $\delta_{24}$  much better than DUNE, while T2HKK performs better than DUNE but worse than T2HK.

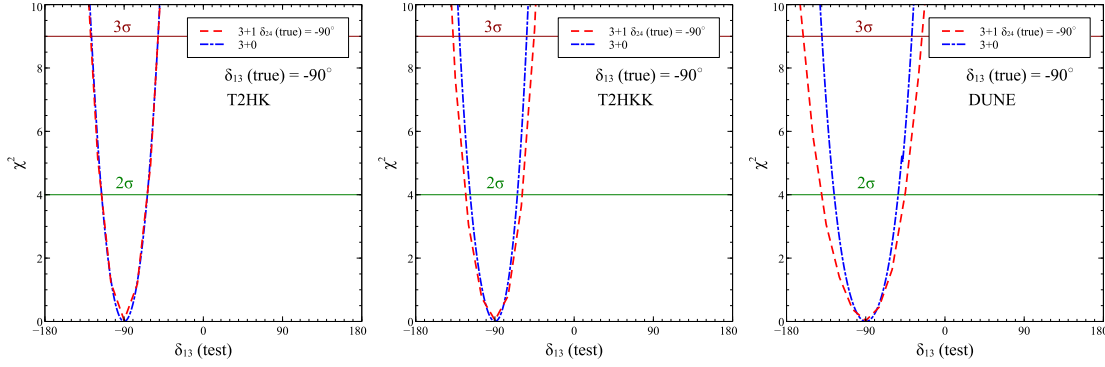


Figure 4.20: The expected precision on  $\delta_{13}$  for the 3+0 and 3+1 scenarios. The left panel is for T2HK, the middle panel is for T2HKK and the right panel is for DUNE. The blue dash-dotted curves are for the 3+0 case and the red dashed curves are for 3+1 case in both theory and data. The curves are  $\delta_{24}(\text{true}) = -90^\circ$ .

We also see, as before, that for DUNE the precision on  $\delta_{24}$  is expected to be better for  $\delta_{24}(\text{true}) = \pm 90^\circ$  compared to when  $\delta_{24}(\text{true}) = 0^\circ$  or  $180^\circ$ . For T2HK, this dependence of precision on  $\delta_{24}$  measurement on  $\delta_{24}(\text{true})$  is less pronounced. The effect of  $\theta_{34}$  on the measurement of  $\delta_{24}$  is also minimal. Finally, note that there is an anti-correlation between  $\delta_{13}$  and  $\delta_{24}$ . This comes from the term  $P_4(\delta_{13} + \delta_{24})$  of Eq. (4.25).

The Fig. 4.19 also shows how the measurements of  $\delta_{24}$  and  $\delta_{13}$  improve as we combine DUNE with either T2HK or T2HKK. We see that combining DUNE with T2HKK improves the precision considerably, with the combined precision of DUNE and T2HKK becoming slightly better than the precision expected from T2HK alone. Combining DUNE with T2HK improves the precision even further, albeit only marginally since T2HK alone can measure the phases rather precisely.

The question on how the measurement of the standard CP phase  $\delta_{13}$  gets affected by the sterile mixing angle phases in the 3+1 scenario is another pertinent question that one can ask. The Fig. 4.20 shows how the expected precision on  $\delta_{13}$  changes in the presence of sterile neutrinos. The left panel is for T2HK, the middle panel is for T2HKK and the right panel is for DUNE. The blue dashed curves are for the standard 3+0 case with no sterile neutrinos while the red dash-dotted curves are for the 3+1 case with  $\delta_{24} = -90^\circ$  in data. The other standard and sterile neutrino oscillation parameters are taken in data as

described above and the fit performed as before. The Fig. 4.20 shows that the expected precision on  $\delta_{13}$  worsens when the sterile neutrino is present. From Eq. (4.16) one can see that there is an anti-correlation between  $\delta_{13}$  and  $\delta_{24}$  which makes the  $\delta_{13}$  precision worse. For DUNE, the effect is more compared to T2HK and T2HKK. For T2HK, the  $\delta_{13}$  measurement is seen to be nearly unaffected. DUNE measures  $\delta_{24}$  worse than T2HK and T2HKK and hence the corresponding measurement of  $\delta_{13}$  worsens due to the anti-correlation mentioned above. Table 4.3 summarises the expected precision on  $\delta_{13}$  for the 3+0 and 3+1 scenario for four benchmark values of  $\delta_{24}(\text{true})$ . We see that DUNE's measurement of  $\delta_{13}$  gets affected for all  $\delta_{24}$  while the effect on T2HK's measurement of  $\delta_{13}$  is negligible.

Exps	3+0( $\delta_{13}^{\text{tr}} = -90^\circ$ ) $\delta_{13}(\text{test})$	3+1( $\delta_{24}^{\text{tr}} = 0^\circ$ ) $\delta_{13}(\text{test})$	3+1( $\delta_{24}^{\text{tr}} = 90^\circ$ ) $\delta_{13}(\text{test})$	3+1( $\delta_{24}^{\text{tr}} = -90^\circ$ ) $\delta_{13}(\text{test})$	3+1( $\delta_{24}^{\text{tr}} = 180^\circ$ ) $\delta_{13}(\text{test})$
<b>DUNE</b>	$[-125.3^\circ, -53.6^\circ]$	$[-143.3^\circ, -48.8^\circ]$	$[-139.1^\circ, -48.2^\circ]$	$[-139.0^\circ, -46.2^\circ]$	$[-137.6^\circ, -45.2^\circ]$
<b>T2HK</b>	$[-115.3^\circ, -64.2^\circ]$	$[-116.9^\circ, -66.6^\circ]$	$[-114.0^\circ, -65.5^\circ]$	$[-113.2^\circ, -65.0^\circ]$	$[-113.9^\circ, -63.5^\circ]$
<b>T2HKK</b>	$[-117.6^\circ, -65.1^\circ]$	$[-123.5^\circ, -63.2^\circ]$	$[-121.1^\circ, -60.0^\circ]$	$[-121.3^\circ, -58.1^\circ]$	$[-121.1^\circ, -57.3^\circ]$

Table 4.3: The  $2\sigma$  allowed  $\delta_{13}(\text{test})$  ranges for the three experiments both in 3+0 and 3+1 scenario. In both the scenarios, assumed true value of  $\delta_{13}$  is  $-90^\circ$  while in 3+1 case, we give the allowed ranges of  $\delta_{13}(\text{test})$  for  $\delta_{24}^{\text{tr}} = 0^\circ, 90^\circ, -90^\circ, 180^\circ$ . Here  $\delta^{\text{tr}}$  stands for  $\delta(\text{true})$ .

### 4.4.3 Measurement of the mixing angles

Prospects of measuring the sterile neutrino mixing angles at long-baseline experiments DUNE [74] and T2HK [75] has been studied before. Here we study how well the sterile mixing can be constrained by combining data from these experiments. We also present the sensitivity of the individual experiment DUNE, T2HK and T2HKK. Here we consider two complementary approaches. We first assume that sterile neutrino mixing does exist (as in the last subsection) and see how precisely the data from long-baseline experiments can measure and constrain the angles  $\theta_{14}$  and  $\theta_{24}$ <sup>6</sup>. We next consider the alternate situation

<sup>6</sup>We do not study the mixing angle  $\theta_{34}$  in this work. As discussed before, this affects  $P_{\mu e}$  and  $P_{\mu\mu}$  only mildly through matter effects. To constrain this angle, we need to consider the neutral current data, which has been done in [77, 78, 92].

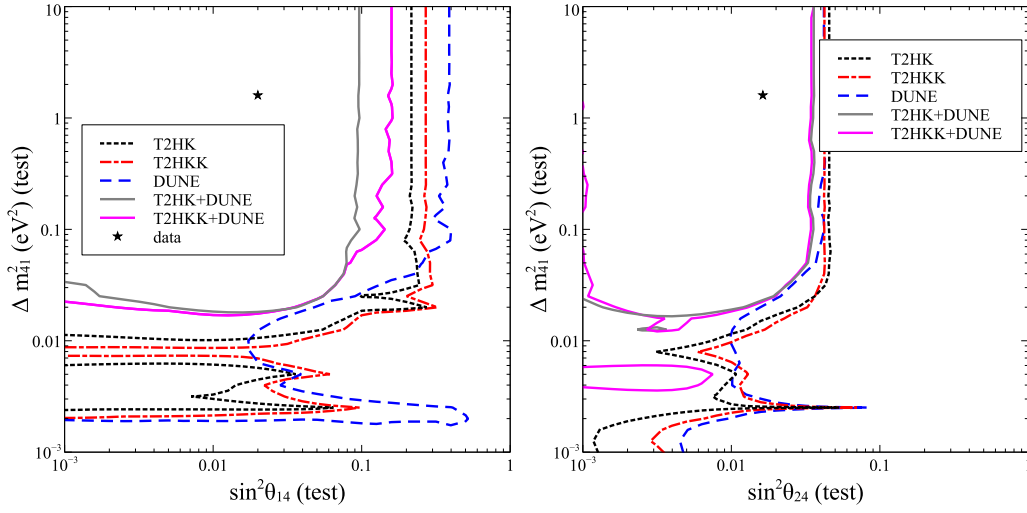


Figure 4.21: The left panel shows the expected 95 % C.L contours in the  $\sin^2 \theta_{14}(\text{test})$ - $\Delta m_{41}^2(\text{test})$  plane, while the right panel shows the 95 % C.L. contours in the  $\sin^2 \theta_{24}(\text{test})$ - $\Delta m_{41}^2(\text{test})$  plane. The colour code is same as Fig. 4.19.

where the active-sterile oscillations do not really exist and then we see how well DUNE, T2HK and T2HKK, as well as their combination, could put upper bounds on the sterile neutrino mixing angles  $\theta_{14}$  and  $\theta_{24}$ .

#### 4.4.3.1 Measuring the sterile mixing angles when 3+1 is true

In this subsection, we assume that the 3+1 scenario is indeed true in nature and the mixing angles  $\theta_{14}$  and  $\theta_{24}$  are indeed non-zero. We perform a  $\chi^2$  analysis with prospective data generated in the 3+1 scenario and fitted within the 3+1 scenario and give expected allowed C.L. regions in the sterile neutrino parameter spaces. As before, we take the true sterile oscillation parameters at the following benchmark values:  $\Delta m_{41}^2(\text{true}) = 1.7 \text{ eV}^2$ ,  $\theta_{14}(\text{true}) = 8.13^\circ$ ,  $\theta_{24}(\text{true}) = 7.14^\circ$ ,  $\theta_{34}(\text{true}) = 0^\circ$  which are consistent with [120]. The standard oscillation parameters are taken and treated as discussed before. The  $\chi^2$  is marginalised over all relevant parameters in the fit and no Gaussian priors are included.

In Fig. 4.21, we show the contours in  $\sin^2 \theta_{14}(\text{test})$ - $\Delta m_{41}^2(\text{test})$  plane (left panel) and  $\sin^2 \theta_{24}(\text{test})$  -  $\Delta m_{41}^2(\text{test})$  plane (right panel). The colour code is same as Fig. 4.19. The point where the data is generated is shown by the black star in the two panels. The results

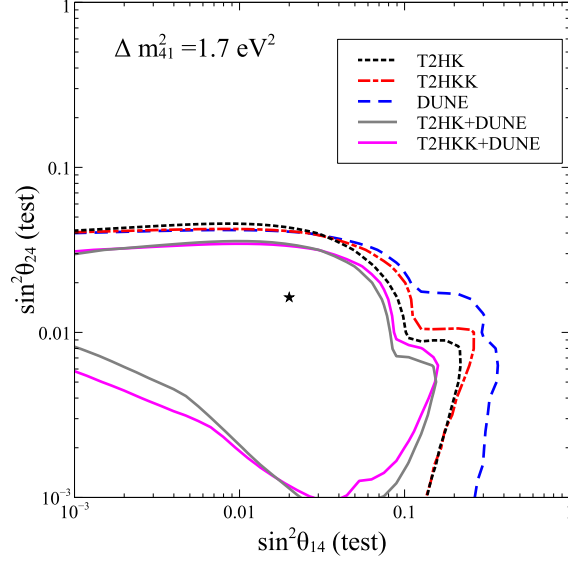


Figure 4.22: The expected 95 % C.L contours in  $\sin^2 \theta_{24}(\text{test})$ - $\sin^2 \theta_{14}(\text{test})$  plane. The colour code is same as Fig. 4.19.

show that in both panels, T2HK gives better results than both DUNE and T2HKK. Again, T2HKK is better than DUNE. Combining T2HK/T2HKK and DUNE experiments improves the results and the expected allowed ranges for the sterile neutrino mixing parameters shrink. The precision expected from the combined data from T2HK and DUNE is nearly the same as that from T2HKK and DUNE, which for the former is only marginally better.

Fig. 4.22 shows the contours in the  $\sin^2 \theta_{14}(\text{test})$ - $\sin^2 \theta_{24}(\text{test})$ . The colour code for the different data sets considered is the same as Fig. 4.19. We note that the expected upper limit on  $\sin^2 \theta_{24}$  is the same for all the three individual experiments for  $0.001 < \sin^2 \theta_{14} < 0.03$ . Also, the expected upper bound on  $\sin^2 \theta_{14}$  is seen to be better for T2HK than DUNE. Combining the experiments can improve the measurement of the sterile neutrino mixing angles as seen from the solid contours in Fig. 4.22. In particular, we now see a lower bound on  $\sin^2 \theta_{24}$ .

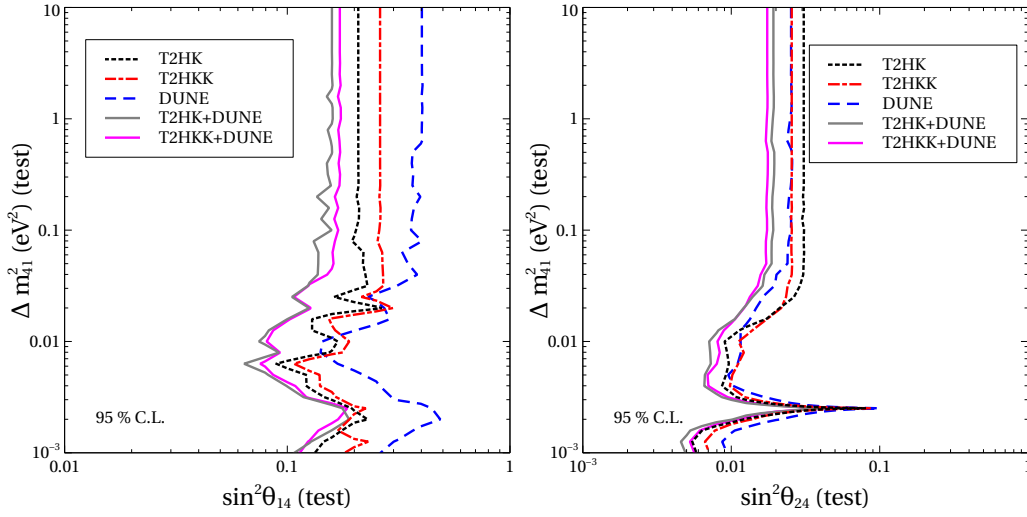


Figure 4.23: The expected 95 % C.L exclusion curves in the  $\sin^2 \theta_{14}(\text{test})$ - $\Delta m_{41}^2(\text{test})$  plane shown in the left panel and in the  $\sin^2 \theta_{24}(\text{test})$ - $\Delta m_{41}^2(\text{test})$  plane shown in the right panel. The data in these plots correspond to standard three-generation oscillation scenario with no sterile mixing while the fit is done in the 3+1 framework to obtain the exclusion contours. The colour code is same as Fig. 4.19.

#### 4.4.3.2 Excluding the sterile hypothesis when 3+1 is not true

If the sterile neutrino hypothesis was wrong and there was no mixing between the active and sterile neutrinos, the next-generation experiments would falsify it. There are a series of new short-baseline experiments planned which will be testing this hypothesis [95, 99, 106]. Even the near detector of planned long-baseline experiments are well-suited to check the sterile neutrino mixing as their baseline and energy match well to correspond to the maximum of  $\Delta m_{41}^2$ -driven oscillations [106]. In the same vein, it is pertinent to ask how well the next-generation long-baseline experiments could constrain this hypothesis since the oscillation probabilities for long-baseline experiments also depend on the sterile neutrino mixing and phases even though the  $\Delta m_{41}^2$ -driven oscillations themselves average out. While some work in this direction has already been done in the literature [74, 75], we will present here, for the first time, the sensitivity of T2HKK set-up to the sterile neutrino mixing angles  $\theta_{24}$  and  $\theta_{14}$ . We will also present the expected sensitivity from the combined prospective data-sets of T2HK (or T2HKK) and DUNE, which has not been studied before.



In Fig. 4.23, we show the exclusion curves for the 3+1 hypothesis expected from the next-generation long-baseline experiments. The left panel of Fig. 4.23 shows the 95 % C.L. exclusion plots in the  $\Delta m_{41}^2(\text{test})$ - $\sin^2 \theta_{14}(\text{test})$  plane while the right panel shows the results in  $\Delta m_{41}^2(\text{test})$ - $\sin^2 \theta_{24}(\text{test})$  plane. Here we generate the data assuming the standard three-generation neutrino scenario and then fit it with the 3+1 scenario. The blue dashed, black dotted and red dash-dotted curves show the exclusion plots for DUNE, T2HK and T2HKK, while the magenta and grey solid curves show the expected exclusion sensitivity for DUNE+T2HKK and DUNE+T2HK, respectively. If only three neutrinos exist in nature, then the parameter region in the top-right of the plots are excluded at 95% C.L. Again, as in the previous results, T2HK constrains  $\theta_{14}$  better than both T2HKK and DUNE for all values of  $\Delta m_{41}^2$  in the range  $10^{-3} \text{ eV}^2$  to  $10 \text{ eV}^2$ . Combining DUNE with T2HK and T2HKK can improve the constraint on  $\sin^2 \theta_{14}$  compared to the individual experiments. Since for higher values of  $\Delta m_{41}^2$  the oscillations average out, the experiments become almost insensitive to the value of  $\Delta m_{41}^2$ . For  $0.1 \text{ eV}^2 < \Delta m_{41}^2 < 10.0 \text{ eV}^2$ , DUNE, T2HKK and T2HK can exclude  $\sin^2 \theta_{14} \gtrsim 0.4$ ,  $\sin^2 \theta_{14} \gtrsim 0.27$  and  $\sin^2 \theta_{14} \gtrsim 0.21$ , respectively, at 95 % C.L. For the same range of values of  $\Delta m_{41}^2$ , DUNE+T2HK and DUNE+T2HKK could put slightly tighter constrain on  $\sin^2 \theta_{14}$  and the excluded regions are expected to be  $\sin^2 \theta_{14} \gtrsim 0.165$  and  $\sin^2 \theta_{14} \gtrsim 0.18$  at 95% C.L., respectively.

The results presented in the right panel show the capability of these experiments to constrain  $\sin^2 \theta_{24}$ . If  $\Delta m_{41}^2$  is small and lies in the range  $10^{-3} \text{ eV}^2 < \Delta m_{41}^2 < 0.01 \text{ eV}^2$ , T2HK gives better constraint on  $\sin^2 \theta_{24}$  than both DUNE and T2HKK. But for higher values of  $\Delta m_{41}^2$ , in the range of  $0.014 \text{ eV}^2 < \Delta m_{41}^2 < 0.1 \text{ eV}^2$ , the performance of DUNE is better than both T2HK and T2HKK. For  $0.1 \text{ eV}^2 < \Delta m_{41}^2 < 10.0 \text{ eV}^2$ , performance of T2HKK is almost similar to that of DUNE. Similar behaviour can be seen in the combined case. In the lower  $\Delta m_{41}^2$  region, DUNE+T2HK could constrain  $\sin^2 \theta_{24}$  slightly better than DUNE+T2HKK. But in the higher  $\Delta m_{41}^2$  region, DUNE+T2HKK is expected to perform better than DUNE+T2HK. The expected exclusion sensitivity for DUNE, T2HKK and T2HK in the range  $0.1 \text{ eV}^2 < \Delta m_{41}^2 < 10.0 \text{ eV}^2$  are given as  $\sin^2 \theta_{24} \gtrsim 0.026$ ,

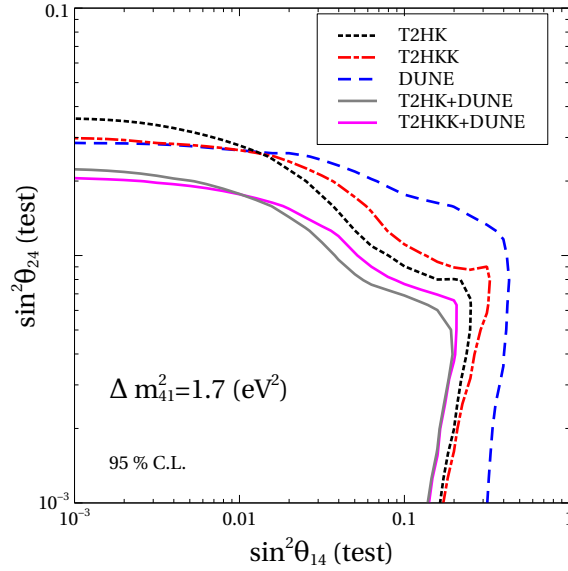


Figure 4.24: The expected 95 % C.L exclusion curves in the  $\sin^2 \theta_{14}(\text{test})$ - $\sin^2 \theta_{24}(\text{test})$  plane for a fixed  $\Delta m_{41}^2 = 1.0 \text{ eV}^2$ . The colour code is same as Fig. 4.19.

$\sin^2 \theta_{24} \gtrsim 0.026$  and  $\sin^2 \theta_{24} \gtrsim 0.03$ , at 95% C.L. Similarly, the expected exclusion limit for DUNE+T2HKK and DUNE+T2HK at 95% C.L. are  $\sin^2 \theta_{24} \gtrsim 0.017$  and  $\sin^2 \theta_{24} \gtrsim 0.019$ , respectively, for  $0.1 \text{ eV}^2 < \Delta m_{41}^2 < 10.0 \text{ eV}^2$ .

In Fig. 4.24, we show the expected exclusion contour in  $\sin^2 \theta_{14}(\text{test})$ - $\sin^2 \theta_{24}(\text{test})$  plane. Here, the region outside the contour is excluded at 95% C.L. The figure represents the slice at  $\Delta m_{41}^2 = 1.7 \text{ eV}^2$  of the contour in the  $\sin^2 \theta_{14}$ ,  $\sin^2 \theta_{24}$ ,  $\Delta m_{41}^2$  space. The colour code is the same as in Fig. 4.23. Here also, we observe better capability of T2HK to constrain  $\sin^2 \theta_{14}$ - $\sin^2 \theta_{24}$  parameter space than DUNE and T2HKK in most regions of the parameter space. The plot also shows that constraint on  $\sin^2 \theta_{24}$  is complicated. We see that T2HK is better than DUNE and T2HKK in constraining  $\sin^2 \theta_{24}$  for  $\sin^2 \theta_{14} \gtrsim 10^{-2}$ . However, for  $\sin^2 \theta_{14} \lesssim 10^{-2}$  DUNE and T2HKK perform better than T2HK in constraining  $\sin^2 \theta_{24}$ . Combining the data-sets improves the expected sensitivity on both the sterile mixing angles.

## 4.5 A new degeneracy in the sterile neutrino sector at long-baseline experiments

In this section, we will discuss a new fake solution that exists in the appearance channel at long-baseline experiments [146]. We will show both analytically as well numerically that the appearance probability is the same for values of  $\Delta m_{41}^2$  for which the fast oscillations are averaged out and for  $\Delta m_{41}^2 = (1/2)\Delta m_{31}^2$ . The fake solution does not appear for the disappearance channel.

### 4.5.1 Fake solution in the appearance probability

If we put the approximation  $\Delta m_{21}^2 = 0$  and the condition  $\delta_{13} + \delta_{24} = 0$  in Eq. (4.13-4.16), we get,

$$\begin{aligned}
 P_{\mu e} = & \frac{1}{2} \sin^2(2\theta_{\mu e}^{4\nu}) \\
 & + (X^2 \sin^2(2\theta_{\mu e}^{3\nu}) - \frac{1}{4} \sin^2(2\theta_{13}) \sin^2(2\theta_{\mu e}^{4\nu})) \sin^2(\Delta_{31}) \\
 & + X \sin(2\theta_{\mu e}^{3\nu}) \sin(2\theta_{\mu e}^{4\nu}) \cos(2\theta_{13}) \sin^2(\Delta_{31}) .
 \end{aligned} \tag{4.24}$$

On the other hand, for values of  $\Delta m_{41}^2 \ll 1 \text{ eV}^2$ , the oscillations due to this mass scale will survive the detector resolutions and show-up at the long-baseline detector. If we continue using the approximation  $\Delta m_{21}^2 = 0$  while allowing the  $\Delta m_{41}^2$ -driven oscillatory terms, the

expression for the probability becomes,

$$\begin{aligned}
P_{\mu e} = & \sin^2(2\theta_{\mu e}^{4\nu})[\sin^2(\theta_{13}) \sin^2(\Delta_{43}) + \cos^2(\theta_{13}) \sin^2(\Delta_{41})] \\
& - \cos(\delta_{13} + \delta_{24})X \sin(2\theta_{\mu e}^{4\nu}) \sin(2\theta_{\mu e}^{3\nu})[\sin^2(\Delta_{43}) - \sin^2(\Delta_{41})] \\
& + \frac{1}{2} \sin(\delta_{13} + \delta_{24})X \sin(2\theta_{\mu e}^{4\nu}) \sin(2\theta_{\mu e}^{3\nu})[\sin(2\Delta_{43}) - \sin(2\Delta_{41})] \\
& + (X^2 \sin^2(2\theta_{\mu e}^{3\nu}) - \frac{1}{4} \sin^2(2\theta_{13}) \sin^2(2\theta_{\mu e}^{4\nu})) \sin^2(\Delta_{31}) \\
& + \cos(\delta_{13} + \delta_{24})X \sin(2\theta_{\mu e}^{3\nu}) \sin(2\theta_{\mu e}^{4\nu}) \cos(2\theta_{13}) \sin^2(\Delta_{31}) \\
& + \frac{1}{2} \sin(\delta_{13} + \delta_{24})X \sin(2\theta_{\mu e}^{3\nu}) \sin(2\theta_{\mu e}^{4\nu}) \sin(2\Delta_{31}). \tag{4.25}
\end{aligned}$$

If we use the condition  $\delta_{24} + \delta_{13} = 0$  in Eq. (4.25) we get,

$$\begin{aligned}
P_{\mu e} = & \sin^2(2\theta_{\mu e}^{4\nu})[\sin^2(\theta_{13}) \sin^2(\Delta_{43}) + \cos^2(\theta_{13}) \sin^2(\Delta_{41})] \\
& - X \sin(2\theta_{\mu e}^{4\nu}) \sin(2\theta_{\mu e}^{3\nu})[\sin^2(\Delta_{43}) - \sin^2(\Delta_{41})] \\
& + (X^2 \sin^2(2\theta_{\mu e}^{3\nu}) - \frac{1}{4} \sin^2(2\theta_{13}) \sin^2(2\theta_{\mu e}^{4\nu})) \sin^2(\Delta_{31}) \\
& + X \sin(2\theta_{\mu e}^{3\nu}) \sin(2\theta_{\mu e}^{4\nu}) \cos(2\theta_{13}) \sin^2(\Delta_{31}). \tag{4.26}
\end{aligned}$$

Now, for the particular choice  $\Delta m_{41}^2 = \frac{1}{2} \Delta m_{31}^2$  the oscillation probability reduces to,

$$\begin{aligned}
P_{\mu e} = & \sin^2(2\theta_{\mu e}^{4\nu}) \sin^2\left(\frac{\Delta_{31}}{2}\right) \\
& + (X^2 \sin^2(2\theta_{\mu e}^{3\nu}) - \frac{1}{4} \sin^2(2\theta_{13}) \sin^2(2\theta_{\mu e}^{4\nu})) \sin^2(\Delta_{31}) \\
& + X \sin(2\theta_{\mu e}^{3\nu}) \sin(2\theta_{\mu e}^{4\nu}) \cos(2\theta_{13}) \sin^2(\Delta_{31}). \tag{4.27}
\end{aligned}$$

We can see from Eq. (4.24) and Eq. (4.27) that the oscillation probability for these two cases are equal, except for the first term. But at the oscillation maximum,  $\Delta_{31} = \frac{\pi}{2}$ , the first term of the Eq. (4.27) becomes  $\frac{1}{2} \sin^2 2\theta_{\mu e}^{4\nu}$ . So at the oscillation maximum the oscillation probability for the  $\Delta m_{41}^2 > 1 \text{ eV}^2$  case given by Eq. (4.24) becomes exactly equal to the oscillation probability for the  $\Delta m_{41}^2 = \frac{1}{2} \Delta m_{31}^2$  case given by Eq. (4.27). This produces a fake solution in  $\Delta m_{41}^2$  at the energy corresponding to  $\Delta m_{31}^2$  oscillation maximum for

a given baseline  $L$ . Note that the above condition for the fake solution was obtained for oscillations in vacuum. As mentioned before, using the corresponding expression in constant density matter we would get the fake solution in matter at the energy that gives the oscillation maximum for  $\Delta m_{31}^2{}^m$  for a given baseline  $L$ . One can check that for earth matter effect in experiments like T2HK and DUNE the energy at which we get oscillation maximum for  $\Delta m_{31}^2{}^m$  is very similar to that for  $\Delta m_{31}^2$ . We will quantify the effect of matter on the fake solution shortly in Fig. 4.25.

For energies away from the  $\Delta m_{31}^2$ -driven first oscillation maximum, the oscillatory term  $\sin^2(\frac{\Delta_{31}}{2}) \neq 1/2$  exactly and hence, the above mentioned fake solution is not exact. However, we see that the fake solution is achieved even outside the  $\Delta m_{31}^2$ -driven first oscillation maximum, albeit approximately. To explore this further, let  $P^{\Delta m_{31}^2/2}$  be the oscillation probability for  $\Delta m_{41}^2 = \Delta m_{31}^2/2$  and  $P^{ave}$  for  $\Delta m_{41}^2 \sim 1\text{eV}^2$ , and let  $\Delta P$  be the difference between  $P^{\Delta m_{31}^2/2}$  and  $P^{ave}$ :

$$\begin{aligned}\Delta P &= P^{\Delta m_{31}^2/2} - P^{ave}, \\ &= \sin^2(2\theta_{\mu e}^{4\nu}) \left[ \sin^2\left(\frac{\Delta m_{31}^2 L}{8E}\right) - \frac{1}{2} \right].\end{aligned}\quad (4.28)$$

The term  $\sin^2\left(\frac{\Delta m_{31}^2 L}{8E}\right)$  takes values only in the range  $[0,1]$ . Hence,  $\Delta P$  is also bounded, and lies between  $-0.5 \sin^2(2\theta_{\mu e}^{4\nu}) \leq \Delta P \leq 0.5 \sin^2(2\theta_{\mu e}^{4\nu})$ . Therefore, for  $\sin^2(2\theta_{\mu e}^{4\nu})$  small,  $\Delta P_{max}$  is also expected to be small. For example, if  $\sin^2(2\theta_{\mu e}^{4\nu}) \sim 10^{-3}$ , then  $\Delta P_{max} \sim O(10^{-3})$ , whereas the oscillation probability  $P_{\mu e} \sim O(10^{-2})$ , so we can say that there is an approximate degeneracy for all energies for small values of  $\sin^2(2\theta_{\mu e}^{4\nu})$ . In our simulations we have used the value of  $\sin^2(2\theta_{\mu e}^{4\nu})$  that lies within the currently allowed range obtained from global analysis of all short baseline data including LSND and MiniBooNE [120] and corresponds to  $10^{-3}$  in our case.

The Fig. 4.25 shows the probability curves for T2HK (left panels) and DUNE (right panels) as a function of energy. The solid curves are for the case  $\Delta m_{41}^2 = 1.6 \text{ eV}^2$  after averaging over the fast oscillations induced by the high mass-squared difference, while

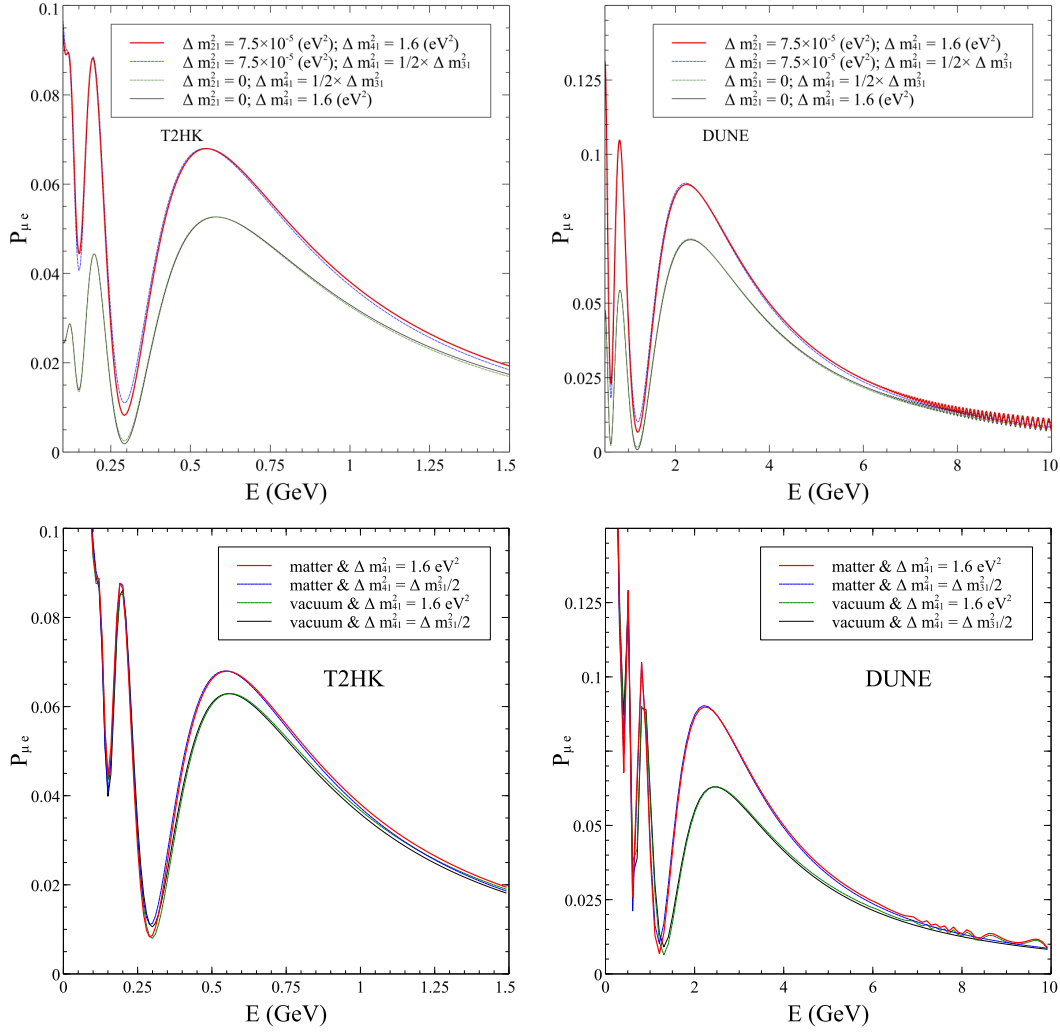


Figure 4.25: Appearance probability as a function of energy for T2HK (left panels) and DUNE (right panels). The solid curves are for the case  $\Delta m_{41}^2 = 1.6 \text{ eV}^2$  after averaging over the fast oscillations induced by the high mass-squared difference, while the dashed curves are for the case when  $\Delta m_{41}^2 = \frac{1}{2} \Delta m_{31}^2$ . The red solid and blue curves are for  $\Delta m_{21}^2 = 7.5 \times 10^{-3} \text{ eV}^2$  while the green and black curves are for the approximate case of  $\Delta m_{21}^2 = 0$ . The fast oscillations due  $\Delta m_{41}^2$  has been averaged out by Gaussian smearing.

the dashed curves are for the case when  $\Delta m_{41}^2 = \frac{1}{2} \Delta m_{31}^2$ . In the top panels, we show the impact of non-zero  $\Delta m_{21}^2$  on the fake solution while in the bottom panels we show the effect of matter on the fake solution. In the top (bottom) panels the red solid and blue curves are for  $\Delta m_{21}^2 = 7.5 \times 10^{-3} \text{ eV}^2$  (matter) while the green and black curves are for the case of  $\Delta m_{21}^2 = 0$  (vacuum). All curves are drawn for  $\Delta m_{31}^2 = 2.75 \times 10^{-3} \text{ eV}^2$ ,  $\delta_{13} + \delta_{24} = 0$ ,  $\theta_{13} = 8.5^\circ$ ,  $\theta_{23} = 45^\circ$ ,  $\theta_{14} = 8.13^\circ$ ,  $\theta_{24} = 7.14^\circ$  and  $\theta_{34} = 0$ . From Fig. 4.25, the existence of the fake solution between high values of  $\Delta m_{41}^2$  and  $\Delta m_{41}^2 = \frac{1}{2} \Delta m_{31}^2$  can be

easily seen. The probabilities for the two cases mentioned above are almost same. Very small differences are seen at energies away from the oscillation maximum, for reasons discussed above. Due to the finite resolution of the detector, this tiny difference is not expected to be differentiated by the detector and hence we expect to see two degenerate solutions for two values of  $\Delta m_{41}^2$ .

### 4.5.2 Numerical results

We have used GLoBES [81, 82] and the necessary code [83, 84] for sterile neutrino oscillation for the simulation of the long-baseline experiments. For this work, we have taken baseline of 295 km and fiducial volume of 374 kton with 1.3 MW beam,  $2.5^\circ$  off-axis from the beam axis for T2HK and 1300 km baseline with 34 kton liquid Argon detector for DUNE. The energy resolution is taken as  $15\%/\sqrt{E}$ . For all our analysis, we used  $\Delta m_{21}^2 = 7.5 \times 10^{-5} \text{eV}^2$ ,  $\Delta m_{31}^2 = 2.5 \times 10^{-3} \text{eV}^2$ ,  $\theta_{12} = 33.48^\circ$ ,  $\theta_{13} = 8.5^\circ$ ,  $\theta_{23} = 45^\circ$  and  $\delta_{13} = -90^\circ$  for the standard mixing parameters, consistent with the current best-fit [24]. And for sterile sector,  $\theta_{14} = 8.13^\circ$ ,  $\theta_{24} = 7.14^\circ$  are taken and  $\theta_{34}$  and  $\delta_{34}$  are taken to be zero as they have very small effect. The phase  $\delta_{24}$  and  $\Delta m_{41}^2$  will be mentioned for different plots shown in the results subsection.

The Fig. 4.26 shows the  $\chi^2$  as a function of  $\Delta m_{41}^2$  (test) for appearance channel only. The top panels are for T2HK while the bottom panels are for DUNE. In the left panels, we show different  $\chi^2$  curves for different combinations of CP-violating phases  $\delta_{13}$  and  $\delta_{24}$  while in the right panels, we show different curves for different values of  $\Delta m_{31}^2$  in the data. In all panels, the data have been generated for  $\Delta m_{41}^2 = 1.6 \text{eV}^2$ . From the left panels we can see that when  $\delta_{13} = -90^\circ$  and  $\delta_{24} = 90^\circ$ , we get two (nearly degenerate) solutions in  $\Delta m_{41}^2$ . One solution corresponds to all values  $\Delta m_{41}^2 \gtrsim 0.01 \text{eV}^2$  for which  $\Delta m_{41}^2$ -driven oscillations are averaged out at the far detector of the experiment. This is the true solution since for all these values of  $\Delta m_{41}^2$  the fast oscillations are averaged out as for  $\Delta m_{41}^2 = 1.6 \text{eV}^2$  in the data. In addition, there is a fake solution at  $\Delta m_{41}^2 \simeq (1/2)\Delta m_{31}^2$  at which the

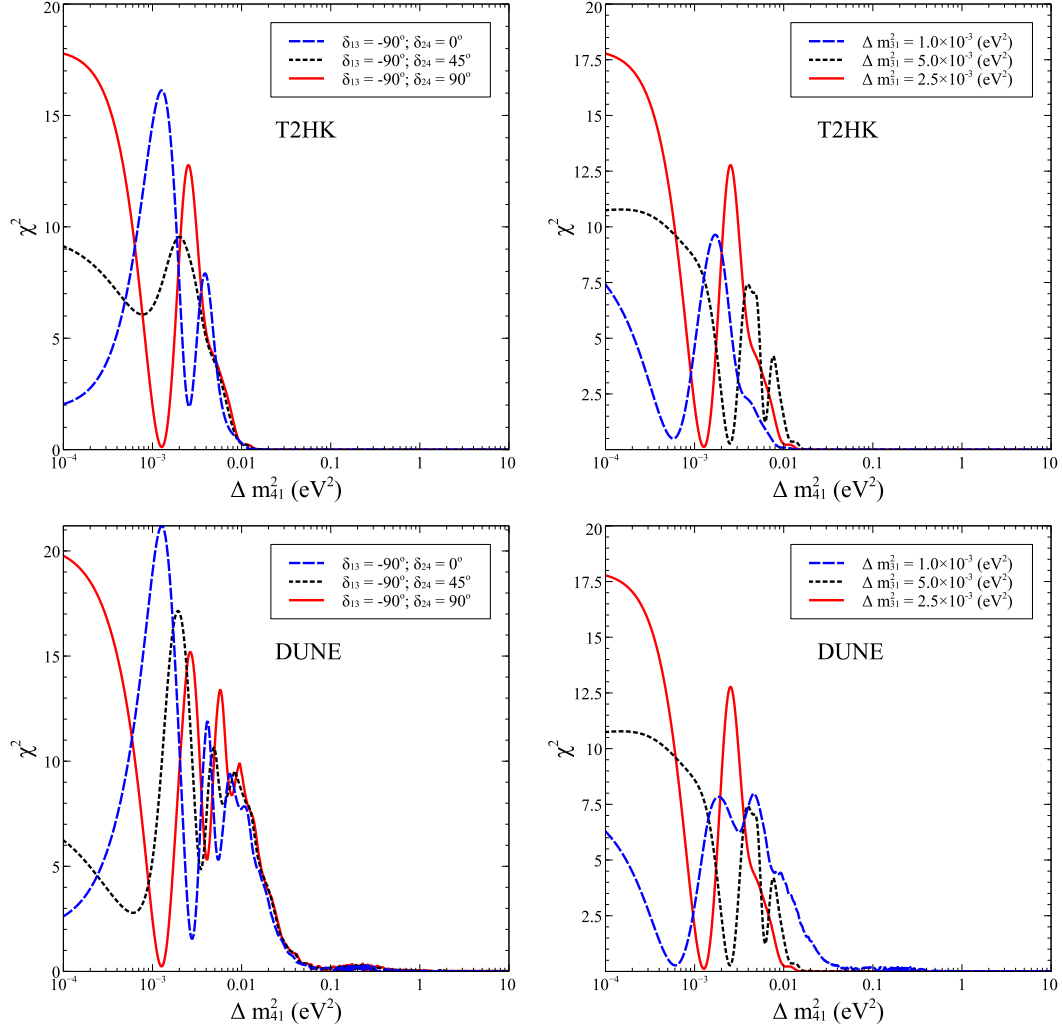


Figure 4.26:  $\chi^2$  as a function of  $\Delta m_{41}^2$  for different combinations of CP-violating phases (left panels) and various values of  $\Delta m_{31}^2$  (right panels). Top panels are for T2HK while bottom panels are for DUNE.



value of  $\chi^2$  is nearly zero. This degeneracy corresponding to  $(\delta_{24} + \delta_{13}) = 0$  was explained in the previous subsection 4.5.1 in terms of the probabilities, both analytically as well as numerically. The fact that the  $\chi^2$  at the fake solution is slightly different from zero comes mainly due to two reasons - (i) in this plot we have taken  $\Delta m_{21}^2$  non-zero, and (ii) as discussed before, the  $\chi^2$ s have been obtained using the full energy range of T2HK and DUNE, while the exact degeneracy exists only at the oscillation maximum.

Note from the figure that for all other combinations of  $\delta_{13} + \delta_{24}$ , the  $\chi^2$  at  $\Delta m_{41}^2 \simeq (1/2)\Delta m_{31}^2$  is far from zero. However, for both the other combinations of  $\delta_{13} + \delta_{24}$  plotted in the figure, there are dips in the value of  $\chi^2$  at values of  $\Delta m_{41}^2$  other than the true values corresponding to the data. Therefore, one can expect to see islands of allowed  $\Delta m_{41}^2$  at values close to  $(1/2)\Delta m_{31}^2$  for all combinations of  $\delta_{13} + \delta_{24}$ . While for  $\delta_{13} + \delta_{24} = 0$ , this fake island is expected to appear as a nearly degenerate solution, for all other combinations it would appear only at a higher C.L. Note also that though for T2HK there is dip at only one fake value of  $\Delta m_{41}^2$ , for DUNE there are multiple dips. This is because DUNE is a wide-band beam experiment while T2HK is a narrow-beam experiment.

The fake solution is further explored in the right panels of Fig. 4.26. Here the data is generated for only the case  $\delta_{13} + \delta_{24} = 0$  with  $\delta_{13} = -90^\circ$  and  $\delta_{24} = 90^\circ$  but for different values of  $\Delta m_{31}^2$ . The red solid, blue dashed and the black dotted curves are for  $\Delta m_{31}^2 = 2.5 \times 10^{-3} \text{ eV}^2$ ,  $\Delta m_{31}^2 = 1.0 \times 10^{-3} \text{ eV}^2$  and  $\Delta m_{31}^2 = 5.0 \times 10^{-3} \text{ eV}^2$ , respectively. As the  $\delta_{13} + \delta_{24} = 0$ , there are degeneracies present in all of the three curves. And it is interesting to note that the fake solution is always at half of the value  $\Delta m_{31}^2$ .

In Fig. 4.26, we saw that the fake solution of  $\Delta m_{41}^2$  always appears at half of  $\Delta m_{31}^2$ . In Fig. 4.27 we further illustrate it for T2HK. The plot for DUNE is identical and not shown here for brevity. The x-axis represents the value of  $\Delta m_{31}^2$  in the data and the red dots represent the corresponding value of the fake  $\Delta m_{41}^2$  solution when the true solution is taken at  $\Delta m_{41}^2 = 1.6 \text{ eV}^2$ . The black line corresponds to  $\Delta m_{41}^2 = \frac{1}{2}\Delta m_{31}^2$ . We can see from Fig. 4.27 that this line fits the red points very well, so indeed the fake solution

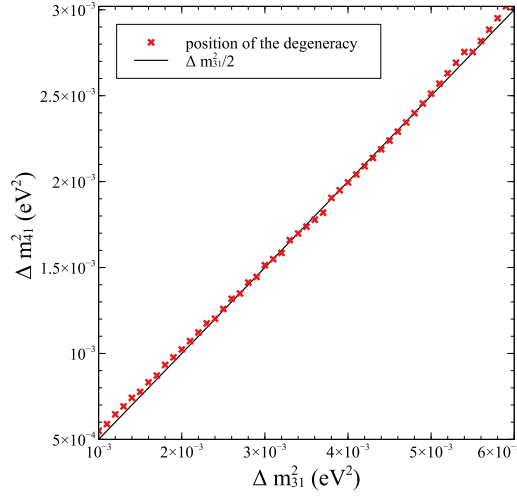


Figure 4.27: The figure shows the positions of the fake solutions. The red data points show the positions of the fake solutions in  $\Delta m^2_{41}$  as a function of  $\Delta m^2_{31}$  and the black straight line is a linear fit to red points corresponding to  $\Delta m^2_{41} = (1/2)\Delta m^2_{31}$ .

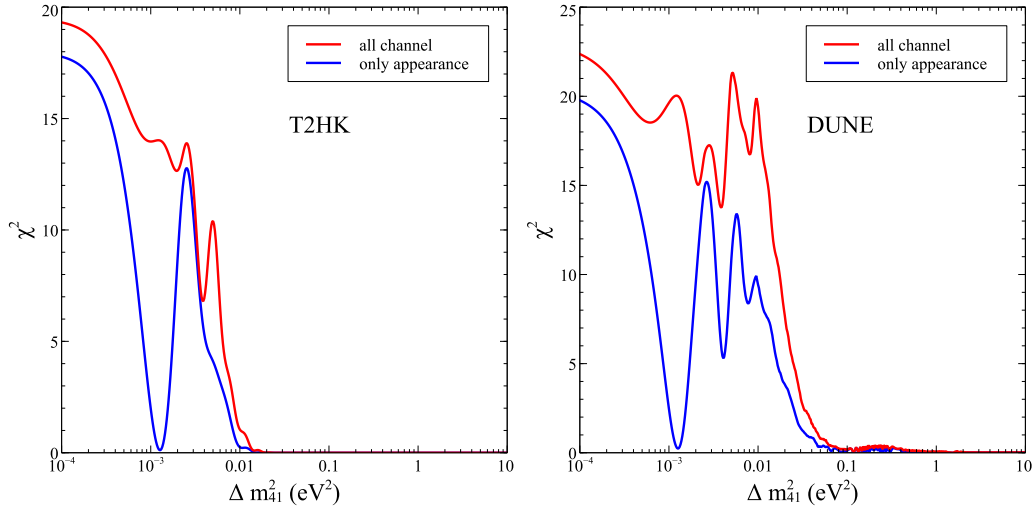


Figure 4.28: Impact of disappearance channel on removing the  $\Delta m^2_{41}$  fake solution. The blue lines show the  $\chi^2$  as a function of  $\Delta m^2_{41}$  (test) for the appearance channel only for T2HK (left panel) and DUNE (right panel). The red lines show the corresponding  $\chi^2$  when both disappearance and appearance data are taken together in the fit.

is at half of the value  $\Delta m^2_{31}$ . In all figures shown so-far, we have only considered the appearance channel in the long-baseline experiments. This is because the fake solution presented in this paper comes only in the appearance channel. The disappearance channel does not have this fake solution and hence should water down the emergence of the fake  $\Delta m^2_{41}$  island. In Fig. 4.28 we show the impact of adding the disappearance data into

the analysis. The blue curve shows the  $\chi^2$  as a function of  $\Delta m_{41}^2$  for the appearance channel only, while the red curve shows the results when data from both appearance and disappearance channels are combined to obtain the  $\chi^2$ . We can see from the figure that introduction of disappearance channels removes the fake solution. The left panel is for T2HK and the right panel is for DUNE. The impact of the disappearance channel in lifting the degeneracy is visible in both experiments.



## NSI at long-baseline experiments

It has been established that the presence of matter NSIs, in general, reduces the sensitivity of DUNE to standard oscillation parameters. The main reason behind this reduction is the interplay between oscillations due to standard and non-standard parameters that give rise to new kinds of degeneracies for long-baseline experiments [125, 126]. It has been shown [147] that for sufficiently large values of the NSI parameters one could expect a degeneracy between the sign of  $\Delta m_{31}^2$  and  $\delta$ , affecting the sensitivity of DUNE to the neutrino mass ordering [147, 148]. For  $\theta_{23}$  and CP measurements, studies have revealed that there are two other degeneracies. The first kind is due to an interplay between the oscillation parameter  $\theta_{23}$  and the NSI parameters. This leads to a reduction of the DUNE sensitivity to  $\theta_{23}$  and even fake so-called octant solutions [125, 126]. The second kind is due to an interplay between  $\delta$  and the NSI parameters, opening up the possibility of a reduced expected sensitivity for this parameter at DUNE. Since the NSI paradigm brings in a large number of parameters, the statistical analysis of the projected data at DUNE becomes cumbersome and challenging. The analysis with a full matter NSI parameter scan was performed in Refs. [125, 126] for a three years running of the experiment in the neutrino mode and three years in the antineutrino mode. To the best of our knowledge, the impact of source and detector NSIs at DUNE has not been studied before.

Any theory, which gives rise to the matter NSIs, would almost always also give rise to source and detector NSIs, and hence, it is imperative to consider them together

in a complete analysis. The neutrino oscillation probabilities in the presence of both source/detector and matter NSIs have been calculated before [84] and are seen to depend on these parameters in a correlated way. It is therefore pertinent to ask if these correlation could alter in any way the expected sensitivity of DUNE.

In this work [130], we perform a complete analysis of the expected sensitivity of DUNE, allowing for both source/detector and matter NSIs. We study the combined effect of source/detector and matter NSIs and look at possible correlations between them at the level of oscillation probabilities. We point out the importance of the event spectrum in disentangling standard oscillations from oscillations driven by NSI parameters. We next calculate the expected sensitivity of DUNE for standard and NSI parameters from a full scan of the NSI parameter space, including all relevant source/detector and matter NSIs. Finally, we explore the effect of runtime on the precision measurement at DUNE.

## 5.1 Neutrino oscillations with non-standard interactions

The presence of flavour off-diagonal operators beyond the SM is manifest in the phenomenon of neutrino oscillations. In the standard picture of neutrino oscillations, a neutrino produced at a source in association with a charged lepton  $\ell_\alpha$  is simply

$$|\nu_\alpha^s\rangle = |\nu_\alpha\rangle, \quad (5.1)$$

i.e. the weak-interaction eigenstate with isospin  $T^3 = +1/2$ . Similarly, a neutrino that produces a charged lepton  $\ell_\beta$  at a detector is

$$\langle \nu_\beta^d | = \langle \nu_\beta |, \quad (5.2)$$

which is also the weak-interaction eigenstate. Between the source and the detector, the propagation of neutrinos with energy  $E$  is governed by the time-evolution equation

$$i \frac{d}{dt} \begin{bmatrix} \nu_e \\ \nu_\mu \\ \nu_\tau \end{bmatrix} = \frac{1}{2E} \left\{ U^\dagger \begin{bmatrix} 0 & 0 & 0 \\ 0 & \Delta m_{21}^2 & 0 \\ 0 & 0 & \Delta m_{31}^2 \end{bmatrix} U + \begin{bmatrix} A & 0 & 0 \\ 0 & 0 & 0 \\ 0 & 0 & 0 \end{bmatrix} \right\} \begin{bmatrix} \nu_e \\ \nu_\mu \\ \nu_\tau \end{bmatrix}. \quad (5.3)$$

Here,  $U$  is the leptonic mixing matrix that is parametrized in terms of three mixing angles  $\theta_{12}$ ,  $\theta_{13}$  and  $\theta_{23}$  and one Dirac CP-violating phase  $\delta_{CP}$ . The evolution of neutrino states also depends on the two independent mass-squared differences  $\Delta m_{ij}^2 = m_i^2 - m_j^2$ . When neutrinos propagate through the earth, the coherent forward scattering of  $\nu_e$  off electrons results in the matter potential  $A = 2\sqrt{2}G_F n_e E$ , where  $n_e$  is the number density of electrons. Thus, standard neutrino oscillation probabilities depend on six oscillation parameters, and are modified by matter effects.

Beyond the SM, it is possible to have CC-like operators that affect the interactions of neutrinos with charged leptons. If these operators are not diagonal in flavour basis, then the production and the detection of neutrinos are affected. The neutrino state produced at the source in association with the charged lepton  $\ell_\alpha$  then also has components of the other flavours

$$|\nu_\alpha^s\rangle = |\nu_\alpha\rangle + \sum_{\gamma=e,\mu,\tau} \mathcal{E}_{\alpha\gamma}^s |\nu_\gamma\rangle, \quad (5.4)$$

and similarly at the detector,

$$\langle \nu_\beta^d | = \langle \nu_\beta | + \sum_{\gamma=e,\mu,\tau} \mathcal{E}_{\gamma\beta}^d \langle \nu_\gamma |. \quad (5.5)$$

The matrices  $\mathcal{E}^s = (\mathcal{E}_{\alpha\gamma}^s)$  and  $\mathcal{E}^d = (\mathcal{E}_{\gamma\beta}^d)$  that represent the source and the detector NSIs, respectively, are in general complex matrices with 18 real parameters each. These are the nine amplitudes  $|\mathcal{E}_{\alpha\beta}^{s/d}|$  and nine phases  $\varphi_{\alpha\beta}^{s/d}$ . Note that the definitions of  $\mathcal{E}_{\alpha\gamma}^s$  and  $\mathcal{E}_{\gamma\beta}^d$  follow the convention used in Ref. [149].

The NC-like operators affect the propagation of neutrinos through matter, inducing more terms similar to the matter potential. The modified time-evolution equation is

$$i \frac{d}{dt} \begin{bmatrix} \nu_e \\ \nu_\mu \\ \nu_\tau \end{bmatrix} = \frac{1}{2E} \left\{ U^\dagger \begin{bmatrix} 0 & 0 & 0 \\ 0 & \Delta m_{21}^2 & 0 \\ 0 & 0 & \Delta m_{31}^2 \end{bmatrix} U + A \begin{bmatrix} 1 + \varepsilon_{ee}^m & \varepsilon_{e\mu}^m & \varepsilon_{e\tau}^m \\ \varepsilon_{\mu e}^m & \varepsilon_{\mu\mu}^m & \varepsilon_{\mu\tau}^m \\ \varepsilon_{\tau e}^m & \varepsilon_{\tau\mu}^m & \varepsilon_{\tau\tau}^m \end{bmatrix} \right\} \begin{bmatrix} \nu_e \\ \nu_\mu \\ \nu_\tau \end{bmatrix}. \quad (5.6)$$

The entry 1 in the  $e - e$  position of the matter effect matrix stands for the standard matter effect, while the parameters  $\varepsilon_{\alpha\beta}^m$  represent the matter NSIs. Note that the definitions of  $\varepsilon_{\alpha\beta}^m$  also follow the convention used in Ref. [149]. Since the Hamiltonian has to be Hermitian, we have the relations  $\varepsilon_{\alpha\beta}^m = \varepsilon_{\beta\alpha}^{m*}$ . Thus, there are six amplitudes and three phases, i.e. nine real parameters in the matter NSI matrix. Subtracting a constant multiple of the identity matrix does not affect the eigenvectors, and hence, oscillation probabilities. Therefore, we subtract the element  $\varepsilon_{\mu\mu}^m$  from all the diagonal elements. We define  $\varepsilon_{ee}^{m'} = \varepsilon_{ee}^m - \varepsilon_{\mu\mu}^m$  and  $\varepsilon_{\tau\tau}^{m'} = \varepsilon_{\tau\tau}^m - \varepsilon_{\mu\mu}^m$  and treat these two new parameters as the physical parameters of the system.

A comprehensive study of the bounds on NSI parameters has been carried out by the authors of Ref. [150]. The 90 % bounds on the source/detector NSI parameters<sup>1</sup> from their study are as follows

$$|\varepsilon_{\alpha\beta}^{s/d}| < \begin{bmatrix} 0.041 & 0.025 & 0.041 \\ 0.026 & 0.078 & 0.013 \\ 0.12 & 0.018 & 0.13 \end{bmatrix}. \quad (5.7)$$

For the matter NSI parameters, we follow the discussion in Ref. [151]. In that paper, the authors have used the bounds from Ref. [150] along with more recent results from SK and

---

<sup>1</sup>Strictly speaking, the NSI parameters that affect neutrino oscillations are combinations of the NSI parameters that enter the Lagrangian, depending on the Lorentz structure of the current involved in the process. In this study, we assume for the sake of simplicity that the bounds from Ref. [150] apply directly to the oscillation NSI parameters.



MINOS [149, 152, 153] to obtain the following bounds

$$|\mathcal{E}_{\alpha\beta}^m| < \begin{bmatrix} 4.2 & 0.3 & 3.0 \\ 0.3 & - & 0.04 \\ 3.0 & 0.04 & 0.15 \end{bmatrix}. \quad (5.8)$$

Throughout this article, we will refer to the bounds listed above as the ‘current bounds’.

Analytical expressions for the neutrino oscillation probabilities in the presence of source/detector and matter NSIs are given in Ref. [84]. The expressions are derived as perturbative expansions in the small parameters  $\Delta m_{21}^2/\Delta m_{31}^2$  and  $\sin \theta_{13}$  up to linear order in the NSI parameters. In Fig. 5.1, we show the change in the  $\nu_\mu \rightarrow \nu_e$  oscillation probability  $P_{\mu e}$  as the NSI parameters are varied one at a time within their allowed range at 90 % C.L. The dark curve within the band corresponds to standard oscillations when the value of the NSI parameter is zero. Since the existing bounds on matter NSIs are weaker, we observe that they affect the probability more, resulting in bands that are much wider. Therefore, we expect them to change the event rates at DUNE and affect the measurement of parameters.

## 5.2 Simulation results

In our simulation, we use the neutrino flux corresponding to a 1.2 MW beam with 120 GeV protons. The expected flux at DUNE will have beam power between 1.2 MW and 2.3 MW and proton energy between 80 GeV and 120 GeV. Thus, the configuration we are using gives a conservative estimate of the net statistics that the experiment will accumulate. Unless stated otherwise, we assume that the experiment will run with five years in neutrino mode and five years in antineutrino mode.

The 40 kiloton liquid argon detector is assumed to have an energy resolution of 15 % for  $\nu_e$  and 20 % for  $\nu_\mu$ . For NC events, however, the reconstructed energy of the neutrino

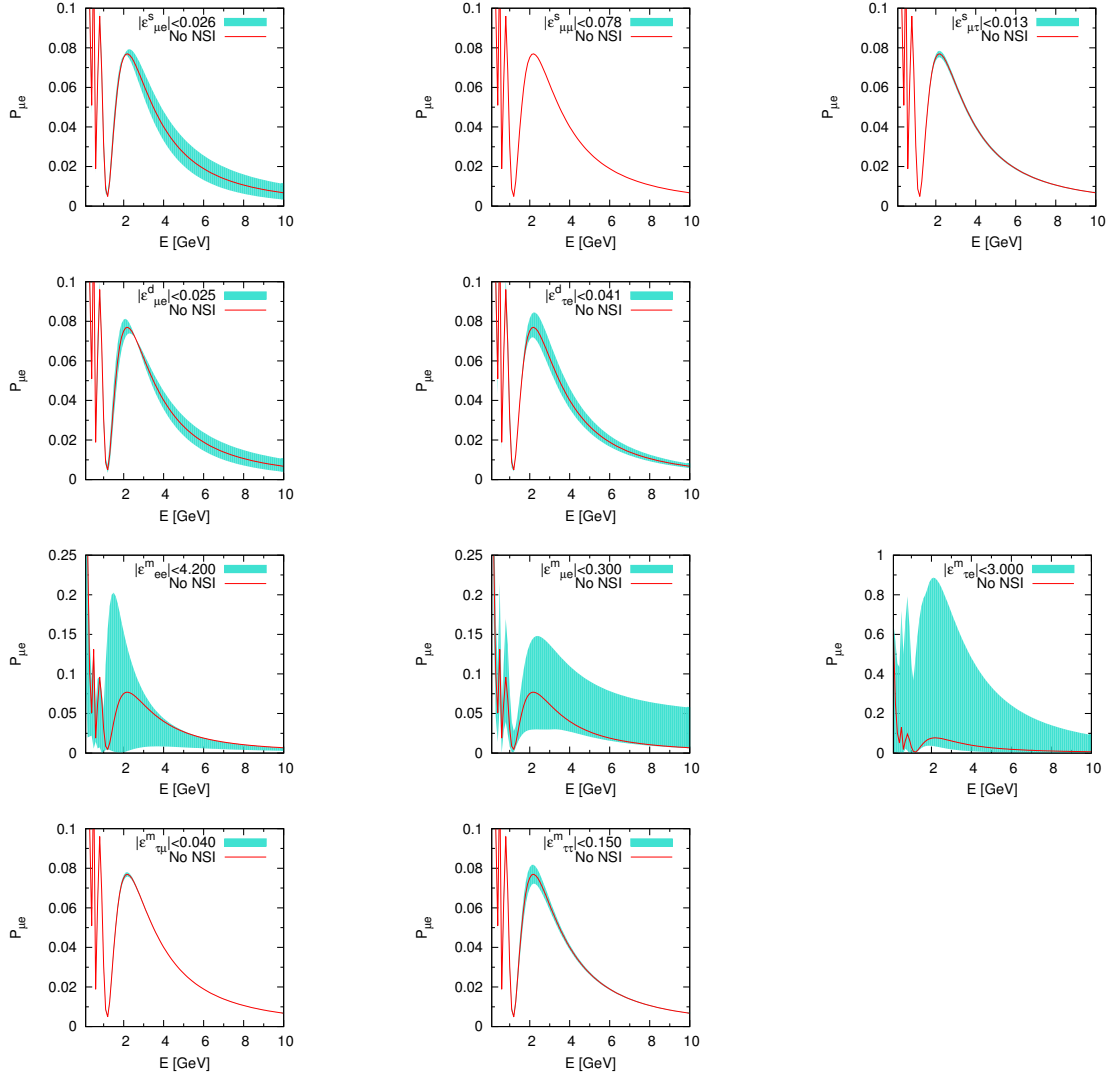


Figure 5.1: Variation in the neutrino oscillation probability  $P_{\mu e}$  as a function of neutrino energy  $E$  with some of the NSI parameters varied in their allowed range. The central dark curve corresponds to the case of no NSIs. The values of the standard oscillation parameters used in generating these figures are  $\theta_{12} = 33.5^\circ$ ,  $\theta_{13} = 8.48^\circ$ ,  $\theta_{23} = 42^\circ$ ,  $\delta_{CP} = -90^\circ$ ,  $\Delta m_{21}^2 = 7.50 \times 10^{-5} \text{ eV}^2$  and  $\Delta m_{31}^2 = 2.45 \times 10^{-3} \text{ eV}^2$ .

has a wide spread to lower energies, because of the production of pions and other hadrons. Therefore, we use a smearing matrix to simulate the effect of the reconstruction of these events.

The primary backgrounds to the electron appearance and muon disappearance signal events come from the NC backgrounds and intrinsic  $\nu_e$  contamination in the flux. In addition, there is a wrong-sign component in the flux. The problem of wrong sign events is more severe for the antineutrino run, since the neutrino component in the antineutrino

flux is larger than the antineutrino component in the neutrino flux. We have taken all of these backgrounds into account in our simulation of the experiment. From an experimental point of view, various cuts are imposed on the observed events in order to eliminate as much of the background as possible. Furthermore, in our simulation, the effect of these cuts is to appear as efficiency factors that reduce the number of events. The full specifications of the detector that we have used can be found in Ref. [27]. Apart from the usual uncertainties in the flux and the cross-section, the presence of source/detector NSIs can also affect the calibration of the expected number of events. In our analysis, we have included systematic errors in the normalization of the flux at the 5 % (20 %) level for signal (background) events.

For our simulation, we have made use of the GLOBES package [81, 82]. The scanning of the multi-dimensional parameter space was achieved by a Markov Chain Monte Carlo using the MonteCUBES package [85]. As a result, all of our results are to be interpreted in terms of Bayesian credible regions rather than frequentist confidence levels, i.e. the 90 % credible region is the part of parameter space that will contain 90 % of the posterior probability as opposed to the 90 % C.L. contours that contain the points in parameter space where the simulated result would be within the 90 % least extreme experimental outcomes. We have written a GLOBES-compatible probability engine to handle the full parameter space and calculate the oscillation probabilities in the presence of both source/detector and matter NSIs.

Since we are primarily interested in the  $\nu_\mu \rightarrow \nu_e$  and  $\nu_\mu \rightarrow \nu_\mu$  oscillation probabilities, the relevant source NSI parameters are  $\varepsilon_{\mu e}^s$ ,  $\varepsilon_{\mu\mu}^s$  and  $\varepsilon_{\mu\tau}^s$ , while the relevant detector NSI parameters are  $\varepsilon_{ee}^d$ ,  $\varepsilon_{e\mu}^d$ ,  $\varepsilon_{\mu e}^d$ ,  $\varepsilon_{\mu\mu}^d$ ,  $\varepsilon_{\tau e}^d$  and  $\varepsilon_{\tau\mu}^d$ . The matter NSI parameters affect the propagation of neutrinos and are all relevant since intermediate states are summed over. Furthermore, based on the analytical expressions and our preliminary simulations, we reduce the set of relevant source/detector parameters to  $\varepsilon_{\mu e}^s$ ,  $\varepsilon_{\mu\mu}^s$ ,  $\varepsilon_{\mu\tau}^s$ ,  $\varepsilon_{\mu e}^d$  and  $\varepsilon_{\tau e}^d$ . Thus, our final simulations are run over the parameter space spanned by five complex source/detector NSI

parameters and three complex and two real matter NSI parameters. As for the standard oscillation parameters, we fix the parameters  $\Delta m_{21}^2$  and  $\theta_{12}$  and vary the others.

The best-fit values of the standard parameters are  $\theta_{12} = 33.5^\circ$ ,  $\theta_{13} = 8.48^\circ$ ,  $\theta_{23} = 42^\circ$ ,  $\delta_{CP} = -90^\circ$ ,  $\Delta m_{21}^2 = 7.50 \times 10^{-5} \text{ eV}^2$  and  $\Delta m_{31}^2 = 2.45 \times 10^{-3} \text{ eV}^2$  which are consistent with the global fits to neutrino oscillation data [154–156]. These parameters are marginalized over their  $3\sigma$  ranges allowed by the global fits with the corresponding priors. For the NSI parameters, we use the bounds listed before. The true values of these NSI parameters are either set to zero or to a non-zero value equal to half of the  $1\sigma$  bounds. The true values of all NSI phases are zero, and they are free to vary in the entire  $[-180^\circ, 180^\circ)$  range.

### 5.2.1 Effect on precision measurements at DUNE

The current generation of long-baseline neutrino oscillation experiments T2K and NOvA are already collecting data and have provided a hint of the value of  $\delta_{CP}$  [157, 158]. This also gives hints about the neutrino mass ordering and octant of  $\theta_{23}$  [157, 159]. If the data collected over the next few years do not confirm these hints, then it may be possible for DUNE to make these measurements. At any rate, we expect that data from DUNE will enable us to measure these unknown parameters at a higher confidence level.

It becomes important to question whether the presence of NSIs will adversely affect the precision measurement of these parameters or not. Many recent studies have explored this question for DUNE [124–126, 128, 148] in the context of matter NSIs. In Fig. 5.2, we show the effect of NSIs on the precision measurement of  $\theta_{23}$  and  $\delta_{CP}$  when the true values of these parameters are  $42^\circ$  and  $-90^\circ$ , respectively. In the left panel, we have set the true values of all NSI parameters to zero. We have then scanned the parameter space for four different cases, where the parameter space consists of (a) only the standard oscillation parameters, (b) standard parameters and source/detector NSI parameters, (c) standard parameters and matter NSI parameters and (d) standard parameters, source/detector NSI

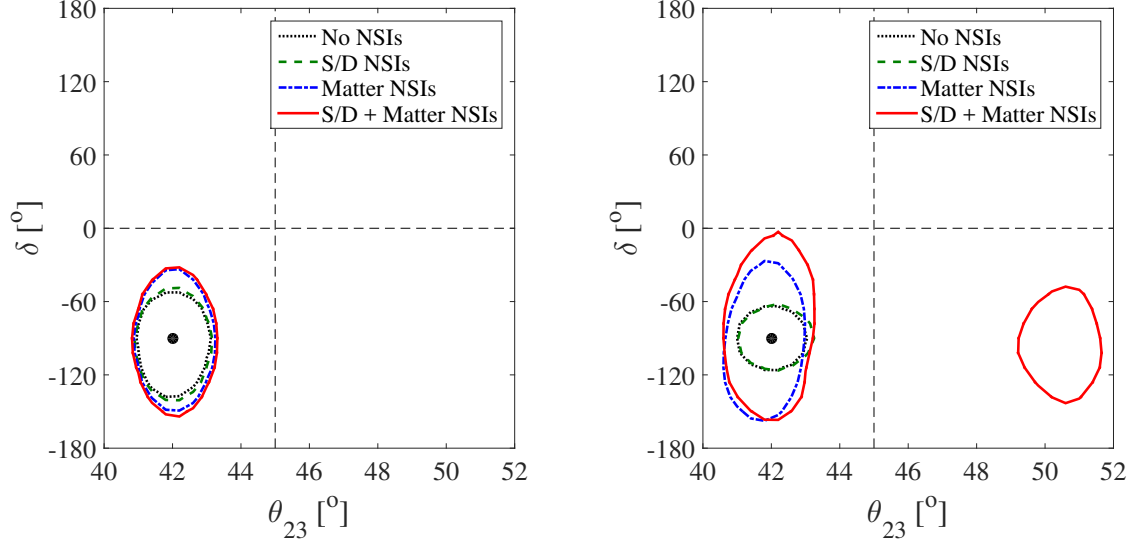


Figure 5.2: Sensitivity of DUNE in the  $\theta_{23} - \delta_{CP}$  plane. The simulated true values of these parameters are  $42^\circ$  and  $-90^\circ$ , respectively. The contours enclose the allowed region at 90 % credible regions obtained by marginalizing over only the standard parameters, standard parameters and source/detector NSI parameters, standard parameters and matter NSI parameters, and standard parameters and all NSI parameters. In the left (right) panel, the true values of the NSI parameters are taken to be zero (non-zero).

parameters and matter NSI parameters. The results are displayed as different contours in the parameter space as the 90 % credible regions. This plot shows how the precision in  $\theta_{23}$  and  $\delta_{CP}$  changes as we change our assumption about the parameter space when there are no NSIs in nature. We observe that the sensitivity in  $\theta_{23}$  is not affected by scanning the extra parameter space. Another significant feature is that the source/detector NSIs do not play much of a role. This is expected since the current bounds restrict the allowed range of these parameters. There is some worsening of the sensitivity to  $\delta_{CP}$ . In the right panel, we have given a similar plot, but with non-zero values of the NSI parameters. This plot shows the successive worsening of precision as more NSIs are introduced. The innermost contour displays the allowed region, where NSIs are present in nature, but we only choose to marginalize over the standard parameters. The sensitivity to the standard parameters obtained from such an analysis would be erroneously optimistic. In order to see the actual worsening of sensitivity because of the presence of NSIs, we compare the dotted black curve of the left panel (zero NSIs, standard oscillation scenario) with the solid red curve of the left panel (non-zero NSIs, all NSI parameters included in the fit). We find that the

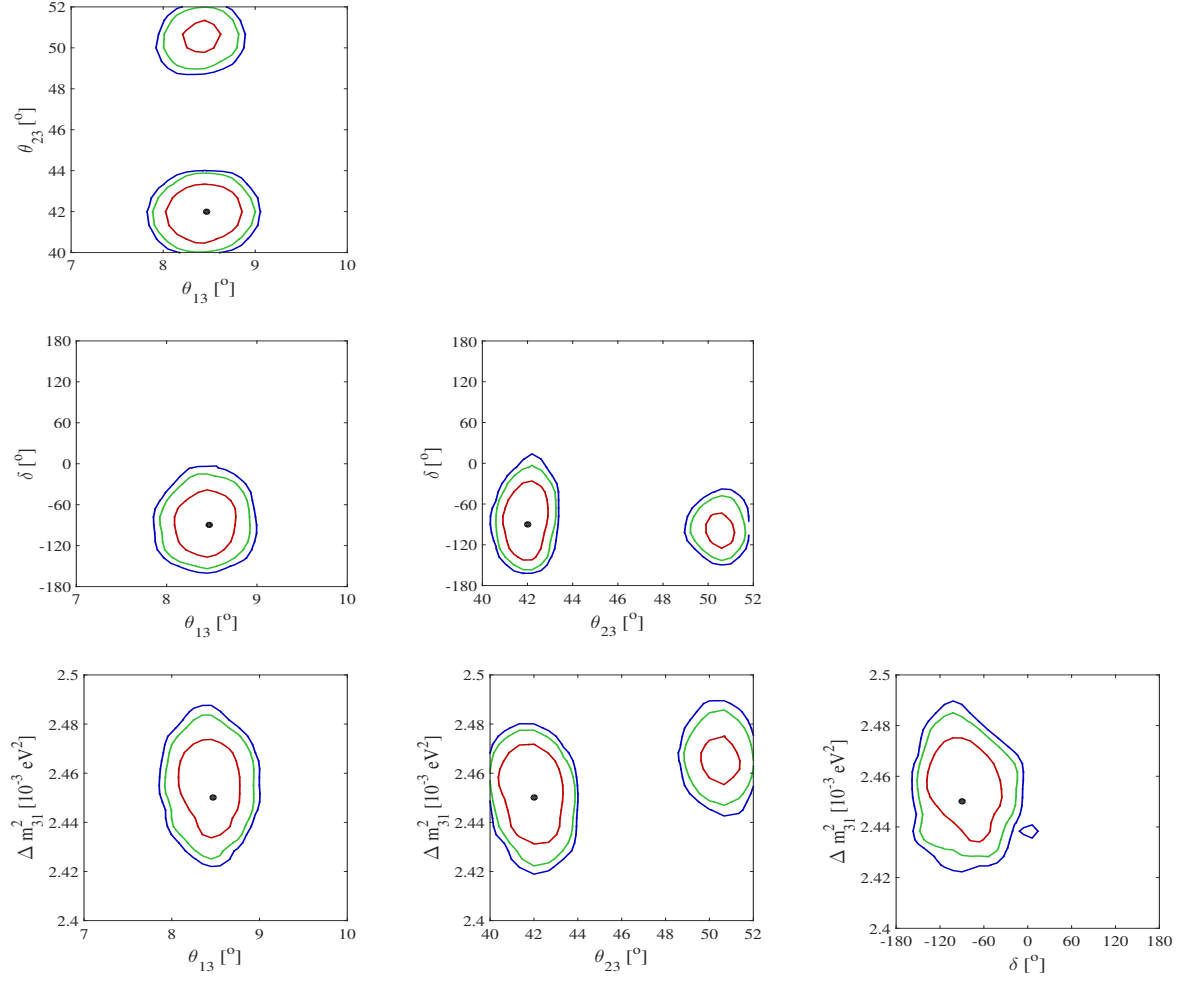


Figure 5.3: Precision in the standard oscillation parameters in the presence of NSIs at DUNE. The contours shown correspond to 68 % (red), 90 % (green) and 95 % (blue) credible regions.

error in the measurement of  $\delta_{CP}$  (the size in  $\delta$  of the 90 % credible region) increases from around  $90^\circ$  to almost  $180^\circ$ . In addition, we find a degenerate solution in  $\theta_{23}$  in the wrong octant. These additional degeneracies have been studied recently in Refs. [125, 126].

For completeness, we compute the precision in  $\theta_{13}$ ,  $\theta_{23}$ ,  $\delta_{CP}$  and  $\Delta m^2_{31}$  that DUNE will reach in the presence of NSIs. The results are shown in Fig. 5.3, where a striking feature is the appearance of a degenerate solution in  $\theta_{23}$ .

### 5.2.2 Constraining NSI parameters at DUNE

So far, we have discussed the effect of NSIs on the measurement of the standard oscillation parameters. In addition, DUNE can place bounds on the NSI parameters due to its high statistics. In order to estimate these projected bounds from DUNE, we set the true values of the NSI parameters to zero. Varying the fit values, we construct the 90 % credible region for the value of the parameter placed by DUNE. These 90 % credible regions are obtained by marginalizing over all the other parameters. In Table 5.1, we list the 90 % credible upper bounds that DUNE can impose. We have performed the computations for three different cases: (a) the only NSIs are source/detector NSIs, (b) the only NSIs are matter NSIs and (c) all NSIs exist simultaneously.

Parameter	Only source/detector NSIs	Only matter NSIs	All NSIs	Current bound
$ \mathcal{E}_{\mu e}^s $	0.017		0.022	0.026
$ \mathcal{E}_{\mu\mu}^s $	0.070		0.065	0.078
$ \mathcal{E}_{\mu\tau}^s $	0.009		0.014	0.013
$ \mathcal{E}_{\mu e}^d $	0.021		0.023	0.025
$ \mathcal{E}_{\tau e}^d $	0.028		0.035	0.041
$\mathcal{E}_{ee}^m$		(-0.7, +0.8)	(-0.8, +0.9)	(-4.2, +4.2)
$ \mathcal{E}_{\mu e}^m $		0.051	0.074	0.330
$ \mathcal{E}_{\tau e}^m $		0.17	0.19	3.00
$ \mathcal{E}_{\tau\mu}^m $		0.031	0.038	0.040
$\mathcal{E}_{\tau\tau}^m$		(-0.08, +0.08)	(-0.08, +0.08)	(-0.15, +0.15)

Table 5.1: Expected 90 % credible regions on NSI parameters from DUNE.

In general, investigating Table 5.1, we see that in going from the case of (a) only source/detector NSIs or (b) only matter NSIs to the case of (c) both source/detector and matter NSIs, the bounds imposed by DUNE get weaker. This is expected because of the expansion of the parameter space. (For  $|\mathcal{E}_{\mu\mu}^s|$ , the precision appears to improve marginally after the inclusion of all NSIs. This is merely an artifact of the randomness inherent in the Monte Carlo simulation and should be taken with a pinch of salt. The relative difference between the two numbers is small enough for them to be practically equal within the precision of our Monte Carlo simulation.) Using all NSIs, we find that all bounds are improved or basically the same as the current bounds. We also see that the

most general bounds imposed on the source/detector NSI parameters are only slightly better than the existing bounds. This shows that the main contribution to the sensitivity to these parameters comes from the prior introduced for them. Data from DUNE itself contribute only to the extent of providing more statistics without any significant physics advantage. On the other hand, we find that the bounds on matter NSI parameters are made substantially more stringent than the existing bounds. In particular, the bounds on  $\varepsilon_{ee}^{m'}$ ,  $|\varepsilon_{\mu e}^m|$  and  $|\varepsilon_{\tau e}^m|$  are improved by a factor of around five to 15, whereas the bounds on  $|\varepsilon_{\tau\mu}^m|$  and  $\varepsilon_{\tau\tau}^{m'}$  are more or less the same. Our results on the bounds on the matter NSI parameters are consistent with the ones obtained in Ref. [126]. It is worth pointing out that the current bounds on the NSI parameters were derived assuming the existence of only one NSI parameter at a time, whereas we have obtained our bounds by allowing all relevant parameters to vary at the same time.

### 5.2.3 Correlations between source/detector and matter NSIs

Beyond the SM, CC-like and NC-like NSIs presumably, arise from the same model of new physics. Therefore, it is natural to assume that both source/detector and matter NSIs exist. It is interesting to probe the presence of correlations between various kinds of NSI parameters in neutrino oscillations. It is straightforward to pinpoint such correlations from the analytical expressions for the oscillation probabilities given in Ref. [84]. The non-standard terms in  $P_{\mu e}$  up to linear order in  $\sin \theta_{13}$  arising from  $\varepsilon_{\tau e}^d$  and  $\varepsilon_{\tau e}^m$  are



$$\begin{aligned}
P_{\mu e} \supset & -4\varepsilon_{\tau e}^d \tilde{s}_{13} s_{23}^2 c_{23} \cos \delta_{CP} \left[ \sin^2 \frac{AL}{4E} - \sin^2 \frac{\Delta m_{31}^2 L}{4E} - \sin^2 \frac{(\Delta m_{31}^2 - A)L}{4E} \right] \\
& -2\varepsilon_{\tau e}^d \tilde{s}_{13} s_{23}^2 c_{23} \sin \delta_{CP} \left[ \sin \frac{AL}{2E} - \sin \frac{\Delta m_{31}^2 L}{2E} + \sin \frac{(\Delta m_{31}^2 - A)L}{2E} \right] \\
& +4\varepsilon_{\tau e}^m \tilde{s}_{13} s_{23}^2 c_{23} \cos \delta_{CP} \left[ \sin^2 \frac{AL}{4E} - \sin^2 \frac{\Delta m_{31}^2 L}{4E} + \sin^2 \frac{(\Delta m_{31}^2 - A)L}{4E} \right] \\
& +2\varepsilon_{\tau e}^m \tilde{s}_{13} s_{23}^2 c_{23} \sin \delta_{CP} \left[ \sin \frac{AL}{2E} - \sin \frac{\Delta m_{31}^2 L}{2E} + \sin \frac{(\Delta m_{31}^2 - A)L}{2E} \right] \\
& +8\varepsilon_{\tau e}^m \tilde{s}_{13} s_{23}^2 c_{23} \cos \delta_{CP} \frac{A}{\Delta m_{31}^2 - A} \sin^2 \frac{(\Delta m_{31}^2 - A)L}{4E}, \tag{5.9}
\end{aligned}$$

where we have assumed the NSI parameters to be real and used the notation  $\tilde{s}_{13} = s_{13} \Delta m_{31}^2 / (\Delta m_{31}^2 - A)$ . Close to the oscillation maximum, these terms can be combined into one term proportional to  $\varepsilon_{\tau e}^m - \varepsilon_{\tau e}^d$ . Similarly, the terms involving  $\varepsilon_{\tau e}^d$  and  $\varepsilon_{\mu e}^m$  enter the formula as

$$\begin{aligned}
P_{\mu e} \supset & -4\varepsilon_{\tau e}^d \tilde{s}_{13} s_{23}^2 c_{23} \cos \delta_{CP} \left[ \sin^2 \frac{AL}{4E} - \sin^2 \frac{\Delta m_{31}^2 L}{4E} - \sin^2 \frac{(\Delta m_{31}^2 - A)L}{4E} \right] \\
& -2\varepsilon_{\tau e}^d \tilde{s}_{13} s_{23}^2 c_{23} \sin \delta_{CP} \left[ \sin \frac{AL}{2E} - \sin \frac{\Delta m_{31}^2 L}{2E} + \sin \frac{(\Delta m_{31}^2 - A)L}{2E} \right] \\
& -4\varepsilon_{\mu e}^m \tilde{s}_{13} s_{23}^2 c_{23}^2 \cos \delta_{CP} \left[ \sin^2 \frac{AL}{4E} - \sin^2 \frac{\Delta m_{31}^2 L}{4E} + \sin^2 \frac{(\Delta m_{31}^2 - A)L}{4E} \right] \\
& -2\varepsilon_{\mu e}^m \tilde{s}_{13} s_{23}^2 c_{23}^2 \sin \delta_{CP} \left[ \sin \frac{AL}{2E} - \sin \frac{\Delta m_{31}^2 L}{2E} + \sin \frac{(\Delta m_{31}^2 - A)L}{2E} \right] \\
& +8\varepsilon_{\mu e}^m \tilde{s}_{13} s_{23}^3 c_{23} \cos \delta_{CP} \frac{A}{\Delta m_{31}^2 - A} \sin^2 \frac{(\Delta m_{31}^2 - A)L}{4E}. \tag{5.10}
\end{aligned}$$

These can be combined to give a term proportional to  $\varepsilon_{\mu e}^m + \varepsilon_{\tau e}^d$  close to the oscillation maximum. Thus, we expect to have a correlation between  $\varepsilon_{\tau e}^d$  and  $\varepsilon_{\tau e}^m$  and an anticorrelation between  $\varepsilon_{\tau e}^d$  and  $\varepsilon_{\mu e}^m$ . The current bounds on the source/detector NSI parameters are more stringent than those on the matter NSI parameters. Therefore, in scanning over the parameter space, these correlations get washed out. However, if we make the assumption that these two types of NSI parameters have comparable bounds, then the correlations

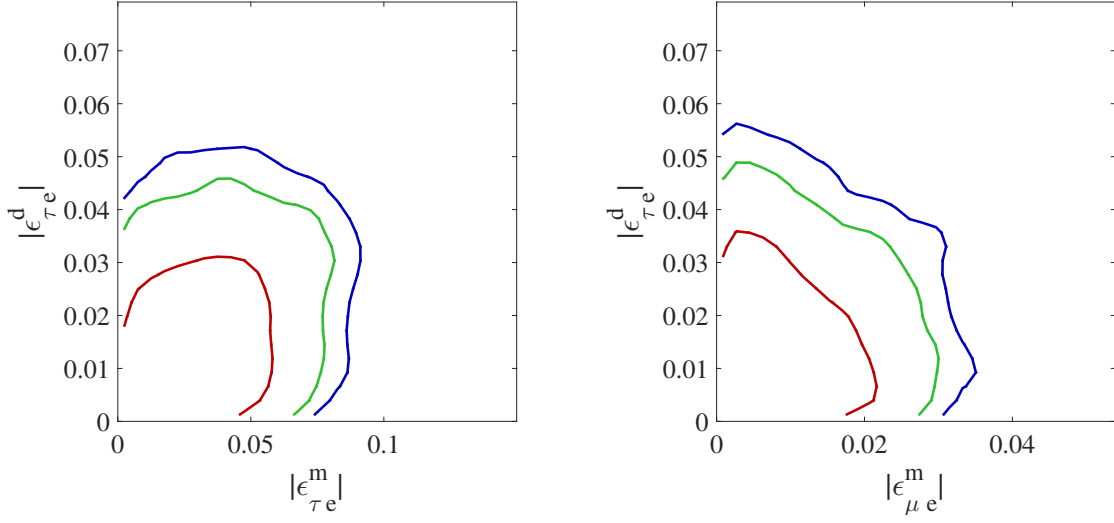


Figure 5.4: Correlations between matter NSI parameters and source/detector NSI parameters at DUNE. The 68 % (red), 90 % (green) and 95 % (blue) credible regions are shown in the  $\epsilon_{\tau e}^m - \epsilon_{\tau e}^d$  plane in the left panel and in the  $\epsilon_{\mu e}^m - \epsilon_{\tau e}^d$  plane in the right panel.

are visible. This can be observed in the panels of Fig. 5.4. In generating these plots, we have made use of the assumptions listed above and used the (more stringent) priors of the source/detector NSI parameters for the matter NSI parameters as well. The true values assigned to the NSI parameters are half of the bounds used. The correlations appear very weak because (a) the parameter space that has been scanned over is very large, (b) the conditions for the correlation include a very small value of  $\theta_{13}$  and (c) the signal events have a spread in energy away from the oscillation maximum. With the current bounds, which are very large for the matter NSI parameters, one does not see any clear correlation between the two types of NSI parameters. In Figs. 5.5 and 5.6, we show the correlations between all the source/detector and matter NSI parameters given their existing bounds.

#### 5.2.4 Effect of statistics

Finally, we make a note of the effect of statistics on the precision measurements at DUNE in the presence of NSIs and on the measurement of these NSI parameters. In the preceding sections, we have assumed a runtime for DUNE of five years with neutrinos and

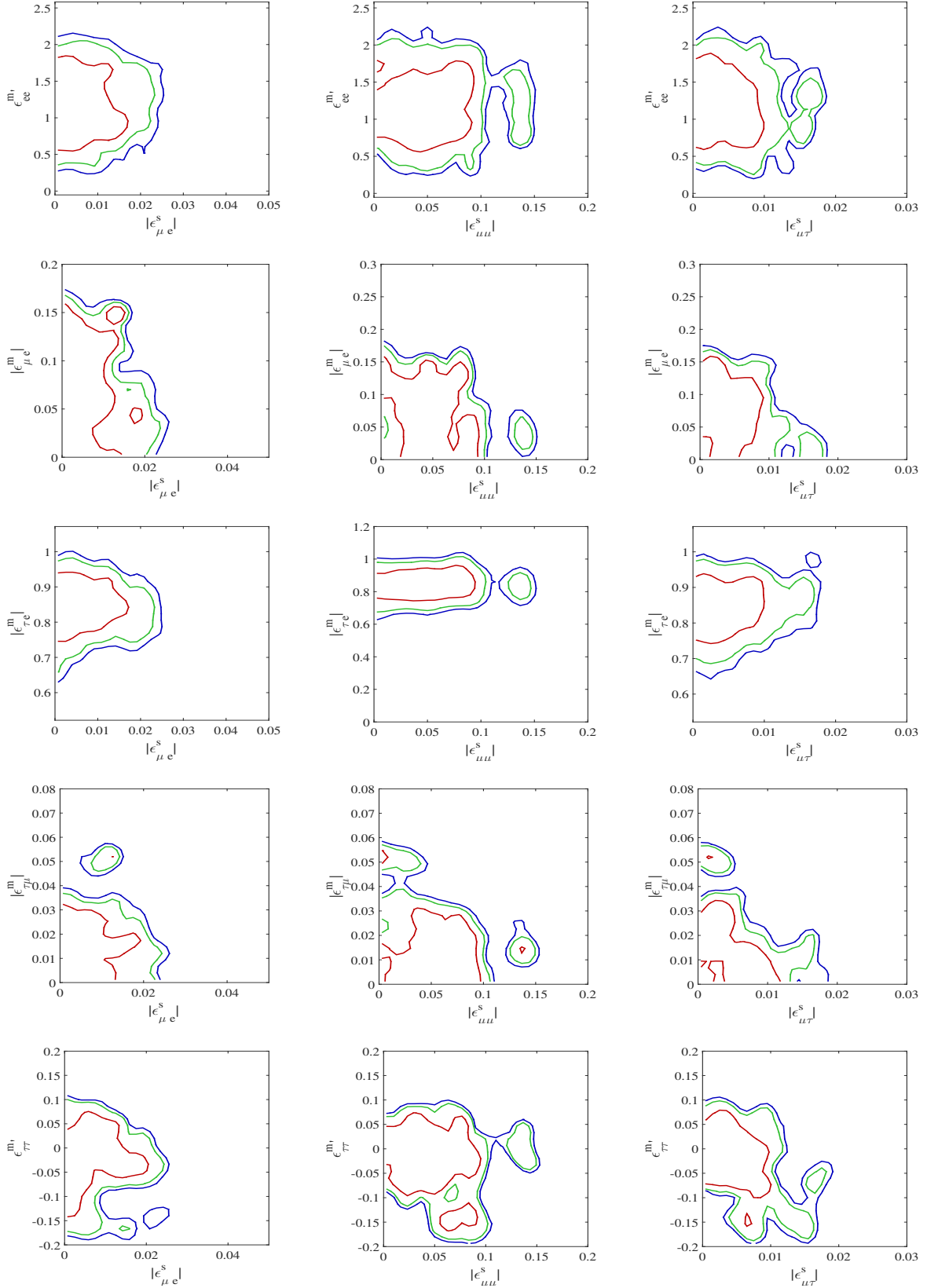


Figure 5.5: Correlations between matter NSI parameters and source NSI parameters with current bounds at DUNE. The 68 % (red), 90 % (green) and 95 % (blue) credible regions are shown.

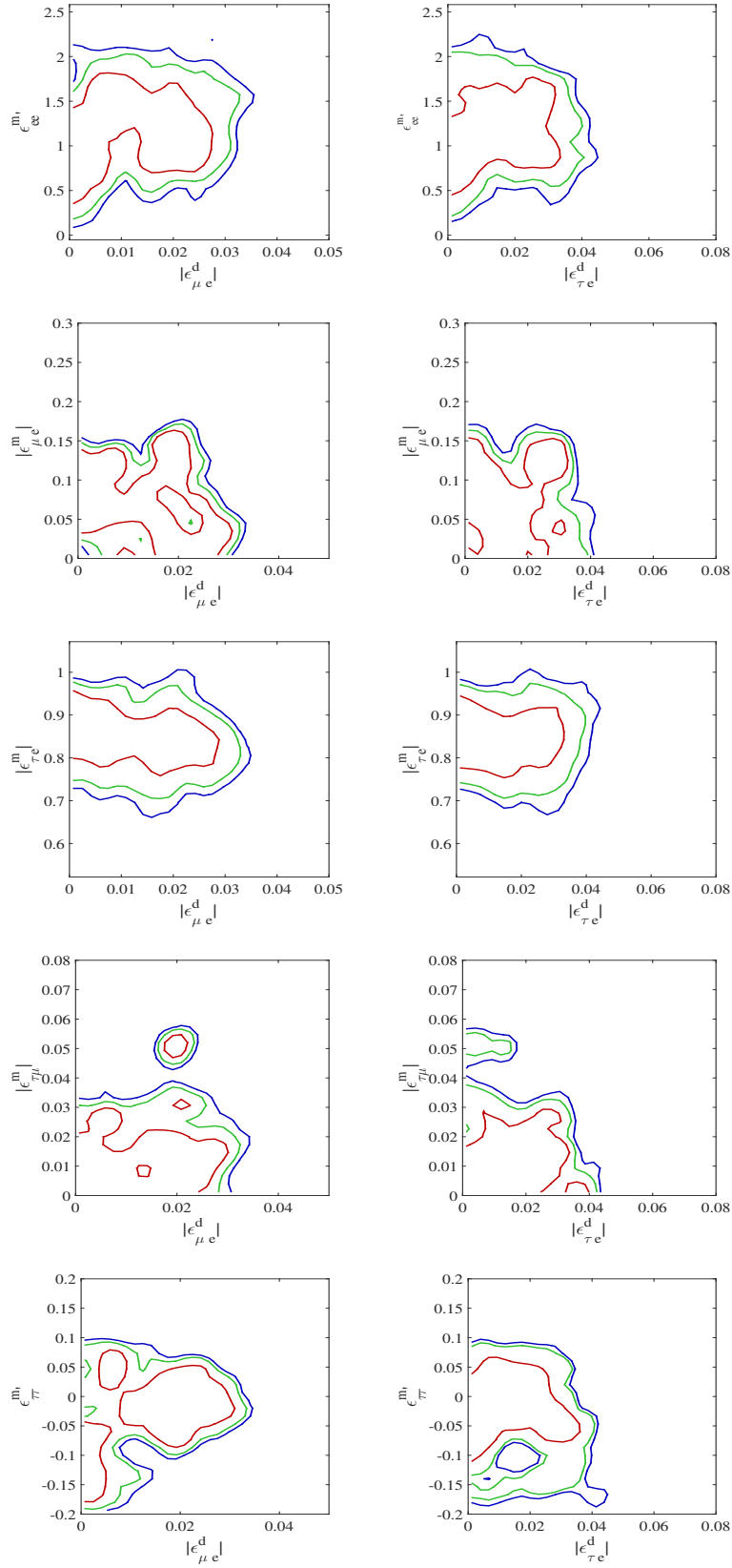


Figure 5.6: Correlations between matter NSI parameters and detector NSI parameters with current bounds at DUNE. The 68 % (red), 90 % (green) and 95 % (blue) credible regions are shown.

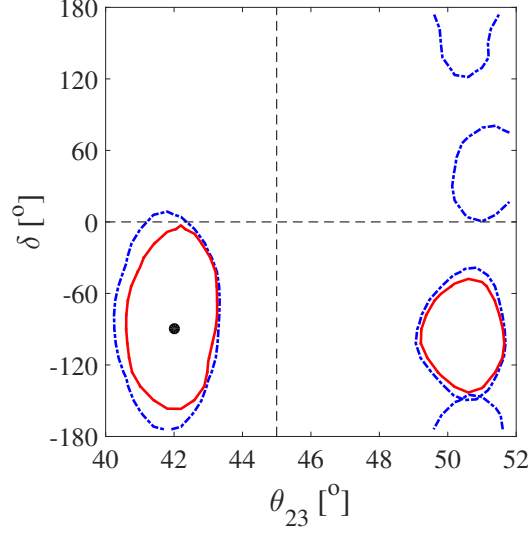


Figure 5.7: Sensitivity of DUNE in the  $\theta_{23} - \delta_{CP}$  plane with 3+3 years (blue, dashed contours) and 5+5 years (red, solid contours) of data. The simulated true values of these parameters are  $42^\circ$  and  $-90^\circ$ , respectively. The contours enclose the 90 % credible regions.

antineutrinos each (5+5). In this section, we discuss the results with lower statistics. In particular, we have re-run our simulations, assuming three years of running in each mode (3+3). Comparing results from the two cases gives an indication of the effect of statistics on the results.

In Fig. 5.7, we have shown this comparison for the precision measurements of  $\theta_{23}$  and  $\delta_{CP}$  at DUNE in the presence of all NSIs. The values of the NSI parameters are taken to be the same non-zero values used in generating the right panel of Fig. 5.2. Comparing the contours corresponding to the cases of 5+5 and 3+3, we find that the precision in  $\delta_{CP}$  is significantly worsened. It has been shown that the combination of neutrino and antineutrino run helps in lifting the  $\theta_{23} - \delta_{CP}$  degeneracy, hence allowing for an accurate measurement of  $\delta_{CP}$  [57, 159–162]. Usually, it is sufficient to have a short run in the antineutrino mode that is just adequate to resolve the degeneracy. In this case, however, the presence of NSIs introduces additional sources of CP violation. Therefore, there are additional regions of the parameter space that are allowed owing to the lower statistics.

Furthermore, we have also checked the bounds imposed on the NSI parameters in

the case of 3+3. Once again, the experiment is seen to have much better sensitivity to the matter NSI parameters than to the source/detector NSI parameters. We find that the bounds are only slightly worse than those shown in Table 5.1 expected from the case of 5+5. Thus, the main advantage of collecting more data with DUNE is to determine the value of  $\delta_{CP}$  with higher precision.

## Invisible neutrino decay at long-baseline experiments

The decay of neutrino can be of two ways: In one case, one or more active neutrino states will decay into states which are singlet under the standard model gauge group. In such theories, the active neutrino state(s) will decay into invisible or sterile state(s) and such types of decays are called invisible neutrino decay. If neutrinos are Dirac particles, then such decay can happen if there is a coupling between neutrinos and a scalar boson [163, 164]

$$\nu_j \rightarrow \bar{\nu}_{iR} + \chi \quad (6.1)$$

where  $\nu_{iR}$  is a right-handed singlet and  $\chi$  is an iso-singlet scalar carrying a lepton number. If neutrinos are Majorana, then such decay requires a pseudo-scalar coupling between the Majorana particles, sterile neutrino and the Majoron [165, 166]

$$\nu_j \rightarrow \nu_s + J \quad (6.2)$$

and this Majoron  $J$  should be dominantly singlet to comply with the constraints from LEP on the  $Z$  invisible decay widths. The other possibility of neutrino decay is the visible decay [167–169] where, one or more neutrino states can decay into another lighter active neutrino state. The decay modes are  $\nu_j \rightarrow \bar{\nu}_i + J$  or  $\nu_j \rightarrow \nu_i + J$ . However, visible neutrino decay is tightly constrained from observations.

Neutrino decay as the solution to the solar neutrino problem was proposed very early

days [170]. This was pure decay solution to the solar neutrino problem. Later, neutrino decay along with oscillation was also considered [164, 171–177]. These studies assumed  $\nu_2$  of being unstable and put bound on the lifetime  $\tau_2$  of  $\nu_2$ . The recent bound obtained for the lifetime of  $\nu_2$  from solar neutrino data is  $\tau_2/m_2 > 1.04 \times 10^{-3}$  s/eV at 99 % confidence level [178]. The decay of  $\nu_1$  and  $\nu_2$  can also be constrained from the supernovae data. The most stringent bound on the  $\nu_1$  and  $\nu_2$  came from the SN1987A supernova data. The bound obtained from that supernova is  $\tau/m > 10^5$  s/eV. However, these data could not constrain the  $\nu_3$  as the solar neutrino does not involve  $\nu_3$  and SN1987A data only has electron type neutrinos and there is very small  $\nu_3$  component in the  $\nu_e$ .

Constraints on the decay of  $\nu_3$  come from atmospheric and long-baseline experiments. A pure decay solution was considered to explain the atmospheric problem but this analysis could not provide a better fit to the data [179]. Neutrino decay with non-trivial mixing was considered in [180, 181] to explain the atmospheric data of SK assuming decaying component of  $\nu_\mu$  and these studies were able to explain the L/E dependence of the SK data, however, [182] showed that this model gives a worse fit, if, zenith angle dependence is considered instead of L/E dependence. In [180] and [182], it was assumed that  $\Delta m^2 > 0.1$  eV<sup>2</sup> to evade the constraints from K-decay bounds. This led to the averaging of the  $\Delta m^2$  dependent terms. These constraints are removed if one considers sterile neutrino states unmixed with the active states. There are two types of theories in the literature in this context. The one is where the  $\Delta m^2$  is kept unconstrained [183] and the other,  $\Delta m^2 \ll 10^{-4}$  eV<sup>2</sup> [184]. Both of them were able to explain the SK data, but, later SK collaboration showed that only oscillation solution gives better fit to the data [185] than the decay with oscillation case considered in [184]. A global analysis [186] was done involving atmospheric and MINOS data and this gave best-fit for the no-decay case, however, oscillation along with decay also gave reasonable fit. This analysis put a bound on neutrino life-time as  $\tau_3/m_3 > 2.9 \times 10^{-10}$  s/eV at 90 % confidence level. Recently an analysis was done using MINOS and early data T2K and it gave a best-fit value of  $\tau_3/m_3 = 1.2 \times 10^{-11}$  s/eV and prefers decay slightly more than only oscillation scenario



[187]. However, this analysis also put a bound on  $\tau_3/m_3$  as  $\tau_3/m_3 > 2.8 \times 10^{-12} \text{s/eV}$ . For the future, prospects of neutrino decay were also considered for JUNO [188] and INO [189]. In this context, it is worthwhile to say that IceCUBE can constrain lifetime of  $\nu_3$  upto 10 sec with 100 TeV energetic neutrino from an astrophysical source at 1 Gpc [190]. In this thesis, invisible neutrino decay is studied in the context of future long-baseline experiment DUNE [143] and currently running experiments like NOvA and T2K [191].

## 6.1 Propagation of neutrino in presence of decay

Assuming the  $\nu_3$  state to decay into a sterile neutrino and a singlet scalar ( $\nu_3 \rightarrow \bar{\nu}_4 + J$ ), the flavor and mass eigenstates get related as,

$$\begin{pmatrix} \nu_\alpha \\ \nu_s \end{pmatrix} = \begin{pmatrix} U & 0 \\ 0 & 1 \end{pmatrix} \begin{pmatrix} \nu_i \\ \nu_4 \end{pmatrix}. \quad (6.3)$$

Here,  $\nu_\alpha$  with  $\alpha = e, \mu, \tau$  denote the flavor states and  $\nu_i$ ,  $i = 1, 2, 3$  denote the three mass states corresponding to the active neutrinos.  $U$  is the standard  $3 \times 3$  PMNS mixing matrix. We assume that  $m_3 > m_2 > m_1 > m_4$  for NH while  $m_2 \approx m_1 > m_3 > m_4$  for IH. This implies that for both NH and IH, the third mass state can decay to a lighter sterile state. Note that  $\Delta m_{34}^2$  is unconstrained from meson decay bound since  $m_4$  is the mass of a sterile state with which the active neutrinos do not mix. The effect of decay can be incorporated in the propagation equation by introducing a term  $m_3/\tau_3$  in the evolution equation: <sup>1</sup>

$$i \frac{d}{dx} \begin{pmatrix} \nu_e \\ \nu_\mu \\ \nu_\tau \end{pmatrix} = \left[ U \left[ \frac{1}{2E} \begin{pmatrix} 0 & 0 & 0 \\ 0 & \Delta m_{21}^2 & 0 \\ 0 & 0 & \Delta m_{31}^2 \end{pmatrix} - i \frac{m_3}{2E\tau_3} \begin{pmatrix} 0 & 0 & 0 \\ 0 & 0 & 0 \\ 0 & 0 & 1 \end{pmatrix} \right] U^\dagger + \begin{pmatrix} A & 0 & 0 \\ 0 & 0 & 0 \\ 0 & 0 & 0 \end{pmatrix} \right] \begin{pmatrix} \nu_e \\ \nu_\mu \\ \nu_\tau \end{pmatrix}, \quad (6.4)$$

<sup>1</sup>This implicitly assumes that the neutrino mass matrix and the decay matrix can be simultaneously diagonalised and the mass eigenstates are the same as the decay eigenstates [179, 192].

where the term  $A = 2\sqrt{2}G_F n_e E$  represents the matter potential due to neutrino electron scattering in matter,  $G_F$  denotes the Fermi coupling,  $E$  is the energy, and  $n_e$  the electron density. For the antineutrinos, the matter potential comes with a negative sign. The fourth sterile state being decoupled from the other states except through the interaction which induces the decay does not affect the propagation. We solve the Eq. (6.4), in matter numerically using Runge-Kutta technique assuming the PREM density profile [193] for the Earth matter.

## 6.2 Invisible neutrino decay from NOvA and T2K data

In this section, we present the current constraints on  $\tau_3/m_3$  from the recent data from NOvA and T2K, using the full three generation oscillation framework with matter effects [191]. We also study the effect of decay on the measurement of  $\theta_{23}$  and  $\Delta m_{32}^2$ . As was shown in [143, 187], there can be significant impact on the measured value of  $\theta_{23}$  if decay is present. We will study how presence of decay changes the best-fit values of  $\theta_{23}$  and  $\Delta m_{32}^2$  as well as the C.L. contours allowed by the T2K and NOvA data.

The first result of muon-neutrino disappearance from NOvA came in 2016 [194], where they used  $2.74 \times 10^{20}$  POT and got the best-fit  $\Delta m_{32}^2 = (2.52^{+0.20}_{-0.18}) \times 10^{-3} \text{ eV}^2$  and  $\sin^2 \theta_{23} = 0.43$  and  $0.60$ . This was immediately followed with first result on electron appearance data [158] with the same exposure. Next disappearance data came in 2017 [195] which used  $6.05 \times 10^{20}$  POT and gave  $\Delta m_{32}^2 = (2.67 \pm 0.11) \times 10^{-3} \text{ eV}^2$ , while for  $\sin^2 \theta_{23}$  they obtained two statistically degenerate values  $0.404^{+0.030}_{-0.022}$  and  $0.624^{+0.022}_{-0.030}$  and claimed that the NOvA data disfavors maximal mixing at  $2.6\sigma$ . Results from the combined analysis of NOvA's appearance and disappearance data was presented in [196]. So while T2K prefers maximal mixing for  $\theta_{23}$ , the early analysis from the NOvA showed  $2.6\sigma$  preference for non-maximal mixing. This tension between the two experiments led several authors to propose new physics ideas to explain the tension between the two

datasets. However, the NOvA collaboration has recently done an improved re-analysis of their disappearance dataset [197]. The newer analysis mainly addresses better the energy resolution of the hadron sample leading to an improved neutrino energy resolution. They have divided the muon events into four quantiles of different resolutions from  $\sim 6\%$  to  $\sim 12\%$ , based on their hadronic energy fraction. This approach changed the measurement of  $\theta_{23}$  at NOvA with maximal  $\theta_{23}$  mixing being preferred by NOvA as well.

The T2K experiment announced their first result with  $1.43 \times 10^{20}$  protons on target (POT) on electron appearance in 2011 [198]. With six observed electron candidate events and 1.5 expected backgrounds, T2K gave the first direct evidence of non-zero  $\theta_{13}$  at  $2.5\sigma$  C.L. The first results announcement on muon disappearance came a year later in 2012 [199] with the same POT of  $1.43 \times 10^{20}$  and gave a best-fit of  $\Delta m_{32}^2 = 2.65 \times 10^{-3} \text{ eV}^2$  and  $\sin^2 2\theta_{23} = 0.98$ . The first anti-neutrino result from T2K was published in [200], where they used  $\bar{\nu}_\mu$  beam with  $4.01 \times 10^{20}$  POT and obtained best fit of  $\sin^2 \theta_{23} = 0.45$  and  $\Delta m_{32}^2 = 2.51 \times 10^{-3} \text{ eV}^2$ , very consistent with the measurements obtained using the  $\nu_\mu$  beam. The T2K collaboration has published their results periodically since the first announcements and their data-sets and best-fit oscillation parameters have remained consistent, with  $\theta_{23}$  close to maximal. The latest result from T2K [201] used  $7.482 \times 10^{20}$  POT for neutrino mode and  $7.471 \times 10^{20}$  POT for anti-neutrino data. This currently gives the best fit  $\Delta m_{32}^2 = 2.52 \pm 0.08 (2.51 \pm 0.08) \times 10^{-3} \text{ eV}^2$  and  $\sin^2 \theta_{23} = 0.55^{+0.05}_{-0.09} (0.55^{+0.05}_{0.08})$  for normal(inverted) ordering, using both electron appearance as well as muon disappearance data.

### 6.2.1 Simulation details

The simulation is done using a modified version of GLoBES, with modifications needed for real data analysis.

For the analysis of NOvA, we have taken a 14 kt detector at a baseline of 812 km with

constant matter density. We have taken 8.5% energy resolution for electron events and 6% resolution for muon events. The signal efficiency is chosen to be 99 % for electron events and 91 % for muon events. We normalize the number of events as well as the shape, to match the best-fit event spectra given in [196] for electrons ( $6.04 \times 10^{20}$  POT) and in [197] for muons ( $8.85 \times 10^{20}$  POT).

For the analysis of T2K, we have taken a 22.5 kt detector at a baseline of 295 km with constant matter density. The energy resolution is taken 8.5 %. The signal efficiency is chosen to be 51.5 % for electron events and 90 % for muon events. We normalise the event spectra as well as shape, to match the event spectra given in [201] which corresponds to  $7.482 \times 10^{20}$  POT in neutrino mode and  $7.471 \times 10^{20}$  POT for anti-neutrino mode.

In all our analysis, we have assumed normal hierarchy. We have kept  $\theta_{12}$ ,  $\theta_{13}$  and  $\Delta m_{21}^2$  fixed in the fit as these parameters are very precisely measured from the past experiments and we have marginalised over  $\theta_{23}$ ,  $\Delta m_{31}^2, \tau_3/m_3$  and  $\delta_{CP}$  as required. The ranges of the marginalisation are the following: for  $\theta_{23}$  it is from  $38^\circ$  to  $53^\circ$ , for  $\Delta m_{31}^2$ , it is from  $2.3 \times 10^{-3} \text{s/eV}^2$  to  $2.6 \times 10^{-3} \text{s/eV}^2$ , for  $\delta_{CP}$ , it is the full  $360^\circ$  range and for  $\tau_3/m_3$ , the range is from  $10^{-13} \text{s/eV}$  to  $10^{-9} \text{s/eV}$ .

## 6.2.2 Results

In Fig. 6.1 we show the constraint on  $\tau_3/m_3$  from the current data of NOvA and T2K, where the latest appearance, as well as disappearance data sets of both experiments, have been taken into consideration in the analysis. The green solid curve is obtained using NOvA data alone, the dark red dotted curve is obtained using T2K data alone, while the black dashed curve is obtained from a combined analysis of NOvA and T2K data. The parameters  $\theta_{23}$  and  $\Delta m_{32}^2$  are marginalised in the fit over their  $3\sigma$  allowed ranges and  $\delta_{CP}$  is marginalised over its full range. It can be seen from the Fig. 6.1, that for both experiments the no decay scenario is slightly disfavoured and the best-fit value from the

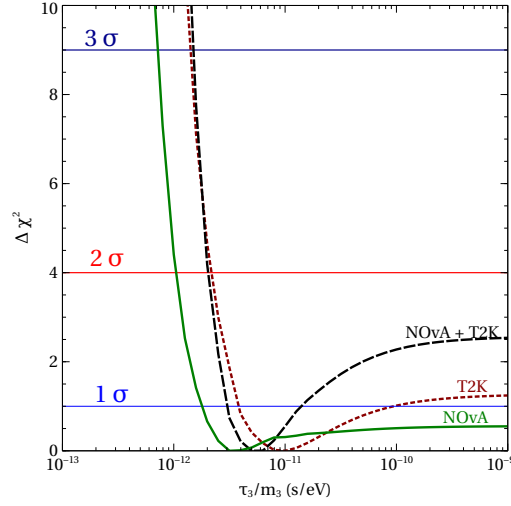


Figure 6.1:  $\Delta\chi^2 = \chi^2 - \chi_{\min}^2$  vs  $\tau_3/m_3$  obtained from the analysis of T2K data (red dashed line), NOvA data (solid green line) and T2K+NOvA data (black long dashed line).

fit comes for non-zero decay. NOvA and T2K both have slightly more  $\chi^2$  for the no-decay case than the best-fit  $\chi^2$  however, these results are not statistically significant. Best-fit value of NOvA, T2K and their combination are  $\tau_3/m_3 = 3.16 \times 10^{-12}$  s/eV,  $1 \times 10^{-11}$  s/eV and  $\tau_3/m_3 = 5.01 \times 10^{-12}$  s/eV respectively. The minimum  $\chi^2$  ( $\chi_{\min}^2$ ) for NOvA, T2K and the combined case are 10.38, 69.34 and 87.19, respectively, which are slightly less than the standard oscillation fit, for which the  $\chi_{\min}^2$  are 10.93, 70.39 and 88.65, respectively. Therefore, the invisible decay scenario we consider in this work, fits the data slightly better than the standard oscillation case. The data sets also set a lower bound on the lifetime. The  $3\sigma$  lower bound on  $\tau_3/m_3$  from NOvA data is seen to be  $\tau_3/m_3 \geq 7.22 \times 10^{-13}$  s/eV, while from T2K it is  $\tau_3/m_3 \geq 1.41 \times 10^{-12}$  s/eV. The  $3\sigma$  combined constraint from both experiments taken together is  $\tau_3/m_3 \geq 1.50 \times 10^{-12}$  s/eV. It can be clearly seen from Fig. 6.1, that the sum of the two  $\Delta\chi^2$  is less than the  $\Delta\chi^2$  for the combined analysis. This points at a synergy between the two experiments. This synergy results in an improved fit for the decay scenario compared to standard oscillation when we perform the combined analysis of the two experiments.

To understand why both the data prefer decay over standard oscillation, we give the muon event rates in Fig. 6.2. The left panel is for NOvA and the right panel is for T2K.

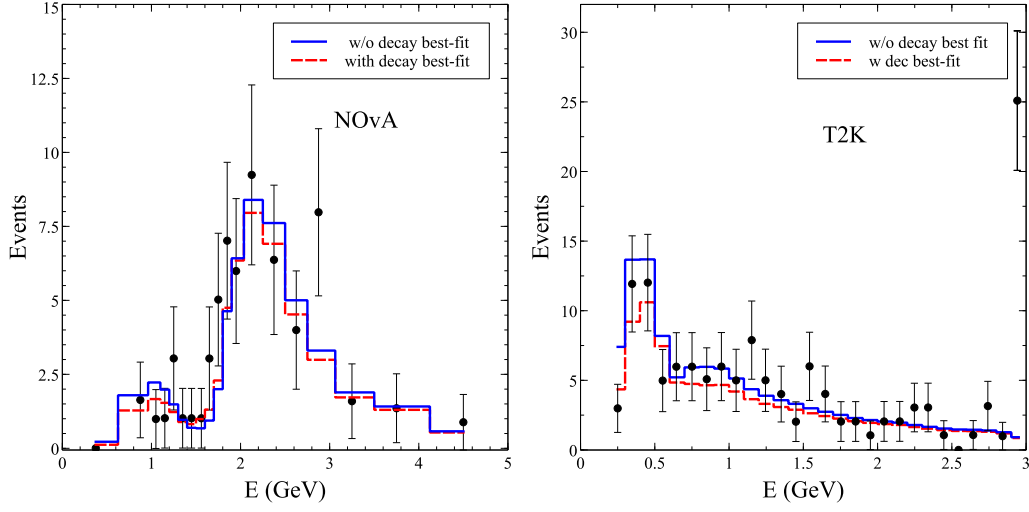


Figure 6.2: Muon event spectra for NOvA and T2K. The left panel is for NOvA while the right panel is for T2K. The black dots with the error-bar are actual data points. The error bars correspond to the  $1\sigma$  statistical error.

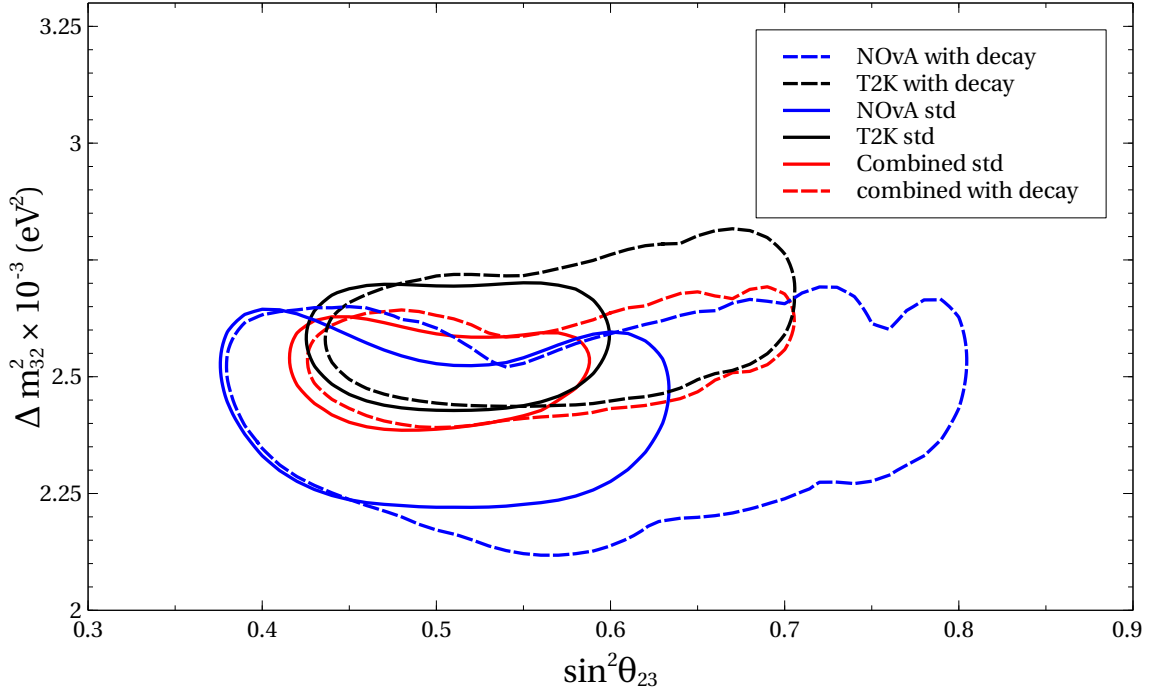


Figure 6.3: The 95 % C.L. allowed areas obtained in the  $\sin^2 \theta_{23} - \Delta m^2_{32}$  plane, from analysis of T2K data (red lines), NOvA data (green lines) and T2K+NOvA data (black lines). The solid lines are for standard three-generation oscillations while the dashed lines are for oscillation with decay.

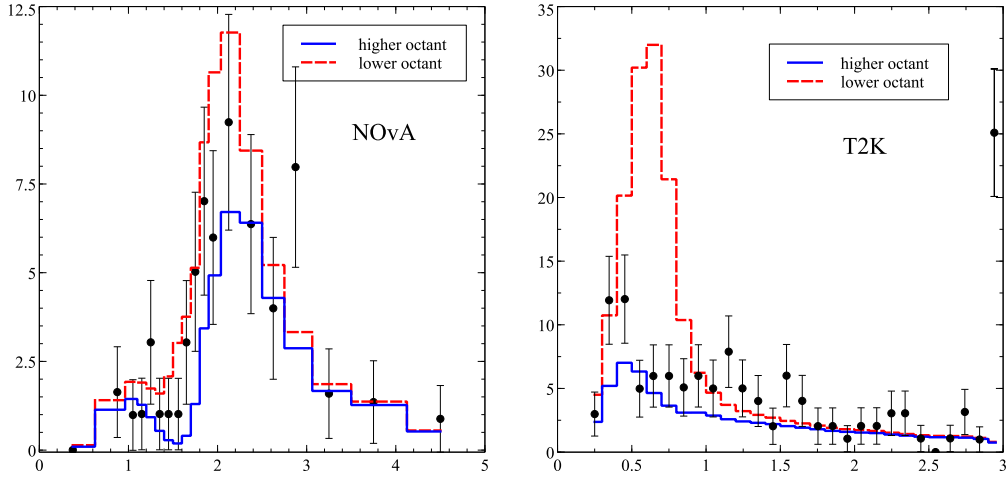


Figure 6.4: Muon event spectra for NOvA and T2K. The left panel is for NOvA while the right panel is for T2K. The black dots with the error-bar are actual data points. The error bars correspond to the  $1\sigma$  statistical error.

The blue solid lines show the event spectra for the standard best-fit, while the red dashed lines show the event spectra for decay best-fit. The black dots are data points with  $1\sigma$  statistical error bar. From the NOvA plot, it can be seen that the red dashed line fits the data better than the blue solid line. Between 1 and 2 GeV, where the oscillation maximum lies, the red dashed line almost exactly fits the data. For the T2K plot, again the red dashed line fits the data better than the blue solid line. Therefore, for both data sets, the decay with oscillation fits the data better than the only oscillation case.

Fig. 6.3 shows the allowed region in the  $\sin^2 \theta_{23}$  vs  $\Delta m_{32}^2$  plane at 95 % C.L. The solid curves are for only oscillation case without decay whereas the dashed curves are for the case where  $\nu_3$  are allowed to decay. The fit is marginalised over  $\delta_{CP}$  in both cases and over  $\tau_3/m_3$  as well for the case of decay plus oscillation. The blue curves are for NOvA, the black curves are for T2K and the red curves are for the combined analysis. For the standard case the best-fit points ( $\sin^2 \theta_{23}$ ,  $\Delta m_{32}^2$ ) are  $(0.45, 2.41 \times 10^{-3} \text{ eV}^2)$ ,  $(0.52, 2.56 \times 10^{-3} \text{ eV}^2)$  and  $(0.46, 2.51 \times 10^{-3} \text{ eV}^2)$  for NOvA, T2K and the combined cases, respectively. On the other hand, for the case with decay and oscillation the corresponding best-fit points are:  $(0.48, 2.39 \times 10^{-3} \text{ eV}^2)$ ,  $(0.62, 2.62 \times 10^{-3} \text{ eV}^2)$  and  $(0.48, 2.52 \times 10^{-3} \text{ eV}^2)$  for NOvA, T2K and the combined cases, respectively. The interesting point to notice

here is that for all cases, the allowed region of the parameter space increases significantly when decay is considered along with oscillation. Also note that with inclusion of decay, the best-fit shifts towards higher values of  $\sin^2 \theta_{23}$ . This behaviour is very similar to what was seen in [187] in the context of MINOS and T2K and in [143] in the context of DUNE. The shift of  $\theta_{23}$  to higher values in presence of decay can be understood in terms of the survival probability given in [187] in the two-generation approximation neglecting matter effect,

$$P_{\mu\mu}^{2G} = \left[ \cos^2 \theta_{23} + \sin^2 \theta_{23} \exp(-m_3 L / \tau_3 E) \right]^2 - \sin^2 2\theta_{23} \exp(-m_3 L / \tau_3 E) \sin^2 \left( \frac{\Delta m_{31}^2 L}{4E} \right). \quad (6.5)$$

In Eq. (6.5), there is an exponential suppression due to neutrino decay in both the oscillatory as well as the non-oscillatory term. Therefore for a given  $\theta_{23}$ , the survival probability for the decay case will be less than the standard oscillation case. Hence, when decay is considered in the fit, the value of  $\sin^2 \theta_{23}$  increases in order to reproduce the same probability obtained for the standard case.

From Fig. 6.4, one can understand why more region of higher octant is allowed than the lower octant for the case with decay. The left(right) panel of Fig. 6.4 show the muon events for NOvA(T2K). In each of the plots, the blue solid line is for  $\sin^2 \theta_{23}$  in higher octant and the red dashed line is for  $\sin^2 \theta_{23}$  in the lower octant. The black dots are the data points with  $1\sigma$  statistical error bar. In both of the plots, it can be seen that the blue solid lines fit the data points reasonably whereas the red dashed lines do not fit the data at all. This shows why more region of the higher octant is allowed for the decay case than the lower octant.

Fig. 6.5 gives the allowed region in the  $\sin^2 \theta_{23}$  vs  $\tau_3/m_3$  plane at 95 % C.L. with  $\Delta m_{32}^2$  marginalised over its current  $3\sigma$  range and  $\delta_{CP}$  marginalised over full range. The blue solid, black dashed and red dashed-dotted curves are for NOvA, T2K and the combined



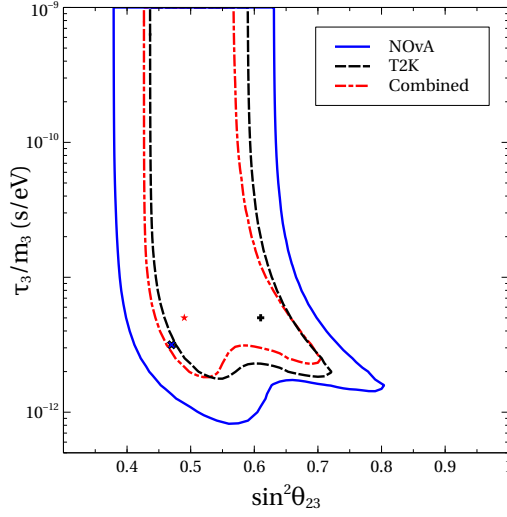


Figure 6.5: The 95 % C.L. allowed areas obtained in the  $\tau_3/m_3 - \sin^2 \theta_{23}$  plane, from analysis of T2K data (black dashed line), NOvA data (blue solid line) and T2K+NOvA data (red dashed-dotted line).

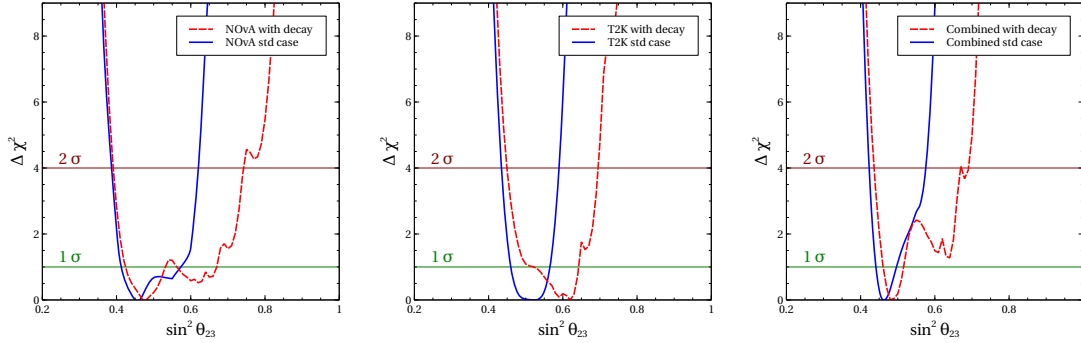


Figure 6.6:  $\Delta\chi^2$  vs  $\sin^2 \theta_{23}$ , where the  $\chi^2$  is marginalised over all other parameters.

analysis, respectively. The blue cross gives the best-fit for NOvA ( $0.47, 3.16 \times 10^{-12}$  s/eV), the black plus gives the best-fit for T2K ( $0.61, 5.011 \times 10^{-12}$  s/eV) and the red star gives the best-fit for the combined case ( $0.49, 5.011 \times 10^{-12}$  s/eV). Again as in Fig. 6.3, the best-fit is seen to be for finite  $\tau_3/m_3$ .

Fig. 6.6 gives the  $\Delta\chi^2$  vs  $\sin^2 \theta_{23}$  for the standard case and the decay plus oscillation case. The fit is marginalised over  $\Delta m_{32}^2$  and  $\delta_{CP}$  for the standard case and over  $\Delta m_{32}^2$ ,  $\tau_3/m_3$  and  $\delta_{CP}$  for the decay plus oscillation case. The left panel is for NOvA, the middle panel is for T2K and the right panel is for the combined analysis. In all the panels the blue solid curves are for the standard oscillation case while the red dashed curves represent

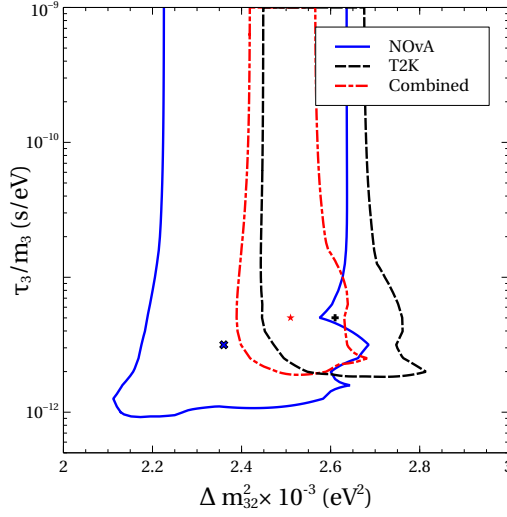


Figure 6.7: The 95 % C.L. allowed areas obtained in the  $\tau_3/m_3 - \Delta m_{32}^2$  plane, from analysis of T2K data (black dashed line), NOvA data (blue solid line) and T2K+NOvA data (red dashed-dotted line).

the decay with oscillation case. For T2K our standard oscillation best-fit  $\sin^2 \theta_{23} = 0.52$  matches very well with the best-fit obtained by the T2K collaboration [201]. For NOvA on the other hand, our best-fit for standard oscillation comes at  $\sin^2 \theta_{23} = 0.45$  while the NOvA collaboration gets their best-fit at  $\sin^2 \theta_{23} = 0.558^{+0.041}_{-0.033}$  in the higher octant. The reason for this mild mis-match could be because our experimental simulation is based on GLoBES which cannot include all systematics in a rigorous manner. However, the figure shows that the  $\chi^2$  differences between the minima of the two octant is less than 1, and hence the best-fit obtained by us for the higher octant is not so different from the correct value obtained from the collaboration.

Fig. 6.7 gives the allowed region in the  $\Delta m_{32}^2$  vs  $\tau_3/m_3$  plane at 95 % C.L. with  $\theta_{23}$  marginalised over current  $3\sigma$  allowed region and  $\delta_{CP}$  marginalised over full range. The blue curve is for NOvA, the black is for T2K and the red is for the combined case. The blue cross gives the best-fit for NOvA ( $2.36 \times 10^{-3}$ ,  $3.16 \times 10^{-12}$ ), the black plus for the T2K ( $2.61 \times 10^{-3}$ ,  $5.011 \times 10^{-12}$ ) and the red star is for the combined best-fit ( $2.51 \times 10^{-3}$ ,  $5.011 \times 10^{-12}$ ). The above best-fit values are in units of ( $\text{eV}^2$ ,  $\text{s/eV}$ ).

Fig. 6.8 gives the  $\Delta\chi^2$  vs  $\Delta m_{32}^2$  with  $\theta_{23}$  and  $\delta_{CP}$  marginalised for the standard and  $\theta_{23}$ ,

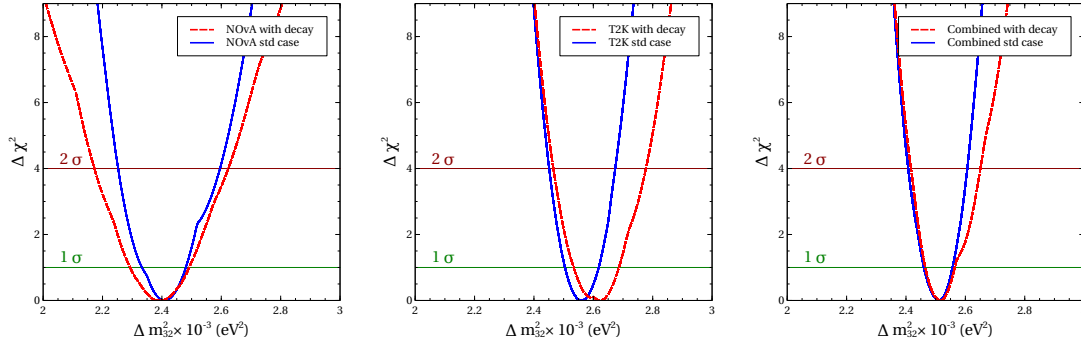


Figure 6.8:  $\Delta\chi^2$  vs  $\Delta m_{32}^2$ , where the  $\chi^2$  is marginalised over all other parameters.

$\delta_{CP}$  and  $\tau_3/m_3$  marginalised for the case of decay plus oscillation. Just as in Fig. 6.6, the left panel is for NOvA, the middle is for T2K and the right panel is for the combined case. The blue solid curves are for the standard case whereas the red dashed curves are for the decay plus oscillation case. It can be seen from the figure that for NOvA the allowed range of  $\Delta m_{32}^2$  increases on both sides while for T2K the best-fit  $\Delta m_{32}^2$  shifts towards higher values and as a result the allowed range shifts towards the right.

To check the compatibility of the two data sets, we have calculated the parameter goodness of fit for  $\theta_{23}$  and  $\Delta m_{32}^2$  with both hypothesis. For  $\theta_{23}$ , the parameter goodness of fit is 90% for the standard oscillation and 97% for the decay case. For the measurement of  $\Delta m_{32}^2$ , the parameter goodness of fit is 43% for the standard case and 57 % for the decay case. In both cases, the decay is fitting the data better than the standard case.

### 6.3 Invisible neutrino decay at DUNE and its effect on $\theta_{23}$ measurement

In this section we study the constraints on  $\tau_3/m_3$  from simulated data of the DUNE experiment assuming invisible decay of the neutrinos [143]. We perform a full three flavor study and include the matter effect during the propagation of the neutrinos through the Earth. We obtain constraints on the life time of the unstable state from the simulated

DUNE data. For obtaining this we assume the state  $\nu_3$  to be unstable and obtain the constraints on  $\tau_3/m_3$ . We also study the discovery potential and precision of measuring  $\tau_3/m_3$  at DUNE assuming decay is present in nature. In addition, we explore how the decay lifetime  $\tau_3$  is correlated with the mixing angle  $\theta_{23}$  leading to approximate degeneracy between the two parameters. We will study how this affects the sensitivity of DUNE to the mixing angle  $\theta_{23}$  and its octant. The sensitivity of DUNE, to determine the standard oscillation parameters like the mass hierarchy and  $\delta_{CP}$  could also in principle get affected if the heaviest state is unstable, and we study this here.

### 6.3.1 Experiment and simulation details

We use the GLoBES package [81, 82] to simulate the DUNE experiment. In our simulation, we have used neutrino and antineutrino flux from a 120 GeV, 1.2 MW proton beam at Fermilab and a 40 kt far detector. All our simulations are for a runtime of 5+5 years (5 years in  $\nu$  and 5 years in  $\bar{\nu}$ ) and we take both appearance and disappearance channels into account, unless otherwise stated. For the charged current (CC) events we have used 20% energy resolution for the  $\mu$  and 15% energy resolution for the  $e$ .

The primary background to the electron appearance and muon disappearance signal events come from the neutral current (NC) background and the intrinsic  $\nu_e$  contamination in the flux. In addition, there is a wrong-sign component in the flux. The problem of wrong-sign events is severe for the antineutrino run, since the neutrino component in the antineutrino flux is larger than the antineutrino component in the neutrino flux. We have taken all these backgrounds into account in our analyses. In order to reduce the backgrounds, several cuts are taken. The effects of these cuts have been imposed in our simulation through efficiency factor of the signal. We have included 2% (10%) signal (background) normalization errors and 5% energy calibration error as systematic uncertainties. The full detector specification can be found in Ref. [27] and we have closely followed it. A final comment on our treatment of the NC backgrounds is in order. Since

neutrino decay is a non-unitary phenomenon, we expect that the NC events at DUNE would be impacted depending on the decay lifetime. Hence, one would expect that the NC background too would depend on the decay lifetime. However, we have checked that for standard three-generation oscillations, the NC background is 71 events out of a total of 347 background events. In presence of decay ( $\tau_3/m_3 = 1.2 \times 10^{-11}$  s/eV), the NC background changes to 65, while the total background is 338. This implies that the NC background changes by about 8.5% only. We have also checked that including decay in the NC background changes the  $\chi^2$  only in the first place in decimal and is not even visible in the plots. Hence, for simplicity we keep the NC background fixed at the standard value.

Throughout this paper we use the following true values for the standard oscillation parameters:  $\theta_{12} = 34.8^\circ$ ,  $\theta_{13} = 8.5^\circ$ ,  $\Delta m_{21}^2 = 7.5 \times 10^{-5}$  eV,  $\Delta m_{31}^2 = 2.457 \times 10^{-3}$  eV and  $\delta_{CP} = -90^\circ$ . The true value of  $\theta_{23}$  will be specified for every plot that we will present. We marginalize our  $\chi^2$  over  $\theta_{13}$ ,  $\theta_{23}$ ,  $\delta_{CP}$  and  $\Delta m_{31}^2$ , which are allowed to vary within their allowed  $3\sigma$  ranges. We add a Gaussian prior on  $\theta_{13}$  with the current  $1\sigma$  range on this parameter. We keep the hierarchy normal in the simulated data for all the results presented in this paper. In this paper we have used “true” to specify the parameters used for generating the simulated data and “test” to specify the parameters in the fit.

### 6.3.2 Numerical results

We will first present results on how well DUNE will be able to constrain or discover the lifetime of the unstable  $\nu_3$  state. We will then turn our focus on how the measurement of standard oscillation physics at DUNE might get affected if  $\nu_3$  were to be unstable.

#### 6.3.2.1 Constraining the $\nu_3$ lifetime

The left panel of Fig. 6.9 shows the potential of DUNE to constrain the lifetime of  $\nu_3$  normalized to its mass  $m_3$ . In order to obtain this curve we generate the data for a no-

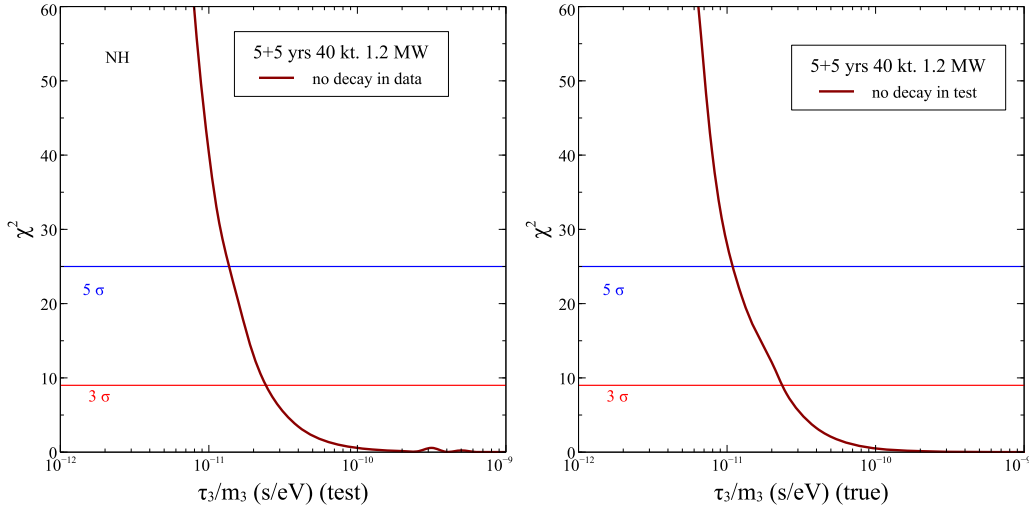


Figure 6.9: The left panel of this figure shows the expected sensitivity of DUNE to constraining the decay parameter  $\tau_3/m_3$ . The right panel of this figure presents the potential of DUNE to discover a decaying  $\nu_3$ . See text for details.

decay case and fit this data for an unstable  $\nu_3$ . The data was generated at the values of oscillation parameters given in subsection III and  $\theta_{23} = 42^\circ$ . We marginalize the  $\chi^2$  over all standard oscillation parameters as mentioned above. We see that at the  $3\sigma$  level DUNE could constrain  $\tau_3/m_3 > 2.38 \times 10^{-11}$  s/eV, whereas at 90% C.L. the corresponding expected limit would be  $\tau_3/m_3 > 4.50 \times 10^{-11}$  s/eV. This can be compared with the current limit on  $\tau_3/m_3 > 2.8 \times 10^{-12}$  s/eV that we have from combined MINOS and T2K analysis [187]. Therefore, DUNE is expected to improve the bounds on  $\nu_3$  lifetime by at least one order of magnitude.<sup>2</sup> The right panel of Fig. 6.9 shows the discovery potential of a decaying neutrino at DUNE. To obtain this curve we generated the data taking a decaying  $\nu_3$  into account and fitted it with a theory for stable neutrinos. True value of  $\theta_{23} = 42^\circ$  for this plot and the other oscillation parameters are taken as before. The  $\chi^2$  so obtained is then marginalized over the standard oscillation parameters in the fit. The resultant marginalized  $\chi^2$  is shown in the right panel of Fig. 6.9 as a function of the  $\tau_3/m_3(\text{true})$ . DUNE is expected to discover a decaying neutrino at the  $3\sigma$  C.L. for  $\tau_3/m_3 > 2.38 \times 10^{-11}$  s/eV and the 90% C.L. for  $\tau_3/m_3 > 4.27 \times 10^{-11}$  s/eV.

<sup>2</sup>Note that by the time DUNE will be operative, the current experiments would have improved their statistics and hence bounds on standard and non-standard parameters. Even then after the full run of these experiments, DUNE will have more sensitivity compared to the full run of NOvA and T2K [191].

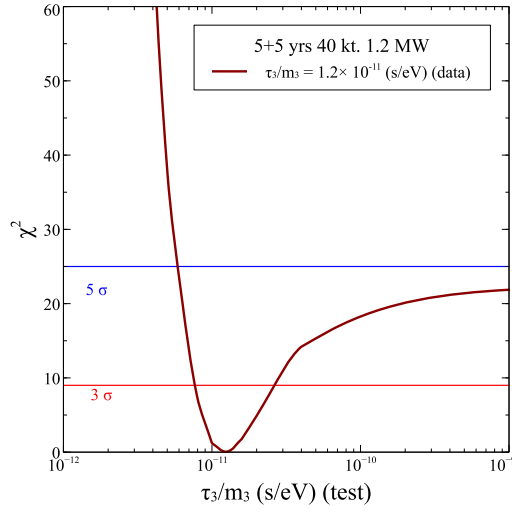


Figure 6.10: The  $\chi^2$  as a function of  $\tau_3/m_3(\text{test})$ , showing the precision with which  $\tau_3/m_3$  could be measured at DUNE when its true value is  $1.2 \times 10^{-11}$  s/eV.

Assuming that the  $\nu_3$  is indeed unstable with a decay width corresponding to  $\tau_3/m_3 = 1.2 \times 10^{-11}$  s/eV, we show in Fig. 6.10 how well DUNE will be able to constrain the lifetime of the decaying  $\nu_3$ . It is seen from the figure that in this case not only can DUNE exclude the no decay case above  $3\sigma$ , but can also measure the value of the decay parameter with good precision. The corresponding  $3\sigma$  and 90% C.L. ranges are  $2.63 \times 10^{-11} > \tau_3/m_3 > 7.62 \times 10^{-12}$  and  $1.71 \times 10^{-11} > \tau_3/m_3 > 9.29 \times 10^{-12}$  in units of s/eV, respectively.

### 6.3.2.2 Constraining $\theta_{23}$ and its octant

Fig. 6.11 gives the neutrino oscillation probability for both the appearance and disappearance channels. The left panels give the probability for the appearance channel while the right panels show the probability for the disappearance channel. The top panels show the impact of decay on the probabilities for  $\tau_3/m_3 = 1.2 \times 10^{-11}$  s/eV while the bottom panels show the effect when  $\tau_3/m_3 = 1.0 \times 10^{-12}$  s/eV. The solid lines and the short-dashed lines show the probabilities for the standard stable case. The blue solid lines in all the four panels are for  $\theta_{23} = 42^\circ$  and  $\theta_{13} = 8.5^\circ$  and no decay. The change in the probabilities when decay is switched on for the same set of oscillation parameters is shown in all the

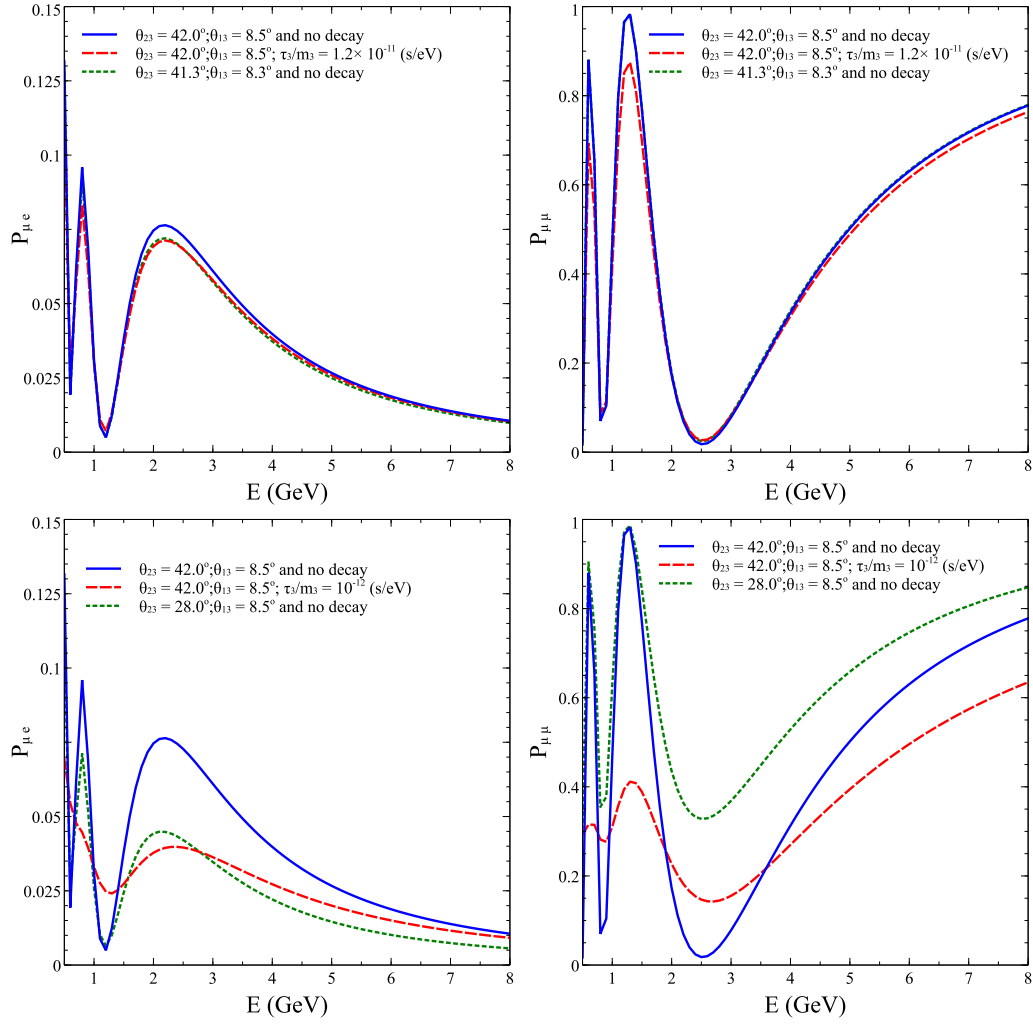


Figure 6.11: The appearance (left panels) and disappearance (right panels) channel neutrino probabilities as a function of neutrino energy. The different lines are described in the legends and also in the text. The top panels show the effect of  $\nu_3$  decay for a larger value of  $\tau_3/m_3$  while the bottom panels show the effect for a smaller value of  $\tau_3/m_3$ .

panels by the red long-dashed line. The first thing to note from this figure is that  $P_{\mu e}$  decreases while  $P_{\mu\mu}$  increases at the oscillation maximum. The opposite trend is seen for the case when the oscillatory term goes to zero. However, net probability for both appearance as well as disappearance channels decrease in the case of decay. This is because in our model the  $\nu_3$  decays to invisible states which do not show-up at the detector. As expected, the extent of decrease of the probability increases as we lower  $\tau_3/m_3$  or in other words increase the decay rate, as can be seen by comparing the top panels with the bottom ones. For  $\tau_3/m_3 = 1.0 \times 10^{-12}$  s/eV we see a drastic change in the probability plots,



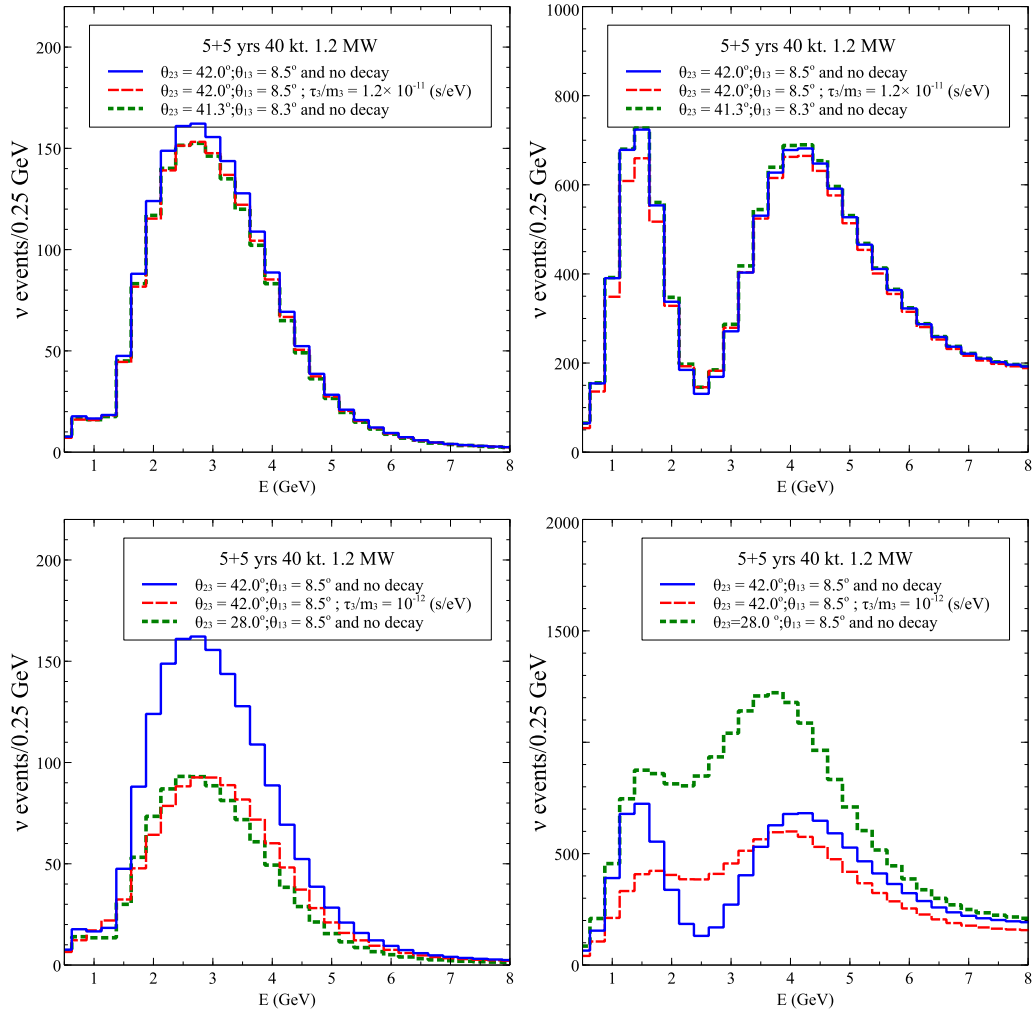


Figure 6.12: Same as in Fig. 6.11 but showing neutrino events at DUNE instead of probabilities. The left panels show the electron appearance events, while the right panels show the muon disappearance events. The top panels show the impact of a larger  $\tau_3/m_3$ , while the bottom panels are for a smaller  $\tau_3/m_3$ .

thereby allowing DUNE to restrict these values of  $\tau_3/m_3$ , as we had seen in the previous subsection.

Next we turn to show the correlation between the decay lifetime  $\tau_3/m_3$  and the mixing angles, in particular, the mixing angle  $\theta_{23}$ . In Fig. 6.11 we show that the appearance channel probability  $P_{\mu e}$  for the case with decay (shown by the red long-dashed lines) can be mimicked to a large extent by the no decay scenario if we reduce the value of  $\theta_{23}$ . These probability curves are shown by the green short-dashed lines. For the top panels

we can achieve reasonable matching between the decay and no decay scenario if the  $\theta_{23}$  is reduced from  $42^\circ$  to  $41.3^\circ$  and  $\theta_{13}$  is slightly changed from  $8.5^\circ$  to  $8.3^\circ$ . The matching is such that the green dashed lines is hidden below the red dashed lines in the top panels. In the lower panels, since the  $\nu_3$  lifetime is chosen to be significantly smaller, we see a more drastic effect of  $\theta_{23}$ . In the lower panels the with decay case for  $P_{\mu e}$  at  $\theta_{23} = 42^\circ$  can be somewhat matched by the no decay case if we take a much reduced  $\theta_{23} = 28^\circ$ . However, the disappearance channel is not matched between the red long-dashed and green short-dashed line for the value of  $\theta_{23}$  that is needed to match the appearance channel for the decay and no decay cases.

This correlation between  $\tau_3/m_3$  and  $\theta_{23}$  in  $P_{\mu e}$  can be understood as follows. No decay corresponds to infinite  $\tau_3/m_3$ . As we reduce  $\tau_3/m_3$ ,  $\nu_3$  starts to decay into invisible states reducing the net  $P_{\mu e}$  around the oscillation maximum. This reduction increases as we continue to lower  $\tau_3/m_3$ . On the other hand, it is well known that  $P_{\mu e}$  increases linearly with  $\sin^2 \theta_{23}$  at leading order. Therefore, it is possible to obtain a given value of  $P_{\mu e}$  either by reducing  $\tau_3/m_3$  or by reducing  $\sin^2 \theta_{23}$ . Therefore, it will be possible to compensate the decrease in  $P_{\mu e}$  due to decay by increasing the value of  $\sin^2 \theta_{23}$ . Hence, if we generate the appearance data taking decay, we will be able to fit it with a theory for stable neutrinos by suitably reducing the value of  $\sin^2 \theta_{23}$ .

The correlation between  $\tau_3/m_3$  and  $\theta_{23}$  for the survival channel on the other hand is complicated. For simplicity, let us understand that within the two-generation framework first, neglecting matter effects. The effect of three-generations will be discussed a little later and the effect of earth matter is not crucial for the DUNE energies in this discussion. The survival probability in the two-generation approximation is given by [187]

$$P_{\mu\mu}^{2G} = \left[ \cos^2 \theta_{23} + \sin^2 \theta_{23} e^{-\frac{m_3 L}{\tau_3 E}} \right]^2 - \sin^2 2\theta_{23} e^{-\frac{m_3 L}{2\tau_3 E}} \sin^2 \left( \frac{\Delta m_{31}^2 L}{4E} \right). \quad (6.6)$$

The Eq. (6.6) shows that decay affects both the oscillatory term as well as the constant term in  $P_{\mu\mu}$ , causing both to reduce. Therefore, it is not difficult to see that with decay

included, the value of  $\theta_{23}$  should be increased to get the same  $P_{\mu\mu}$  as in the no decay case. Hence, in this case again if we generate the disappearance data taking decay, we will be able to fit it with a theory for stable neutrinos by suitably reducing the value of  $\theta_{23}$ . However, note that the dependence of  $P_{\mu\mu}$  on  $\theta_{23}$  and  $\tau_3/m_3$  is different from the dependence of  $P_{\mu e}$  on  $\theta_{23}$  and  $\tau_3/m_3$  and hence we never get the same fitted value of  $\theta_{23}$  for the two channels. This is evident in Fig. 6.11 where in the lower panel the appearance probability fits between decay case and  $\theta_{23} = 42^\circ$  and no decay case and  $\theta_{23} = 28^\circ$ . However, this does not fit the disappearance probability simultaneously. One can check that the above understanding of the correlation between  $\theta_{23}$  and  $\tau_3/m_3$  is true for the full three-generation case too. We will show below the probabilities for the full three-generation case with decay and matter effects obtained by an exact numerical computation.

In order to see the correlation between  $\tau_3/m_3$  and  $\theta_{23}$  at the event level, we plot in Fig. 6.12 the appearance (electron) and disappearance (muon) events for 5 years of running of DUNE in the neutrino channel. One will expect a similar behaviour for the antineutrinos as well. The respective panels and the three plots in each panel are arranged in exactly the same way as in Fig. 6.11. We note that all the features that were visible at the probability level in Fig. 6.11 are also seen clearly at the events level in Fig. 6.12. Neutrino events are seen to reduce with the onset of neutrino decay, with the extent of reduction increasing sharply with the value of the decay rate ( $1/\tau_3$ ). The electron event spectrum for the case with decay can be seen to be roughly mimicked with that without decay but with a lower value of the  $\theta_{23}$ , the required change in the value of  $\theta_{23}$  increasing with the decay rate ( $1/\tau_3$ ). On the other hand for the lower panel, the muon spectrum in absence of decay (shown by the green lines) would need a different value of  $\theta_{23}$  to match the muon spectrum in presence of decay (shown by the red lines). This mismatch between the fitted value of  $\theta_{23}$  between the appearance and disappearance channels can hence be expected to be instrumental in breaking the approximate degeneracy between  $\tau_3/m_3$  and  $\theta_{23}$ .

In order to study the impact of decay on the expected  $\theta_{23}$  sensitivity of DUNE, we

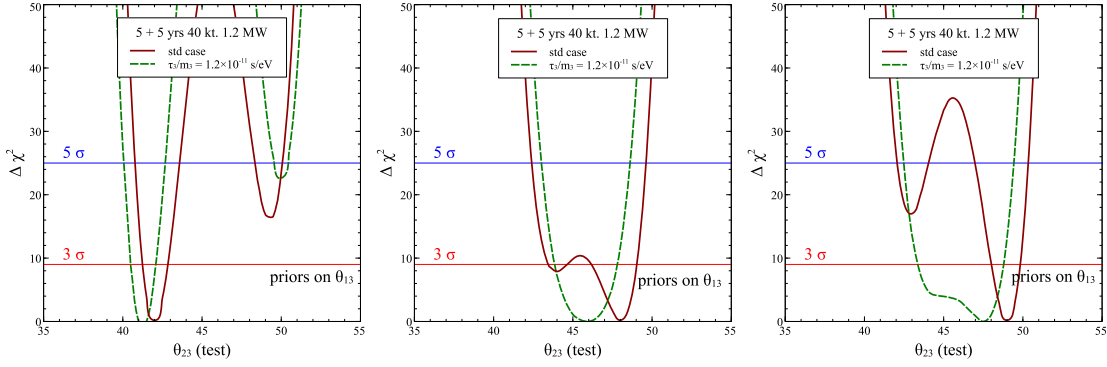


Figure 6.13:  $\chi^2$  as a function of  $\theta_{23}(\text{test})$ . The left, middle and right panels are for the cases when the data is generated at  $\theta_{23} = 42^\circ$ ,  $\theta_{23} = 48^\circ$  and  $\theta_{23} = 49.3^\circ$ , respectively. The dark red solid curves are for the standard case when both data and fit are done within the three-generation framework of stable neutrinos. The green dashed curves are for the case when the data is generated for unstable  $\nu_3$  with  $\tau_3/m_3 = 1.2 \times 10^{-11}$  s/eV but it is fitted assuming stable neutrinos.

show in Fig. 6.13 the  $\chi^2$  as a function of  $\theta_{23}(\text{test})$ . The left panel is for the case when the data is generated at  $\theta_{23} = 42^\circ$ , middle panel is for data at  $\theta_{23} = 48^\circ$  and the right panel is for data at  $\theta_{23} = 49.3^\circ$ . The dark red solid curves are for the standard case when both data and fit are done within the three-generation framework of stable neutrinos. The green dashed curves are for the case when the data is generated for unstable  $\nu_3$  with  $\tau_3/m_3 = 1.2 \times 10^{-11}$  s/eV but it is fitted assuming stable neutrinos. For generating the data all other oscillation parameters are taken as mentioned before in subsection III. The fits are marginalised over  $\theta_{13}$ ,  $\delta_{CP}$  and  $\Delta m_{31}^2$  in their current  $3\sigma$  ranges. Before we proceed to look at the impact of decay on the measurement of  $\theta_{23}$  at DUNE, let us expound some features of  $\theta_{23}$  for standard three-generation oscillation scenario. A comparison of the red curves in the three panels of Fig. 6.13 shows that the left panel and the right panel look like near mirror images of each other, while the middle panel looks different. Note that  $42^\circ$  is as far removed from  $\theta_{23} = 45^\circ$  as  $48^\circ$ , however the  $\chi^2$  curves for the  $\theta_{23} = 42^\circ$  and  $\theta_{23} = 48^\circ$  cases appear different. This is due to three-generation effects coming from the non-zero  $\theta_{13}$  [202]. The values of  $\theta_{23}$  in HO and LO that correspond to the same effective

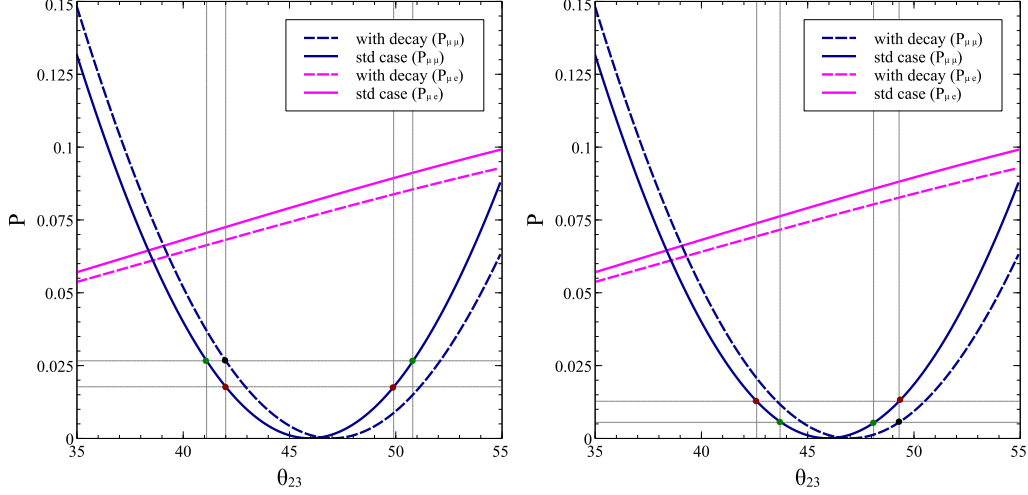


Figure 6.14: The probabilities  $P_{\mu\mu}$  (blue lines) and  $P_{\mu e}$  (magenta lines), shown as a function of  $\theta_{23}$ . The plots have been drawn for the DUNE baseline and  $E = 2.5$  GeV, taking all oscillation parameters as mentioned in subsection III. The left and right panels are identical apart from the horizontal and vertical lines which show the probabilities for the cases when the data is generated at  $\theta_{23} = 42^\circ$  (left panel) and  $\theta_{23} = 49.3^\circ$  (right panel). The solid curves show the probabilities for the standard case while the dashed curves are for the case for unstable  $\nu_3$  with  $\tau_3/m_3 = 1.2 \times 10^{-11}$  s/eV. The probabilities are shown for the full three-generation framework including earth matter effect. The black dot shows the point at which data is generated for the decay case, while the green dots show the points which give the same  $P_{\mu\mu}$  as the black dot, but for the standard case. The red dots show the  $P_{\mu\mu}$  for the data generated for the standard case at  $\theta_{23} = 42^\circ$  (left panel) and  $\theta_{23} = 49.3^\circ$  (right panel) and the corresponding fake minima when fitted by the standard case.

mixing angle  $\theta_{\mu\mu}$  and which gives the same  $P_{\mu\mu}$  are given as [202]

$$\sin \theta_{23}^{LO} = \frac{\sin \theta_{\mu\mu}^{LO}}{\cos \theta_{13}} \quad ; \quad \sin \theta_{23}^{HO} = \frac{\sin \theta_{\mu\mu}^{HO}}{\cos \theta_{13}} \quad (6.7)$$

$$\theta_{\mu\mu}^{LO} = 90^\circ - \theta_{\mu\mu}^{HO} , \quad (6.8)$$

which gives  $\theta_{23} = 49.3^\circ$  as the mixing angle that gives the same  $P_{\mu\mu}$  as  $\theta_{23} = 42^\circ$  instead of  $\theta_{23} = 48^\circ$ , as we would expect in the two-generation case. In order to further illustrate this point, we show in Fig. 6.14 the survival probability  $P_{\mu\mu}$  (blue lines) as a function of  $\theta_{23}$  for the standard case (solid line) and decay case (dashed line). Also shown are the corresponding oscillation probability  $P_{\mu e}$  (magenta lines) for the standard case (solid line) and decay case (dashed line). The plots have been drawn for the DUNE baseline and

$E = 2.5$  GeV, taking all oscillation parameters as mentioned in subsection III. The energy 2.5 GeV corresponds to oscillation maximum at the DUNE baseline where the DUNE flux peaks. We note that for the standard oscillations case,  $P_{\mu\mu} \simeq 0$  corresponds to a value of  $\theta_{23} \simeq 46^\circ$  and not  $45^\circ$  as in the two-generation case. We also note that  $P_{\mu\mu}$  at  $\theta_{23} = 42^\circ$  in LO is matched by the  $P_{\mu\mu}$  at  $\theta_{23} \simeq 49.9^\circ$  in HO, the small difference between the value of  $\theta_{23}^{HO}$  derived from Eq. (6.8) and the exact numerical results shown in Fig. 6.14 come from earth matter effects mainly.

The solid red curves in Fig. 6.13 showing the  $\chi^2$  vs.  $\theta_{23}(\text{test})$  for the standard oscillation case match well with the solid blue probability curves in Fig. 6.14. For the left panel, data is generated at  $\theta_{23} = 42^\circ$  and the absolute and fake minima come at  $\theta_{23}(\text{test}) = 42^\circ$  and  $49.5^\circ$ , respectively. On the other hand for the right panel, data is generated at  $\theta_{23} = 49.3^\circ$  and the absolute and fake minima come at  $\theta_{23}(\text{test}) = 49.3^\circ$  and  $43.0^\circ$ , respectively. Note that since  $P_{\mu\mu}$  is nearly matched at the true and fake minima points, the disappearance data would return a  $\chi^2 \simeq 0$  at both the true as well as fake minima points giving an exact octant degeneracy. The main role of the disappearance data is only to determine the position of the minima points in  $\theta_{23}$ . The oscillation probability  $P_{\mu e}$  on the other hand is very different between the true and fake minima points as can be seen from the solid magenta line in Fig. 6.14. Hence, the appearance channel distinguishes between the two and gives a non-zero  $\chi^2$  at the fake minima and breaks the octant degeneracy. We can see from Fig. 6.13 that for the  $\theta_{23} = 42^\circ$  case (left panel), the  $\chi^2$  corresponding to the wrong octant minima is 16.6 while for  $\theta_{23} = 49.3^\circ$  case (right panel) it is 17.1. Hence, for standard oscillation the octant sensitivity at  $\theta_{23} = 42^\circ$  is only slightly worse than the octant sensitivity at  $\theta_{23} = 49.3^\circ$ . The reason for this is that the  $\chi^2$  for octant sensitivity is given in terms of the difference between the appearance channel event spectra for the true and fake  $\theta_{23}$  points. One can see from the solid magenta lines in Fig. 6.14 that this difference is almost the same for the left and right panels for the standard oscillations case and hence the  $\chi^2$  of the fake minima for the solid red lines in the left and right panels in Fig. 6.13 are nearly the same. The octant sensitivity for the

middle panel ( $\theta_{23} = 48^\circ$ ) is significantly poorer since for this case, the difference in the appearance channel probability is much smaller. This happens because this value of  $\theta_{23}$  is too close to effective maximal mixing for  $P_{\mu\mu}$  (cf. Eqs. (6.7 and (6.8)).

Next we look at the impact of including neutrino decay in data on  $\theta_{23}$  measurement at DUNE, shown by the green dashed lines in Fig. 6.13. These lines are obtained by generating data including decay but fitting them with standard three-generation oscillations with stable neutrinos. We notice that compared to the red solid lines for the standard case, the position of minima as well as the  $\chi^2$  at the fake minima have changed. For the left panel ( $\theta_{23} = 42^\circ$  in data) the minima points shift to  $\theta_{23}(\text{test}) = 41.0^\circ$  in LO and  $\theta_{23}(\text{test}) = 50.0^\circ$  in HO. Thus, for data with  $\theta_{23}$  in LO, the minima point shifts to lower  $\theta_{23}(\text{test})$  in LO and higher  $\theta_{23}(\text{test})$  in HO. On the other hand for right panel ( $\theta_{23} = 49.3^\circ$  in data) the minima points shift to  $\theta_{23}(\text{test}) = 44.5^\circ$  in LO and  $\theta_{23}(\text{test}) = 47.5^\circ$  in HO. Thus, for data with  $\theta_{23}$  in HO, the minima point shifts to higher  $\theta_{23}(\text{test})$  in LO and lower  $\theta_{23}(\text{test})$  in HO. Note that none of the minima now correspond to the true value of  $\theta_{23}$  at which the data is generated. Note also that the gap between the two minima points has increased for the case with data in LO and decreased for the case with data in HO.

The shifting of minima for both the LO and HO data points can be understood easily in terms of the left and right panels of Fig. 6.14, respectively. This figure shows  $P_{\mu\mu}$  (and  $P_{\mu e}$ ) at the oscillation maximum as a function of  $\theta_{23}$ . The solid lines are for no decay while the dashed lines are for decay and oscillations. An important thing we can note in this figure is that with decay the  $P_{\mu\mu}$  curve gets shifted towards the right. Even the effective maximal mixing point gets shifted further towards higher values of  $\theta_{23}$ . The left panel of Fig. 6.14 shows the data point for the disappearance channel for  $\theta_{23} = 42^\circ$  by the black point on the blue dashed line, which includes decay. This  $P_{\mu\mu}$  has to be reproduced by the no decay theory in the fit. The corresponding minima points can be obtained by following the blue solid line and are shown by the green dots, at  $\theta_{23} = 41.1^\circ$  and  $\theta_{23} = 50.8^\circ$ . This matches well with the minima on the green dashed line in the left panel of Fig. 6.13. The

point where data is generated for the HO case in Fig. 6.13 is shown by the black dot in the right panel of Fig. 6.14. The corresponding fit points coming from  $P_{\mu\mu}$  can be seen at the green dots in this panel at  $\theta_{23} = 43.7^\circ$  and  $\theta_{23} = 48.1^\circ$ . Note that since the decay causes the  $P_{\mu\mu}$  curve to shift towards the right, all minima points in  $\theta_{23}$  are shifted towards the left. However, when one compares the minima in the true and fake octants, it turns out that the two minima get further separated for the LO case (left panel), while for the HO case (right panel) they come closer together. This is consistent with the gap between the minima increasing for the left panel and decreasing for the right panel in Fig. 6.13. As mentioned before, the disappearance data plays the role of determining the minima in the true and fake octant, but brings no significant octant sensitivity since  $P_{\mu\mu}$  can be matched at the true and fake minima, at least at the oscillation maximum. The octant sensitivity comes from the difference in the number of appearance events at the minima points at the true and fake octant. Therefore, since the minima points in the LO case gets further separated for the decay case compared to no decay, the octant sensitivity for LO increases as can be seen from the  $P_{\mu e}$  curve in Fig. 6.14. We can read from the left panel of Fig. 6.13 that the  $\chi^2$  at the minima in the fake octant is 22.6, higher than the case for standard oscillations. On the other hand for the right panel, the minima points come closer in the case of the dashed green lines and the octant sensitivity coming from the appearance channel drops significantly to  $\chi^2 = 4.1$  for the wrong octant since the difference in  $P_{\mu e}$  between the minima points reduces, as can be seen from the right panel of Fig. 6.14.

The impact of decay on the expected constraints in the two-dimensional  $\theta_{23} - \theta_{13}$  plane is shown in Fig. 6.15. As in Fig. 6.13, the left panel shows the results when the data is generated at  $\theta_{23} = 42^\circ$ , middle panel is for  $\theta_{23} = 48^\circ$ , while the right panel gives the results for data corresponding to  $\theta_{23} = 49.3^\circ$ . The point where the data is generated is marked by a star in the  $\theta_{23} - \theta_{13}$  plane. The expected contours correspond to  $3\sigma$  C.L. The dark red solid lines are obtained for the standard case when neutrinos are taken as stable in both the data as well as the fit. The green dashed ones are obtained when we simulate the data assuming an unstable  $\nu_3$  with  $\tau_3/m_3 = 1.2 \times 10^{-11}$  s/eV, but fit it with the standard



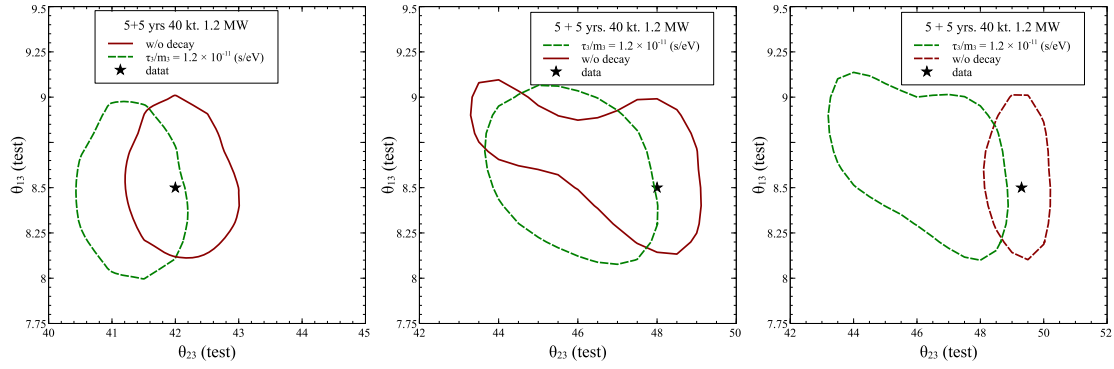


Figure 6.15: The plots show the expected  $3\sigma$  C.L. contours in the  $\theta_{23} - \theta_{13}$  plane for the case when the data is simulated at  $\theta_{23} = 42^\circ$  (left panel),  $\theta_{23} = 48^\circ$  (middle panel), and  $\theta_{23} = 49.3^\circ$  (right panel). The value of  $\theta_{13} = 8.5^\circ$  in all panels. The black stars show the data points in the plane. The dark red solid curves show the expected  $3\sigma$  contour for the standard scenario in absence of decay in data and theory. The green dashed curves show the  $3\sigma$  contour for the case when the data corresponds to a decaying  $\nu_3$  with  $\tau_3/m_3 = 1.2 \times 10^{-11}$  s/eV, which is fitted with a theory where all neutrinos are taken as stable.

case assuming stable neutrinos. The contours are marginalized over test values of  $\delta_{CP}$  and  $\Delta m_{31}^2$  within their current  $3\sigma$  ranges. The impact of decay is visible in all panels. Though the contours change in both mixing angles, the impact on  $\theta_{23}(\text{test})$  is seen to be higher than the impact on  $\theta_{13}(\text{test})$ . As we had seen in details above in Fig. 6.13, the green contours are shifted to lower values of  $\theta_{23}$  in both the left and right panels. The one-to-one correspondence between the allowed  $\theta_{23}(\text{test})$  values at  $3\sigma$  between this figure and Fig. 6.13 can be seen. The mild anti-correlation between the allowed values of  $\theta_{23}(\text{test})$  and  $\theta_{13}(\text{test})$  for the green dashed lines comes mainly from the appearance channel which depends on the product of  $\sin^2 \theta_{23} \sin^2 2\theta_{13}$  at leading order. This anti-correlation is seen to be more pronounced for the middle and right panels because for these cases the  $\theta_{23}$  sensitivity of the data falls considerably in presence of decay and the  $\chi^2$  drops.

The Fig. 6.16 shows the octant sensitivity for 5+5 years of  $(\nu + \bar{\nu})$  running of DUNE. The dark-red solid curve shows the octant sensitivity for the standard case with stable neutrinos. The green dashed curve is for the case when  $\nu_3$  is taken as unstable with  $\tau_3/m_3 = 1.2 \times 10^{-11}$  s/eV in the data, but in the fit we keep it to be stable. We note that the octant sensitivity of DUNE improves for the green dashed line in the lower octant, but in

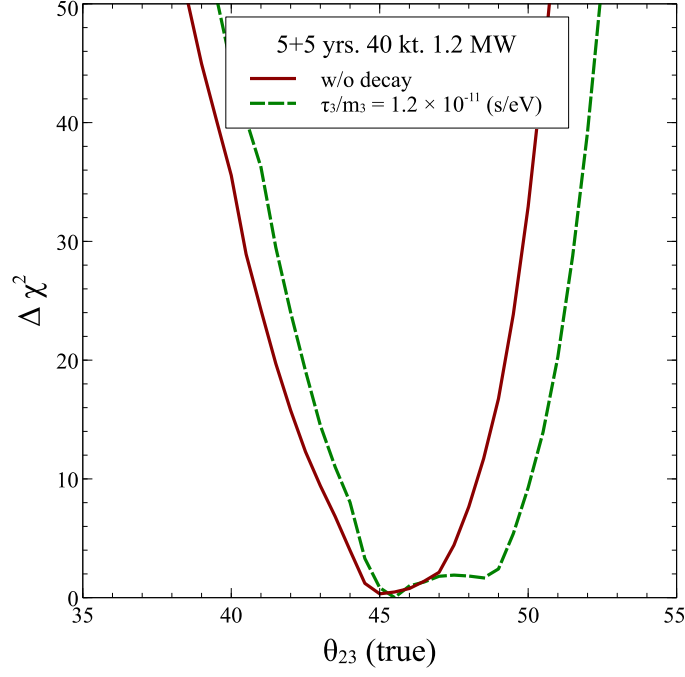


Figure 6.16: Expected octant sensitivity at DUNE. The dark red solid curve is for standard case of stable neutrinos. The green dashed curve is for the case when  $\nu_3$  is taken as unstable with  $\tau_3/m_3 = 1.2 \times 10^{-11}$  s/eV in the data, but in the fit we keep it to be stable.

the higher octant it deteriorates. This is consistent with our observations in Fig. 6.13. For detailed explanation of this, we refer the reader to the detailed discussion above.

### 6.3.2.3 CP-violation and mass hierarchy sensitivity

In Fig. 6.17 we show the expected CP-violation sensitivity at DUNE. As before, the dark red solid curve is for standard case of stable neutrinos. The green dashed curve is for the case when  $\nu_3$  is taken as unstable with  $\tau_3/m_3 = 1.2 \times 10^{-11}$  s/eV in the data, but in the fit we keep it to be stable. The data was generated at the values of oscillation parameters given in subsection III and  $\theta_{23} = 42^\circ$ . Decay in the data is seen to bring nearly no change to the CP-violation sensitivity of DUNE, with only a marginal increase in the CP-violation sensitivity seen at  $\delta_{CP}(\text{true}) \simeq \pm 90^\circ$ .

The impact of decay on the expected mass hierarchy sensitivity at DUNE is shown in Fig. 6.18 for both normal hierarchy (NH) true (left panel) and inverted hierarchy (IH)

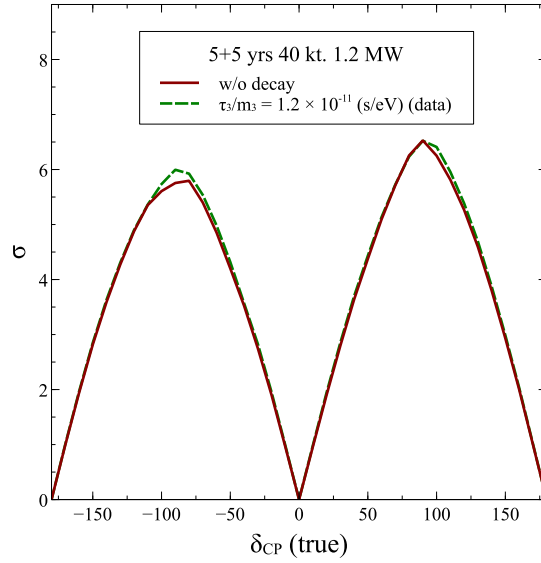


Figure 6.17: Expected CP-violation sensitivity at DUNE. The dark red solid curve is for standard case of stable neutrinos. The green dashed curve is for the case when  $\nu_3$  is taken as unstable with  $\tau_3/m_3 = 1.2 \times 10^{-11}$  s/eV in the data, but in the fit we keep it to be stable.

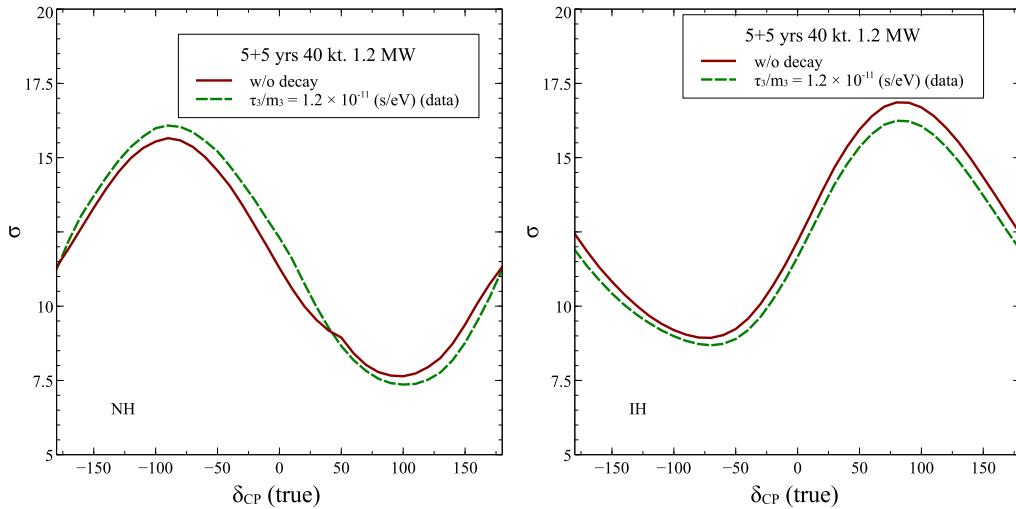


Figure 6.18: Expected mass hierarchy sensitivity at DUNE. The dark red solid curve is for standard case of stable neutrinos. The green dashed curve is for the case when  $\nu_3$  is taken as unstable with  $\tau_3/m_3 = 1.2 \times 10^{-11}$  s/eV in the data, but in the fit we keep it to be stable. The left panel is for NH true while the right panel is for IH true.

true (right panel ). As in all figures shown so-far, the dark red solid curve is for standard case of stable neutrinos. The data was generated at the values of oscillation parameters given in subsection III and  $\theta_{23} = 42^\circ$ . The green dashed curve is for the case when  $\nu_3$  is taken as unstable with  $\tau_3/m_3 = 1.2 \times 10^{-11}$  s/eV in the data, but in the fit we keep it to be stable. For IH true, the effect of decay in data is to marginally reduce the expected mass hierarchy sensitivity for all values of  $\delta_{CP}(\text{true})$ . The impact for the NH true case is more complicated with the expected sensitivity increasing for some values of  $\delta_{CP}(\text{true})$  and decreasing for others. However, the net change in the expected sensitivity is seen to be very small compared to the expected mass hierarchy sensitivity at DUNE. Therefore, we conclude that the expected CP-violation sensitivity and mass hierarchy sensitivity at DUNE remain largely unmodified, whether or not neutrinos decay.

## Conclusions and Future Prospects

### 7.1 Conclusions

In this thesis, we have looked at various new physics scenarios in the context of long-baseline experiments. We have done our analysis for both present experiments (NOvA and T2K) and future experiments (DUNE, T2HK/T2HKK). For future experiments, we performed our analysis in two ways. In one case, we have tried to find the sensitivity of the experiments to the new physics and in the other case, we have studied the effects of the new physics on the standard performances of the experiments.

In chapter 2, we have discussed neutrino oscillations in both vacuum and matter. We also discussed various degeneracies present in neutrino oscillation followed by detailed discussion of various long-baseline experiments in chapter 3.

In chapter 4, we have discussed sterile neutrino in the context of long-baseline experiments. One of the widely discussed new physics scenarios is sterile neutrino. Short baseline experiments like LSND [113] and MiniBooNE [33, 34, 111] observed some excess in the electron appearance channels which could only be explained assuming oscillations driven by  $\Delta m^2 \sim 1 \text{ eV}^2$ . Since this is completely inconsistent with solar and atmospheric neutrino data, we need additional state(s) to explain this. However, the number of active neutrinos is precisely measured to be three from LEP [47]. So, these extra states are called

sterile. If there is only one extra state and it is consistent with both solar and atmospheric mass splitting, it is then called 3+1 scenario. Later, data from many experiment came but they could not give any conclusive result till now and there is tension between various datasets and global fits give very poor goodness of fit [120].

We have explored reach of DUNE near detector to probe the parameter space of LSND [106]. At short baseline like the DUNE near detector, oscillations due to solar and atmospheric splitting do not arise, therefore, we have done our analyse in the effective two generation approximation ( $\Delta m^2, \theta_{\mu e}$ ). As the near detector design of DUNE is not yet final, we have played with various experimental parameters like baseline, mass, backgrounds. We considered three options for the baselines with mass fixed at 5 t: 595 m, 1 km and 3 km. It was observed that with increasing baseline, the sensitivity is increased at higher mixing angles and it is decreased at lower mixing angles and it was found that 595 m baseline gives the optimum sensitivity. We also considered three options for mass: 5 t, 400 t and 1 kt (baseline fixed at 595 m). With increasing mass, the sensitivity increases, however, it saturates above certain mass and becomes independent of statistics. We found that 5 t can almost entirely rule out the LSND parameter space at more than  $4\sigma$  in 5+5 years (5 years in neutrino and 5 years in antineutrino mode). We also studied the effect of systematic uncertainties like energy calibration error, flux normalization error and the effect of decay pipe length, but they do not have much effect on the sensitivity.

If sterile neutrino is present, the oscillation probabilities at the far detectors of the long-baseline experiments get modified and this can affect the standard physics program of the long-baseline experiments. We have considered effect of sterile neutrino in DUNE and T2HK/T2HKK and their combination [69]. The 4 generation oscillation needs six mixing angles and three CP violating phases. We have chosen the parameterization such that the two additional phases  $\delta_{24}$  and  $\delta_{34}$  comes with the angles  $\theta_{24}$  and  $\theta_{34}$  respectively. We investigated CP sensitivity, octant and mass-hierarchy in presence of sterile neutrino. For CP-violation we considered three cases. First, we assumed that we don't know the

source of CP-violation, then we assumed that the source of CP-violation is  $\delta_{13}$  and finally we assumed that the source is  $\delta_{24}$ . In all cases we considered two sets of sterile mixing angles:  $(\theta_{14}, \theta_{24}, \theta_{34}) = (6.5^\circ, 3.5^\circ, 12.5^\circ); (12.0^\circ, 7.0^\circ, 25.0^\circ)$  and varied the three phases from  $[-\pi, \pi]$ . For, the case of source of CP-violation being unknown, we found that for the smaller mixing angles, the CP sensitivity decreases for all combinations of true phases and for larger mixing angles the CP-sensitivity bands are spread on both sides of the the 3+0 curve. This is due to the fact that as the mixing angles increase, the effect of true phases are also increased. We found that while, T2HKK has slightly larger sensitivity than T2HK for 3+0 case, for the larger mixing case, both have almost same sensitivity. And for the combined case of T2HKK and DUNE, we see that the sensitivity is increased by significant amount. The sensitivity is increased more than  $10\sigma$  for some values of  $\delta_{CP}$  and for some combinations of  $\delta_{24}$  and  $\delta_{34}$  it is more than  $5\sigma$  for all values of  $\delta_{CP}$ . For the case, where we assumed that the source of CP is known and it is due to  $\delta_{13}$ , it is found that the CP-sensitivity slightly decreases for both the sets of smaller and larger mixing angles. For the other case, where the source of CP-violation is assumed to be known and due to  $\delta_{24}$ , the CP-sensitivity is reduced drastically. Here for T2HK and T2HKK, the band for the set of larger mixing angles the CP-sensitivity is almost always less than  $5\sigma$  and for the set of smaller mixing angles it is even worse as the sensitivity comes below  $3\sigma$ . However, we found that T2HKK+DUNE manages to get the sensitivity more than  $5\sigma$  for the larger mixing angles for some combinations of  $\delta_{13}$  and  $\delta_{34}$ . We studied the CP-sensitivity with the assumption of unknown mass-hierarchy. For this, we found that for both 3+0 and 3+1 case, the CP-sensitivity is reduced for T2HK whereas the sensitivity remains almost same for T2HKK and T2HKK+DUNE, as T2HKK and DUNE have long enough baseline to break hierarchy degeneracy by themselves. We also showed how the expected mass hierarchy sensitivity of T2HK, T2HKK and T2HKK+DUNE changes in the presence of sterile mixing. Here the effect of increasing the value of the sterile mixing angle was shown to have an interesting effect on the corresponding expected sensitivity of the T2HK and T2HKK set-ups. When the sterile mixing angles are taken to be small,

the neutrino mass hierarchy sensitivity of T2HK and T2HKK is seen to deteriorate in the 3+1 case compared to the 3+0 case, for some values of  $\delta_{13}(\text{true})$ ,  $\delta_{24}(\text{true})$  and  $\delta_{34}(\text{true})$ . However, when the sterile mixing angles were increased the mass hierarchy sensitivity of T2HK and T2HKK increased for nearly all values of  $\delta_{13}(\text{true})$ ,  $\delta_{24}(\text{true})$  and  $\delta_{34}(\text{true})$ . The reason for this behavior was traced to the effect of marginalisation over  $|\Delta m_{31}^2|$ . Finally, we presented the expected octant of  $\theta_{23}$  sensitivity of T2HK, T2HKK and T2HKK+DUNE in the 3+1 scenario. We showed at results for both choices of LO and HO and for two sets of true sterile mixing values and the full range of all the three phases  $\delta_{13}(\text{true})$ ,  $\delta_{24}(\text{true})$  and  $\delta_{34}(\text{true})$ . Again for this case, the expected octant sensitivity appears to be mostly decreasing in the 3+1 case compared to the 3+0 case when the mixing angles are small. But when the true sterile mixing angles are taken to be larger, the octant sensitivity is seen to improve for some sets of values of  $\delta_{13}(\text{true})$ ,  $\delta_{24}(\text{true})$  and  $\delta_{34}(\text{true})$ , especially for T2HKK and T2HKK combined with DUNE.

We looked for capabilities of future long-baseline experiments like DUNE and T2HK to constrain sterile CP phase [76]. In short baseline experiments, the oscillation is only due to  $\Delta m^2 \sim 1 \text{ eV}^2$ . Hence, in short-baseline experiments there is no phase dependence. However, in long-baseline experiments, all the mass-squared differences becomes active and this opens the possibility of exploration of sterile phase in long-baseline experiments. In particular  $\nu_e$  appearance probability in LBL (long-baseline) has  $\delta_{24}$  dependence. We used this channel to constrain  $\delta_{24}$  using DUNE, T2HK/T2HKK and their combination. The  $\delta_{34}$  dependence comes from the matter effect. As the matter effect for DUNE and T2HK/T2HKK are small, the  $\delta_{34}$  dependence is very small and we have not considered this in our work. We have considered 5+5 years of DUNE and 2.5+7.5 years of T2HK/T2HKK runtime. We study the sensitivity for measuring  $\delta_{24}$ . We considered  $\delta_{13} = -90^\circ$  in the data and  $\delta_{24} = 0^\circ, -90^\circ, 90^\circ, 180^\circ$  in the data. We found that T2HK will perform best compared to T2HKK and DUNE. This is due to the fact that T2HK has very high statistics compared to DUNE. When we combined DUNE and T2HK/T2HKK, the expected sensitivity is increased as seen in the  $\delta_{24} - \delta_{34}$  plane. We looked into the



effect of the sterile phase on the measurement of  $\delta_{13}$ . We found that for T2HK the effect is negligible, DUNE is affected most and T2HKK is slightly affected. We also looked at the sensitivity to the sterile mixing angles  $\theta_{14}$  and  $\theta_{24}$  under the assumptions of  $\theta_{34} = 0$ . Here we found that T2HK has best sensitivity to  $\theta_{14}$  and DUNE has worst sensitivity. On the other hand, DUNE and T2HKK have best sensitivity to  $\theta_{24}$  as compared to T2HK. And for both  $\theta_{14}$  and  $\theta_{24}$ , the expected sensitivity is enhanced when we combined them, however, this enhancement is more for  $\theta_{14}$  than  $\theta_{24}$ .

We showed the existence of a fake solution in the  $\nu_\mu \rightarrow \nu_e$  appearance probability, coming from  $\Delta m_{41}^2$  [146]. A fake solution is obtained in  $P_{\mu e}$  at the oscillation maximum for  $\Delta m_{41}^2 = \frac{1}{2}\Delta m_{31}^2$  when the true  $\Delta m_{41}^2$  is large enough such that the fast oscillations due to  $\Delta m_{41}^2$  get averaged out and the condition required for this is  $\delta_{13} + \delta_{24} = 0$ . We showed this analytically as well as numerically for DUNE and T2HK. We used an approximation by choosing  $\Delta m_{21}^2 = 0$  for analytical calculation, however, this does not affect the degeneracy. We also found that the degeneracy is approximate away from the oscillation maximum. We also discussed the impact of earth matter effects and found that it slightly shifts the position of the oscillation maximum. Finally, we investigated the  $\nu_\mu \rightarrow \nu_\mu$  disappearance channel and saw that the degeneracy is lifted as we add the disappearance channel.

In chapter 5, we discussed NSI at DUNE experiment. There is a plethora of models proposed to describe the neutrino mass and mixing or dark matter. Many of these models lead to corrections to the effective neutrino matter interaction vertices through higher order corrections. If such new corrections come from charged-current operators, they will modify the production and detection of neutrinos and if such corrections come from neutral-current operators, they will affect the propagation of neutrino inside matter. All of such new interactions are called non-standard interactions (NSI). The charged-current NSI is called the source and detector type NSI and the neutral current ones are called matter NSI. The matter NSI and its effect on standard oscillation has been widely studied in the literature. However, any theory which gives matter NSIs would almost always give

rise to source and detector NSIs. So it is necessary to study both matter and source and detector NSIs together for a complete study. We study source-detector and matter NSIs for DUNE [130]. In this analysis instead of frequentist analysis, Bayesian methods were incorporated using Markov Chain Monte Carlo to scan the full parameter space. The expected sensitivity of DUNE to the NSI parameters is seen to improve compared to the current bounds. Although the bound does not improve much for source-detector NSIs but the bound improves substantially for matter NSIs (up to a factor of about 15). We also study the effect of NSI parameters on the precision measurement of  $\delta_{23}$  and  $\theta_{23}$  and found appearance of fake solution in the  $\theta_{23} - \delta_{CP}$  plane. The fake solution appear when we assumed both matter as well as source-detector NSIs in the data. Some correlations between source/detector and matter NSIs are observed in the analysis specially between  $\epsilon_{\tau e}^d$  &  $\epsilon_{\tau e}^m$  and  $\epsilon_{\mu e}^d$  &  $\epsilon_{\mu e}^m$ . We also studied the effect of statistics and observed that the negative impact on the precision measurement of  $\delta_{CP}$  and  $\theta_{23}$  went away as we increased the statistics from 3+3 to 5+5 years. However, the correlations observed were persistent even after 5+5 years.

In chapter 6, we discussed invisible neutrino decay for both present and future experiments. In invisible neutrino decay, one or more neutrino mass eigenstates can decay into lower mass sterile states. Although the decay of  $\nu_1$  and  $\nu_2$  are heavily constrained but constraints on the decay of  $\nu_3$  is weak and we have considered the decay of  $\nu_3$  in our analysis.

We investigated the recent NOvA and T2K data for invisible neutrino decay [191]. For T2K, we used the latest disappearance and appearance data given by the collaboration corresponding to  $7.482 \times 10^{20}$  pot for neutrinos and  $7.471 \times 10^{20}$  pot for antineutrinos [201]. For NOvA, we have taken the data announced by the collaboration which correspond to  $6.04 \times 10^{20}$  pot for electrons [196] and  $8.85 \times 10^{20}$  pot for muons [197]. We found that both NOvA and T2K to have slightly more  $\chi^2$  for the with decay case than the standard no-decay case. However, this is not statistically significant as the available statistics is

very less. Where pure oscillation give  $\chi^2_{min} = 10.93, 70.39$  and  $88.65$  for NOvA, T2K and their combination respectively, the oscillation with decay give  $\chi^2_{min} = 10.38, 69.34$  and  $87.19$  respectively. The best-fit for  $\tau_3/m_3 = 5.05 \times 10^{-12}$  s/eV for the combined fit and we found the lower bound on  $\tau_3/m_3$  as  $\tau_3/m_3 \geq 1.50 \times 10^{-12}$  s/eV at  $3\sigma$  level.

We also studied the effect of decay on the measurement of the standard parameters  $\theta_{23}$  and  $\Delta m^2_{32}$ . We found that if we include decay in our fit, the best-fit values for  $\sin^2 \theta_{23}$  and  $\Delta m^2_{32}$  change significantly. The best-fit  $(\sin^2 \theta_{23}, \Delta m^2_{32})$  obtained for the standard oscillation case from analysis of NOvA, T2K and both experiments combined are  $(0.45, 2.41 \times 10^{-3} \text{ eV}^2)$ ,  $(0.52, 2.56 \times 10^{-3} \text{ eV}^2)$  and  $(0.46, 2.51 \times 10^{-3} \text{ eV}^2)$  respectively. On including decay in the fit, the corresponding best-fit points become  $(0.48, 2.39 \times 10^{-3} \text{ eV}^2)$  for NOvA,  $(0.62, 2.62 \times 10^{-3} \text{ eV}^2)$  for T2K and  $(0.48, 2.52 \times 10^{-3} \text{ eV}^2)$  for the NOvA and T2K combined.

We have studied the impact of invisible neutrino decay for the DUNE experiment [143]. We studied the sensitivity of DUNE to constrain  $\tau_3$  and we obtained expected bound  $\tau_3/m_3 \geq 4.50 \times 10^{-11}$  s/eV at 90% confidence level for NH using 5+5 years of DUNE simulation data. We studied the discovery potential of DUNE to discover neutrino decay and found that DUNE can discover a decaying neutrino scenario for  $\tau_3/m_3 > 4.27 \times 10^{-11}$  s/eV at 90% C.L. with its projected run. Then we investigated how precisely DUNE can measure  $\tau_3/m_3$  if decay is present in nature. If we assume  $\tau_3/m_3 = 1.2 \times 10^{-11}$  s/eV in data, we found that the allowed region after 5+5 years will be  $1.71 \times 10^{-11} > \tau_3/m_3 > 9.29 \times 10^{-12}$  s/eV at  $3\sigma$ .

We also looked at the effect of  $\nu_3$  decay on the precision measurement of DUNE. We found an interesting correlation between the  $\theta_{23}$  and  $\tau_3/m_3$ . We considered two cases: in one case, we generated data assuming only pure oscillation and in the other case we generated data assuming decay plus oscillation scenario. Then we fitted both datasets with pure oscillation only. We found that the best-fit of  $\theta_{23}$  shifts towards a lower value in both octant and thus gives erroneous value of  $\theta_{23}$  if decay is present but not considered

in the fit. This is because the effect of decay can be mimicked by a  $\theta_{23}$  which is lower than the actual value. We study the effect of decay in the octant, mass-hierarchy and CP sensitivity also and observed that the octant sensitivity is affected significantly affected because of the correlation between the  $\tau_3/m_3$  and  $\theta_{23}$ .

In conclusion, this thesis looked into various oscillation scenarios beyond the standard framework at the long-baseline neutrino experiments. This includes sterile neutrino, invisible neutrino decay and nonstandard interactions. We studied sterile neutrino sensitivity at DUNE near detector and showed that DUNE has very good sensitivity to the sterile neutrino. We studied the effect of the sterile neutrino mixing and phases on the standard measurement of these experiments and found that sterile neutrino significantly affect the CP-sensitivity, mass-hierarchy and octant measurement. For some cases, the sensitivity reduce and in some cases, the sensitivity is increased We also showed that it is possible to measure the sterile neutrino phases at future long-baseline experiments. We studied neutrino decay in the context of a future experiment DUNE and two ongoing experiments NOvA and T2K. For NOvA and T2K, we have analysed the real data from the experiment and put lower bound on neutrino decay lifetime from these experiments. This analysis have shown that the currently available data slightly prefer invisible neutrino decay. Our analysis gives the best fit from NOvA and T2K for  $\tau_3/m_3$  as  $\tau_3/m_3 = 5.05 \times 10^{-12}$  s/eV and the lower bound obtained for  $\tau_3/m_3$  is  $\tau_3/m_3 \geq 1.50 \times 10^{-12}$  s/eV at  $3\sigma$  level. For DUNE, we showed that it has good sensitivity to invisible neutrino decay and can discover neutrino decay for a large region of the parameter space. We found that the expected bound from DUNE after 5+5 years of running is  $1.71 \times 10^{-11} > \tau_3/m_3 > 9.29 \times 10^{-12}$  s/eV at  $3\sigma$ . We also found an interesting correlation between  $\tau_3/m_3$  and  $\theta_{23}$ . It was found that if we ignore the decay in the fit, the best fit value for  $\theta_{23}$  is shifted towards a smaller values if decay is present in the data. We have also studied neutrino non-standard interactions in the context of DUNE using source-detector and matter NSIs together and have seen good sensitivity to the NSI parameters especially matter NSIs. We also found some correlations between the source/detector and matter NSI parameters. Finally, long-baseline

experiments were found to be good probe for sterile neutrino, non-standard interactions and invisible neutrino decay and it was also observed that these new scenarios affect the performance of these long-baseline experiments.

## 7.2 Future Prospects

There are many problems still present in neutrino oscillation physics. There seem to be inconsistencies between various observations. Solar and KamLAND give different measurement for  $\Delta m_{21}^2$ . While solar neutrino data give  $\Delta m_{21}^2 = 5 \times 10^{-5} \text{ eV}^2$ , the KamLAND gives  $\Delta m_{21}^2 = 7.5 \times 10^{-5} \text{ eV}^2$  as best-fits. This tension has become slightly stronger with the inclusion of latest spectral data from SK and improvement of reactor flux normalization of KamLAND. T2K data (both  $\nu$  and  $\bar{\nu}$ ), NOvA neutrino data prefer maximal  $\theta_{23}$  mixing. However, MINOS neutrino data and NOvA antineutrino data disfavour maximal mixing at about  $\Delta\chi^2 \sim 2$  and  $\Delta\chi^2 \sim 6$ , respectively. With the inclusion of reactor data, this discrepancy increases to  $\Delta\chi^2 \sim 7$  and  $\Delta\chi^2 \sim 9$ , respectively. There is also some tension in the measurement of  $\delta_{CP}$  from T2K and NOvA. T2K neutrino as well as antineutrino appearance data prefer  $3\pi/2$  and disfavour  $\pi/2$  for both normal and inverted hierarchy. NOvA neutrino appearance data support the T2K results, however, NOvA antineutrino appearance data prefer  $\pi/2$  and disfavour  $3\pi/2$  for normal hierarchy. These tensions can be statistical fluctuations, but if they persist, these demand further investigations on these issues.

It has been shown that the presence of NSI can give rise to degenerate solutions of  $\theta_{12}$  in both octants. The generalized mass hierarchy discussed in subsection 2.3.4 makes it impossible for any oscillation experiment to resolve this problem. This so-called dark LMA solution is a major problem in neutrino oscillation physics and further study is needed to address this issue.

Apart from DUNE, T2HK/T2HKK, there are other planned long-baseline experiments

in the coming future. ESS $\nu$ B, P2O are some of the experiments. New physics like sterile neutrino, NSI, neutrino decay and other types of new physics can affect the performances of these experiments. So, the prospects of new physics should be studied in the context of these experiments.



## Bibliography

- [1] C. V. Achar et al., *Detection of muons produced by cosmic ray neutrinos deep underground*, *Phys. Lett.* **18** (1965) 196–199.
- [2] F. Reines, M. F. Crouch, T. L. Jenkins, W. R. Kropp, H. S. Gurr, G. R. Smith, J. P. F. Sellschop, and B. Meyer, *Evidence for high-energy cosmic ray neutrino interactions*, *Phys. Rev. Lett.* **15** (1965) 429–433.
- [3] **Kamiokande-II** Collaboration, K. Hirata et al., *Observation of a Neutrino Burst from the Supernova SN 1987a*, *Phys. Rev. Lett.* **58** (1987) 1490–1493.  
[,727(1987)].
- [4] **IceCube** Collaboration, M. G. Aartsen et al., *First observation of PeV-energy neutrinos with IceCube*, *Phys. Rev. Lett.* **111** (2013) 021103,  
[[arXiv:1304.5356](#)].
- [5] J. N. Bahcall, A. M. Serenelli, and S. Basu, *New solar opacities, abundances, helioseismology, and neutrino fluxes*, *Astrophys. J.* **621** (2005) L85–L88,  
[[astro-ph/0412440](#)].
- [6] J. N. Bahcall and A. M. Serenelli, *How do uncertainties in the surface chemical abundances of the Sun affect the predicted solar neutrino fluxes?*, *Astrophys. J.* **626** (2005) 530, [[astro-ph/0412096](#)].



- [7] R. Davis, Jr., D. S. Harmer, and K. C. Hoffman, *Search for neutrinos from the sun*, *Phys. Rev. Lett.* **20** (1968) 1205–1209.
- [8] J. N. Bahcall, S. Basu, and M. H. Pinsonneault, *How uncertain are solar neutrino predictions?*, *Phys. Lett.* **B433** (1998) 1–8, [[astro-ph/9805135](#)].
- [9] A. Dar and G. Shaviv, *Standard solar neutrinos*, *Astrophys. J.* **468** (1996) 933–946, [[astro-ph/9604009](#)].
- [10] A. Cumming and W. C. Haxton, *He-3 transport in the sun and the solar neutrino problem*, *Phys. Rev. Lett.* **77** (1996) 4286–4289, [[nucl-th/9608045](#)].
- [11] **Kamiokande** Collaboration, Y. Fukuda et al., *Solar neutrino data covering solar cycle 22*, *Phys. Rev. Lett.* **77** (1996) 1683–1686.
- [12] **SAGE** Collaboration, J. N. Abdurashitov et al., *Results from SAGE*, *Phys. Lett.* **B328** (1994) 234–248.
- [13] **GALLEX** Collaboration, P. Anselmann et al., *Solar neutrinos observed by GALLEX at Gran Sasso*, *Phys. Lett.* **B285** (1992) 376–389.
- [14] **Super-Kamiokande** Collaboration, J. Hosaka et al., *Solar neutrino measurements in super-Kamiokande-I*, *Phys. Rev.* **D73** (2006) 112001, [[hep-ex/0508053](#)].
- [15] **SNO** Collaboration, Q. R. Ahmad et al., *Direct evidence for neutrino flavor transformation from neutral current interactions in the Sudbury Neutrino Observatory*, *Phys. Rev. Lett.* **89** (2002) 011301, [[nucl-ex/0204008](#)].
- [16] **SNO** Collaboration, B. Aharmim et al., *Electron energy spectra, fluxes, and day-night asymmetries of B-8 solar neutrinos from measurements with NaCl dissolved in the heavy-water detector at the Sudbury Neutrino Observatory*, *Phys. Rev.* **C72** (2005) 055502, [[nucl-ex/0502021](#)].
- [17] **Kamiokande-II** Collaboration, K. S. Hirata et al., *Experimental Study of the Atmospheric Neutrino Flux*, *Phys. Lett.* **B205** (1988) 416. [[447\(1988\)](#)].

- [18] D. Casper et al., *Measurement of atmospheric neutrino composition with IMB-3*, *Phys. Rev. Lett.* **66** (1991) 2561–2564.
- [19] R. Becker-Szendy et al., *The Electron-neutrino and muon-neutrino content of the atmospheric flux*, *Phys. Rev.* **D46** (1992) 3720–3724.
- [20] **Soudan-2** Collaboration, M. C. Goodman, *The Atmospheric neutrino anomaly in Soudan-2*, *Nucl. Phys. Proc. Suppl.* **38** (1995) 337–342.
- [21] **Super-Kamiokande** Collaboration, Y. Fukuda et al., *Evidence for oscillation of atmospheric neutrinos*, *Phys. Rev. Lett.* **81** (1998) 1562–1567, [[hep-ex/9807003](#)].
- [22] B. Pontecorvo, *Mesonium and anti-mesonium*, *Sov. Phys. JETP* **6** (1957) 429. [*Zh. Eksp. Teor. Fiz.* 33,549(1957)].
- [23] Z. Maki, M. Nakagawa, and S. Sakata, *Remarks on the unified model of elementary particles*, *Prog. Theor. Phys.* **28** (1962) 870–880. [,34(1962)].
- [24] I. Esteban, M. C. Gonzalez-Garcia, A. Hernandez-Cabezudo, M. Maltoni, and T. Schwetz, *Global analysis of three-flavour neutrino oscillations: synergies and tensions in the determination of  $\theta_{23}$ ,  $\delta_{CP}$ , and the mass ordering*, *JHEP* **01** (2019) 106, [[arXiv:1811.05487](#)].
- [25] **T2K** Collaboration, K. Abe et al., *The T2K Experiment*, *Nucl. Instrum. Meth.* **A659** (2011) 106–135, [[arXiv:1106.1238](#)].
- [26] **NOvA** Collaboration, D. S. Ayres et al., *NOvA: Proposal to Build a 30 Kiloton Off-Axis Detector to Study  $\nu_\mu \rightarrow \nu_e$  Oscillations in the NuMI Beamline*, [[hep-ex/0503053](#)].
- [27] **DUNE** Collaboration, R. Acciarri et al., *Long-Baseline Neutrino Facility (LBNF) and Deep Underground Neutrino Experiment (DUNE)*, [[arXiv:1512.06148](#)].

- [28] **Hyper-Kamiokande Working Group** Collaboration, T. Ishida, *T2HK: J-PARC upgrade plan for future and beyond T2K*, in *15th International Workshop on Neutrino Factories, Super Beams and Beta Beams (NuFact2013) Beijing, China, August 19-24, 2013*, 2013. [arXiv:1311.5287](#).
- [29] **Hyper-Kamiokande** Collaboration, K. Abe et al., *Physics potentials with the second Hyper-Kamiokande detector in Korea*, *PTEP* **2018** (2018), no. 6 063C01, [[arXiv:1611.06118](#)].
- [30] **ESSnuSB** Collaboration, E. Baussan et al., *A very intense neutrino super beam experiment for leptonic CP violation discovery based on the European spallation source linac*, *Nucl. Phys.* **B885** (2014) 127–149, [[arXiv:1309.7022](#)].
- [31] A. V. Akindinov et al., *Letter of Interest for a Neutrino Beam from Protvino to KM3NeT/ORCA*, [arXiv:1902.06083](#).
- [32] **LSND** Collaboration, A. Aguilar-Arevalo et al., *Evidence for neutrino oscillations from the observation of anti-neutrino(electron) appearance in a anti-neutrino(muon) beam*, *Phys. Rev.* **D64** (2001) 112007, [[hep-ex/0104049](#)].
- [33] **MiniBooNE** Collaboration, A. A. Aguilar-Arevalo et al., *A Search for Electron Neutrino Appearance at the  $\Delta m^2 \sim 1\text{eV}^2$  Scale*, *Phys. Rev. Lett.* **98** (2007) 231801, [[arXiv:0704.1500](#)].
- [34] **MiniBooNE** Collaboration, A. A. Aguilar-Arevalo et al., *Improved Search for  $\bar{\nu}_\mu \rightarrow \bar{\nu}_e$  Oscillations in the MiniBooNE Experiment*, *Phys. Rev. Lett.* **110** (2013) 161801, [[arXiv:1303.2588](#)].
- [35] T. A. Mueller et al., *Improved Predictions of Reactor Antineutrino Spectra*, *Phys. Rev.* **C83** (2011) 054615, [[arXiv:1101.2663](#)].

- [36] G. Mention, M. Fechner, T. Lasserre, T. A. Mueller, D. Lhuillier, M. Cribier, and A. Letourneau, *The Reactor Antineutrino Anomaly*, *Phys. Rev.* **D83** (2011) 073006, [[arXiv:1101.2755](#)].
- [37] P. Huber, *On the determination of anti-neutrino spectra from nuclear reactors*, *Phys. Rev.* **C84** (2011) 024617, [[arXiv:1106.0687](#)]. [Erratum: *Phys. Rev.* **C85**, 029901(2012)].
- [38] J. N. Bahcall, P. I. Krastev, and E. Lisi, *Limits on electron-neutrino oscillations from the GALLEX Cr-51 source experiment*, *Phys. Lett.* **B348** (1995) 121–123, [[hep-ph/9411414](#)].
- [39] C. Giunti and M. Laveder, *Short-Baseline Active-Sterile Neutrino Oscillations?*, *Mod. Phys. Lett.* **A22** (2007) 2499–2509, [[hep-ph/0610352](#)].
- [40] C. Giunti and M. Laveder, *Short-Baseline Electron Neutrino Disappearance, Tritium Beta Decay and Neutrinoless Double-Beta Decay*, *Phys. Rev.* **D82** (2010) 053005, [[arXiv:1005.4599](#)].
- [41] C. Giunti and M. Laveder, *Statistical Significance of the Gallium Anomaly*, *Phys. Rev.* **C83** (2011) 065504, [[arXiv:1006.3244](#)].
- [42] **KARMEN** Collaboration, B. Armbruster et al., *Upper limits for neutrino oscillations  $\mu$ -anti-neutrino  $\rightarrow$  electron-anti-neutrino from muon decay at rest*, *Phys. Rev.* **D65** (2002) 112001, [[hep-ex/0203021](#)].
- [43] F. Dydak et al., *A Search for Muon-neutrino Oscillations in the  $\Delta m^2$  Range  $0.3\text{-eV}^2$  to  $90\text{-eV}^2$* , *Phys. Lett.* **134B** (1984) 281.
- [44] **NOMAD** Collaboration, P. Astier et al., *Search for  $\nu(\mu) \rightarrow \nu(e)$  oscillations in the NOMAD experiment*, *Phys. Lett.* **B570** (2003) 19–31, [[hep-ex/0306037](#)].

- [45] **IceCube** Collaboration, M. G. Aartsen et al., *Searches for Sterile Neutrinos with the IceCube Detector*, *Phys. Rev. Lett.* **117** (2016), no. 7 071801, [[arXiv:1605.01990](#)].
- [46] **MiniBooNE** Collaboration, A. A. Aguilar-Arevalo et al., *A Search for muon neutrino and antineutrino disappearance in MiniBooNE*, *Phys. Rev. Lett.* **103** (2009) 061802, [[arXiv:0903.2465](#)].
- [47] **ALEPH, DELPHI, L3, OPAL, SLD, LEP Electroweak Working Group, SLD Electroweak Group, SLD Heavy Flavour Group** Collaboration, S. Schael et al., *Precision electroweak measurements on the Z resonance*, *Phys. Rept.* **427** (2006) 257–454, [[hep-ex/0509008](#)].
- [48] L. Wolfenstein, *Neutrino Oscillations in Matter*, *Phys. Rev.* **D17** (1978) 2369–2374. [,294(1977)].
- [49] S. P. Mikheyev and A. Yu. Smirnov, *Resonance Amplification of Oscillations in Matter and Spectroscopy of Solar Neutrinos*, *Sov. J. Nucl. Phys.* **42** (1985) 913–917. [,305(1986)].
- [50] T.-K. Kuo and J. T. Pantaleone, *Neutrino Oscillations in Matter*, *Rev. Mod. Phys.* **61** (1989) 937.
- [51] S. P. Mikheyev and A. Yu. Smirnov, *Resonant neutrino oscillations in matter*, *Prog. Part. Nucl. Phys.* **23** (1989) 41–136.
- [52] E. K. Akhmedov, R. Johansson, M. Lindner, T. Ohlsson, and T. Schwetz, *Series expansions for three flavor neutrino oscillation probabilities in matter*, *JHEP* **04** (2004) 078, [[hep-ph/0402175](#)].
- [53] H. Minakata and H. Nunokawa, *Exploring neutrino mixing with low-energy superbeams*, *JHEP* **10** (2001) 001, [[hep-ph/0108085](#)].

- [54] G. L. Fogli and E. Lisi, *Tests of three flavor mixing in long baseline neutrino oscillation experiments*, *Phys. Rev.* **D54** (1996) 3667–3670, [[hep-ph/9604415](#)].
- [55] J. Burguet-Castell, M. B. Gavela, J. J. Gomez-Cadenas, P. Hernandez, and O. Mena, *Superbeams plus neutrino factory: The Golden path to leptonic CP violation*, *Nucl. Phys.* **B646** (2002) 301–320, [[hep-ph/0207080](#)].
- [56] V. Barger, D. Marfatia, and K. Whisnant, *Breaking eight fold degeneracies in neutrino CP violation, mixing, and mass hierarchy*, *Phys. Rev.* **D65** (2002) 073023, [[hep-ph/0112119](#)].
- [57] S. K. Agarwalla, S. Prakash, and S. U. Sankar, *Resolving the octant of  $\theta_{23}$  with T2K and NOvA*, *JHEP* **07** (2013) 131, [[arXiv:1301.2574](#)].
- [58] P. Coloma, P. B. Denton, M. C. Gonzalez-Garcia, M. Maltoni, and T. Schwetz, *Curtailing the Dark Side in Non-Standard Neutrino Interactions*, *JHEP* **04** (2017) 116, [[arXiv:1701.04828](#)].
- [59] **CHOOZ** Collaboration, M. Apollonio et al., *Initial results from the CHOOZ long baseline reactor neutrino oscillation experiment*, *Phys. Lett.* **B420** (1998) 397–404, [[hep-ex/9711002](#)].
- [60] F. Boehm et al., *Results from the Palo Verde neutrino oscillation experiment*, *Phys. Rev.* **D62** (2000) 072002, [[hep-ex/0003022](#)].
- [61] **Double Chooz** Collaboration, F. Ardellier et al., *Double Chooz: A Search for the neutrino mixing angle  $\theta_{13}$* , [hep-ex/0606025](#).
- [62] **RENO** Collaboration, J. K. Ahn et al., *RENO: An Experiment for Neutrino Oscillation Parameter  $\theta_{13}$  Using Reactor Neutrinos at Yonggwang*, [arXiv:1003.1391](#).

- [63] **Daya Bay** Collaboration, W. Wang, *The Hunt for  $\theta(13)$  at the Daya Bay nuclear power plant*, *AIP Conf. Proc.* **1222** (2010), no. 1 494–497, [[arXiv:0910.4605](#)].
- [64] **CHOOZ** Collaboration, M. Apollonio et al., *Search for neutrino oscillations on a long baseline at the CHOOZ nuclear power station*, *Eur. Phys. J.* **C27** (2003) 331–374, [[hep-ex/0301017](#)].
- [65] **T2K** Collaboration, K. Abe et al., *Search for CP Violation in Neutrino and Antineutrino Oscillations by the T2K Experiment with  $2.2 \times 10^{21}$  Protons on Target*, *Phys. Rev. Lett.* **121** (2018), no. 17 171802, [[arXiv:1807.07891](#)].
- [66] R. Gandhi, B. Kayser, M. Masud, and S. Prakash, *The impact of sterile neutrinos on CP measurements at long baselines*, *JHEP* **11** (2015) 039, [[arXiv:1508.06275](#)].
- [67] D. Dutta, R. Gandhi, B. Kayser, M. Masud, and S. Prakash, *Capabilities of long-baseline experiments in the presence of a sterile neutrino*, *JHEP* **11** (2016) 122, [[arXiv:1607.02152](#)].
- [68] S. K. Agarwalla, S. S. Chatterjee, and A. Palazzo, *Physics Reach of DUNE with a Light Sterile Neutrino*, *JHEP* **09** (2016) 016, [[arXiv:1603.03759](#)].
- [69] S. Choubey, D. Dutta, and D. Pramanik, *Imprints of a light Sterile Neutrino at DUNE, T2HK and T2HKK*, *Phys. Rev.* **D96** (2017), no. 5 056026, [[arXiv:1704.07269](#)].
- [70] S. Gupta, Z. M. Matthews, P. Sharma, and A. G. Williams, *The Effect of a Light Sterile Neutrino at NOvA and DUNE*, *Phys. Rev.* **D98** (2018), no. 3 035042, [[arXiv:1804.03361](#)].

- [71] M. Ghosh, S. Gupta, Z. M. Matthews, P. Sharma, and A. G. Williams, *Study of parameter degeneracy and hierarchy sensitivity of NOvA in presence of sterile neutrino*, *Phys. Rev.* **D96** (2017), no. 7 075018, [[arXiv:1704.04771](#)].
- [72] S. K. Agarwalla, S. S. Chatterjee, A. Dasgupta, and A. Palazzo, *Discovery Potential of T2K and NOvA in the Presence of a Light Sterile Neutrino*, *JHEP* **02** (2016) 111, [[arXiv:1601.05995](#)].
- [73] S. K. Agarwalla, S. S. Chatterjee, and A. Palazzo, *Octant of  $\theta_{23}$  in danger with a light sterile neutrino*, *Phys. Rev. Lett.* **118** (2017), no. 3 031804, [[arXiv:1605.04299](#)].
- [74] J. M. Berryman, A. de Gouvêa, K. J. Kelly, and A. Kobach, *Sterile neutrino at the Deep Underground Neutrino Experiment*, *Phys. Rev.* **D92** (2015), no. 7 073012, [[arXiv:1507.03986](#)].
- [75] K. J. Kelly, *Searches for new physics at the Hyper-Kamiokande experiment*, *Phys. Rev.* **D95** (2017), no. 11 115009, [[arXiv:1703.00448](#)].
- [76] S. Choubey, D. Dutta, and D. Pramanik, *Measuring the Sterile Neutrino CP Phase at DUNE and T2HK*, *Eur. Phys. J.* **C78** (2018), no. 4 339, [[arXiv:1711.07464](#)].
- [77] R. Gandhi, B. Kayser, S. Prakash, and S. Roy, *What measurements of neutrino neutral current events can reveal*, *JHEP* **11** (2017) 202, [[arXiv:1708.01816](#)].
- [78] P. Coloma, D. V. Forero, and S. J. Parke, *DUNE Sensitivities to the Mixing between Sterile and Tau Neutrinos*, *JHEP* **07** (2018) 079, [[arXiv:1707.05348](#)].
- [79] P. Ballett, M. Hostert, S. Pascoli, Y. F. Perez-Gonzalez, and Z. Tabrizi, *Z's in neutrino scattering at DUNE*, [arXiv:1902.08579](#).
- [80] P. Ballett, M. Hostert, S. Pascoli, Y. F. Perez-Gonzalez, Z. Tabrizi, and R. Zukanovich Funchal, *Neutrino Trident Scattering at Near Detectors*, *JHEP* **01** (2019) 119, [[arXiv:1807.10973](#)].



- [81] P. Huber, M. Lindner, and W. Winter, *Simulation of long-baseline neutrino oscillation experiments with GLoBES. (General Long Baseline Experiment Simulator)*, *Computer Physics Communications* **167** (May, 2005) 195–202, [[hep-ph/0407333](#)].
- [82] P. Huber, J. Kopp, M. Lindner, M. Rolinec, and W. Winter, *New features in the simulation of neutrino oscillation experiments with GLoBES 3.0. (General Long Baseline Experiment Simulator)*, *Computer Physics Communications* **177** (Sept., 2007) 432–438, [[hep-ph/0701187](#)].
- [83] J. Kopp, *Efficient numerical diagonalization of hermitian  $3 \times 3$  matrices*, *Int. J. Mod. Phys. C* **19** (2008) 523–548, [[physics/0610206](#)]. Erratum *ibid.* **C19** (2008) 845.
- [84] J. Kopp, M. Lindner, T. Ota, and J. Sato, *Non-standard neutrino interactions in reactor and superbeam experiments*, *Phys. Rev. D* **77** (2008) 013007, [[arXiv:0708.0152](#)].
- [85] M. Blennow and E. Fernandez-Martinez, *Neutrino oscillation parameter sampling with MonteCUBES*, *Comput. Phys. Commun.* **181** (2010) 227–231, [[arXiv:0903.3985](#)].
- [86] S. Goswami, *Accelerator, reactor, solar and atmospheric neutrino oscillation: Beyond three generations*, *Phys. Rev. D* **55** (1997) 2931–2949, [[hep-ph/9507212](#)].
- [87] **Super-Kamiokande** Collaboration, A. Himmel, *New Limits on Sterile Neutrino Mixing with Atmospheric Neutrinos*, *Phys. Procedia* **61** (2015) 612–618.
- [88] **NEOS** Collaboration, Y. J. Ko et al., *Sterile Neutrino Search at the NEOS Experiment*, *Phys. Rev. Lett.* **118** (2017), no. 12 121802, [[arXiv:1610.05134](#)].

- [89] **DANSS** Collaboration, I. Alekseev et al., *Search for sterile neutrinos at the DANSS experiment*, *Phys. Lett.* **B787** (2018) 56–63, [[arXiv:1804.04046](#)].
- [90] **MINOS** Collaboration, P. Adamson et al., *Search for sterile neutrino mixing in the MINOS long baseline experiment*, *Phys. Rev.* **D81** (2010) 052004, [[arXiv:1001.0336](#)].
- [91] **MINOS+** Collaboration, P. Adamson et al., *Search for sterile neutrinos in MINOS and MINOS+ using a two-detector fit*, *Phys. Rev. Lett.* **122** (2019), no. 9 091803, [[arXiv:1710.06488](#)].
- [92] **NOvA** Collaboration, P. Adamson et al., *Search for active-sterile neutrino mixing using neutral-current interactions in NOvA*, *Phys. Rev.* **D96** (2017), no. 7 072006, [[arXiv:1706.04592](#)].
- [93] **T2K** Collaboration, K. Abe et al., *Search for short baseline  $\nu_e$  disappearance with the T2K near detector*, *Phys. Rev.* **D91** (2015) 051102, [[arXiv:1410.8811](#)].
- [94] **MiniBooNE** Collaboration, A. A. Aguilar-Arevalo et al., *Significant Excess of ElectronLike Events in the MiniBooNE Short-Baseline Neutrino Experiment*, *Phys. Rev. Lett.* **121** (2018), no. 22 221801, [[arXiv:1805.12028](#)].
- [95] **MicroBooNE, LAr1-ND, ICARUS-WA104** Collaboration, M. Antonello et al., *A Proposal for a Three Detector Short-Baseline Neutrino Oscillation Program in the Fermilab Booster Neutrino Beam*, [arXiv:1503.01520](#).
- [96] **OscSNS** Collaboration, *OscSNS: A Precision Neutrino Oscillation Experiment at the SNS*, [arXiv:1305.4189](#).
- [97] S. K. Agarwalla and P. Huber, *LSND reloaded*, *Phys. Lett.* **B696** (2011) 359–361, [[arXiv:1007.3228](#)].
- [98] J. Spitz, *A Sterile Neutrino Search with Kaon Decay-at-rest*, *Phys. Rev.* **D85** (2012) 093020, [[arXiv:1203.6050](#)].

- [99] M. Antonello et al., *Search for 'anomalies' from neutrino and anti-neutrino oscillations at  $\Delta_m^2 \sim 1\text{eV}^2$  with muon spectrometers and large LAr-TPC imaging detectors*, [arXiv:1203.3432](#).
- [100] B. J. P. Jones, *The Status of the MicroBooNE Experiment*, *J. Phys. Conf. Ser.* **408** (2013) 012028, [[arXiv:1110.1678](#)].
- [101] I. V. Chuvilo, I. M. Kapchinskii, D. G. Koshkarev, P. R. Zenkevich, V. K. Plotnikov, and Yu. G. Globenko, *High-current collective accelerators*, *At. Energ.* **37** (1974) 223–227.
- [102] D. Neuffer, *Design considerations for a muon storage ring*, *eConf* **C801002** (1980) 199–203.
- [103] **STEREO** Collaboration, H. Almazán et al., *Sterile Neutrino Constraints from the STEREO Experiment with 66 Days of Reactor-On Data*, *Phys. Rev. Lett.* **121** (2018), no. 16 161801, [[arXiv:1806.02096](#)].
- [104] **PROSPECT** Collaboration, J. Ashenfelter et al., *The PROSPECT Physics Program*, *J. Phys.* **G43** (2016), no. 11 113001, [[arXiv:1512.02202](#)].
- [105] **SoLid** Collaboration, V. Pestel, *The SoLid short baseline neutrino detector*, *PoS EPS-HEP2017* (2018) 511.
- [106] S. Choubey and D. Pramanik, *Constraints on Sterile Neutrino Oscillations using DUNE Near Detector*, *Phys. Lett.* **B764** (2017) 135–141, [[arXiv:1604.04731](#)].
- [107] B. Choudhary, R. Gandhi, M. S. R., Mishra, and J. Strait, *LBNE-INDIA, Proposal of Indian Institutions and Fermilab Collaboration for Participation in the Long-Baseline Neutrino Experiment at Fermilab*, .
- [108] **NP04 Collaboration** Collaboration, F. Cavanna, *Yearly report on ProtoDUNE Single Phase NP04 (2016)*, Tech. Rep. CERN-SPSC-2016-018. SPSC-SR-185, CERN, Geneva, Apr, 2016.

- [109] **LBNE** Collaboration, C. Adams et al., *The Long-Baseline Neutrino Experiment: Exploring Fundamental Symmetries of the Universe*, in *Snowmass 2013: Workshop on Energy Frontier Seattle, USA, June 30-July 3, 2013*, 2013.  
[arXiv:1307.7335](#).
- [110] M. Bishai, *Private Communication*, .
- [111] **MiniBooNE** Collaboration, A. A. Aguilar-Arevalo et al., *Event Excess in the MiniBooNE Search for  $\bar{\nu}_\mu \rightarrow \bar{\nu}_e$  Oscillations*, *Phys. Rev. Lett.* **105** (2010) 181801, [[arXiv:1007.1150](#)].
- [112] I. Esteban, M. C. Gonzalez-Garcia, M. Maltoni, I. Martinez-Soler, and T. Schwetz, *Updated fit to three neutrino mixing: exploring the accelerator-reactor complementarity*, *JHEP* **01** (2017) 087, [[arXiv:1611.01514](#)].
- [113] **LSND** Collaboration, C. Athanassopoulos et al., *Candidate events in a search for anti-muon-neutrino  $\rightarrow$  anti-electron-neutrino oscillations*, *Phys. Rev. Lett.* **75** (1995) 2650–2653, [[nucl-ex/9504002](#)].
- [114] J. N. Abdurashitov et al., *Measurement of the response of a Ga solar neutrino experiment to neutrinos from an Ar-37 source*, *Phys. Rev.* **C73** (2006) 045805, [[nucl-ex/0512041](#)].
- [115] Y. Declais et al., *Search for neutrino oscillations at 15-meters, 40-meters, and 95-meters from a nuclear power reactor at Bugey*, *Nucl. Phys.* **B434** (1995) 503–534.
- [116] **Daya Bay** Collaboration, F. P. An et al., *Search for a Light Sterile Neutrino at Daya Bay*, *Phys. Rev. Lett.* **113** (2014) 141802, [[arXiv:1407.7259](#)].
- [117] **Daya Bay, MINOS** Collaboration, P. Adamson et al., *Limits on Active to Sterile Neutrino Oscillations from Disappearance Searches in the MINOS, Daya Bay,*

- and Bugey-3 Experiments, *Phys. Rev. Lett.* **117** (2016), no. 15 151801, [[arXiv:1607.01177](#)]. [Addendum: *Phys. Rev. Lett.* 117,no.20,209901(2016)].
- [118] **MINOS** Collaboration, P. Adamson et al., *Active to sterile neutrino mixing limits from neutral-current interactions in MINOS*, *Phys. Rev. Lett.* **107** (2011) 011802, [[arXiv:1104.3922](#)].
- [119] K. Bora, D. Dutta, and P. Ghoshal, *Probing Sterile Neutrino Parameters with Double Chooz, Daya Bay and RENO*, *JHEP* **12** (2012) 025, [[arXiv:1206.2172](#)].
- [120] S. Gariazzo, C. Giunti, M. Laveder, and Y. F. Li, *Updated Global 3+1 Analysis of Short-BaseLine Neutrino Oscillations*, *JHEP* **06** (2017) 135, [[arXiv:1703.00860](#)].
- [121] **DUNE** Collaboration, T. Alion et al., *Experiment Simulation Configurations Used in DUNE CDR*, [arXiv:1606.09550](#).
- [122] A. de Gouvêa, K. J. Kelly, and A. Kobach, *CP-invariance violation at short-baseline experiments in 3+1 neutrino scenarios*, *Phys. Rev.* **D91** (2015), no. 5 053005, [[arXiv:1412.1479](#)].
- [123] N. Klop and A. Palazzo, *Imprints of CP violation induced by sterile neutrinos in T2K data*, *Phys. Rev.* **D91** (2015), no. 7 073017, [[arXiv:1412.7524](#)].
- [124] M. Masud, A. Chatterjee, and P. Mehta, *Probing CP violation signal at DUNE in presence of non-standard neutrino interactions*, *J. Phys.* **G43** (2016), no. 9 095005, [[arXiv:1510.08261](#)].
- [125] A. de Gouvêa and K. J. Kelly, *Non-standard Neutrino Interactions at DUNE*, *Nucl. Phys.* **B908** (2016) 318–335, [[arXiv:1511.05562](#)].
- [126] P. Coloma, *Non-Standard Interactions in propagation at the Deep Underground Neutrino Experiment*, *JHEP* **03** (2016) 016, [[arXiv:1511.06357](#)].

- [127] J. Liao, D. Marfatia, and K. Whisnant, *Degeneracies in long-baseline neutrino experiments from nonstandard interactions*, *Phys. Rev.* **D93** (2016), no. 9 093016, [[arXiv:1601.00927](#)].
- [128] M. Masud and P. Mehta, *Nonstandard interactions spoiling the CP violation sensitivity at DUNE and other long baseline experiments*, *Phys. Rev.* **D94** (2016) 013014, [[arXiv:1603.01380](#)].
- [129] S. K. Agarwalla, S. S. Chatterjee, and A. Palazzo, *Degeneracy between  $\theta_{23}$  octant and neutrino non-standard interactions at DUNE*, *Phys. Lett.* **B762** (2016) 64–71, [[arXiv:1607.01745](#)].
- [130] M. Blennow, S. Choubey, T. Ohlsson, D. Pramanik, and S. K. Raut, *A combined study of source, detector and matter non-standard neutrino interactions at DUNE*, *JHEP* **08** (2016) 090, [[arXiv:1606.08851](#)].
- [131] K. N. Deepthi, S. Goswami, and N. Nath, *Challenges posed by non-standard neutrino interactions in the determination of  $\delta_{CP}$  at DUNE*, *Nucl. Phys.* **B936** (2018) 91–105, [[arXiv:1711.04840](#)].
- [132] J. Liao, D. Marfatia, and K. Whisnant, *Nonstandard neutrino interactions at DUNE, T2HK and T2HKK*, *JHEP* **01** (2017) 071, [[arXiv:1612.01443](#)].
- [133] S. Fukasawa, M. Ghosh, and O. Yasuda, *Sensitivity of the T2HKK experiment to nonstandard interactions*, *Phys. Rev.* **D95** (2017), no. 5 055005, [[arXiv:1611.06141](#)].
- [134] D. Dutta and P. Ghoshal, *Probing CP violation with T2K, NOvA and DUNE in the presence of non-unitarity*, *JHEP* **09** (2016) 110, [[arXiv:1607.02500](#)].
- [135] D. Dutta, P. Ghoshal, and S. Roy, *Effect of Non Unitarity on Neutrino Mass Hierarchy determination at DUNE, NOvA and T2K*, *Nucl. Phys.* **B920** (2017) 385–401, [[arXiv:1609.07094](#)].

- [136] M. Blennow, P. Coloma, E. Fernandez-Martinez, J. Hernandez-Garcia, and J. Lopez-Pavon, *Non-Unitarity, sterile neutrinos, and Non-Standard neutrino Interactions*, *JHEP* **04** (2017) 153, [[arXiv:1609.08637](#)].
- [137] D. Dutta, P. Ghoshal, and S. K. Sehrawat, *Octant of  $\theta_{23}$  at long baseline neutrino experiments in the light of Non Unitary Leptonic mixing*, *Phys. Rev.* **D95** (2017), no. 9 095007, [[arXiv:1610.07203](#)].
- [138] F. J. Escrihuela, D. V. Forero, O. G. Miranda, M. Tórtola, and J. W. F. Valle, *Probing CP violation with non-unitary mixing in long-baseline neutrino oscillation experiments: DUNE as a case study*, *New J. Phys.* **19** (2017), no. 9 093005, [[arXiv:1612.07377](#)].
- [139] S.-F. Ge, P. Pasquini, M. Tortola, and J. W. F. Valle, *Measuring the leptonic CP phase in neutrino oscillations with nonunitary mixing*, *Phys. Rev.* **D95** (2017), no. 3 033005, [[arXiv:1605.01670](#)].
- [140] F. J. Escrihuela, D. V. Forero, O. G. Miranda, M. Tortola, and J. W. F. Valle, *On the description of nonunitary neutrino mixing*, *Phys. Rev.* **D92** (2015), no. 5 053009, [[arXiv:1503.08879](#)]. [Erratum: *Phys. Rev.* **D93**, no. 11, 119905 (2016)].
- [141] S.-F. Ge and A. Yu. Smirnov, *Non-standard interactions and the CP phase measurements in neutrino oscillations at low energies*, *JHEP* **10** (2016) 138, [[arXiv:1607.08513](#)].
- [142] J. Tang, Y. Zhang, and Y.-F. Li, *Probing Direct and Indirect Unitarity Violation in Future Accelerator Neutrino Facilities*, *Phys. Lett.* **B774** (2017) 217–224, [[arXiv:1708.04909](#)].
- [143] S. Choubey, S. Goswami, and D. Pramanik, *A study of invisible neutrino decay at DUNE and its effects on  $\theta_{23}$  measurement*, *JHEP* **02** (2018) 055, [[arXiv:1705.05820](#)].

- [144] S. S. Chatterjee, A. Dasgupta, and S. K. Agarwalla, *Exploring Flavor-Dependent Long-Range Forces in Long-Baseline Neutrino Oscillation Experiments*, *JHEP* **12** (2015) 167, [[arXiv:1509.03517](#)].
- [145] J. M. Berryman, A. de Gouvêa, K. J. Kelly, O. L. G. Peres, and Z. Tabrizi, *Large, Extra Dimensions at the Deep Underground Neutrino Experiment*, *Phys. Rev.* **D94** (2016), no. 3 033006, [[arXiv:1603.00018](#)].
- [146] S. Choubey, D. Dutta, and D. Pramanik, *Exploring a New Degeneracy in the Sterile Neutrino Sector at Long-Baseline Experiments*, [arXiv:1811.08684](#).
- [147] P. Coloma and T. Schwetz, *Generalized mass ordering degeneracy in neutrino oscillation experiments*, *Phys. Rev.* **D94** (2016), no. 5 055005, [[arXiv:1604.05772](#)]. [Erratum: *Phys. Rev.* **D95**, no. 7, 079903 (2017)].
- [148] M. Masud and P. Mehta, *Nonstandard interactions and resolving the ordering of neutrino masses at DUNE and other long baseline experiments*, *Phys. Rev.* **D94** (2016), no. 5 053007, [[arXiv:1606.05662](#)].
- [149] T. Ohlsson, *Status of non-standard neutrino interactions*, *Rept. Prog. Phys.* **76** (2013) 044201, [[arXiv:1209.2710](#)].
- [150] C. Biggio, M. Blennow, and E. Fernandez-Martinez, *General bounds on non-standard neutrino interactions*, *JHEP* **08** (2009) 090, [[arXiv:0907.0097](#)].
- [151] S. Choubey, A. Ghosh, T. Ohlsson, and D. Tiwari, *Neutrino Physics with Non-Standard Interactions at INO*, *JHEP* **12** (2015) 126, [[arXiv:1507.02211](#)].
- [152] **Super-Kamiokande** Collaboration, G. Mitsuka et al., *Study of Non-Standard Neutrino Interactions with Atmospheric Neutrino Data in Super-Kamiokande I and II*, *Phys. Rev.* **D84** (2011) 113008, [[arXiv:1109.1889](#)].



- [153] **MINOS** Collaboration, P. Adamson et al., *Search for flavor-changing non-standard neutrino interactions by MINOS*, *Phys. Rev.* **D88** (2013), no. 7 072011, [[arXiv:1303.5314](#)].
- [154] F. Capozzi, G. L. Fogli, E. Lisi, A. Marrone, D. Montanino, and A. Palazzo, *Status of three-neutrino oscillation parameters, circa 2013*, *Phys. Rev.* **D89** (2014) 093018, [[arXiv:1312.2878](#)].
- [155] D. V. Forero, M. Tortola, and J. W. F. Valle, *Neutrino oscillations refitted*, *Phys. Rev.* **D90** (2014), no. 9 093006, [[arXiv:1405.7540](#)].
- [156] M. C. Gonzalez-Garcia, M. Maltoni, and T. Schwetz, *Updated fit to three neutrino mixing: status of leptonic CP violation*, *JHEP* **11** (2014) 052, [[arXiv:1409.5439](#)].
- [157] **T2K** Collaboration, K. Abe et al., *Measurements of neutrino oscillation in appearance and disappearance channels by the T2K experiment with  $6.6 \times 10^{20}$  protons on target*, *Phys. Rev.* **D91** (2015), no. 7 072010, [[arXiv:1502.01550](#)].
- [158] **NOvA** Collaboration, P. Adamson et al., *First measurement of electron neutrino appearance in NOvA*, *Phys. Rev. Lett.* **116** (2016), no. 15 151806, [[arXiv:1601.05022](#)].
- [159] M. Ghosh, S. Goswami, and S. K. Raut, *Implications of  $\delta_{CP} = -90^\circ$  towards determining hierarchy and octant at T2K and T2K-II*, *Mod. Phys. Lett.* **A32** (2017), no. 06 1750034, [[arXiv:1409.5046](#)].
- [160] P. Coloma, H. Minakata, and S. J. Parke, *Interplay between appearance and disappearance channels for precision measurements of  $\theta_{23}$  and  $\delta$* , *Phys. Rev.* **D90** (2014) 093003, [[arXiv:1406.2551](#)].

- [161] M. Ghosh, P. Ghoshal, S. Goswami, N. Nath, and S. K. Raut, *New look at the degeneracies in the neutrino oscillation parameters, and their resolution by T2K, NOvA and ICAL*, *Phys. Rev.* **D93** (2016), no. 1 013013, [[arXiv:1504.06283](#)].
- [162] N. Nath, M. Ghosh, and S. Goswami, *The physics of antineutrinos in DUNE and determination of octant and  $\delta_{CP}$* , *Nucl. Phys.* **B913** (2016) 381–404, [[arXiv:1511.07496](#)].
- [163] A. Acker, S. Pakvasa, and J. T. Pantaleone, *Decaying Dirac neutrinos*, *Phys. Rev.* **D45** (1992) 1–4.
- [164] A. Acker and S. Pakvasa, *Solar neutrino decay*, *Phys. Lett.* **B320** (1994) 320–322, [[hep-ph/9310207](#)].
- [165] G. B. Gelmini and M. Roncadelli, *Left-Handed Neutrino Mass Scale and Spontaneously Broken Lepton Number*, *Phys. Lett.* **99B** (1981) 411–415.
- [166] Y. Chikashige, R. N. Mohapatra, and R. D. Peccei, *Are There Real Goldstone Bosons Associated with Broken Lepton Number?*, *Phys. Lett.* **98B** (1981) 265–268.
- [167] C. W. Kim and W. P. Lam, *Some remarks on neutrino decay via a Nambu-Goldstone boson*, *Mod. Phys. Lett.* **A5** (1990) 297–299.
- [168] A. Acker, A. Joshipura, and S. Pakvasa, *A Neutrino decay model, solar anti-neutrinos and atmospheric neutrinos*, *Phys. Lett.* **B285** (1992) 371–375.
- [169] M. Lindner, T. Ohlsson, and W. Winter, *A Combined treatment of neutrino decay and neutrino oscillations*, *Nucl. Phys.* **B607** (2001) 326–354, [[hep-ph/0103170](#)].
- [170] J. N. Bahcall, N. Cabibbo, and A. Yahil, *Are neutrinos stable particles?*, *Phys. Rev. Lett.* **28** (1972) 316–318. [,285(1972)].
- [171] Z. G. Berezhiani, G. Fiorentini, M. Moretti, and A. Rossi, *Fast neutrino decay and solar neutrino detectors*, *Z. Phys.* **C54** (1992) 581–586.

- [172] Z. G. Berezhiani, M. Moretti, and A. Rossi, *Matter induced neutrino decay and solar anti-neutrinos*, *Z. Phys.* **C58** (1993) 423–428.
- [173] S. Choubey, S. Goswami, and D. Majumdar, *Status of the neutrino decay solution to the solar neutrino problem*, *Phys. Lett.* **B484** (2000) 73–78, [[hep-ph/0004193](#)].
- [174] A. Bandyopadhyay, S. Choubey, and S. Goswami, *MSW mediated neutrino decay and the solar neutrino problem*, *Phys. Rev.* **D63** (2001) 113019, [[hep-ph/0101273](#)].
- [175] A. S. Joshipura, E. Masso, and S. Mohanty, *Constraints on decay plus oscillation solutions of the solar neutrino problem*, *Phys. Rev.* **D66** (2002) 113008, [[hep-ph/0203181](#)].
- [176] A. Bandyopadhyay, S. Choubey, and S. Goswami, *Neutrino decay confronts the SNO data*, *Phys. Lett.* **B555** (2003) 33–42, [[hep-ph/0204173](#)].
- [177] R. Picoreti, M. M. Guzzo, P. C. de Holanda, and O. L. G. Peres, *Neutrino Decay and Solar Neutrino Seasonal Effect*, *Phys. Lett.* **B761** (2016) 70–73, [[arXiv:1506.08158](#)].
- [178] **SNO** Collaboration, B. Aharmim et al., *Constraints on Neutrino Lifetime from the Sudbury Neutrino Observatory*, *Phys. Rev.* **D99** (2019), no. 3 032013, [[arXiv:1812.01088](#)].
- [179] J. A. Frieman, H. E. Haber, and K. Freese, *Neutrino Mixing, Decays and Supernova Sn1987a*, *Phys. Lett.* **B200** (1988) 115–121.
- [180] V. D. Barger, J. G. Learned, S. Pakvasa, and T. J. Weiler, *Neutrino decay as an explanation of atmospheric neutrino observations*, *Phys. Rev. Lett.* **82** (1999) 2640–2643, [[astro-ph/9810121](#)].

- [181] P. Lipari and M. Lusignoli, *On exotic solutions of the atmospheric neutrino problem*, *Phys. Rev.* **D60** (1999) 013003, [[hep-ph/9901350](#)].
- [182] G. L. Fogli, E. Lisi, A. Marrone, and G. Scioscia, *Super-Kamiokande data and atmospheric neutrino decay*, *Phys. Rev.* **D59** (1999) 117303, [[hep-ph/9902267](#)].
- [183] S. Choubey and S. Goswami, *Is neutrino decay really ruled out as a solution to the atmospheric neutrino problem from Super-Kamiokande data?*, *Astropart. Phys.* **14** (2000) 67–78, [[hep-ph/9904257](#)].
- [184] V. D. Barger, J. G. Learned, P. Lipari, M. Lusignoli, S. Pakvasa, and T. J. Weiler, *Neutrino decay and atmospheric neutrinos*, *Phys. Lett.* **B462** (1999) 109–114, [[hep-ph/9907421](#)].
- [185] **Super-Kamiokande** Collaboration, Y. Ashie et al., *Evidence for an oscillatory signature in atmospheric neutrino oscillation*, *Phys. Rev. Lett.* **93** (2004) 101801, [[hep-ex/0404034](#)].
- [186] M. C. Gonzalez-Garcia and M. Maltoni, *Status of Oscillation plus Decay of Atmospheric and Long-Baseline Neutrinos*, *Phys. Lett.* **B663** (2008) 405–409, [[arXiv:0802.3699](#)].
- [187] R. A. Gomes, A. L. G. Gomes, and O. L. G. Peres, *Constraints on neutrino decay lifetime using long-baseline charged and neutral current data*, *Phys. Lett.* **B740** (2015) 345–352, [[arXiv:1407.5640](#)].
- [188] T. Abrahão, H. Minakata, H. Nunokawa, and A. A. Quiroga, *Constraint on Neutrino Decay with Medium-Baseline Reactor Neutrino Oscillation Experiments*, *JHEP* **11** (2015) 001, [[arXiv:1506.02314](#)].
- [189] S. Choubey, S. Goswami, C. Gupta, S. M. Lakshmi, and T. Thakore, *Sensitivity to neutrino decay with atmospheric neutrinos at the INO-ICAL detector*, *Phys. Rev.* **D97** (2018), no. 3 033005, [[arXiv:1709.10376](#)].

- [190] M. Bustamante, J. F. Beacom, and K. Murase, *Testing decay of astrophysical neutrinos with incomplete information*, *Phys. Rev.* **D95** (2017), no. 6 063013, [[arXiv:1610.02096](#)].
- [191] S. Choubey, D. Dutta, and D. Pramanik, *Invisible neutrino decay in the light of NOvA and T2K data*, *JHEP* **08** (2018) 141, [[arXiv:1805.01848](#)].
- [192] J. M. Berryman, A. de Gouvêa, D. Hernández, and R. L. N. Oliveira, *Non-Unitary Neutrino Propagation From Neutrino Decay*, *Phys. Lett.* **B742** (2015) 74–79, [[arXiv:1407.6631](#)].
- [193] A. M. Dziewonski and D. L. Anderson, *Prem profile*, *Phys. Earth and Planet Int.* **25** (1981) 297.
- [194] **NOvA** Collaboration, P. Adamson et al., *First measurement of muon-neutrino disappearance in NOvA*, *Phys. Rev.* **D93** (2016), no. 5 051104, [[arXiv:1601.05037](#)].
- [195] **NOvA** Collaboration, P. Adamson et al., *Measurement of the neutrino mixing angle  $\theta_{23}$  in NOvA*, *Phys. Rev. Lett.* **118** (2017), no. 15 151802, [[arXiv:1701.05891](#)].
- [196] **NOvA** Collaboration, P. Adamson et al., *Constraints on Oscillation Parameters from  $\nu_e$  Appearance and  $\nu_\mu$  Disappearance in NOvA*, *Phys. Rev. Lett.* **118** (2017), no. 23 231801, [[arXiv:1703.03328](#)].
- [197] A. Radovic, *Latest Oscillation Results from NOvA*, *Fermilab JETP seminar* (January 12, 2018).
- [198] **T2K** Collaboration, K. Abe et al., *Indication of Electron Neutrino Appearance from an Accelerator-produced Off-axis Muon Neutrino Beam*, *Phys. Rev. Lett.* **107** (2011) 041801, [[arXiv:1106.2822](#)].

- [199] **T2K** Collaboration, K. Abe et al., *First Muon-Neutrino Disappearance Study with an Off-Axis Beam*, *Phys. Rev.* **D85** (2012) 031103, [[arXiv:1201.1386](#)].
- [200] **T2K** Collaboration, K. Abe et al., *Measurement of Muon Antineutrino Oscillations with an Accelerator-Produced Off-Axis Beam*, *Phys. Rev. Lett.* **116** (2016), no. 18 181801, [[arXiv:1512.02495](#)].
- [201] **T2K** Collaboration, K. Abe et al., *Measurement of neutrino and antineutrino oscillations by the T2K experiment including a new additional sample of  $\nu_e$  interactions at the far detector*, *Phys. Rev.* **D96** (2017), no. 9 092006, [[arXiv:1707.01048](#)]. [Erratum: *Phys. Rev.* **D98**, no. 1, 019902 (2018)].
- [202] S. K. Raut, *Effect of non-zero  $\theta(13)$  on the measurement of  $\theta(23)$* , *Mod. Phys. Lett.* **A28** (2013) 1350093, [[arXiv:1209.5658](#)].